Important Notice

Advanced Marine Seismic Methods: Ocean-Bottom and Vertical Cable Analyses

by

Carlos Rodriguez Suarez

Ph.D. Thesis
University of Calgary
Department of Geology and Geophysics
February, 2000

CREWES

Consortium for Research in
Elastic Wave Exploration Seismology

Thesis defence committee:

Supervisor, Robert R. Stewart, Geology and Geophysics

Larry R. Lines, Geology and Geophysics

Gary F. Margrave, Geology and Geophysics

Michael A. Slawinski, Mechanical Engineering

Robert H. Tatham, University of Texas at Austin

Abstract

An overview of ocean-bottom and vertical-cable seismic acquisition and processing techniques, including applications and limitations, is presented.

Shear-wave velocities for ocean-bottom marine sediments were calculated using literature data and offshore-Brazil geotechnical data. Transmission and reflection coefficients for P- and S-wave mode conversion were obtained for sea bottom and Tertiary sediment interfaces. I conclude that most S-wave data recorded on ocean-bottom cables in Tertiary sections are related to upcoming P- to S- conversions at deeper interfaces.

A 2-D seismic line (Valhall Field, Norway) and a 3-D survey (Teal South, Gulf of Mexico), both acquired using four-component (4-C) receivers placed in ocean bottom cables, are processed.

In the 2-D line, P-P reflection data recorded by hydrophone and vertical geophone components did not provide interpretable images of the reservoir region. The P-SV reflections recorded by radial geophone component gives reasonable converted-wave (P-S) images.

In the 3-D survey, the best quality structural data were present on the P-P reflections recorded by the hydrophone, followed by P-P data recorded in the vertical geophone and then P-SV data recorded by radial geophone components. No significant differences were found among three methods used for cable deployment (trenched, sandbagged, and laid) in the P-P data recorded by the hydrophone; the taped system seems to give better results for P-SV data recorded on the radial component. Little compressional wave energy was found on the radial geophone component, but the vertical geophone component is contaminated with SV energy that correlated with the radial motion.

From the analysis of vertical cable geometry, it was found that using a single vertical cable attached to the sea floor, good fold and lateral coverage can be obtained with the use of a reasonable number of receivers per cable and densely spaced surface shot points. However, poor offset and azimuth distribution per bin occurs. When several cables are used fold, offset and azimuth distribution can be improved with optimised cable positioning. Expressions relating coverage with seismic acquisition parameters and water depth were empirically derived; these expressions may give preliminary parameters for vertical cable survey design.

Acknowledgements

To my wife, Monica, for all her love, support, and help during these long three and a half years. Now is the time to go to the mountains and have a (expanded) family again.

To my advisor, Prof. Robert Stewart, for his various suggestions and valuable hints concerning my research.

To Mr. Xinxiang Li and Dr. Gustavo Ponce Correa, for all their friendly help and fine discussions about distinct subjects – seismic being just one of them.

To PETROBRAS, for support and trust, by giving me the opportunity to expand my knowledge. Special thanks for Mr. Airton H. Okada, Dr. Lideniro Alegre, and Mr. Miton J. de Souza and Ms. Nazareth Carril.

To department and CREWES professors for all discussions, ideas, suggestions and arguments along my time as a student at U of C. I especially recognise Prof. Gary Margrave, Prof. Ed Krebes, Prof. Larry Lines, and Prof. John Bancroft. To CREWES staff, especially Ms. Louise Forgues, Mr. Mark Kirtland and Ms. Han-Xing Lu, for their support on everyday life. Special thanks to Mr. Henry Bland and Mr. Darren Foltinek, for their constant computer-systems and software help.

To CREWES students, for the same reasons listed above, plus some drink and food at Grad Lounge, Kananaskis, or New Orleans - when not in someone's house. I will miss Chanpen, Jeetu, Nasser, Saul, Todor, and Yong.

To CREWES sponsors, without whom it would not be possible to have so much software and hardware, absolutely necessary in my research, available.

To Prof. John Castagna (Univ. of Oklahoma), Prof. Ian Hutcheon and Ms. Regina Shedd, for their help and suggestions at the beginning of this journey and during some of its difficult times.

To Drs. C. Pettenati-Auziére (CGG), Peter Cary (Sensor), Eivind Fromyr (PGS), Jan Langhammer (PGS), Bill Pramik (PGS), and Zyg Shevchek (Mobil), for their valuable discussions and information about aspects of seismic

acquisition and processing.

To Mr. Paulo Roberto Maldonado, from PETROBRAS, for his help on releasing the geotechnical information from offshore Brazil.

To Amoco Exploration and Production, Amoco Norway and their partners in the Valhall License (Amerada Hess Norge, Elf Petroleum Norge and Enterprise Oil Norge) and PGS Norway for the permission to present the Valhall data. To Mr. Christian Strand, from PGS, and Dr. Mark Harrison, from Matrix Geoservice Ltd., for information and discussions about Valhall data acquisition and processing. To Ms. Medina Deuling (Department of Geography), for geographical-UTM co-ordinate conversion in the Valhall area.

To Mr. Brian Hoffe (CREWES) and Mr. Roger Entralgo (ERCH) for their information about the Teal South survey.

To Ms. Susan Collins (from GX Technology) for her support and help in using GX 3D-VSP^{TM} and to Mr. Ricardo Rubio (PETROBRAS) for preparing the seismic interpretation and velocities used in vertical cable analyses.

Finally, to the members of my candidacy and thesis defense committees, for spending their valuable time and attention evaluating my (lack of) knowledge and the work that I have (and have not) done.

To my wife, parents, and future offspring.

Table of Contents

Abstract ... iii

Acknowledgements ... v

Table of Contents ... ix

List of Tables ... xii

List of Figures ... xiii

Chapter I – Introduction ... 1

Chapter II – The Ocean Bottom Cable (OBC) Technique ... 5

II.1 Shear-wave applications ... 5

II.2 OBC technique: overview and examples ... 8

II.3 OBC acquisition ... 16

II.4 OBC data processing ... 27

II.5 Discussion ... 34

Chapter III – Sea-Bottom Shear-Wave Velocities and Mode Conversions ... 35

III.1 Introduction ... 35

III.2 Physical properties of marine sediments: overview of literature data ... 35

III.3 Shear-wave velocities from offshore Brazil: direct measurements and geotechnical data ... 38

III.4 Mode conversion for down- and up-going wavefields ... 44

III.5 Discussion ... 56

Chapter IV – Analysing 4-C 2-D OBC Data from the Valhall Field, Norway ... 57

IV.I Introduction *57*

IV.2 Valhall field: geology and seismic aspects *57*

IV.3 Seismic acquisition *62*

IV.4 Processing sequence in ProMAX: results and comments *64*

- IV.4.1 Hydrophone and vertical geophone components 66
- IV.4.2 Radial component 70
- IV.4.3 Transverse component 78
- IV.4.4 P-S flow in vertical component, P-P flow in radial and transverse components 79

IV.5 Discussion *80*

Chapter V – Processing the Teal South 4C-4D Seismic Survey 83

V.1 Introduction *83*

V.2 Seismic data acquisition *85*

V.3 Pre-processing and quality control *88*

V.4 Vertical geophone (P-P reflections) and hydrophone components *96*

V.5 Radial and transverse (P-SV reflections) geophone components *105*

V.6 Comparison of cable deployment techniques *113*

V.7 - P-S energy in vertical geophone component, P-P in radial geophone . *118*

V.8 – Azimuthal anisotropy (VTI) checked by azimuth stack *123*

V.9 – Acquisition footprints *126*

V.10 - Discussion *130*

Chapter VI – Vertical Cable: Survey Design and Preliminary Processing. 133

VI.1 Introduction *133*

VI.2 Vertical cable technique: overview and examples *134*

VI.3 Survey design: geological model and ray tracing *142*

VI.4 Target imaging: results and comments *148*

VI.5 Empirical expressions for coverage *163*

VI.6 3-D vertical cable processing using EOM *165*

VI.6.1 Introduction.................................. 165
VI.6.2 Geological model and ray tracing 166
VI.6.3 Data processing: results and comments.................................. 171

VI.7 Discussion *174*

Chapter VII – Conclusions 177

References 181

Appendix I – Acquisition parameters for the Valhall seismic survey (after PGS, 1996) 201

Appendix II – Acquisition parameters for Teal South seismic survey (after Baker Hughes, 1999).................................. 203

Appendix III - Matlab function used to obtain bin fold, azimuth and offset distribution 205

List of Tables

Table 3.4.1 - Elastic parameters for reservoir (turbidite) and overburden Tertiary rocks. 47

Table 6.3.1- Velocity parameters, Poisson's ratio and thickness values for layers in the numerical geological model..144

Table 6.6.2.1 - P-wave velocities and densities of model layers: minimum, maximum, and average...166

List of Figures

Figure 2.3.1 - Examples of a 4-C receiver (left) and the same receiver connected to a cable (right) (after Entralgo and Wadsworth, 1999). 16

Figure 2.3.2 - Examples of ocean bottom cables (after Entralgo and Wadsworth, 1999). 17

Figure 2.3.3 - Examples of single nodes 4-C receivers (after Entralgo and Wadsworth, 1999). Mechanical arms of remote operated vehicles (ROV) plant the sensors. 18

Figure 2.3.4 - Examples of 4-C receivers in an ocean bottom cable (after Caldwell et al., 1999). From left to right, the hydrophone (pressure sensitive), radial (inline), transverse (crossline) and vertical components. Weight distribution gives a better coupling and receiver array groups may be formed. 19

Figure 2.4.1 – Asymptotic approximation for conversion point. 30

Figure 3.2.1 – Top: V_P values for marine sediments from Hamilton (1976; 1979). Observe the distinct curves for siliciclastic and sand lithologies. Bottom: V_S values for marine sediments from Hamilton (1976; 1979). Unlike V_P, the curves for different lithologies are similar. All curves from in-situ measurements. 37

Figure 3.3.1 – Concomitant offshore acquisition of conventional geotechnical and V_S information (after de Lange, 1991). 39

Figure 3.3.2 – Correlation between S_U (shear strength) and μ (dynamic shear modulus) for cores from 9 m of shallow sediments in the Barents Sea (after Theilen and Pecher, 1991). Observe that the correlation is close to linear, μ being about 200 times greater than S_U. 41

Figure 3.3.3 – Correlation factor f ($=\mu/S_U$). Average from six offshore Brazil locations where both V_s and S_U were measured in-situ. 42

Figure 3.3.4 – V_S obtained from averaging in-situ direct and indirect (geotechnical) data in 30 locations offshore Brazil (continuous line). Also shown for comparison are values expected from Hamilton (dashed) and second order (dash-dot) and exponential (dotted) fit equations of the continuous line data. The empirical expressions are valid for a common ('soft') sea bottom. 43

Figure 3.4.1 –Transmission coefficient variation at sea-bottom (down-going incident P-wave) for different sediment thickness considered for elastic parameters averaging. PP (top) and PS (bottom). 46

P mode. For the P-S mode, it can be seen that more shear wave is generated as deeper sediments are considered in the average. This is expected, as a drastic increase in V_S occurs in these shallow depths. In Figure 3.3.4, for instance, V_S at 20 m is four times greater than that at just below sea floor. 46

Figure 3.4.2 – Transmission coefficients for downgoing PP (dashed) and PS (solid) seismic waves in a sea/sediment interface. Energy (proportional to square of amplitude) for PP is more

than 100 times larger than for PS. *48*

Figure 3.4.3 – Reflection coefficient at top of turbidite reservoir for P-S (solid) and S-S (dash-dot) seismic waves. Up to 70^0, modes have (relatively) close reflection coefficient values. *48*

Figure 3.4.4 – Amplitude coefficients for PP-S mode (PP transmission at sea bottom and P-S conversion at reservoir top, solid line) and PS-S mode (PS conversion at sea bottom and S-S reflection at reservoir top, dash-dot line). Clearly, PP-S mode has much higher energy than PS-S. *49*

Figure 3.4.5 – Ratio between PP-S energy and PS-S energy, clipped to a maximum value of 500. It is shown that PP-S energy is rarely less than 50 times greater than PS-S energy, and values over 100 may be expected from most angles used in seismic acquisition. *50*

Figure 3.4.6 – Average of 30 in-situ density values measurements in marine sediments. Depths of 5,20,90 and 160 m were defined as boundaries to analyse mode conversion. These values were also used for V_S calculation in this chapter. *51*

Figure 3.4.7 – Transmission coefficients for up-going P-wave (PP dashed and PS solid) at (from top to bottom) interfaces located at 5, 20, and 90 m depth. Most energy does not suffer mode conversion. *53*

Figure 3.4.8 – Transmission coefficients for up-going P-wave (PP dashed and PS solid) at 160 m depth (top) and for up-going S-wave (SS dashed and SP solid) at 5 m (middle) and 20 m (bottom). Most energy does not suffer mode conversion. *54*

Figure 3.4.9 – Transmission coefficients for up-going S-wave (SS dashed and SP solid) at 90 m (top) and 160 m (middle) and for S- and P-wave up-going at sea-bottom (bottom, PP dashed, SP solid). Most energy does not suffer mode conversion. *55*

Figure 4.2.1. (a) Localisation of the Valhall field; (b) indication of seismic line on a depth map of the top of the chalk (both after Leonard and Munns, 1987). *59*

Figure 4.2.2 – Correlation between increasing porosity and decreasing V_P (left) and V_S (right), obtained from Cretaceous chalk cores in the Valhall area (after D'Angelo et al., 1997). *61*

Figure 4.4.1 - Hydrophone CDP gather (from a position out of the gas chimney). Amplitude recovery and minimum-phase deconvolution applied. *67*

Figure 4.4.2 – Average amplitude spectrum from all traces and time 0.0 to 6.0 s hydrophone gather (Figure 4.4.1). Observe the strong notches around 10 and 20 Hz. *67*

Figure 4.4.3 - Vertical component CDP gather (from a position out of gas chimney). Observe very low frequencies and velocities of Scholte waves. *68*

Figure 4.4.4 - Amplitude spectrum from vertical component gather (Figure 4.4.3). Observe strong notches and energy decreases toward higher frequencies. *68*

Figure 4.4.5 - Migrated section of hydrophone data. Observe pushdown and reflection-free zone at the centre of the line. *69*

Figure 4.4.6 - Migrated section of vertical component data. 69
Figure 4.4.7 - NMO-corrected common-conversion-point asymptotic binning (ACCP) gather of radial component data. 72
Figure 4.4.8 - Amplitude spectrum of radial component ACCP gather (Figure 4.4.7). Observe the strong notches inside the signal band (5-30 Hz). 72
Figure 4.4.9 - NMO-corrected common scatter point (CSP) radial-component gather after equivalent offset migration (EOM). Observe higher energy content than ACCP gather (Figure 4.4.7). 74
Figure 4.4.10 - Amplitude spectrum of radial-component CSP gather (Figure 4.4.9). Observe the flatten spectrum (neglecting notches) in the signal bandwidth. 74
Figure 4.4.11 – Conventional stack using asymptotic binning (with V_P/V_S =2.5) of the radial-component data. 76
Figure 4.4.12 - Kirchhoff migration on data from Figure 4.4.11. 76
Figure 4.4.13 - Converted-wave DMO, conventional stack, Kirchhoff migration in radial-component data. Compare with Figures 4.4.12 and 4.4.14 (see text for discussion). 77
Figure 4.4.14 - Equivalent-offset migration (EOM) and conventional stack in radial-component data. Compare with Figures 4.4.12 and 4.4.13 (see text for discussion). 77
Figure 4.4.15 - Conventional stack (V_P/V_S =2.5) after ACCP (asymptotic binning) in transverse-component data. 78
Figure 4.4.16 - P-S flow (ACCP binning and conventional stack) applied in vertical-component data. Events in this section correlates with events in vertical-component data processed with P-P flow (Figure 4.4.6). 79
Figure 4.4.17 - P-P flow applied in radial-component data. 80
Figure 5.1.1 – Location of the Teal South field in the Gulf of Mexico (after Ebrom et al., 1998b). 84
Figure 5.2.1 – Map view of shot point (grey) and receiver (white) position. Observe shot gaps (due to obstacles), four receiver cables along E-W (with six units), and three cables along N-S (four units). E-W cables and westernmost N-S cable were trenched, middle N-S cable was laid on sea-bottom and had receivers taped to the cable and easternmost N-S cable was laid on sea-bottom and had receivers taped and sandbagged. Distances in metres. 86
Figure 5.2.2 – 4-C receiver unit used in data acquisition (left) and the same unit attached (taped) to a cable (right) (after www.erch.com). 87
Figure 5.2.3 – 4-C receiver unit of Figure 5.2.2 being sandbagged (after www.erch.com). This method is licensed by Atlantic Richfield Co (Sullivan, 1995). 87
Figure 5.2.4 – Recording buoy (left) and tape with seismic data being recovered (right) (after www.erch.com). 88
Figure 5.3.1 – Map view of CDP fold for vertical and hydrophone (left) and radial and transverse

after ACCP binning using Vp/Vs of 2.0 (right). Note poor coverage distribution and very high number of zero-fold bins (in the histogram) for the horizontal components..................................89

Figure 5.3.2 – Reorientation of horizontal components. On left the input (original) data from a specific source-receiver pair (from left, vertical, radial and transverse components). In the middle, the three components after horizontal rotation: most horizontal energy is aligned in the source-receiver direction (trace 2). At right the traces after vertical rotation (not used in this processing). The thick lines from around 1310 to 1370 ms shows the time window used for the energy alignment. Top right shows the original (acquisition) orientation on thin axis and the energy alignment along the new direction (dots and thick axis). The new radial component is defined by this energy alignment, the new transverse by its orthogonal. Bottom right is as top right, but for a (new) radial and vertical hodogram. 91

Figure 5.3.3 – Comparison of two radial component traces before (left) and after (right) reorientation. Both traces are related to the same shot point, the left trace for a receiver located west of the shot (negative offset), the trace at right at east of the shot point (positive offset). The thick line at the top shows the original component azimuth (close to 90^0); the thin line the new (source-receiver) azimuth after reorientation. Observe that on the left trace the azimuth is not changed, while for the trace at right an 180^0 phase change occurs. The apparent phase difference is due to different travel time plus different static correction (not applied yet). 92

Figure 5.3.4 – Map view of average energy per trace for vertical (top left), hydrophone (top right), radial (bottom left) and transverse (bottom right) components. Observe higher heterogeneity for energy distribution in hydrophone component. 94

Figure 5.3.5 – Average dominant frequency per trace for vertical (top left), hydrophone (top right), radial (bottom left) and transverse (bottom right). No explanation could be found for the sharp variation in the dominant frequency distribution (most clearly seen in the hydrophone at the arrow location, but present in all components). Relatively low frequency in vertical (20 Hz) may be due to presence of S-wave energy...95

Figure 5.4.1 – Example of CDP gathers for vertical (left) and hydrophone (right) components. ...96

Figure 5.4.2 – Amplitude spectra of CDP gathers (Figure 5.4.1) for vertical geophone (left) and hydrophone (right) components. 97

Figure 5.4.3 – Static corrections for the source, obtained in the vertical component and applied to all components. First (left) and third (right) run of residual statics by cross-correlation. No hand statics were applied for the shots. 98

Figure 5.4.4 – Static receiver corrections for hydrophone: hand (left) and residual (right), both after the first iteration...99

Figure 5.4.5 – Comparison of migrated P-P data without (left) and with (right) DMO for vertical geophone (top) and hydrophone (bottom) components...100

Figure 5.4.6 – Velocity analysis after DMO. Black function show velocity picked on data without DMO, white function velocity picked after DMO. 101

Figure 5.4.7 – Amplitude spectra of stacked and migrated sections (without DMO, Figure 5.4.5) for vertical geophone (left) and hydrophone (right) components. 101

Figure 5.4.8 – Comparison between data after DMO, stack and post-stack finite difference migrated (left) and after EOM and stack (right). Vertical component results are on top and hydrophone at bottom. Observe lower frequency and less event continuity in EOM results.......103

Figure 5.4.9 – Processing flow for vertical and hydrophone component. The shot static was obtained only in the vertical flow. In the hydrophone amplitude recovery, an inelastic correction (α) of 0.002 was also used. 104

Figure 5.5.1 – Radial component ACCP gather after horizontal reorientation and asymptotic binning (V_P/V_S =2.0) and its amplitude spectrum..106

Figure 5.5.2 – Hand (left) and residual (right) radial component receiver statics, both after three runs...106

Figure 5.5.3 – Comparison between stacked data after ACCP binning (V_P/V_S = 2.0) from radial (left) and transverse (right) components. The radial component has better quality. Trace interval 25 m..107

Figure 5.5.4 – Comparison between stacked radial data without (left) and with (right) converted-wave DMO. Bin fold is shown at the top of the sections (folds are different – and more homogeneous in the DMO case – due to DMO binning). Trace interval 25 m. 108

Figure 5.5.5 – Comparison between conventional (left) and depth variant stack (right) for the P-SV data recorded on the radial component. Poor result on depth-variant stack is probably related to use of incorrect V_P/V_S ratios. Bin fold is shown at the top of the sections. Trace interval 25 m. 109

Figure 5.5.6 – Comparison between conventional (left) and anisotropic stack (right) for the P-SV data recorded on the radial component. Bin fold is shown at the top of the sections. Trace interval 25 m..110

Figure 5.5.7 – Comparison between post-stack finite-difference migration (left) and EOM followed by stack (right). Trace interval 25 m. 111

Figure 5.5.8 – Processing flow for radial and transverse components. 112

Figure 5.6.1 – Comparison between data collected using cable trenched 1 m below sea bottom (left) and cable with taped receivers (right). Hydrophone recording of the P-P data at top and radial geophone recording of the P-SV data at bottom. Trace distance 25 m. 114

Figure 5.6.2 – Comparison between data collected from cable trenched (left) and with sensors taped and sandbagged (right). Hydrophone recording of the P-P data at top and radial geophone recording of the P-SV data at bottom. Trace distance 25 m. 115

Figure 5.6.3 – Comparison between data collected from cable taped and sandbagged (left) and taped (right). Hydrophone recording of the P-P data at top and radial geophone recording of the P-SV data at bottom. Trace distance 25 m. 116

Figure 5.6.4 – Amplitude spectra of stacked section for hydrophone recording of the P-P data (top) and radial geophone recording of the P-SV data (bottom) components data. 118

Figure 5.7.1 – Comparison between radial component data processed with 'conventional' flow (shown in Figure 5.5.8), at left, and the same data processed with P-wave parameters, at right. Trace interval 25 m...119

Figure 5.7.3 – Effect of receiver-ghost (receiver-side multiple) in hydrophone (W phone) and vertical geophone (Z phone) components for up-going P-P energy close to vertical. For high (≥ 0.35) R_1 (sea-bottom reflection coefficient), receiver ghost is more attenuated in the vertical geophone (Z) than in the hydrophone (W) component (modified from Brown and Yan, 1999)...122

Figure 5.8.1 – Azimuth stack for P-P (hydrophone, at top) and P-SV (radial geophone, at bottom) data. Compare 0^0-45^0 to 180^0-225^0 and 90^0-135^0 to 270^0-315^0. Bin fold shown at top of the picture. Trace distance 25 m...125

Figure 5.9.1 – Time-slices for P-P (hydrophone) at 1.0 s (top) and P-SV (radial geophone) at 1.5 s (bottom). Effect of shot point direction (along N-S) is clear in the data, especially in the P-SV data....127

Figure 5.9.2 – Time-slices for P-P (hydrophone) at 2.0 s (top) and P-SV (radial geophone) at 3.0 s (bottom). The shot point footprint (N-S direction) can be seen in both data sets......................128

Figure 5.9.3 – Time-slices for P-P (hydrophone) at 3.0 s (top) and P-SV (radial geophone) at 4.5 s (bottom). The shot point footprint (N-S direction) can be seen in both data sets......................129

Figure 6.2.1 – Acquisition schemes for streamer (left) and vertical cable (right) (after Krail, 1997). 135

Figure 6.2.2 – Scheme of a vertical-cable (after Krail, 1994a)....136

Figure 6.2.3 – On left, indication of up- and down-going rays' illumination. On right, example of shot (left) and receiver (right) gathers of physical modelling data. Both pictures after Guimarães et al. (1998). 137

Figure 6.2.4 – Comparison between data from Gulf of Mexico, acquired with streamer and processed with 3-D post-stack migration (left), and data acquired with vertical cable and processed using 3-D pre-stack depth migration (right) (after Krail, 1994b). 138

Figure 6.2.5 – Comparison between streamer (left) and vertical cable (right) sections, showing a salt diapir. Both data processed with 3-D pre-stack depth migration (after Anderson et al., 1997). The authors conclude the results are similar....139

Figure 6.3.1 – 3-D view of the geological model (1,000 m water depth). Target is the fourth interface from top, around 3,000 m. Five cables are also shown. Distances in metres...............143

Figure 6.3.2 – (a) vertical section along Y-axis showing slight curvature of target (around 3,000 m) for the 50 m water depth model; (b) vertical section along X-axis showing interfaces (including target) dipping around 6% for the 500 m water depth model. Maximum target thickness 20 m. (distances in metres, not to scale)....144

Figure 6.3.3 – Top (map) view of model limits (0 to 6,000), shot point grid (diamonds, from 1,000 to 5,000) and target (grey square, 2,000 to 4,000). Five cables are also shown, indicated by black dots. Distances in metres. 145

Figure 6.3.4 – Example of source-receivers ray paths. Source at sea-level and receivers along cable at the centre of the model. 146

Figure 6.3.5 – Vertical profiles (along X direction) showing source-receiver rays for three shots in the P-P (left) and PP-SP (right) modes. Observe PP-SP images points close to the cable. 147

Figure 6.4.1 – Fold for one cable at centre and 500 m water depth: 16 hydrophones spaced 30 m (left) and 32 hydrophones spaced 15 m (right). Shot point grid 100 X 200 m. Observe coverage more than doubles when twice receivers are used. 148

Figure 6.4.2 – Fold for one cable (with 16 hydrophones spaced 30 m) at centre and 500m water depth; shot point grid of 100 x 200 m (left) and 50 x 100 m (right). Smaller shooting grid gives higher and more homogenous coverage. 149

Figure 6.4.3 – Fold for one cable at centre, 500 m water depth, 16 hydrophones spaced 30 m, SP grid 100 X 200 m. At left, P-P mode, at right PP-SP mode. Converted wave gives higher and more homogeneous coverage, but over a smaller area than P-P. 150

Figure 6.4.4 – Fold for 500 m water depth, 16 hydrophones (spaced 30 m) per cable and 100 x 200 m shot point grid. On the left, two cables parallel to X-axis (constant Y), on the right two cables along Y-axis (constant X). Cable position indicated by white dots. Different results due to slight curvature of top target (Figure 6.3.2a). 151

Figure 6.4.5 – Fold for 500 m water depth, 16 hydrophones per cable, 100 x 200 m shot point grid and 4 cables. From left to right: “central”, “corner” and “middle” configurations. Cable positions showed by white dots. Higher and more homogeneous distribution is obtained using “central” design. 152

Figure 6.4.6 – Fold for dipping layers (6% dip to the right, see Figure 6.3.2b), water depth 500m, 1 cable at centre, 16 hydrophones spaced 30 m. Shooting along dip (left) and strike (right) directions. Dip direction shooting slightly more homogeneous. 153

Figure 6.4.7 – Comparison between shot point grid along X-Y direction (left) and grid 45^0 to X- and Y-axis (right). 500 m water depth, one cable, 16 hydrophones 30 m apart, shot point distance 100 m, shooting line distance 200 m. Observe significant footprint for diagonal grid shooting direction. 154

Figure 6.4.8 – Comparison between 16 hydrophones spaced 60 m (left) and 32 receivers spaced

30 m (right) for a single cable at 1,000 m water depth. Shot point grid 100 x 200 m. As for water depth of 500 m, the coverage merely doubles. 154

Figure 6.4.9 – Comparison between "shallow" (left) and "deep" (right) receiver array. Water depth 1,000 m, one cable, 16 sensors spaced 30 m, shot point grid 100 x 200 m. See text for discussion. 155

Figure 6.4.10 – Comparison between 100 x 200 m (left) and 50 x 100 m (right) shot point grids. Water depth 1,000 m, one cable, 16 hydrophones spaced 60 m. Much higher and better distributed coverage occurs for a smaller shot point grid. 156

Figure 6.4.11 – Comparison between one single cable (left) and four cables in a "central" configuration (right). Water depth 1,000 m, 16 receivers spaced 60 m, shot point grid 100 x 200 m. The use of four cables presents more improvement here than for the 500 m water depth case (see Figure 6.4.5). 157

Figure 6.4.12 – Comparison for target shallower (left) and deeper (right) than previous examples. Water depth 1,000 m, one cable, 16 hydrophones 60 m apart, shot point grid 100 x 200 m. 157

Figure 6.4.13 – Comparison between coverage for no dipping (left) and dipping layer for 1,000 m water depth. One cable, 16 hydrophones spaced 60 m, shot point grid 100 x 200 m. Fold variation in the presence of dip can be considered as minimum. 158

Figure 6.4.14 – Comparison for PP-SP mode among the use of one (left) and four (middle) cables in a 4 x 4 km^2 shooting aperture and one cable in a 6 x 6 km^2 shooting aperture. 1,000 m water depth, 16 receivers per cable 60 m apart, shot point grid 100 x 200 m. Although the use of four cables gives better results, to increase shooting aperture is probably much cheaper. 159

Figure 6.4.15 – Coverage for shallow (50 m) water depth: one cable (left), four central cables (middle) and PP-SP mode (right). All uses 16 hydros/cable and 100 x 200 m shot point grid. See text for discussion. 160

Figure 6.4.16 - Coverage for land (weathering layer 50 m thick): one cable (left), four central cables (middle) and PP-SP mode (right). All uses 16 hydros/cable and 100 x 200 m SP grid....160

Figure 6.4.17 – Offset distribution: near (upper row), middle (central row) and far (lower row) for one cable (left column), four "central" plus four "corner" cables (middle column) and four "central" plus four "middle" cables (right column). Water depth 500 m, 16 hydrophones per cable, shooting grid 100 x 200 m. Cable position shown by white dots (except for left column, which has one cable at model centre). 161

Figure 6.4.18 – Azimuth distribution: 0^0 to 60^0 plus 180^0 to 240^0 (upper row), 60^0 to 120^0 plus 240^0 to 300^0 (central row) and 120^0 to 180^0 plus 300^0 to 360^0 (lower row) for one cable (left column), four "central" plus four "corner" cables (middle column) and four "central" plus four "middle" cables (right column). Water depth 500 m, 16 hydrophones per cable, shooting grid 100 x 200 m. Cable position shown by white dots (except for left column, which has one cable at model centre). 162

Figure 6.6.2.1 – 3-D view of the geologic model. From top to bottom the interfaces are sea level (model top, at depth zero), sea bottom, Upper/Lower Miocene boundary, Miocene/Oligocene boundary, reservoir (smallest area extent horizon), and Cretaceous (model bottom). Note that the Cretaceous, gently dipping to east (increasing X), is the most structured interface. Cretaceous interface was not considered in seismic data generation. Most vertical cables are also shown. Distance in metres. 167
Figure 6.6.2.3 shows some rays propagating in the model and Figure 6.6.2.4 shows some examples of shot gathers from the numerical modelled seismic data. 169
Figure 6.6.2.3 – Rays propagating through the model for one shot point and 16 receivers placed in a cable. The direct wave is also shown. 170
Figure 6.6.2.4 – Numerical model shot gathers. The events (top to bottom) are direct waves and reflections from sea bottom, Upper/Lower Miocene boundary, and Miocene/Oligocene boundary and target reservoir. Reflections from the target reservoir are not captured in all shot gathers. .170
Figure 6.6.3.1 – Common scatter point (CSP) gathers after EOM, without NMO correction. Events from top to bottom are reflections from sea bottom, Upper/Lower Miocene boundary, Miocene/Oligocene boundary and reservoir target. After NMO correction and stack, most (but not all) diffuse energy around hyperbolic reflections will vanish. Observe direct wave has vanished. Noise above 200 ms and below 3400 ms is due to display gain. 172
Figure 6.6.3.2 – Stacked section after EOM. Noise is caused by diffuse energy generated during EOM that was not attenuated with NMO correction and stack. 173
Figure 6.6.3.3 – Vertical cable processing flow using EOM. The receiver statics correction step may be difficult and time consuming for real data. 174

Chapter I – Introduction

Offshore oil and gas reserves represent a significant, if not total, amount of hydrocarbon reserves in many countries. Perhaps more so than on land, marine seismic data offer much information about the geological targets is given by seismic data.

Important aspects of marine seismic acquisition are the source, the receivers, and the navigation (positioning) system. The source and navigation systems currently used are largely considered as satisfactory for exploration and exploitation of oil and gas fields. They are, respectively, an air-gun array, where each element injects energy in the water through the liberation of compressed air, and DGPS (Differential Global Positioning System), where satellites are used to obtain the vessel position with high accuracy.

In general, the receivers – the hydrophones – consist of some piezoelectric material, which responds to pressure variations in the water, set in a cable (streamer) towed by the seismic ship. Vessels can now tow up to twelve streamers at the same time, and streamer lengths of 12 km have been used when few cables are pulled. Although towed streamers have been successfully used for decades, they have some limitations and undesirable characteristics. The most important are:

- hydrophone streamers in the water column cannot directly record shear (S)-wave information, as S waves do not propagate in the water;
- in the presence of obstacles (platforms and buoys), it is necessary to use the undershooting technique, where the receiver is towed by one vessel and the source by another vessel running in parallel; this technique is expensive, does not properly image shallow reservoirs, and often is not effective, as the cable must be in general at least 500 m away from any obstacle;
- a 3-D survey has poor azimuthal distribution, as it consists of several parallel 2-D lines;
- in areas where extreme ambient (swell) noise – due to bad weather – occurs

most of the year, the acquisition period can be very short;

- maritime currents cause the towed cable to feather, putting the receivers at erroneous positions on 2-D surveys and making necessary the acquisition of expensive additional lines (in-fill) to complete the coverage on 3-D surveys;
- it is not possible to guarantee, on time-lapse (4-D) seismic, the same position for the receivers for repeated survey.

Therefore, a natural question that arises is why not use fixed receivers on the sea bottom, or vertically in the water layer? The first option has been done since the 1930's for geological studies and later for earthquakes and nuclear explosion monitoring purposes, using the so-called ocean bottom seismometers (OBS).

In early 1980's (Zachariadis *et al.*, 1983), some work was done for hydrocarbon exploration with cables especially designed to operate on the sea bottom – the ocean-bottom cable (OBC). The cable was laid at the water bottom, and pulled straight and at desired position with tension applied on its ends. The main purpose of that system was to make possible the acquisition in a very congested area in the Gulf of Mexico.

In late 1980's, Barr and Sanders (1989) presented the idea of summing vertical geophone and hydrophone data to attenuate strong spectral notches caused by receiver ghost reverberation (receiver-side multiples) – the dual-sensor technique.

The next natural step was to upgrade the geophone used in the cable, from one (vertical) to three Cartesian components, adding the benefits of recording shear-wave data. The advent of the 4-C (hydrophone and 3-component geophone) technique opened a completely new area of investigation. The recording of the converted-shear (P-S) wave has been successfully used to image areas where the presence of gas generates a strong attenuation in the compressional (P) wave (Berg *et al.*, 1994a,b) – but additional information is also obtained.

A different approach is to create vertical, instead of horizontal, receiver arrays. This technique has also shown promising results in different environments, particularly deep waters (Krail, 1994b). The advantages vertical cables have over OBCs are use in areas with a hard (basalt, reefs) and/or pipeline congested sea floor, no coupling varying concern (especially interesting on time-lapse surveys), and less problematic operation in deep-water.

An overview of both techniques, which still have problems in acquisition and processing issues to be solved, is presented in this thesis.

For marine shear-wave recordings, one currently has to rely on conversion from P-wave energy generated in water column. If P- to -S conversion occurs at sea bottom, it is possible to use, after simple manipulations, all algorithms available for conventional common-depth-point (CDP) processing. If the conversion occurs upon reflection at sediment interfaces, then the CDP concept is not valid. Analysing geotechnical measurements in shallow marine sediments and published information (Hamilton 1976, 1979; Hovem *et al.*, 1991), it was concluded that, in most geological scenarios involving Tertiary sediments, the conversion does not occur at the sea floor. Also studied is transmission and mode conversion of up-going (reflected) seismic energy (both S- and P-) in the shallow sedimentary layers.

This thesis also presents results of processing 2-D (North Sea) and 3-D (Gulf of Mexico) seismic data acquired using OBC. It is shown that, despite some approximations and limiting assumptions, good images can be obtained from converted waves. It is believed that improvements will occur with the use of processing steps assisted by additional geological information in these areas.

Analyses of vertical-cable survey-design were performed, in a simple, but still realistic, 2.5-D geological model. From these analyses, it is observed that good coverage can be expected from the vertical cable technique, even when relatively few cables are used. However, more cables may be necessary for reasonable offset and azimuth distributions. General equations are empirically derived that can be used as first guess on vertical-cable survey design. Preliminary processing was done using a Kirchhoff pre-stack time migration algorithm developed by Bancroft and Geiger (1994) and adapted for vertical-receiver arrays by Bancroft and Xu (1998).

Efficient application of pre-stack migration techniques is one of the principal benefits of sparsely spaced vertical cable techniques.

Chapter II – The Ocean Bottom Cable (OBC) Technique

II.1 Shear-wave applications

Some books (Dohr, 1985; Danbom and Domenico, 1986; Tatham and McCormack, 1991) and several technical articles (e.g. Kristiansen, 1998; Amundsen *et al.*, 1999;) present how shear-wave information can be used in hydrocarbon seismic exploration. Imaging, prediction of fluid and lithology, and anisotropic studies are the main applications.

Imaging through gas can be achieved as S-waves are much less affected by porefill in porous rocks than P-waves (Thomsen *et al.*, 1997; Arntsen *et al.*, 1999; chapter IV of this thesis). Also imaging beneath high velocity layers, such as salt and basalt, may be improved due to possible strong P-S mode conversion at these layers (Gulati and Stewart, 1997; Longshaw *et al.*, 1998; Li *et al.*, 1998). Higher S- than P- impedance contrasts have been used for reservoir imaging (Margrave *et al.*, 1998; MacLeod *et al.*, 1999).

In theory, the S-wave lower velocities (and consequently shorter wavelength for the same frequency) can generally give them a higher vertical resolution than P-waves. However, shear waves are more strongly attenuated (high frequency loss) than P-waves. The reason for this phenomenon, observed in most surface seismic data, is not yet completely understood. It is believed that higher absorption occurs due to the inherent particle displacement, which causes the energy to be much more attenuated in the higher frequencies than P-waves (Krebes, 1989; Hovem *et al.*, 1991). Some VSP data show comparable frequency content for P-P and P-S (Geis *et al.*, 1990; Zhang *et al.*, 1994), indicating that most attenuation occurs in the shallow (and less consolidated), perhaps more heterogeneous layers. This conclusion can be extended for marine sediments as well, according to Hovem *et al.* (1991). Additionally, the shorter wavelength of S-waves requires more “cycles” over the travel path than P-waves. Even for the S-wave source acting efficiently, S-waves will be more strongly attenuated.

Two potential uses reported by Durham (1999), both being tested in the Gulf of Mexico, are 1) the distinction between “fizz water” (small amounts of gas dissolved in water, without any economic value) to commercial gas accumulations, and 2) to obtain a better image for the base of salt bodies, as this interface is a strong P-S mode converter.

Shear waves can also be used for indication of shallow-sediment flow areas during deep-water well drilling. These areas, which may be very harmful and dangerous to drilling operations, cause severe economic losses. As an example, during 14 months in the Gulf of Mexico, seven deep-water wells were lost due to flow of water in the shallow sediments. This problem is also common in the North Sea. The cost of a deep-water well in these areas may reach US$ 25 to 40 million. According to Sparkman (*in* Durham, 1999), water flow occurs in 80% of deep-water wells.

The cause for this problem is not yet well known, but seems related to sand and limestone fractures. During a workshop at the 1998 SEG Conference (New Orleans), the effect of a “well-kick” was compared with the Mt. St. Helen eruption. At the same workshop, it was concluded that rapid lateral changes in V_P/V_S ratios could be used as an indicator (together with low V_P values) for these shallow water flow zones.

Another theoretically possible idea is the use of Scholte waves. Scholte waves are interface (Stoneley) waves, which propagate along the water/sediment boundary. The particle motion is elliptical and the amplitude decays exponentially with depth.

Scholte waves are sometimes present in OBC records and look similar to land ground-roll (high amplitude, low frequency, and very low velocity); they are more common on a soft and muddy sea bottom. As land ground roll, these waves carry information about the shallow sedimentary section, and could perhaps indicate the presence of rapid flow zones. In practice, though, this analysis is probably much more complicated than the use of V_P/V_S ratios and would give information only about very shallow flow zones.

According to Stewart (1997), the main advantages of converted (P-S) over pure shear (S-S) waves are:

- the use of conventional P-wave sources; pure shear waves are generated (in general) by horizontal vibrators; these vibrators are very expensive, not very efficient (some energy is lost as P-wave) and can cause environmental damage; Iverson *et al.* (1989) report shear-wave sources being specially problematic in areas of soft ground, such as plowed farms or sand;
- the large S- statics and absorption are not present for the source, only for the receiver;
- there is less S-wave splitting (which is difficult to correct) in the data (splitting will occur only for the up-going wavefield) ; and
- the total recording time is less for P-S than S-S events.

Seafloor vibrators have been used for shallow geotechnical marine surveys. However, their deployment is very time-consuming and currently they are restricted to shallow imaging.

The V_P/V_S value, a parameter used in lithology and fluid analysis and prediction, may be obtained by isochronal ratio, after correlation of events on P-P and P-S sections, or directly from interval velocities. The second approach is used when depth migration is applied.

Castagna *et al.* (1985) found, to first order, a linear relation between shear and compressional wave velocities for both, water saturated and dry clastic silicate sedimentary rocks. According to the authors, an increase in porosity or clay content causes an increase in V_P/V_S value for siliciclastic rocks. The authors present an example for noncalcareous shales in the Gulf Coast, where V_P/V_S for shales can be 10% higher than that for sandstones.

Wiest and Edelmann (1984) report ratios between four and eight in unconsolidated near-surface layers. For P-waves, a two-layer model can be assumed, in general, for land surveys. S-waves, though, present slowly increasing velocities due to higher compaction and consolidation over depth, and do not show abrupt velocity increases.

V_P/V_S ratios of nine have been found for the shallow sediments in the North Sea (John E. Battie, *in* Strand, 1997). These very high ratios are not uncommon in shallow marine sediments. This will be discussed in more detail in the next chapter.

II.2 OBC technique: overview and examples

The already defined OBC concept is a development from the ocean bottom seismometer (OBS) technique, which has been used for several decades.

In OBC acquisition, as the receivers are in a quieter environment than conventional marine streamer, a high signal-to-noise ratio can be obtained and downtime (no operation time) due to bad weather is reduced. Also, very close to zero-offset data may be acquired, which is not possible in streamer acquisition. Also, a 3-D azimuthal coverage can be obtained, as several azimuths are sampled, unlike conventional marine 3-D, where several 2-D parallel lines are combined to form a data volume. A very important advantage is the possibility of shear wave recording. Main disadvantages of the streamer are considerable higher cost and more difficult velocity analysis (as different offsets may come from different azimuths).

OBS advantages over hydrophone sonobuoys listed by Zachariadis *et al.* (1983) are simpler deployment and recovery, quieter environment and use of geophones (plus hydrophones). On OBS acquisition, single receiver units (in general composed of a 3-C geophone and a hydrophone) are used to record data. Loncarevic (1983) provides a good overview of this method. According to him, this technique was first used in the mid-1930s. At that time, the geology of oceanic areas was almost completely unknown. The demand for nuclear explosion discrimination (from earthquakes) gave some incentives for OBS use after World War II, but the expectations were not fulfilled because: 1) the noise at marine sites was not much lower than that on land, and 2) the instruments cost, complexity and unreliability. Only in late 1960's, thanks to microelectronics advances, did OBS use become widespread. Currently, they are used in studies of earthquake, continental margins and adjacent ocean basins, subduction zones, spreading centres and fracture zones.

Mobil Oil Co. evaluated the use of academic OBS designs for refraction work in 1975 (Zachariadis *et al.*, 1983). Good data quality justified Mobil to develop a project for OBS building. In early 1979, field tests showed better results for OBS than buoys. The authors mention OBS weights 315 kg (700 pounds) and had additional 450 kg (1000 pounds) of ballast weights - but it is not clear if it is to a single unit or the whole set of receivers.

More recently, Mjelde *et al.* (1991) present an example of OBS use to map structures below volcanic rocks (basalt) in northern Norway. Also shown is the existence of consistent anisotropy (up to 12%) in the lower crust. Twenty-one 3-C OBSs were used in eight profiles on a 3-D grid.

The same author (Mjelde *et al.,* 1995) gives another example of OBS use, in the Voring basin, northern Norway. Twenty-seven 3-C OBSs were used, with 75 OBSs deployments done, with a 50 m shot point interval. The maximum frequencies recorded were 40 or 20 Hz, the lower limit allowing doubled recording time due to small sampling interval. The data had considerable information about deep sedimentary and crystalline structures. Also, a more detailed study was performed over a flat spot, using 20 OBSs in a 200 m receiver spacing.

Hughes *et al.* (1995) report the use of OBS data for imaging and modelling in the Faeroe-Shetland Basin, the results indicating potential exploration areas and also some possible existence of hydrocarbons source rocks.

Berg *et al.* (1996) present the use of densely spaced OBS in an exploration study on the Voring Basin (offshore Norway). The purpose was a flat spot anomaly analysis. Twenty OBSs, approximately 200 m apart, were dropped to 1,300 m water depth. The OBSs had neither an inclinometer nor compass. From the interpretation, done by event correlation with surface seismic data, a

V_P/V_S ratio of 2.6 (indicating partly unconsolidated shales) was obtained for the overburden and 1.8 for the presumed reservoir – indicating a geologic facies dominated by sand. Outside the flat spot, a ratio around 2.0 was obtained, indicating that hydrocarbons could be present in the assumed reservoir.

OBSs were used for underground flow monitoring in a deep well in Southern North Sea, Norway (Kolbjornsen *et al.*, 1991). During drilling, the rig had to be moved and the well abandoned due to overpressure. Three months later, when a new rig was connected, the pressure showed a considerable decrease, showing internal underground flow. Four geophones where placed in the sea bottom around the new rig, to monitor vertical movement of fluids (mainly hydrocarbons). The data showed periods, lasting typically for 30 minutes, of very high seismic activity; the energy release pattern were reported to be similar to microearthquake. Each period had a different source location. Although the cause of the seismic energy recorded is not completely understood, the authors guessed moving hydrocarbon within shallow (above 800 m) sands caused it.

Zachariadis and Bowden (1986) report one of the first acquisitions using the ‘modern’ OBC technique. They called it a “fixed position deployment”, and the method was developed to be used in areas of strong underwater currents (which cause large streamer feathering) and/or with navigational obstacles (such as production or exploration platforms or buoys). Other advantages listed by the authors are elimination of tow noise, more precise positioning and uniform acquisition pattern. A prototype solid cable, with 60 hydrophones spaced 50 m, was anchored at both ends, and laid on the water bottom under tension. It was designed to be used down to depths of 300 m. In their paper, there is a detailed description of cable construction and operational parameters (e.g., receiver positioning). The processing sequence was similar to land data. The final seismic data was said to be superior to streamer data and, maybe surprisingly, the authors consider that the cost of an OBC 3-D operation could be favourable to streamer. No comment was made about the receiver ghost.

Mobil Oil Co., which was one of the early pioneers in using this technique for hydrocarbon exploration, stopped using OBC surveys in the middle 1980's for economical reasons, and not data quality, which was considered good. The acquisition was expensive and cost inefficient because equipment had to be stored during winter (Zyg Shevchek, 1999, personal communication). Due to OBC high costs, even now Mobil limits its application to areas where seismic boat acquisition is restricted and/or where multi-azimuth data is necessary.

Barr and Sanders (1989) present a method to attenuate the receiver ghost by adding hydrophone and vertical geophone component data – the dual sensor. Deconvolution techniques are not able to attenuate very strong receiver ghosts, present in the signal bandwidth for common water depths. In their method, it is necessary to know the water-bottom reflection coefficient, which is obtained by an additional acquisition small survey, or directly from the data.

The use of a three-component geophone was a natural extension of the dual-sensor method. Adding a hydrophone to a 3-C geophone created a new type of seismic data, called four-component (4-C). The pioneering use of multicomponent sensors on the seabed for seismic exploration can be attributed to a group in Statoil under the leadership of Eivind Berg. Landro (1999) gives a good description about the dawn of this technique, which is summarised below. It started in the late 1980s, when Berg convinced Statoil to invest substantially in this idea. A 4-C prototype sensor was available in 1991, and a test was performed in the Tommeliten field, using a remote operated vehicle (ROV) for receiver planting. The result of this acquisition, presented in Berg *et al.* (1994a,b), became quite famous. They called the technique SUMIC (for SUbsea seisMIC), and its main purpose was to image reservoirs below sediments with disseminated (2-4%) gas, which causes strong absorption and scattering of P-waves. Most principles established in that survey are still observable for many 4-C operations around the world today. These are:

- a good P-S image on horizontal geophone components for areas over gas chimneys;
- P-wave energy stronger in hydrophone and vertical geophone components

and weak in horizontal geophone components;

- S-wave much stronger than P- in radial (along the line) geophone component;
- transverse (crossline) geophone component made mainly of lateral (out of sagittal plane) reflections; and
- weak (if present at all) Scholte waves in the vertical geophone component.

One remarkable exception is the P-S conversion, as the authors considered most conversion to occur at (or close to) sea bottom. After later analysis, though, they concluded P-S conversion took place up reflection at the target interfaces, not at the sea-bottom (Robert Stewart, 1997, personal communication).

The possibility of imaging areas previously almost invisible to P-P reflection imaging caused fast and relatively widespread use of the 4-C technique. Several papers (e.g., Thomsen *et al.*, 1997; Caldwell *et al.*, 1999; Arntsen *et al.*, 1999) describe how poorly imaged areas on conventional compressional (P-P) data could now be mapped using converted-wave (P-S) energy recorded at the sea floor. It is a common practice to acquire a 2-D test line in the desired area, to verify issues as appropriated conversion and receiver coupling. Given positive results, a more expensive 3-D can be acquired.

Western Geophysical Co. was contracted, in 1997, to perform what was perhaps the first 3-D 4-C survey in the world. The aim is better imaging of reservoir channel sands in the Oseberg field (North Sea), operated by Norsk Hydro (Bill Schrom, *in* McBarnet, 1997a). At a similar time, Geco-Prakla claimed to have acquired the first world 4-C commercial survey, based on 230 km of data offshore Netherlands, to improve image below multiple gas reservoirs and map hydrocarbon saturation changes. The system used in this survey is able to operate in water depths ranging from 20 to 700 m (Olav Horberg, *in* McBarnet, 1997a).

4-C technology has been used widely in the North Sea. As of April 1999, 80 to 90% of commercial acquisitions have been done there (W. Sognnes, *in* Durham, 1999). According to J. Caldwell *(in* Durham, 1999), imaging below gas clouds using 4-C recording of P-SV reflections has been always successfully, being the lowest risk application for the technique. Considerable 4-C use is presently occurring in the Gulf of Mexico, too (Ebrom *et al.*, 1998a; Nolte *et al.*, 1999).

Sonneland *et al.* (1995a,b) report that in the SUMIC technique there is no compromise on the sensor coupling quality. Their expectations for 4-C OBC use were 1) illumination in areas where P-wave give poor information (e.g. Valhall and others oil field in the North Sea), 2) lithology prediction in new exploration areas, and 3) reservoir characterisation and monitoring.

According to McBarnet (1997c), OBC has been useful mainly for 1) acquisition around man-made obstructions, and 2) subsalt imaging in Gulf of Mexico and southern North Sea. He reports that OBC is an expensive option (that companies want to pay for) that has provided high quality coverage, higher signal frequency bandwidth, no offset limitations, lower noise and reduced dependence on weather conditions. Besides the cost, the main downsides listed by him are water-depth limitation (150 to 200 m, at that time) and its restriction to highly targeted areas.

Mobil Oil Co. current studies in OBC use are restricted to evaluation of contractor technology including repeatability studies (deep-water time-lapse seismic), proper hydrophone-vertical geophone combination, navigation and positioning issues, and data quality in harsh condition areas (Zyg Shevchek, 1999, personal communication).

Western Geophysical is currently working on two 4-D/4-C acquisitions: the Teal South (Gulf of Mexico, operated by Texaco) and Stratfjord (North Sea, operated by Statoil). A somewhat common acquisition problem happened for the first Teal South 3-D: instrument cables, left permanently on the sea bottom to improve repeatability, were missing, probably caught by fishing (shrimp) boats (G. Sparkman, *in* Durham, 1999). Chapter V of this thesis presents the processing of the second 3-D (Phase II) of Teal project. Geco-Prakla is working on a 4-D seismic using buried cables in the Foinaven field (North Sea) for BP.

CGG adopts a different approach, using individual nodes positioned, deployed and retrieved from the sea bed by the use of ROVs. Bruce Nelson (*in* McBarnet, 1997c) thinks most 4-D surveys will opt for buried cables.

Another 4D seismic survey is reported by Moldoveanu *et al.* (1996), in southern Louisiana transition zones (water depth 0 to 6 m). A comparison between a single hydrophone buried at 6.1 m (20 ft) and a linear array of six marsh geophones laid on the sea bottom showed the hydrophone is less susceptible to mud roll and has higher frequency content. An additional test was burying the hydrophones at 3.3, 6.1, and 10.7 m (11, 20 and 35 ft); a 12 dB gain in the signal was obtained from receivers at 3.3 to 10.7 m.

Brink *et al.* (1996) and Granholm *et al.* (1996) present an example of the use of S-waves as a check for interpretation of a potential flat spot. The study was performed on the Voring Basin area, where the challenges are complex fault zones and the presence of intrusions and extrusions. A down-hole seismic tool with six gimballed 3-C geophones and two hydrophones was used, at a water depth of 1,270 m. Good coupling, expected to occur only by the receiver units weight, was confirmed by amplitude and phase analyses of the direct wave. They conclude that most P-S conversion occurred at the sea bottom. The results from S-wave data showed that amplitude anomalies present in P-wave data were more likely caused by fluid contact, and also supported the geological model previous thought for that area.

The use of converted-shear waves (P-S) to image a reservoir top (Eocene unconsolidated turbidites), and shales inside it, is reported by MacLeod *et al.* (1999) in the Alba Field, North Sea, at 60 m water depth. Very weak acoustic impedance contrasts occur between the reservoir and overburden rocks and between the sands and shales. To map these shales is extremely important because horizontal wells are used for oil production. Dipole sonic logs indicate strong contrast for S-wave impedance at these interfaces, suggesting strong P-S mode conversion would occur at the reservoir top and at the shales. A 2-D OBC test line was acquired by two different companies; based on the 2-D line good results, a 67 km^2 3-D was acquired during eight weeks. Large S-wave statics were found. Good agreement was obtained between far offset P-P and P-S sections. A secondary objective of the survey - mapping water movement in the reservoir (the oil-water contact has a good acoustic impedance contrast) after four years of production and water injection - was also achieved by comparing OBC P-wave data with previous streamer data. The total cost for the survey - around US$ 6 million - is relatively small compared to the cost of a single well in the area - around US$ 20 million.

Jin (1999) reports compressional- and shear-wave OBC data give better results in obtaining rock physics parameters than P-waves alone, presenting an example from 120 m water depth at North Sea.

The processing results for a 3-D/4-C OBC data over the Valhall field are presented by Brzostowski *et al.* (1999). The 3-D data was acquired after a 2-D experimental line (Thomsen *et al.*, 1997; chapter IV of this thesis) showed that a good image could be obtained from converted waves in an area where P-wave data quality is poor due to shallow gas.

The use of geophone receivers attached to the bottom of vertical cable arrays of hydrophones (the vertical-cable technique is described in chapter VI) has been tested, as it has clear advantages. The main problem in practice is the very strong noise recorded in the geophones due to the vicinity of the vertical cable – the cable-geophones distance necessary to avoid this noise being so large it becomes almost impossible to use them in the same seismic acquisition (Bill Pramik, 1999, personal communication).

II.3 OBC acquisition

There are two main types of receivers on the sea floor: continuing cables and free-stand “nodes”. In hydrocarbon applications, the cable system is the most common. It is similar to geophone distributions on land, with receivers' attached to (or inside) cables and these cables distributed along the survey area. The cable deployment and operation can be done in several ways. Figure 2.3.1 shows an example of a 4-C receiver and its attachment to a cable.

Figure 2.3.2 shows four different kinds of cable, all of them quite similar in the way they work. The streamer type allows the design of receiver arrays, as it is possible to have adjacent sensors connected to form a group.

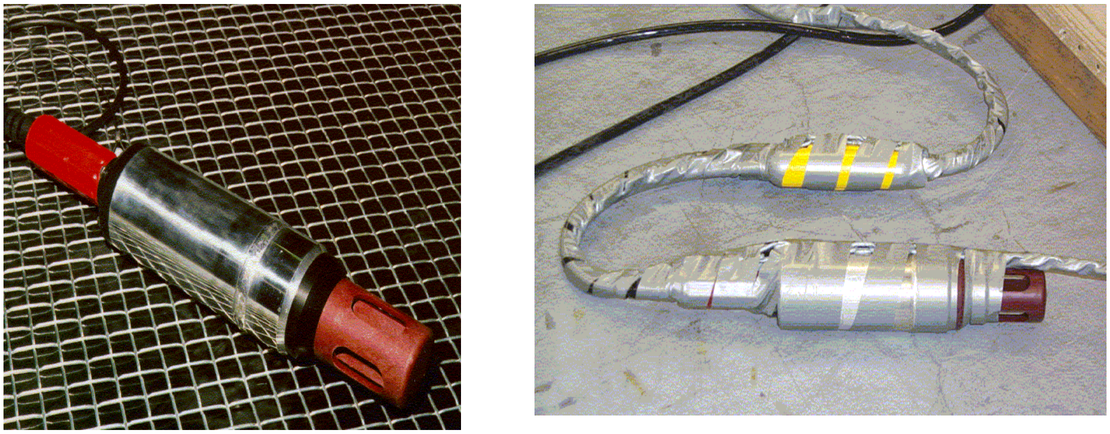

Figure 2.3.1 - Examples of a 4-C receiver (left) and the same receiver connected to a cable (right) (*after Entralgo and Wadsworth, 1999*).

In the node system, single 4-C units (also connected by communication and power cables) are put on the sea floor using, in general, remote operated vehicles (ROV) with manipulator arms.

In both methods, the receivers are relatively far apart, so a dense shot point grid is used to obtain good coverage.

The use of ROV provides, in the node system, both better coupling and positioning (at least theoretically). Its main problem is the long time – and, consequently, cost – necessary for the operation. In 1997, CGG suggested that a single 3-D should not cover areas greater than 15 km^2 (coverage) and/or 100 km^2 (shot point grid). Larger areas would require repeatability of the survey, being even more expensive.

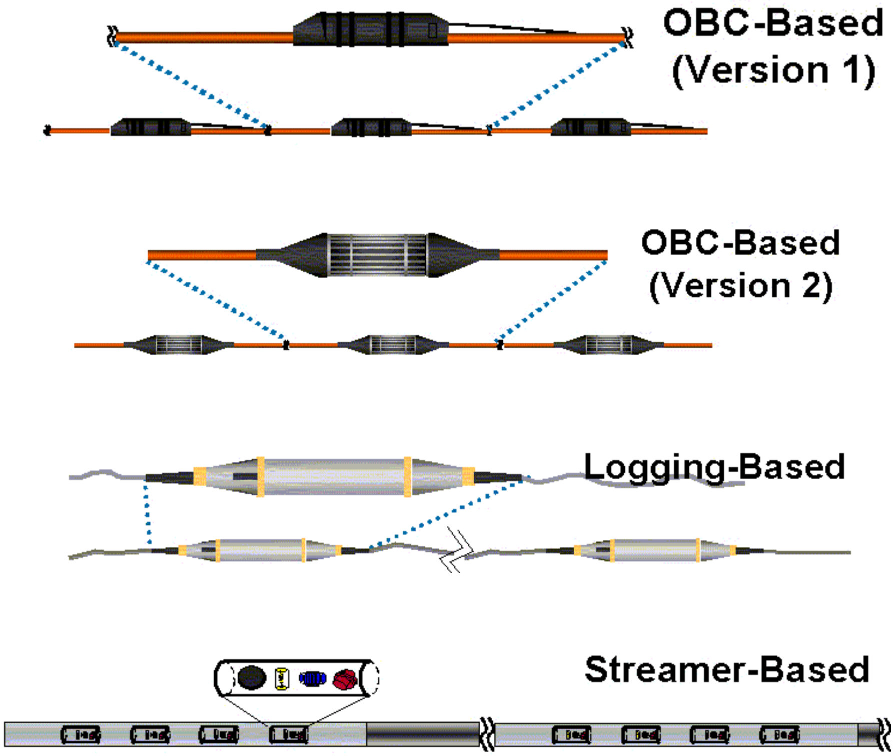

Figure 2.3.2 - Examples of ocean bottom cables (*after Entralgo and Wadsworth, 1999*).

In the node system, 30 to 50 sensors are (generally) spaced at regular intervals of 500 to 600 m. The geophones are fixed inside the "node", unlike gimballed geophones used on OBC. In 1997, the equipment could operate at 1,500 m water depth (C. Pettenati-Auziére, personal communication). After the ROV plants the units at the sea bottom, a video camera (in the ROV) is used for planting and verticality control. Concerning the weather conditions, the working vessel supporting an ROV can operate up to waves 4 m high and/or 30 knots wind – the same limits apply for the operation of shooting vessel.

The node unit used by CGG is a metal cylinder containing three fixed sensors. The hydrophone is located in the outer top part of the cylinder. Three kinds of nodes are presented in Figure 2.3.3.

Figure 2.3.3 - Examples of single nodes 4-C receivers (*after Entralgo and Wadsworth, 1999*). Mechanical arms of remote operated vehicles (ROV) plant the sensors.

The streamer-based cable shown in Figure 2.3.2 is used by Geco-Prakla. The technique is based on a Russian design, where the receivers are placed inside the cable, which is dragged. In this way, a receiver array can be formed. Caldwell *et al.* (1999) say that the weight distribution is optimised to give better coupling, but how this is exactly obtained is not explained. Regarding agitation of sea-bottom sediments – a potential environmental concern – the authors comment that video recording shows cable deployment disturbs the sea bottom less than marine life does. However, the authors do not mention if the same is true during cable dragging. They claim high quality data have been acquired with this method at different water depths (up to 800 m) and over distinct sea floor lithologies (including soft unconsolidated sediments). On an irregular sea bottom, other receivers in the group compensate for a geophone with poor coupling. A detailed scheme of one receiver is given in Figure 2.3.4.

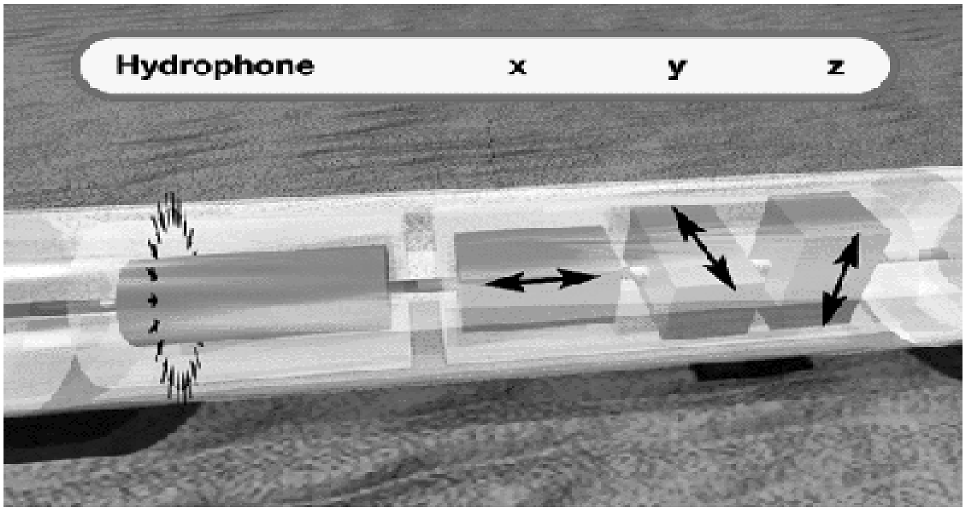

Figure 2.3.4 - Examples of 4-C receivers in an ocean bottom cable (*after Caldwell et al., 1999*). From left to right, the hydrophone (pressure sensitive), radial (inline), transverse (crossline) and vertical components. Weight distribution gives a better coupling and receiver array groups may be formed.

Sanders and Starr (1999) say a typical acquisition crew has four or more vessels: two cable-recorders, one source vessel, and one utility cable vessel. The authors present an overview on the OBC method development.

Currently, equipment issues cause a high cost for OBC, when compared to streamer. As an example, a multicomponent sensor costs 10 times more than a hydrophone (M. Lawrence, *in* Durham, 1999).

Caldwell (1999), analysing several OBC data, concludes that the data quality is high, geophones have a reasonable coupling to sea floor and most P-S conversion occurs at interfaces in depth and not at the sea bottom. These conclusions are independent from which part in the world the data come from. He also reports four different ways of receiver deployment: dragging a cable, draping a cable under tension, draping a cable without tension and remote operated vehicles (ROV) – the last method not using cables, but single receiver units. According to the author, it is not known yet how the use of different receiver system and deployment techniques affect data quality, but some differences do occur for each acquisition configuration. Recent analyses of data sets acquired in the same area using different systems are being performed so some understanding may become possible on the coupling characteristics for each deployment system. An example of data quality variation for different cable deployment techniques is presented in chapter VI.

In the same paper, Caldwell (1999) says that a 3-D OBC is three to six times more expensive than a conventional streamer 3-D. The author points out that vertical and lateral variations in water properties (such as salinity and temperature), and also the presence of currents, do affect the efficiency (for both localisation and coupling) of receiver deployment. This is more critical for deeper waters, where refractions may occur for the very high frequency signal used in receiver localisation. Another use for OBC data pointed by the author, and also during the Deep Water Workshop on 1998 SEG, is the study of shallow water flow zones.

If OBC data is to be merged with previous streamer information, it may be a good idea to use narrow azimuths during the acquisition, to avoid incorrect or different results caused by azimuth variations. Such narrow azimuths may be obtained by shooting lines parallel to receiver lines. This technique is presented in Amundsen *et al.* (1999).

Roche *et al.* (1999) say that determining apparent receiver orientation on OBC acquisition is critical. They present an example from Teal South, where an accuracy of approximately +/- 5 degrees was obtained by using statistical methods.

The main issues for deep-water operations listed by J. Caldwell (*in* Durham, 1999) are 1) the receiver position, 2) the cables have to extremely strong and 3) cable handling difficulties.

Berteussen *et al.* (1997) present the ‘dragged array’ technique, where the cable with the receivers is dragged from position to position. In this technique, developed by PGS, gimballed 3-C geophones and a hydrophone create a single receiver unit (module), the modules being interconnected by cables. The seismic data is digitised in each module, and transmitted to a vessel (or buoy) by a cable.

After the deployment, which does not require the use of an ROV, the receiver cable is dragged to the desired position, care being taken to ensure the cable is completely extended. Then a source vessel executes the desired shot point grid. For the next receiver position, the cable is dragged along the sea bottom. The receiver positioning is confirmed by acoustic transponders. This technique has been tested in the North and Barents Seas, at water depths ranging from 70 to 1,300 m and for sea bottom lithology varying from hard clay to sand.

Seabed coupling and deployment speed were identified by Walter Sognnes (*in* McBarnet, 1997b) as the main problems of the OBC technique. He also mentions shooting patterns as an issue. He stills says that, in the dragged array system used by PGS, the coupling is obtained through the use of heavy pads (around 50 kg), where weight is enough to make an efficient sea bed-receiver contact. Another advantage of this method is its speed, as it is not necessary to retrieve the array, the receiver positioning being done by dragging the cable to the desired location. Still according to Sognnes, the dragged array can be used to any water depth, and no practical problems exist for its utilisation on a 3-D configuration. Due to its cost and complexity, he considers 4-C use will be restricted to highly targeted areas where specific imaging problems have to be solved. For him, a survey will cover between 10 and 100 km^2 and it will take several years until the technology becomes completely developed.

The ‘dragged-array’ technique is capable of acquiring data at a water depth of 1,500 m; as for August 1999, 2 cables 2.4 km long were available (Eivind Fromyr, 1999, personal communication). Chapter IV of this thesis present the result of a 2-D line acquired using this technique in the North Sea.

Barr *et al.* (1996), testing ocean bottom cables in the North Sea, conclude that the coupling ranged from good to excellent.

The information from the literature presented below, although related directly to OBS acquisition, probably are also valid for most OBC acquisition techniques. According to Sutton *et al.* (1981b, *in* Loncarevic, 1983), soft sediments can act as dissipating mechanical springs. Lewis and Tuthill (1981, *in*

Loncarevic, 1983) and Johnson and McAlister (1981, *in* Loncarevic, 1983) say that the coupling on soft sediment can act as a low-pass filter. Zelikovitz and Prothero (1981, *in* Loncarevic, 1983) and Sutton *et al.* (1981a, *in* Loncarevic, 1983), assuming the receiver-sea bottom system as a damped harmonic oscillator, use mathematical theory to suggest an increase of the receivers surface area.

Besides that, Loncarevic (1983) says that a package density slightly greater than sea water density decreases possible undesirable coupling effects (matching instrument and sediments impedance), making the instrument more sensitive to high frequencies and reducing resonant amplifications. If this is to be used, care has to be taken regarding good contact, to avoid cross-coupling and current problems. Still according to Loncarevic (1983), the resonant frequency and coupling effects are functions of shallow-sediment stiffness.

Duennebier and Sutton (1995) discuss OBS responses related to coupling problems. Although OBS characteristics are more related to single units than receivers in cables, some results obtained by the authors should be pertinent to any acquisition system. They conclude that most noise present in horizontal (radial and transverse) components are due to motions in the water, like currents, recorded by the geophone due to poor coupling. The harmful effect of bad coupling is worsened by the different response the geophone has for input motions from water or from a solid and also because sensors over soft sediments (as in general ocean bottom are) are likely to respond to underwater currents. To avoid both problems, they suggest burying the receivers below the sea bottom inside a container that should have a density close to that of the sediment. They also suggest reducing the cross section of the recording unit.

No information was available from any multicomponent receiver manufacturing company on to what extent – if any, at all – these considerations are taken into account in the development and manufacturing of OBC receiver units and/or cables.

Sonneland *et al.* (1995a,b) report a SUMIC acquisition where the receiver spread of 4-C sensors had variable distances between individual units (at that time, there was a limitation of 250 units per acquisition). Each unit had an inclinometer and compass so relative geophone orientation could be known. The main advantage of the SUMIC technique is, according to the authors, the use of ROV for receiver planting on the seabed, allowing a much better coupling and positioning. No reference is made about the cost and acquisition time of this technique, though. An additional advantage related in the paper, shared with other OBC techniques, is the stationary receiver, allowing repetitive surveying for reservoir monitoring.

The maximum offset to be used in the acquisition should be about the same for both P-P and P-S – at least for 3-D design (Stewart, 1997). For P-S data, the coverage fluctuation along the bins may be an issue. A theoretical way to obtain a smoother coverage distribution is to use the formula derived by Lawton (1993)

$$PSbinsize = \frac{2}{1 + V_S / V_P} * PPbinsize\,, \tag{2.3.1}$$

where V_S/V_P is the root mean square (RMS) velocity ratio to the target.

The problem of using different bin size for P-P and P-S data is the comparison between the two data sets after stack and/or migration with a distinct trace interval. For this reason, in general the same bin size is used.

Lawton and Hoffe (1999) discuss OBC survey design regarding P-S imaging. They conclude fold variations, that may cause acquisition footprints, are introduced for different water depths and V_P/V_S ratios when the conversion point is considered to vary with depth.

An overview of receiver and cable positioning is given by Bole *et al.* (1999). The two most commonly used methods are acoustic transponders and seismic first breaks. Acoustic transponders are a high frequency (40 kHz) system, being used for many years in streamer acquisition; the main advantage is the fast positioning, the main disadvantages are the extra cost for additional equipment and personnel, and the presence of surface ghosts. First breaks are directly related to distance (considering water as a constant velocity medium) and processed in a positioning algorithm. Using statistical considerations, errors are minimised due to the large number of measurements. Both methods need correction for water velocity variation, detector depth, and instruments delay. The authors present a comparison (and complementation) between both methods in the Teal South area. A mean difference of 0.61 m in the X direction and –0.41 m in the Y direction was found between the two methods. In the same area, the acoustic system was capable of locating an accidentally dragged cable.

McBarnet (1997c) reports that an essential issue in OBC deployment and retrieval is the sensor integrity. He also reports the main limitation for the expansion of the technique is its difficulty to be used over 200 m of water. According to him, the cable performance in deeper water is problematic due to salt-water attack (difficult to avoid as a cable has numerous takeouts and terminations to be protected) and cable weight.

Beasley *et al.* (1999) report that, over four months, varying currents and wind changed receiver positions for OBC acquisition in a time-lapse survey. However, coverage, offset and azimuth distributions were very close for the two surveys, even if the shot point positions were slightly different. They conclude OBC could produce data with a high degree of repeatability.

Sullivan (1995) presents some tests to decrease noise recorded by OBC geophones in shallow water (below 100 m) and hard rock bottom. From these tests, done in Gulf of Mexico and Cook Inlet (Alaska), he concluded that most noise is random and caused by flow motion and flow-induced disturbance on the wiring (transmitted mechanically to the geophone), from currents orthogonal to the system. Poor coupling increases these effects, as the energy from sea floor particle motion is not properly recorded. He presented a method, based on covering the sensor and wires and cables adjacent to it, with bags filled with sand. According to the author, these sandbags both increase coupling and decrease noise generated by currents. His sandbagged method, licensed by Atlantic Richfield Co., was used in Teal South (chapter V). Also tested by the author with good results was the use of multiple sensors in a group for random noise attenuation.

Roed *et al.* (1996) describe the design, manufacture, deployment and trenching of six parallel cables (each 5 km in length) in deep water (500 m) on the Foinaven Field (North Sea). The purpose was to have permanent sensors for 4-D seismic surveying. The cables, with built-in hydrophones, were buried using ROV with water jetting in depths between 0.5 and 1 m.

According to Orren (1999), although shallow sediments may be important in the success and accuracy of OBC survey, this is not always considered. He suggests V_P and V_S values should be obtained *in loco*, V_P by shallow refraction and V_S by geotechnical testing tools. Based on these values, coupling performance could be predicted, although he does not explain how. To obtain V_P, a mechanical source should be used in the sea floor. His idea of using seismic cone parameter to obtain shear modulus has been used before (Hovem *et al.*, 1991; Esteves, 1996).

Tree (1999) concludes that there is poor vector fidelity (equivalent component response to the same ground motion) in OBC horizontal components, relating this to poor geophone coupling. He recognises good results obtained by the technique, but considers its full potential only will be achieved when the coupling problem is solved. The author also considers resonant frequencies (inversely proportional to the square root of geophone mass) can be very low (10 to 20 Hz) for marine sensors, compared to 100 to 200 Hz for land geophones.

Mjaaland *et al*. (1999) consider vector fidelity so important that they suggested a consortium to be formed, by oil and service companies, to analyse it.

A simple test to determine the relative responses of horizontal components was suggested by Dr. Jan Langhammer (1999, personal communication), from PGS. He reported that analyses of horizontal component energy (using omni-directional source) conducted by PGS have found stronger energy in the radial component. He relates this with a possible effect of cable traction, which could be causing a higher susceptibility in the sensors, aligned with this strength field. The suggested test should be done as shown in Figure 2.3.5. In the 4C-3D used in this thesis (Teal South, chapter V), the opposite from this was found: the transverse energy was higher than the radial.

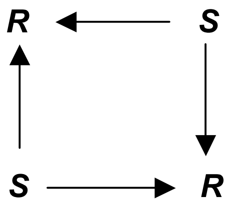

Figure 2.3.5 – Test suggested by Dr. Jan Langhammer to verify relative response of radial and transverse components. S and R are source and multicomponent receiver positions, respectively

According to Gaiser (1998), better coupling is generally found in the radial than in the crossline component, as the radial sensor area is enlarged by the cable direction. The author presents a surface consistency method to correct coupling problems in multi-component geophones, assuming perfect coupling in the radial component. Comparing data after his method was applied with data acquired with geophone planted at sea-bottom by a diver, he showed his method was able to improve the transverse component response for a 20 m water depth OBC. In a later paper (Gaiser, 1999b), he considers the OBC axial geometry causes coupling variation and torsional motion around the cable, which also contributes for a better radial component coupling.

Maxwell (1999) presents a promising new receiver type. Instead of velocity measurement, it is acceleration sensitive. The technology, similar to car airbag control, works with a system keeping a reference mass steady during recording, the seismic energy being proportional to the force applied by the system. The author claims a low intrinsic noise and ultralow distortion in this technique. Other advantages are the small size and its auto capability of vertical direction detection. No results are presented, but it is said that initial field tests showed distinct promise.

II.4 OBC data processing

Processing of marine converted-wave data can be done in a way similar to land data, the main difference being the source should be moved to the sea bottom, which becomes the new datum. Actually, the geometry for OBC has sometimes been treated as if it were a land acquisition, as in some seismic processing software (e.g., ProMAX) geometry for marine data only can be assigned for data acquired with streamers.

Before any processing is done, it is necessary to reverse the polarity for horizontal component symmetric offsets – either positive or negative. This is to correct the reverse trailing spread. For 3-D surveys the polarity reversal correction may be complicated, and should be done during reorientation of horizontal components, by direct wave analyses.

Reorientation of horizontal components is crucial in 3-D surveys as for each source-receiver pair the radial (inline) and transverse (crossline) directions will be different. These directions are defined by maximum energy alignment over a time window (generally, centered at first breaks) along the new radial direction. If the data quality is poor (as sometimes in land surveys), then the planting direction in the field has to be trusted, and a simple angle rotation may have to be performed, without energy alignment considerations.

After reorientation, all energy left in the transverse component, in the isotropic case, should be related to noise or reflections from out of the source-receiver vertical plane (sagittal plane). Strong energy in transverse component may be an indication of anisotropy in the geological layers, as shear waves will split into a fast and a slow S-wave, with particle displacement orthogonal to each other.

For P-S conversion, it is well known that the mode-conversion point position changes with depth, even for horizontal layers. Due to the asymmetry of down and up-going energy for waves converted in the sediments and not at the sea bottom, the use of conventional common mid point (CMP) gathering is not correct. As, in general, the conversion occurs at sediment interfaces and not at sea-bottom (chapter III), a different approach has to be used.

One common approach is the asymptotic approximation to obtain the conversion point. Asymptotic approximation means the intersection between the surface and the line defined by the tangent at infinite to the curve defined by the conversion (=reflection) points defines the so-called common-conversion-point (CCP) or asymptotic common-conversion-point (ACCP) (Figure 2.4.1). In other words, ACCP is the conversion point at infinite depth for a given V_P/V_S.

Although this approximation has obvious limitations – for instance, it works better when offset/depth ratio is less than one – it is a reasonable way to process P-S converted wave in an industrial (commercial) production scale. Practice has shown that it is quite robust, even when a single V_P/V_S ratio is used for all reflection times. As an example, Gaiser and Jackson (1998) consider that errors introduced by asymptotic approximation in the shallow part are probably not very important because most of these data is located in the mute zone (where reflection depth is less than source-receiver offset).

Fromm *et al*. (1985) introduced this technique. Geometrically, this point is the asymptotic to the curve defined by joining all conversion points at different depths (Figure 2.4.1). The analytical expression is

$$X_P \cong X_S \left[\frac{V_P / V_S}{1 + (V_P / V_S)} \right], \tag{2.4.1}$$

where X_P is the source-conversion point offset, X_S the source-receiver offset and V_P and V_S average velocities for down and up wave propagation, respectively.

A value of 2.0 for V_P/V_S ratio is often used as a first guess for a preliminary analysis. Based on the preliminary sections obtained with this value, more precise ratios (time-variant or not) are obtained and used in a new binning.

Eaton *et al.* (1990) showed that this approximation could introduce artifacts. A more precise approach is to consider the depth-variant nature of the conversion point, according to the expression derived by Tessmer and Behle (1988):

$$X_P = \chi + X_S/2\,, \tag{2.4.2}$$

χ is a solution to the quartic equation,

$$\chi^4 + \left(Z^2 - \frac{X_S^2}{2}\right)\chi^2 - Z^2 X_S \left[\frac{(V_P/V_S)^2 + 1}{(V_P/V_S)^2 - 1}\right]\chi + \frac{X_S^2}{16}\left(X_S^2 + 4Z^2\right) = 0\,, \tag{2.4.3}$$

where *Z* is reflector depth.

Other approaches include the use of pre-stack migration algorithm, either in time or depth. For example, Li and Bancroft (1997a,b) used the concept of equivalent offset migration (EOM, introduced by Bancroft and Geiger, 1994) for converted-wave processing. Results using this technique are presented in chapters IV and V.

Independently to the approach used, the bin size for converted wave data should be the same of the compressional data, even if a more homogeneous fold distribution can be obtained if distinct bin sizes are used. The reason for this was explained in previous section, being related to comparison between P-S and P-P seismic sections with different trace intervals.

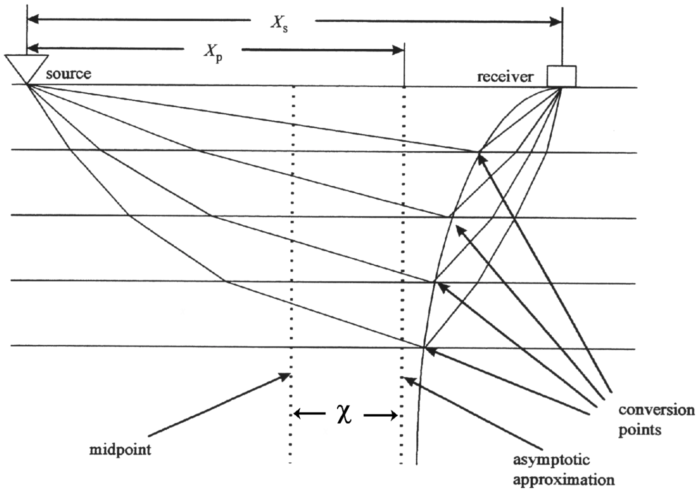

Figure 2.4.1 – Asymptotic approximation for conversion point.

Tessmer and Behle (1988) showed that, to second order of approximation, the total transit time T for converted waves is given by

$$T^2 = T_0^2 + {X_S}^2 / V_{PS}^2, \tag{2.4.4}$$

T_0 zero offset traveltime and V_{PS} RMS converted-wave velocity (P for downgoing wave and S for up-going).

Harrison (1992) showed that correction for geometrical spreading (approximated to spherical divergence) in converted waves can be done using the approach presented by Newman (1973), using NMO velocities, in a way similar to those used for P-P waves.

Conventional (P-P) deconvolution procedures, as minimum phase or spiking, can be used to deconvolve P-S data. Due to the traveltime difference, operator length used on deconvolution for P-S data should be around 50% longer than P-P operator (Harisson, *in* Strand, 1997).

Shot statics, if necessary, are the same for P-P and P-S data. In general, they are obtained during P-P processing.

To correct for shear-wave receiver statics is an important step in the converted wave processing. In land, S-wave statics are 2 to 10 (and even more) times bigger than P-wave statics (Anno, 1986; Tatham and McCormack, 1991; Stewart, 1997).

A problem for shear wave statics is related to their very large values, often greater than the wavelength of the signal. One may have to use a large time window for correlation, which may lead to cycle-skipping problems, depending on signal-to-noise ratio.

Receiver statics have to be calculated for P-S data, as little correlation may exist between P-P and P-S receiver statics.

Theoretically, ground-roll could be used to estimate S-wave statics, as it has a velocity close to S-waves near the surface. According to Stewart (1997), in practice it is difficult because 1) ground-roll is affected by deeper layers and off-line scattering, 2) it is often very dispersive and 3) it has long wavelengths (due to its low frequencies) giving poor precision for static shifts.

In the real data used in this thesis (chapters IV and V), to obtain receiver statics for P-S data was not very problematic. In both cases, hand statics were first obtained by picking an event in a receiver-stacked section. This event was smoothed, and the time difference between the smoothed and original event was considered as being the hand statics. This method has the advantage of preserving apparent structure in the data while not being restricted to flat reflections. Residual statics were obtained by correlation of traces in a gather to a pilot trace, the pilot trace being a stacked trace. Final residual statics values were very low – around the data time sampling interval.

Anno (1986) concludes that S-wave velocity is sensitive to shallow sediment properties (which may have a large lateral variation) while P-wave velocity is more sensitive to saturating fluids. In a marine environment, one may guess differences on the depth where the sediments is below the critical porosity (over this porosity, the grains do not have contact and are in suspension in a fluid, so no real sediment is present) may affect S-wave statics.

Wiest and Edelmann (1984), analysing unconsolidated sediments in northern Germany, showed that P-waves velocities have a remarkable increase at water table from 600 to 1800 m/s, while S-wave velocities, for the same strata, increase gradually from 100 to 400 m/s. One consequence is that S-wave models are vertically and laterally much more complex than P-waves, and do not show a significant velocity increase as P-waves do over a single interface. An important conclusion is that time corrections for the two wave types are largely independent, so S-wave corrections cannot be derived from P-wave corrections through the use of V_P/V_S alone. They also report S-wave corrections being much larger.

If the layers have any dip, a converted-wave DMO algorithm, developed by Harrison (1992) should be used. Strictly speaking, a pre-stack depth migration should be done in the case of dipping layers; although desirable, this option has at least two challenges (Stewart, 1997):

- depth migration is sensitive to velocity, and the velocity is not generally known, and
- it still is a time-consuming process, especially in 3-D data.

What DMO does is to reduce the section to a zero-offset section. Migration is still necessary, though, due to energy scattering and uncollapsed diffractions. DMO is much faster than migration. DMO is close to migration if one thinks that, given offset and traveltime, we need to find from which dip the conversion comes from. DMO is a geometrical operation, calculating, for every shot and receiver, a zero offset point for each sample.

The exploding reflector concept is not quite exact for converted-waves, because the travel path is different for down and up going wave fields. Other than this, the migration procedure is the same: migration tries to collapse diffraction hyperbolas, the only obvious difference being the velocity to be used represents a P-S mode.

To deal with anisotropy effects is more complicated when S-waves are involved, due to the splitting. This occurs because two separate waves are created, for one incident wave, in an anisotropic medium. Stewart (1997) believes some noise present in converted-wave sections is related to splitting.

Gaiser (1999a) suggests the use of distinct horizontal components coordinates systems for different purposes. The conventional source-receiver azimuth should be used to obtain V_P/V_S ratios and another system for birefringence correction and fracture analysis. He presents an example of pre-stack azimuth processing where energy initially present in the transverse component was strongly attenuated after the radial energy was separated in fast and slow S-waves using layer stripping.

Bale *et al.* (1998), processing a 2-D 4-C line in the Danish North Sea, concluded that anisotropy has to be considered in prestack depth migration. They state that a consistent velocity model for depth imaging of converted waves has to consider anisotropy. In their study, this consideration was done by use of Thomsen’s parameters (Thomsen, 1986) on vertical axis transverse isotropy

(VTI) media.

O'Brien and Etgen (1998) consider that streamer data is suited for velocity analysis (due to large offset and narrow azimuth ranges) and Kirchhoff migration. OBC (and vertical cable), on the other hand, offer poor velocity analysis but the possibility of a faster wavefield migration. The authors prefer wavefield than Kirchhoff migration, as they believe it can handle better distinct wave paths and preserve original amplitudes.

For Li *et al.* (1999), an individual processing sequence is necessary for each area, in the same way as a specific OBC survey design is necessary. They also say that residual statics were required to improve the results of a 2-D 4-C line in the Gulf of Mexico.

Thomsen (1998) introduced another step, where transverse anisotropy (with vertical axis – VTI –, in general) could be considered. He argues that in layered anisotropic media an effective velocity ratio (γ_{eff}) should be used for ACCP binning. This ratio is given by

$$\gamma_{eff} = \gamma_{NMO}^{2} / \gamma_{0} \, , \qquad (2.4.5)$$

where γ_{nmo} is the V_P/V_S ratio of NMO velocities and γ_0 is the V_P/V_S ratio for average vertical velocities.

γ_0 is, in general, obtained from event correlation in stacked or migrated sections and γ_{nmo} from the velocities used in the processing. γ_{eff} can be used directly as a replacement for γ_{nmo} or γ_0 in some processing or survey designs algorithms. In both articles the author points out that, when strong lateral velocity variations are present, positive and negative offsets should be processed separately. For 2-D, he gives the example of Valhall data, but for 3-D he recognises the problem is more difficult to solve. Still according to the author, the conversion point has to be determined, rather than assumed, which is generally the case. For this, physical – and not only geometrical – considerations have to be taken into account.

Failures and problems on the assumption that the sediments are isotropic are presented by Thomsen *et al.* (1999) and Amundsen *et al.* (1999), among others. Amundsen *et al.* (1999) stress that anisotropy must be considered for a correct depth image of multicomponent data. Nolte *et al.* (1999), for example, report that it was necessary to account for anisotropy in S-wave velocities on pre-stack depth migration, in other to fit vertical and radial components sections at same depth in data from Gulf of Mexico.

II.5 Discussion

From the literature collection presented in this chapter, it can be concluded that the OBC method still has some issues to be solved.

In acquisition, geophone coupling is a great concern. Which deployment method works better has yet to be answered, and the answer(s) will probably be distinct from area to area.

Vector fidelity ranks second in acquisition issues. Also important are cables and receivers positioning and survey design for converted-wave.

Some good results are reported using the OBC technique in time-lapse seismic surveys. In deep-waters, OBC use is still limited.

Regarding processing of 4-C data, the main issues are:

- proper imaging of converted waves,
- P- and S-waves energy separation,
- estimation of S-wave receiver statics, and
- proper treatment of anisotropy in shear waves.

Despite these problems, several 2-D and 3-D OBC surveys, from different regions of the world and in distinct environments, have shown the technique can be very useful under many circumstances. This is especially true for imaging through gas-contaminated sediments.

Probably the biggest limitation in the use of OBC is its cost, which is, in general, much higher than conventional (streamer) acquisition.

Chapter III – Sea-Bottom Shear-Wave Velocities and Mode Conversions

III.1 Introduction

Analyses of marine seismic data acquired using the ocean bottom cable (OBC) technique generally require some knowledge of the physical properties of marine sediments. The shallow sedimentary section may be especially important, as dramatic changes in elastic parameters are common over small distances. This may affect various algorithms, as for example P-P and P-S wave separation, static corrections, and velocity analysis.

In this chapter, literature, direct measurements and geotechnical data are used to obtain values for shear-wave velocities in shallow marine sediments.

A study on wave mode conversion for the downgoing seismic energy that occurs at the sea floor and a comparison with reflected conversions at a representative interface of Tertiary sediments is presented.

To verify if the presence of S-waves in the vertical component (and P-waves in the horizontal) could be due to mode conversion close to the receivers, conversion for the up-going seismic energy in the shallow sediments and at the sea bottom is also analysed.

III.2 Physical properties of marine sediments: overview of literature data

Hamilton (1976,1979) has one of the first overviews of S-wave velocities in marine sediments. In the earlier paper, he obtained empirically the expressions (z is depth in meters, V_S is S-wave velocity in m/s), for silt clays and turbidites,

$$V_S = 116 + 4.65z \qquad 0<z<36 \qquad (3.2.1)$$

$$V_s = 237 + 1.28z \qquad 36<z<120 \qquad (3.2.2)$$

In the second paper, he found an empirical relation between V_P and V_S (and V_P/V_S values) for marine sediments. In both articles, he used in-situ measurement data from different geographical locations, water depths, and lithologies.

For siliciclastic sediments, he found V_P/V_S ratios of around 13 for shallow sediments, decreasing to around 2.6 at a 1 km depth. For sands, V_P/V_S ratios have high gradients in the first metres, from around nine at 5 m and decreasing to six at 20 m. He had no measurements for unconsolidated or soft limestones. As a final remark, he reiterated that very shallow sediments might have very high V_P/V_S ratios. He reported a value of 46, and believed that even higher values might be found.

One may guess his hypothesis of very high values for V_P/V_S ratios is possible when the porosity goes over 60%, as the material then is not unconsolidated sediment anymore. Instead, it is a suspension of grains in salty water (Nur, 1993); in such case, V_S approaches zero.

It should be pointed that, although Hamilton expected very low V_S values in very shallow (less than 10 m) marine sediments, the use of equation (3.2.1) gives values consistently higher than what is measured in sediments (Richart *et al.*, 1970; Breeding *et al.*, 1991; Lavoie and Anderson, 1991; Figure 3.3.4). This may be due to rapid vertical changes in physical properties of these sediments regarding shear-wave propagation, not considered is his empirical derivations. For these sediments, Breeding *et al.* (1991), Briggs (1991), and Richardson *et al.* (1991) report Biot (1956a; 1956b) poroelastic and Bryan and Stoll (1988) models to have better agreement with measurements. Hamilton’s results are shown in Figure 3.2.1.

Richardson *et al.* (1991), analysing the upper two metres of sediments in shallow water, conclude that the shear modulus is controlled by consolidation for sands, but for fine-grained sediments, other processes are important. Again, according to the authors, V_S values predicted by Hamilton (1976), and Bryan and Stoll (1988) near the sea bottom are often higher than measured values.

Theilen and Pecher (1991), using cores analysis and in-situ measurements from the upper nine metres of sediments in the Barents Sea, found small variation in V_P but a rapid increase (from 10 to 40 m/s) in V_S.

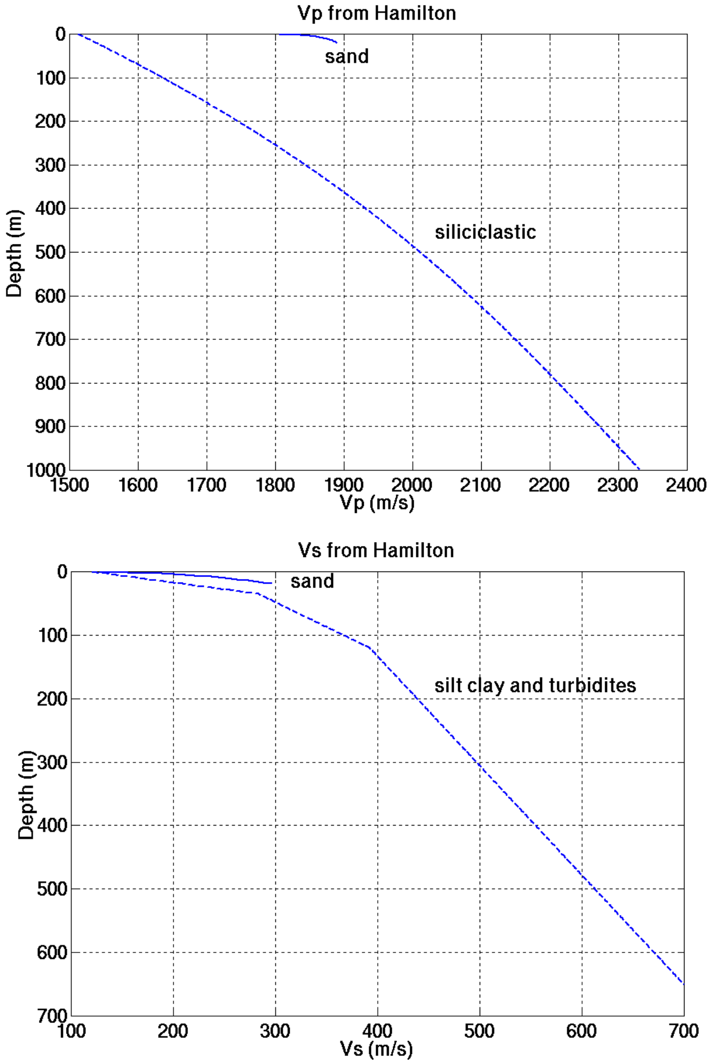

Figure 3.2.1 – *Top*: V_P values for marine sediments from Hamilton (1976; 1979). Observe the distinct curves for siliciclastic and sand lithologies. *Bottom*: V_S values for marine sediments from Hamilton (1976; 1979). Unlike V_P, the curves for different lithologies are similar. All curves from in-situ measurements.

Duennebier and Sutton (1995) consider a value of 20 m/s appropriate for V_S in high-porosity shallow marine sediments in ocean bottom seismometers (OBS) coupling problem analysis. They relate V_S values between 10 and 40 m/s from the literature.

Ayres and Theilen (1999) present data for near-surface sediments (upper

9 m) from the continental slope of the Barents Sea. S-wave velocities are much more sensitive to lithology changes than P-wave (which has a narrow range of velocity values). Most of the floor of the Barents Sea continental slope is covered by sandy clays, marls, and oozes. The sediments have unexpected over-consolidation in the upper meter. V_S vary between 9 m/s and 47 m/s.

III.3 Shear-wave velocities from offshore Brazil: direct measurements and geotechnical data

The values used in this section to obtain elastic parameter came from direct V_S measurements in the shallow sediments and geotechnical data, both obtained offshore Brazil.

The data was acquired at water depth ranging from 20 to 2,000 m and with lithology compositions varying from sand to shales and oozes to limestones. Depths from zero to 132 m below the sea floor were analysed at 30 different locations.

The direct V_S measurements used the seismic cone penetrometer technique, a small VSP-like survey. In this survey, it is possible to combine standard geotechnical tests with in-situ V_S measurements in the same acquisition. Shear-waves, generated in the sea floor by a hydraulic driven spring hammer, are recorded by two orthogonal geophones, mounted horizontally in a piezocone penetrometer. Responses from both geophones are considered in velocity calculation. An umbilical cable connects the geophones to a seismograph. In general, the shear-wave source is activated several times for a constant geophone depth, to increase signal to noise ratio. Interval velocities are obtained directly between two successive measurement depths. An acquisition scheme is shown in Figure 3.3.1. More information about this technique can be found in Robertson *et al.* (1986) and de Lange (1991).

In the Brazilian data velocity measurements were obtained at approximately every five metres (Kubena and Post, 1992). Direct measurements of V_S were performed in six different locations over distinct Brazilian offshore oil and gas fields.

Density information was available in all 30 locations.

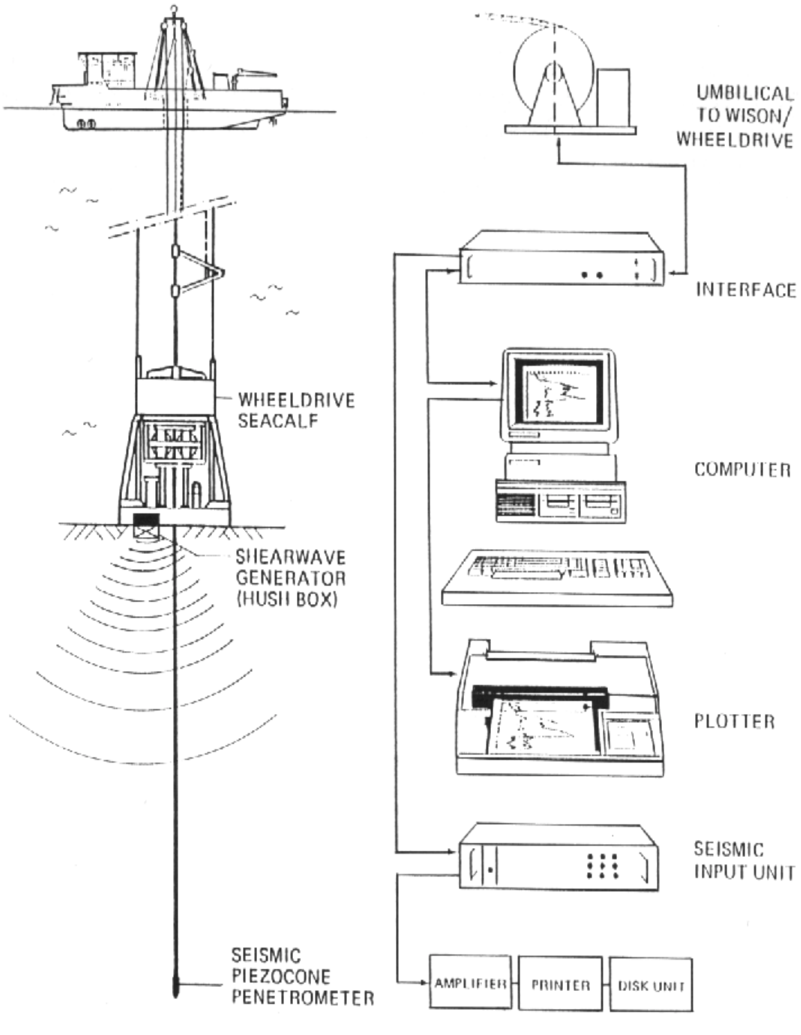

Figure 3.3.1 – Concomitant offshore acquisition of conventional geotechnical and V_S information *(after de Lange, 1991*).

The geotechnical data was acquired to support analyses of offshore installations (drilling and production platforms and pipelines) on the sea bottom. Pure geotechnical data (without V_S measurements) from 26 locations (Kubena and Post, 1992), also over Brazilian oil and gas offshore fields, were also used in the analyses presented here.

To use pure geotechnical information as a source of shear-wave velocity, it is necessary to establish a correlation between the ‘geotechnical’ shear modulus (also called shear strength, or S_U) and the ‘dynamic' shear modulus, or Lame’s constant, μ. The dynamic shear modulus defines shear-wave velocity according to the well-known expression

$$V_s = \sqrt{\mu/\rho} \, , \tag{3.3.1}$$

where ρ is density.

The dynamic modulus derivation is based on very small strain (less than 10^{-6}) and a linear stress-strain regime (Hooke’s Law is valid) (Macelwane and Sohon, 1936; Muskhelishvili, 1963; Sheriff and Geldart, 1995). Geotechnical (or engineer) modulus, however, in general is related to the material break point, involving much larger strains, where Hooke’s Law may not be applicable (strain-stress relation is not linear anymore). Also, frequency may be an important factor.

Nevertheless, some relation between the two parameters is intuitively expected. Richart (1975), based on land data, found that V_S measurements in-situ could be used as an indication for S_U. Some published discussions about this correlation are presented below. In general, the authors are interested in the inverse problem – to obtain geotechnical parameters from seismic measurements.

Theilen and Pecher (1991), analysing cores from the upper nine metres of sediments in the Barents Sea, found a linear correlation between in-situ estimations of geotechnical and dynamic modulus – the dynamic being around 200 times higher than the geotechnical (Figure 3.3.2). The authors believe specific correlation may be obtained for distinct kinds of sediments.

Baldwin *et al.* (1991) also obtained S_U and V_S (using a 1500 Hz signal) in the same samples of marine clays from the Canadian Beaufort Sea (50 m water depth) and Portsmouth (New Hampshire, USA). Unlike the data presented here, their measurements were not in-situ. They also found linear relation between S_U and V_S, but by a factor which was a function of sediment consolidation.

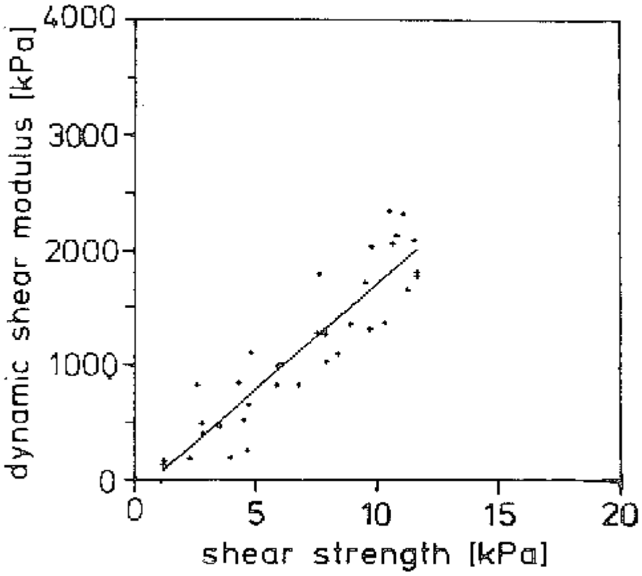

Figure 3.3.2 – Correlation between S_U (shear strength) and μ (dynamic shear modulus) for cores from 9 m of shallow sediments in the Barents Sea *(after Theilen and Pecher, 1991).* Observe that the correlation is close to linear, μ being about 200 times greater than S_U.

In the data presented here, depth-variant correlation factors were obtained by averaging information from the six locations where both S_U and V_S were acquired. These factors *f* were calculated simply by the expression

$$f = \mu / S_U \tag{3.3.2}$$

The results, shown in Figure 3.3.3, were used for V_S calculations in the remaining 24 locations where only S_U was available. The picture shows that, compared to shear modulus, shear strength decreases remarkably for very shallow sediments, which would be intuitively expected. It also shows that the correlation factor value of 200, obtained by Theilen and Pecher (1991) for depths between zero and 9 m, occurs here around 10 m, being higher for shallower sediments.

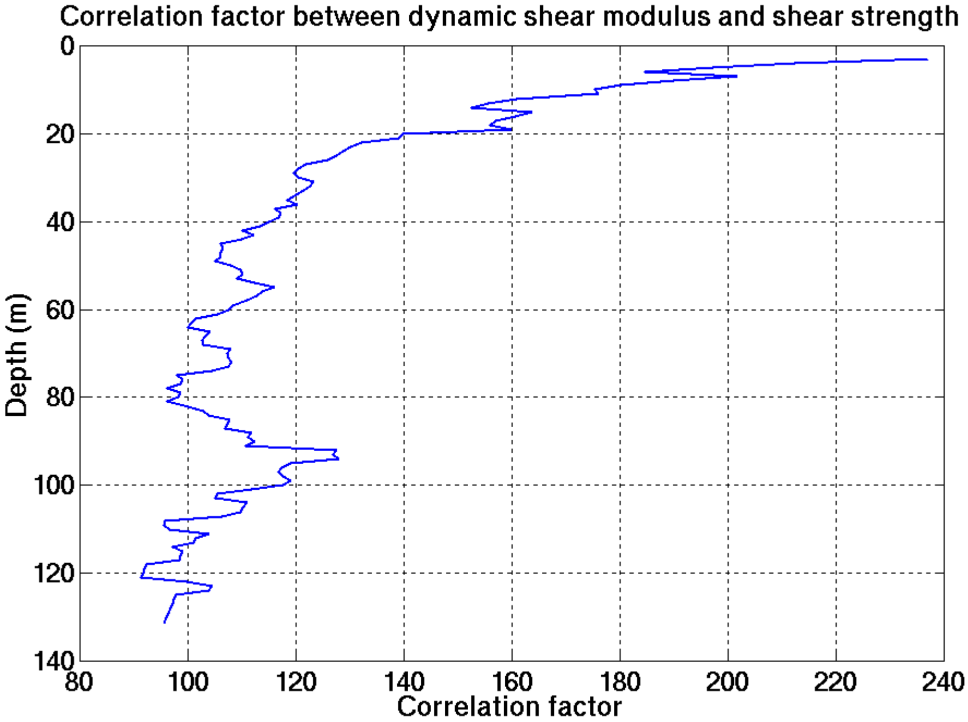

Figure 3.3.3 – Correlation factor *f* (=μ/S_U). Average from six offshore Brazil locations where both V_s and S_U were measured in-situ.

The velocities values obtained from averaging V_S from all 30 locations are presented in Figure 3.3.4. Also shown, for comparison, are the values expected from Hamilton expressions (3.3.1 and 3.3.2).

In general, there is a reasonable agreement between Brazilian sediment values and Hamilton results. The most remarkable discrepancies are around 35 m and in the very shallow (less than 10 m) section. At 36 m Hamilton defined a boundary, using one expression for sediments above it and another for sediments below. Regarding sediments above 10 m, it has already been mentioned that values from Hamilton expressions are higher than what is generally found in the literature. Simple inspection of equation (3.2.1) indicates that, immediately below the sea-floor, Hamilton expect V_S over 100 m/s, what, in general, is not observed in most marine sediments (e.g., Hovem *et al.*, 1991).

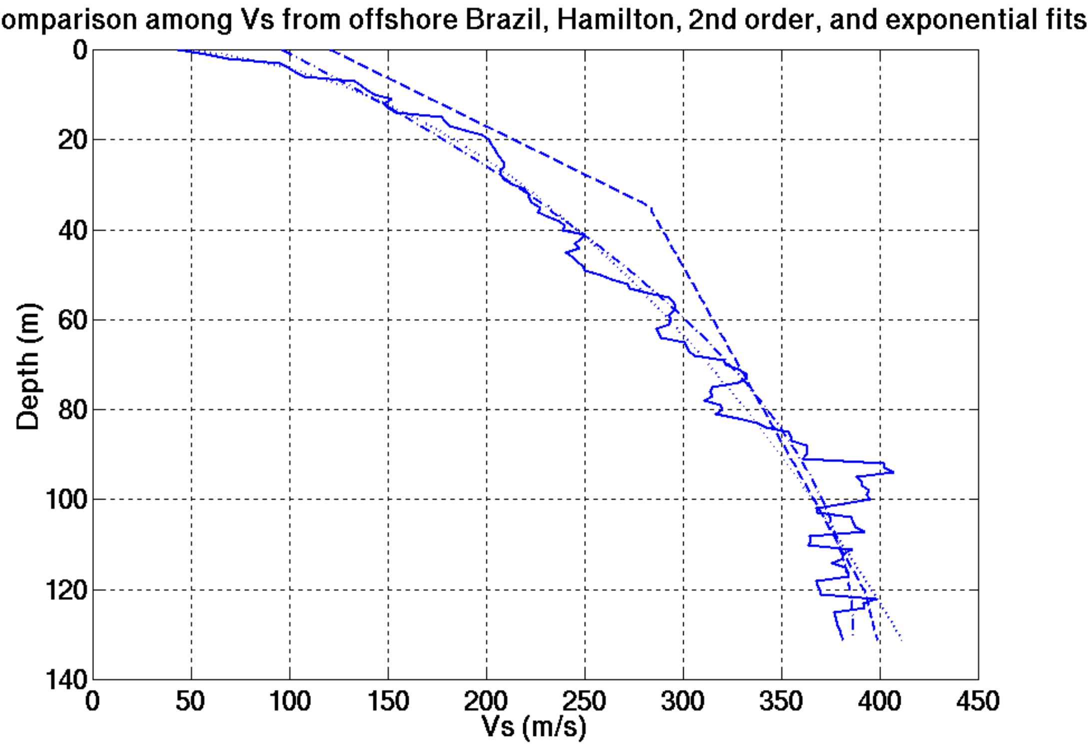

Figure 3.3.4 – V_S obtained from averaging in-situ direct and indirect (geotechnical) data in 30 locations offshore Brazil (continuous line). Also shown for comparison are values expected from Hamilton (dashed) and second order (dash-dot) and exponential (dotted) fit equations of the continuous line data. The empirical expressions are valid for a common ('soft') sea bottom.

Using the measurements from all 30 locations, an empirical second-order equation, based on a least-squares best fit, was obtained. It should be stressed that this equation is very general, and does not consider aspects that may be important, as lithology, consolidation, water depth and so on. Nevertheless, this equation can probably be used as first guess for V_S in marine sediments when no other information is available. This may be especially true for geological environments similar to offshore Brazil – namely, extensional marine basins younger than Jurassic.

The empirical equations are

$$V_S \approx 91.68 + 4.46Z - 0.017Z^2 , \qquad (3.3.3)$$

$$V_S \approx 48z^{0.4387} \qquad (3.3.4)$$

Z is depth in meters from 0 to 130 m, V_S is in m/s.

One can observe expression 3.3.3 is not very different from the ones obtained by Hamilton 20 years ago. Expression 3.3.4 predict shallow velocities better than Hamilton's expressions.

III.4 Mode conversion for down- and up-going wavefields

P-S mode conversion upon transmission through the sea bottom may be important for hard bottoms (V_P>2500 m/s, V_S>1000 m/s, V_P/V_S<3.0), as the critical angle for the P-wave can be relatively small, generating most downgoing energy as S-waves (Tatham and McCormack, 1991). For instance, Tatham and Stoffa (1976) present some examples of conversion at the sea bottom, for shallow sediments with P-wave velocities over 2000 m/s.

According to Amundsen *et al.* (1999), the most important elastic parameter for the PS-SP mode (P converting to downgoing S at the sea-bottom, reflecting as upcoming S and converting back to P at the sea bottom) is the S velocity just below the sea bottom. As an example, the authors say that if a Vp/Vs ratio equal or lower than 3.0 occurs in these sediments, PS-SP amplitudes are comparable to P-P reflection amplitudes. However, as has been outlined in this chapter, almost all measurements presented in the literature (e.g. Hovem *et al.*, 1991) – at different locations, lithologies and water depths around the world – show that V_P/V_S is usually over 5.0.

Besides, most reports on OBC data processing conclude that S-wave energy recorded at sea bottom is generated from P-S conversion at layer interfaces rather than at the sea bottom. In general, this conclusion came from moveout velocity analysis (the velocities are much higher than expected from pure S-S mode) and/or poor imaging when conventional CDP processing is applied to horizontal geophone components.

The comments above indicate that most shear wave energy recorded on the sea bottom is related to upcoming P- to S- conversions from deeper sediment interfaces, not downgoing conversions at the sea bottom. If this is true, in the absence of efficient and economic ocean-bottom shear sources, one is called upon to analyse P-S reflection data.

For these reasons, converted-wave algorithms – P-S velocity analysis, P-S DMO, P-S imaging, etc. – have to be used.

Mode conversion at the sea bottom and at a typical top Tertiary reservoir interface were analysed and compared using the Zoeppritz equations coded in *Matlab* by Prof. Gary Margrave at CREWES.

The near-surface sediments shear wave velocities were obtained by averaging the data from Hamilton (1976; 1979), Baldwin *et al.* (1991), Breeding *et al.* (1991), Briggs (1991), Lavoie and Anderson (1991), Richardson *et al.* (1991), Theilen and Pecher (1991), Duennebier and Sutton (1995), Esteves (1996), Ayres and Theilen (1999) and Brazilian offshore data presented in Figure 3.3.4.

The sea-bottom shear wave velocities were obtained by averaging the upper five metres of sediments. A density of 1.05 g/cm^3 and V_P of 1500 m/s were used for the water layer. V_P in sediments, was obtained from Hamilton (1976,1979) formula for siliciclastics.

A test was performed to verify if the use of averaging different sediment thickness (10 and 20 m) would produce appreciable differences. Figure 3.4.1 shows the results. One can conclude the differences are small, mainly for the P-

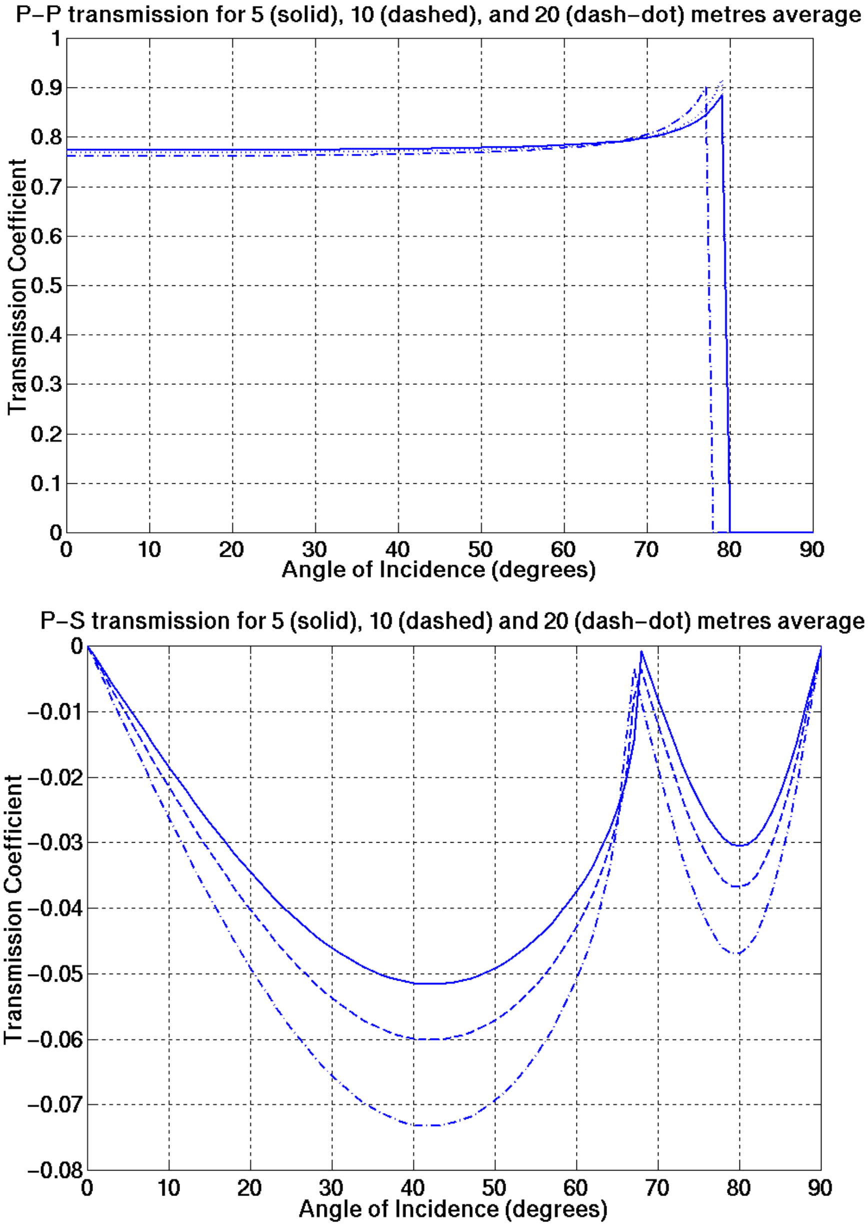

P−P transmission for 5 (solid), 10 (dashed), and 20 (dash−dot) metres average

P−S transmission for 5 (solid), 10 (dashed) and 20 (dash−dot) metres average

Figure 3.4.1 –Transmission coefficient variation at sea-bottom (down-going incident P-wave) for different sediment thickness considered for elastic parameters averaging. PP (top) and PS (bottom).

P mode. For the P-S mode, it can be seen that more shear wave is generated as deeper sediments are considered in the average. This is expected, as a drastic increase in V_S occurs in these shallow depths. In Figure 3.3.4, for instance, V_S at 20 m is four times greater than that at just below sea floor.

For the reservoir / overburden interface, values normally found in unconsolidated turbidite sandstone of Tertiary age were used (Table 3.4.1). It should be pointed out that for these reservoirs the P-wave velocity contrast can be much higher than S-wave. Generally, the density contrast is very large and cannot be neglected in modelling studies.

Layer	V_p (m/s)	V_S (m/s)	density (gm/cm^3)
Overburden	2800	1165	2.4
Turbidite-reservoir	2530	1070	2.1

Table 3.4.1 - Elastic parameters for reservoir (turbidite) and overburden Tertiary rocks.

For a downgoing compressional wave, Figure 3.4.2 shows that, for most incidence angles commonly present in seismic acquisition, PP energy is more than 100 times higher than PS (one should take the square of the amplitude transmission coefficient to analyse energy). This is a strong indication that conversion from P- to S- wave at sea bottom can be expected to be very poor in most marine environments.

Reflection coefficients for incident P- and S- waves at top of a turbidite reservoir are presented in Figure 3.4.3. It can be seen that P-S and S-S modes are of relatively similar values over most incidence angles. The conclusion is that no specific mode seismic energy is dramatically stronger than other for reflections at this interface.

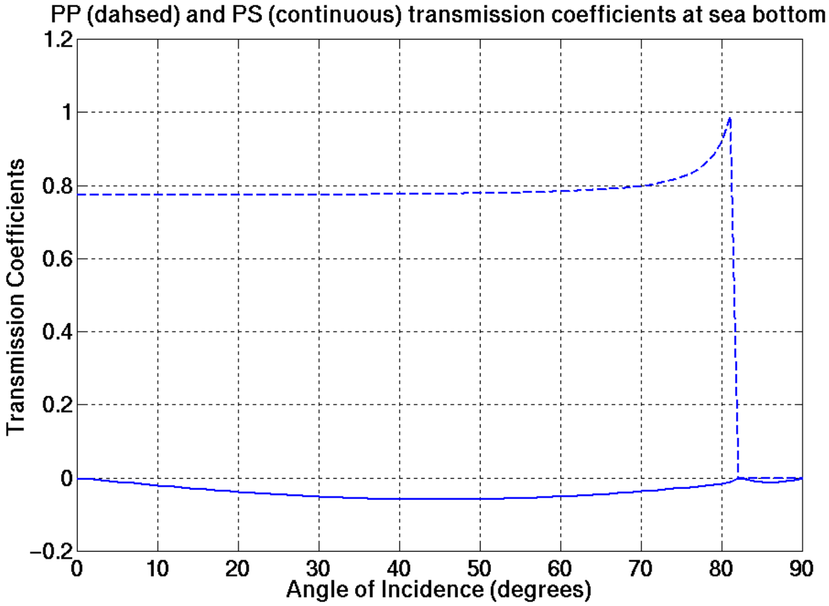

Figure 3.4.2 – Transmission coefficients for downgoing PP (dashed) and PS (solid) seismic waves in a sea/sediment interface. Energy (proportional to square of amplitude) for PP is more than 100 times larger than for PS.

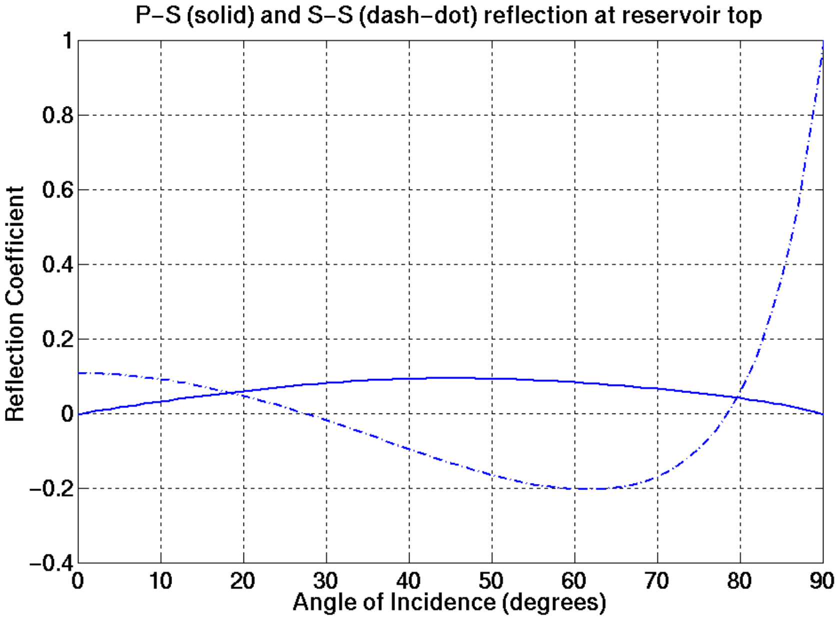

Figure 3.4.3 – Reflection coefficient at top of turbidite reservoir for P-S (solid) and S-S (dash-dot) seismic waves. Up to 70^0, modes have (relatively) close reflection coefficient values.

The next analysis is to multiply the PS transmission coefficient at the sea bottom by the S-S reflection coefficient at reservoir top and compare the result with the product of PP transmission coefficient at sea bottom by P-S reflection at reservoir top. In other words, we compare amplitudes of PS-S and PP-S modes.

The results are shown in Figure 3.4.4. One can conclude most shear wave energy travelling upward should be created by the PP-S mode instead of PS-S mode.

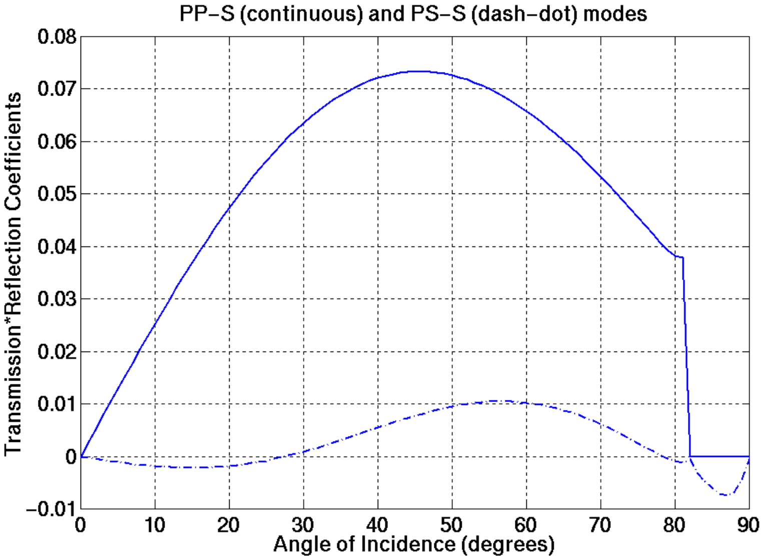

Figure 3.4.4 – Amplitude coefficients for PP-S mode (PP transmission at sea bottom and P-S conversion at reservoir top, solid line) and PS-S mode (PS conversion at sea bottom and S-S reflection at reservoir top, dash-dot line). Clearly, PP-S mode has much higher energy than PS-S.

A quantification of how much greater PP-S mode energy is compared to PS-S mode energy is given in Figure 3.4.5. The energy was considered equal to the amplitude (from Figure 3.4.4) squared. The values of PP-S energy over PS-S energy were clipped arbitrarily at 500 – the ratio values become very large around 26^0 and 80^0, because PSS values tend to zero.

One can see from Figure 3.4.5 that PP-S energy is, in general, over 100 times stronger than PS-S energy.

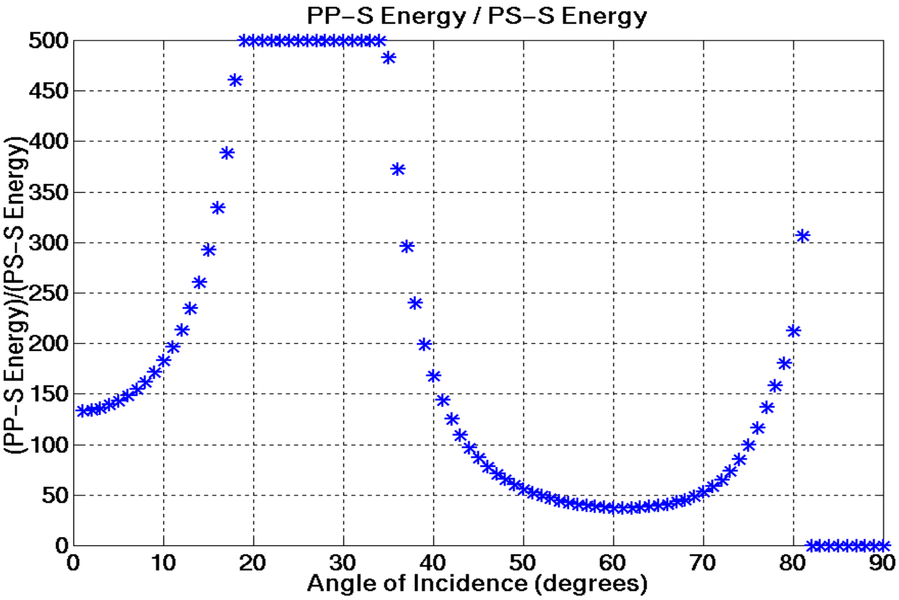

Figure 3.4.5 – Ratio between PP-S energy and PS-S energy, clipped to a maximum value of 500. It is shown that PP-S energy is rarely less than 50 times greater than PS-S energy, and values over 100 may be expected from most angles used in seismic acquisition.

Possible mode conversions (both P- to S- and S- to P-) in the up-going seismic energy were also analysed. This test, suggested by Prof. Gary Margrave, was to verify a possible explanation to a phenomenon sometimes seen in OBC data processing (Ebrom *et al.*, 1998a; Yuan e*t al.*, 1998; Li and Yuan, 1999; chapter V of this thesis): the presence of shear-wave energy in the vertical component while the radial component does not present compressional energy. The presence of S-waves in the vertical component is verified by applying to vertical data the processing flow (velocities, receiver statics, etc) used in the radial component. A similar procedure – using P-P processing flow – is used to verify the presence of P-P energy in horizontal components.

One should expect, by analysing Figures 3.2.1 and 3.3.4 and using Snell's Law, that most up-going shear waves would approach the receivers very close to the vertical, due to the strong decrease in V_S at shallow sediments. So, it is somewhat surprising to find P-S energy in the vertical component, mainly when

P-P energy is not found in horizontal components.

Professor Margrave's idea was to check if S-wave energy present in the vertical component could be due to some compressional energy converted from shear at shallow sediments. If this is the case, the apparent P-P energy will have P-S behaviour (e.g., P-S velocities and traveltimes).

It should be pointed out that the analysis done here is assuming perfectly elastic media, an average over 5 meters (over and below interfaces) for physical properties (V_P, V_S and density), and plane wave propagation. One might argue that very different results could occur if inelastic modelling were used, due to expected very low quality factor for S-waves (Q_S) in shallow marine sediments. Published data (e.g., Hovem *et al.*, 1991) however, suggests Q_S values below 10 are uncommon – in general, Q_S equals one half of Q_P in these sediments.

The interfaces analysed for mode conversion were defined based on density discontinuities (Figure 3.4.6). Main boundaries were observed at 5, 20, 90, and 160 m depth.

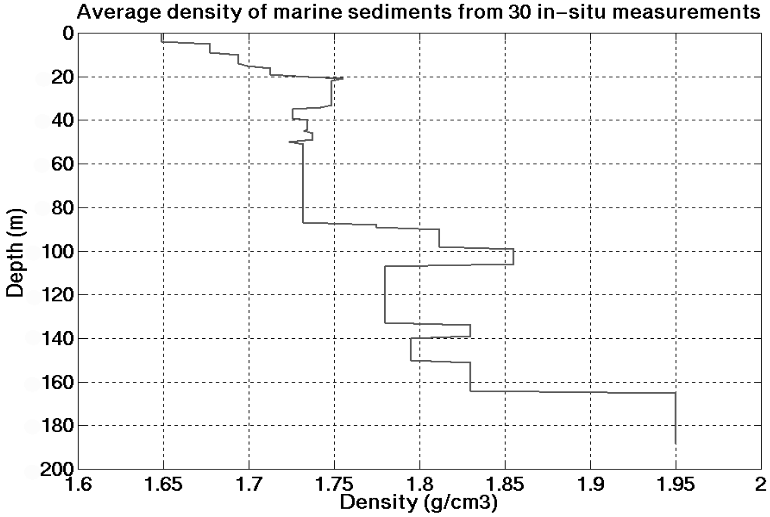

Figure 3.4.6 – Average of 30 in-situ density values measurements in marine sediments. Depths of 5,20,90 and 160 m were defined as boundaries to analyse mode conversion. These values were also used for V_S calculation in this chapter.

The resulting transmission coefficients for mode conversion (P- to S- and

S- to P-) of up-going wavefield are shown from Figure 3.4.7 to Figure 3.4.9.

It is clear in all pictures that the conversion is negligible at all depths, and that most energy transmitted through the interfaces corresponds to the same mode of incident energy.

The highest mode-conversion in all examples occurs at the sea-bottom (bottom in Figure 3.4.9), for S- to P- conversion between 15^0 and 45^0. Even in this situation, though, the energy converted can be considered as marginal, as PP energy is going to be 100 times stronger than the SP.

The main conclusion is that an alternative explanation has to be found to the presence of P-S energy in vertical geophone component while no P-P energy occurs in horizontal components. Perhaps, the most likely explanation is that the shear-wave arrival is coupling onto the vertical geophone due to the mechanical instabilities of the cable and geophone element gimbals. Li and Yuan (1999) also considered this possibility. In some areas, reflection out of the source-receiver vertical plane (sagittal plane) can cause this phenomenon.

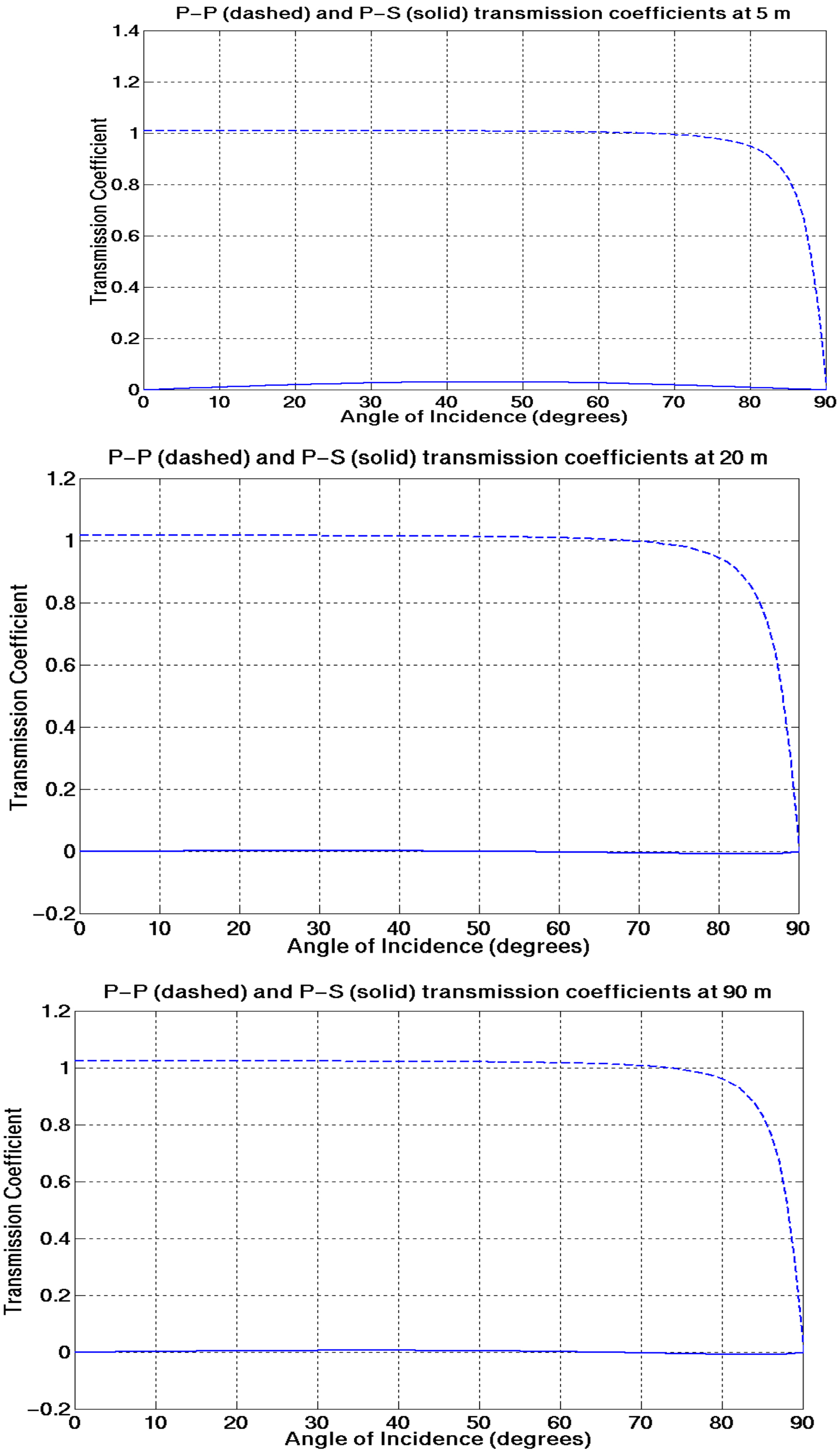

Figure 3.4.7 – Transmission coefficients for up-going P-wave (PP dashed and PS solid) at (from top to bottom) interfaces located at 5, 20, and 90 m depth. Most energy does not suffer mode conversion.

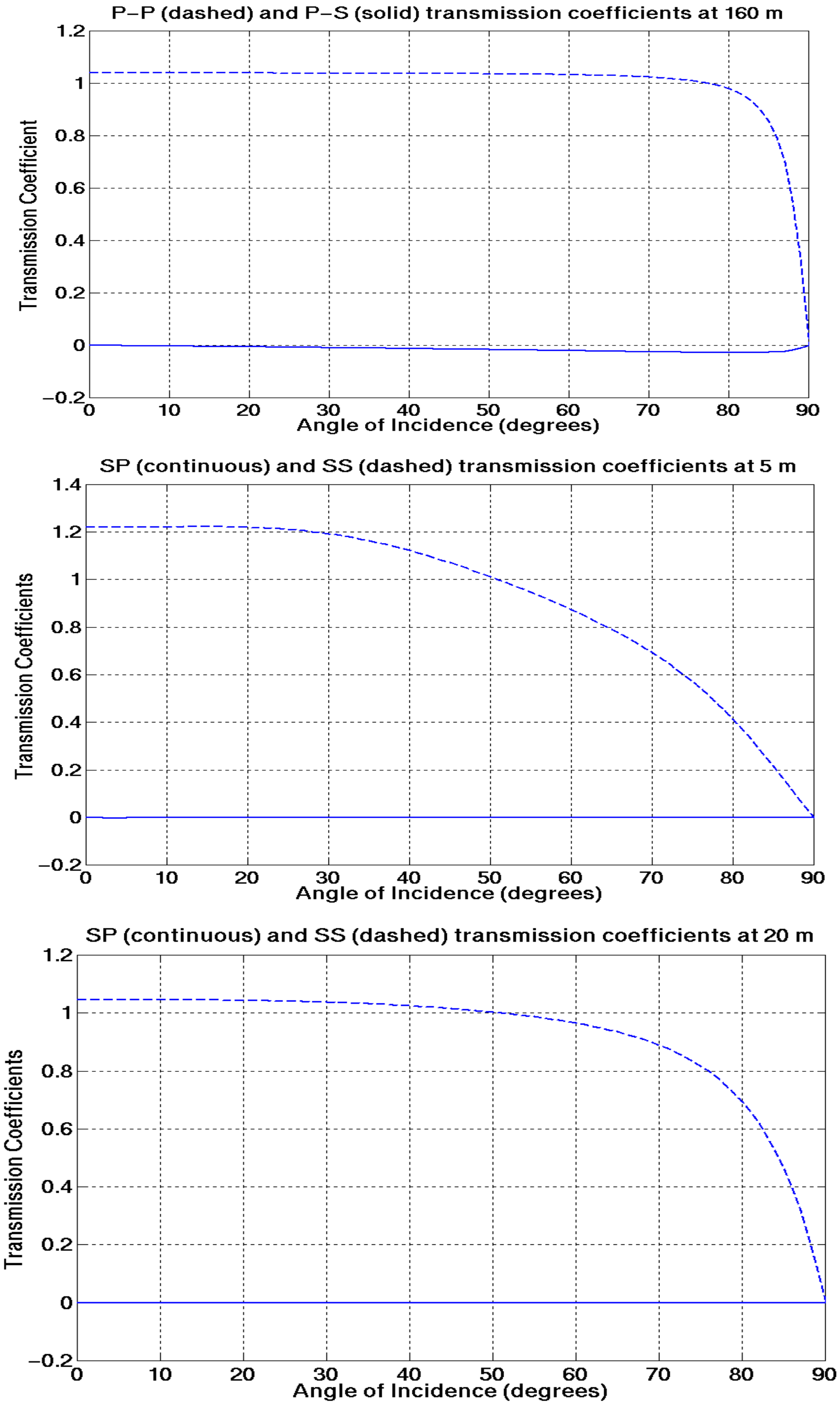

Figure 3.4.8 – Transmission coefficients for up-going P-wave (PP dashed and PS solid) at 160 m depth (top) and for up-going S-wave (SS dashed and SP solid) at 5 m (middle) and 20 m (bottom). Most energy does not suffer mode conversion.

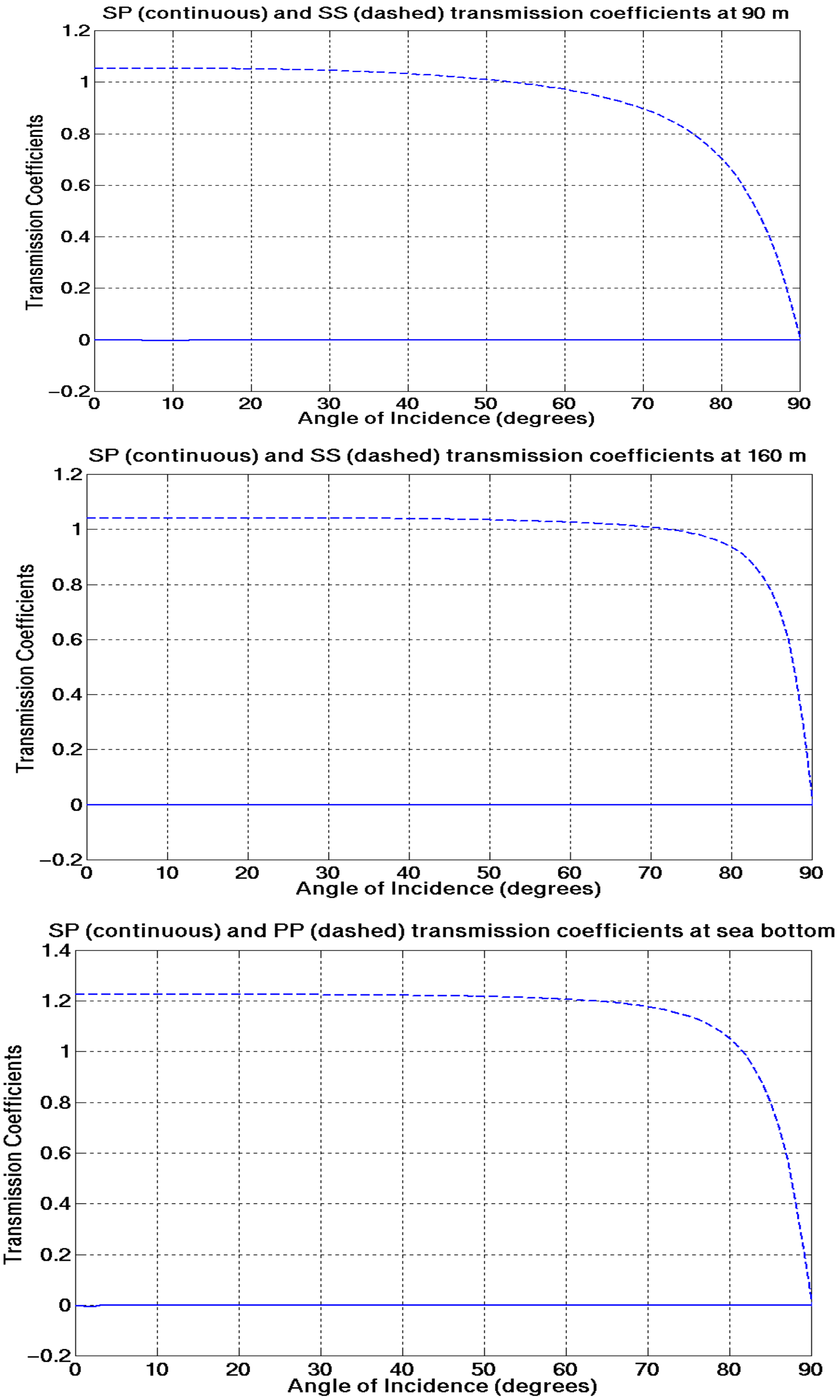

Figure 3.4.9 – Transmission coefficients for up-going S-wave (SS dashed and SP solid) at 90 m (top) and 160 m (middle) and for S- and P-wave up-going at sea-bottom (bottom, PP dashed, SP solid). Most energy does not suffer mode conversion.

III.5 Discussion

Elastic parameters for shallow marine sediments were obtained from literature information (Hamilton (1976,1979); Hovem *et al*. (1991); Esteves (1996)) and previously unpublished geotechnical data from offshore Brazil. Brazilian data showed reasonable agreement with Hamilton's results except in the very shallow (less than 10 m) sedimentary section. A second-order equation to calculate V_S as a function of depth in marine sediments, not significantly different from expressions previously derived by Hamilton, was derived empirically down to a depth of 140 m.

Analyses of transmission and reflection coefficients for compressional- and shear-wave energy mode conversion using Zoeppritz equations were performed for both sea bottom and a typical hydrocarbon reservoir top of Tertiary age. It was concluded that most S-wave reflection energy recorded on the ocean floor by OBC is related to upcoming energy converted at an interface at depth and not from a downgoing shear conversion at the ocean floor.

It was also concluded that, using elastic assumptions, mode conversion (both P- to S- and S- to P-) of the up going energy is negligible in the shallow (above 160 m) sediments and not very strong at sea-bottom (without free-surface effect considerations).

Chapter IV – Analysing 4-C 2-D OBC Data from the Valhall Field, Norway

IV.I Introduction

A 2-D seismic line using four-component (4-C) receivers – a 3-C geophone and a hydrophone placed in a cable – laid on the sea bottom was acquired in 1996 by PGS Reservoir Services AS. Amoco and its partners undertook the survey over the Valhall Field, offshore Norway.

The main objective of the survey was to provide a better image of a chalk reservoir. Converted-waves (P-S) were used, as P-P waves are strongly attenuated and scattered due to the presence of gas in the layers over the reservoir.

As mentioned in chapter II, the OBC technique has been tested – many times successfully – in geological areas with this imaging problem. In this chapter, such an example is presented.

The radial component processed for P-S events resulted in data of reasonable quality, as a continuous image for the target was obtained. A good overall section was generated using the asymptotic common-conversion-point (ACCP) binning and equivalent offset migration (EOM) methods.

IV.2 Valhall field: geology and seismic aspects

The Valhall field, operated by Amoco Norway Oil Company and partners, is located in the southernmost part of the Norwegian North Sea (Figure 4.2.1a). The water depth in the area is around 70 m, and reservoir depth around 2,400 m.

The quality of conventional seismic data is poor because the overburden layers (Tertiary marine shales) are highly gas charged. This causes scattering and signal attenuation of pure P-wave energy. Some other techniques, such as VSP, flattened seismic sections, and seismic inversion have been used to help with this problem (Munns and Mullen, 1987).

The potential reserves of the Valhall and adjacent Hod fields (Figure 4.2.1a) area have been recently estimated to be more than 1 billion barrels of oil (Farmer and Barkved, 1997). A map in depth of the top of the chalk, from Leonard and Munns (1987), is presented in Figure 4.2.1b.

The field has an estimated volume for original oil in place of 2.5 billion barrels, and daily production around 100,000 barrels. It has been on production since 1982. The flank areas of the field, where the imaging problem is not present, are developed trough horizontal wells. In these areas, the target zone is kept on horizontal wells in more than 90% of the horizontal length, compared to 60% for areas with poor image. Drilling is a problem due to combination of overpressure and weak and fault zones (D'Angelo *et al.*, 1997; Thomsen *et al.*, 1999).

The main reservoirs are reworked chalks in the Tor and lower Hod formation (both upper Cretaceous). The Tor formation (Maastrichtian Age) is responsible for 85% of the production and 70 % of oil in place. It has porosity in excess of 40% over most of the field (locally over 50%), permeability between 2 to 15 mD (20 to 120 mD in the crestal area, increased by natural fracturing) and abrupt thickness variation (0 to 80 m, average 25 m). In the Hod formation, the thickness is around 30 m and porosity 35% and above. The top chalk acoustic impedance can be lower or equal to the overlaying Paleocene shales. The bottom of the reservoir has a significant increase in acoustic impedance, being a marked amplitude in the area. The Paleocene sequence can be considered as having a slowly lateral thickness variation (D'Angelo *et al.*, 1997; Farmer and Barkved, 1997; Thomsen *et al.*, 1999).

The high primary porosity values are due to high rates of deposition and lack of consolidation and cementation. They were preserved due to extreme overpressure in the reservoir caused by hydrocarbon migration, in a complex interplay of depositional modes with oil migration timing, burial history, diagenesis and insoluble residue concentrations (Leonard and Munns, 1987; D'Angelo *et al.*, 1997; Farmer and Barkved, 1997).

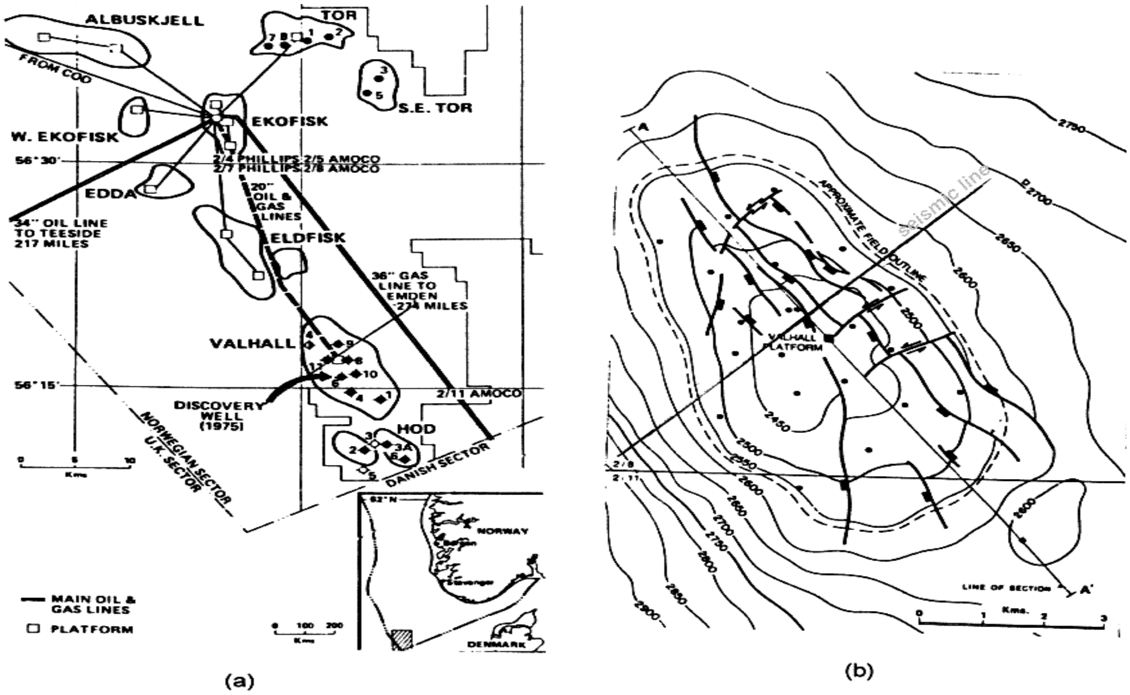

Figure 4.2.1. (a) Localisation of the Valhall field; (b) indication of seismic line on a depth map of the top of the chalk *(both after Leonard and Munns, 1987).*

One model for the reservoir genesis is that sub-aqueous movements (debris flows, slumps, slides, and turbidites) created fast accumulations of redeposited chalks, generating anomalies in the chalk thickness (Leonard and Munns, 1987; D'Angelo *et al.*, 1997). Farmer and Barkved (1997) present a model, using 3-D seismic data and biostratigraphy, where syn-depositional faulting and reworking play an important role in reservoir thickness variation. They concluded that graben areas created during continuous uplift on Late Cretaceous and Early Tertiary were protected from erosion and became depositional centres for the reworked chalk.

The fracturing may cause anisotropic behaviour in the seismic data – if this is true, anisotropy studies become very interesting, as the fracture pattern affect oil production. There are general small-scale faults over the field (Strand, 1997).

As with most oil fields producing from chalk reservoirs in offshore Norway, the trap is structural/stratigraphic. The trap is an asymmetric anticline with a NW-SE trend and steep dip toward west (Nazir and Alcock, 1992, *in* Strand, 1997). The highest uncertainty in the exploration is the presence of porosity, as the reservoir facies is surrounded by pelagic facies. There is a strong variation in reservoir quality, with the thickest areas presenting best porosities and permeabilities (Leonard and Munns, 1987; D'Angelo *et al.*, 1997; Farmer and Barkved, 1997).

Japsen (1998), analysing data from 845 wells throughout the North Sea Basin, obtained a normal velocity-depth trend for the upper Cretaceous. Negative velocity anomalies, present in the central and southern parts of the basin (where the Valhall field is located), are related to overpressures that exceeds 10 MPa, equivalent to a burial depth greater than 1 km relative to the normal trend. According to the author, this overpressure is caused mainly (80%) by disequilibrium compaction due to variations of burial history of an upper Cretaceous chalk, and secondarily by hydrocarbon buoyancy. The chalk occurs in the form of coccolits (debris of planktonic algae), and clastic influx was low at that time.

The main purpose of the seismic analysis is to differentiate the reservoir and non-reservoir chalk facies. D'Angelo *et al.* (1997) report an integrated study combining geological models (sedimentology of chalk deposition, burial histories and reworking of autoctone chalk), petrophysical information from core samples (which showed association between increasing porosity and decreasing velocities for P- and S-waves – Figure 4.2.2), and surface seismic analysis (stratigraphic processing, velocity analysis with a 125 m interval, modelling, inversion and AVO) that allowed the detection and mapping of high-porosity reservoir-quality chalks. They found anomalously low velocity zones, including a gas chimney, at the high and down flank regions of the field. The conclusions of their work were confirmed by an oil discovery.

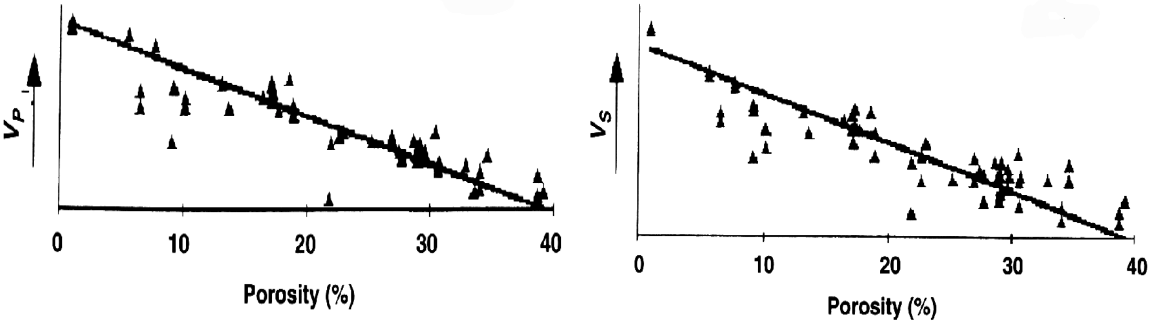

Figure 4.2.2 – Correlation between increasing porosity and decreasing V_P (left) and V_S (right), obtained from Cretaceous chalk cores in the Valhall area (*after D'Angelo et al., 1997)*.

Landro *et al.* (1995), assuming a horizontally layered model and neglecting anisotropy effects, performed an AVO inversion in conventional data over the Valhall field. They considered a single layer over the reservoir, and used P- and S-wave velocities and densities from empirical relationships and well log data. Shear velocities were determined mainly from variation of reflection amplitude with angle of incidence. Corrections for absorption were made using a quality factor (Q) of 250. The V_P/V_S ratios obtained from their work vary between 1.12 and 1.56. According to the authors, these low values do not agree with ultrasonic core measurements, although predicted porosity values from their study were confirmed by a discovery well.

Thomsen *et al.* (1999) say that the presence of artifacts and the mispositioning and blurring of reflectors may occur in converted-wave data in this area, when homogeneous and isotropic assumptions are used in the processing. The authors suggest the use of azimuthal processing and consider anisotropic behaviour.

Strand (1997), based on the processing results in the same data presented here, concluded that good coupling was achieved. His processing flow has some differences from the one used in this chapter. For instance, he used *f-k* filtering to enhance signal before velocity analysis, and obtained predictive deconvolution parameters by trace autocorrelation. He also applied a CDP processing for the radial component, and compared the results with data from ACCP processing, finding the ACCP approach much better, with time moveout closer to a hyperbola in the ACCP case. He considers the absence of high frequencies in the radial component is due to some problems in the P-S processing modules. Although his point may be correct (converted-wave algorithms need further improvement), I think the low frequency content is mainly due to the higher absorption which occurs to shear waves (Krebes, 1989; Hovem *et al.*, 1991), so P-S modes will have, in general, lower frequency content than P-P energy.

From ray tracing results, Strand (1997) pointed out the necessity of careful observation of polarity reversal in CDP and ACCP gathers, due to critical angle reaching, for both P-P and P-S. As final conclusions, he interpreted the data in the inline component to be PP-S mode (not PS-S) and an average V_P/V_S ratio little less than 3.0 from the sea bottom to the reservoir.

IV.3 Seismic acquisition

PGS Reservoir Services AS acquired the sea-bottom seismic survey in June 1996, using a shooting boat (“Professor Polshkov”) and a receiver (“Bergen Surveyor”) vessel. The unique aspect of the acquisition is the receiver system. A cable with eight receiver units – each unit weighting 50 kg and containing one gimballed multicomponent (3-C) geophone and one hydrophone – was laid on the sea bottom (Berteussen *et al.*, 1997; Kommedal *et al.*, 1997). Each unit location defines a station position. Each receiver unit was enclosed in a box, called a ‘pad’ (Strand, 1997).

The cable, with an anchor on one end, is laid on the sea bottom. The receiver vessel pulls the cable to straighten it. Two acoustic transponders were used to determine receiver unit positions. This kind of measurement is affected mainly by water depth and water temperature gradients. For the Valhall survey, Strand (1997) reports that an accuracy of +/- 2 m is expected. The source system – a conventional air gun array with 3,180 cubic inches – is expected to have the same accuracy in its positioning.

After the receiver system is ready, the source vessel traverses directly overhead and parallel to it. Offsets to about eight kilometres on each side of the centre of the cable are used. At the end of the shooting line, the receiver cable was moved 200 m in line for the next position in the south-west direction. The same shooting pattern was repeated. In total, 40 lines were shot, giving approximately 200,000 traces/component in total. During the shooting, the receiver vessel was positioned 500 m ahead and 150 m off-line. This acquisition system is named by PGS as “Dragged Array” (Berteussen *et al.*, 1997; Kommedal *et al.*, 1997).

The receiver and shot point intervals are 25 m. The cable and shooting directions are approximately along the azimuth 237^0 (Figure 4.2.2b). The maximum nominal fold, at the centre of the line, is around 300. The approximate position for CDPs range is shown in Figure 4.2.2b. The sample rate is 2 ms and record time 11.5 s.

As the sea bottom is composed of hard sand, it is believed that good coupling is resulted (Kommedal *et al.*, 1997). No information is available about measurements on the geophone orientation. The position for each receiver was probably obtained through interpolation between the cable’s extremes, although this could not be confirmed.

More acquisition parameters are presented in Appendix I, based on information from PGS (1996).

IV.4 Processing sequence in ProMAX: results and comments

The first step was to resample (with an anti-alias filter) the data from 2 ms to 4 ms to facilitate analyses of this large data set. If any signal is present over 125 Hz, it probably occurs only in the very shallow part of the section. After preliminary processing, an offset limit of 4.0 km (except for equivalent offset migration and converted-wave DMO in the radial channel, where 3.5 km was used) and a maximum time limitation of 6.0 s (hydrophone and vertical components) and 9.0 s (radial and transverse components) were used. The offset limit is especially desirable when either ACCP binning or converted-wave DMO is applied.

To obtain the correct geometry on ProMAX was very complicated and time consuming. Eventually, this problem was resolved using a land configuration. Some receivers had to have their positions corrected manually, using navigation information provided by PGS (1996), the acquisition contractor.

Two corrections were applied aiming true amplitude recovery: 1) geometrical spreading (spherical divergence) according to the inverse of the product of time and the square of velocity (Newman, 1973) ($1/(tV^2)$, the velocity obtained from velocity analysis with a 1.5 km interval), and 2) 1.5 dB/sec correction. As pointed in section 2.4, Harrison (1992) showed that converted-waves amplitudes also can be corrected using Newman (1973) approach, by applying appropriate P-S velocities. Correction for inelastic attenuation, with different values for the attenuation constant α was tested, but the results were not consistent and the correction was omitted. Surface consistent amplitude was applied to decrease amplitude differences associated with recording levels and/or coupling variation.

Probably due to some acquisition gain problem, data from shooting lines 33 to 37 have very low amplitudes. Surface consistent amplitude correction, using shot and receiver domains, solved this problem after three iterations. To remove the presence of some extremely low-frequency “bias” after the surface consistent amplitude correction, a bandpass filter of 0-3-120-125 Hz was applied.

Amplitude spectra show the presence of very strong notches in all geophone components and at the hydrophone. These notches are likely caused by energy reverberation in the water layer, and will be discussed in more detail below.

Velocity analysis was performed every 250 m, with the final velocities obtained after the second iteration. In general, the velocity values are very low, as expected for the presence of gas. The gas implies that some strong lateral velocity variations may occur. Sometimes, the determination of which velocity to be used was problematic, as two different hyperbolas cross each other. Thomsen (1998) offer an explanation for this phenomenon.

Thomsen's explanation points at that this occurs because the traveltimes (and amplitudes) for two traces with same offset but with symmetric source and receiver positions may be different. This difference is due to the largest time for the downgoing P-wave travelling through the gas-charged sediments, then converted to S- at the interface, compared to the downgoing P-wave out of the gas area (with a gas-insensitive up-going S-wave through the gas).

As some events in the stacked sections correspond to reverberation, a minimum phase predictive decon (three gates, operator length and prediction distance varying) was applied after stacking.

From the three post-stack migration algorithms tested – phase-shift, finite difference and Kirchhoff – the last one was chosen. An AGC (1500 ms) was applied before migration, and the velocity used was 90% of the stacking velocity.

A bandpass time-varying filter and F-X Decon were applied after Kirchhoff migration in all sequences (use of F-X Decon was tested both before and after migration, the results after being better). The frequency ranges and time "gates" for the bandpass filters were obtained through spectral analysis using a 1.0 s window.

For display, only every second trace was used.

IV.4.1 Hydrophone and vertical geophone components

A conventional P-P analysis flow was applied in hydrophone and vertical component geophone. A hydrophone gather, from a position out of the gas occurrence, is shown in Figure 4.4.1. The data on Figure 4.4.1 has amplitude recovery and minimum-phase deconvolution applied. Many events are clearly visible, but some of them may represent reverberations. In the amplitude spectrum of this gather (Figure 4.4.2), severe periodic notches, especially at around 10 and 20 Hz, are present. This spectrum corresponds to the average of all traces and samples (times) in the gather of Figure 4.4.1. Between 30 and 100 Hz, the spectrum is approximately flat. Most of this energy is likely noise, as no such high frequency is expected. The steep descent above 110 Hz is due to the anti-alias filter applied during resampling.

A vertical component gather (after amplitude recovery and minimum-phase deconvolution), also from out of the gas area, is shown in Figure 4.4.3. A cone of very low frequency and low velocity events (approximately between 130 and 250 m/s) at small offsets represents the Scholte wave (explained in section 2.1). The spectrum of vertical component data (average of all traces and time from 0.0 to 6.0 s) is shown in Figure 4.4.4. The anticipated exponential decrease of frequency is noted.

Although both gathers are from the same position, the quality in the hydrophone is apparently much better. After data from both components are stacked and migrated, though (Figures 4.4.5 and 4.4.6), the differences are small.

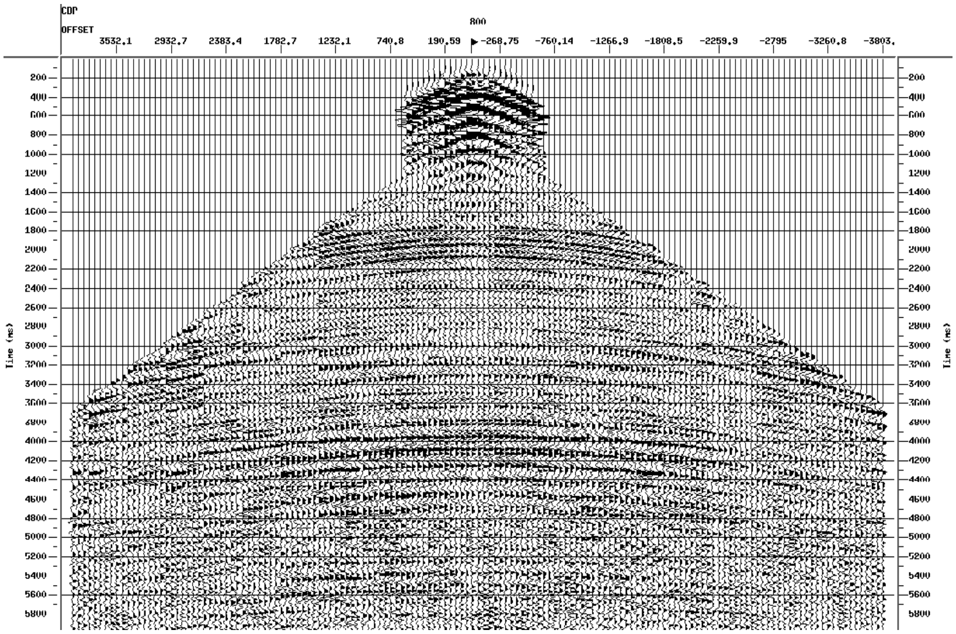

Figure 4.4.1 - Hydrophone CDP gather (from a position out of the gas chimney). Amplitude recovery and minimum-phase deconvolution applied.

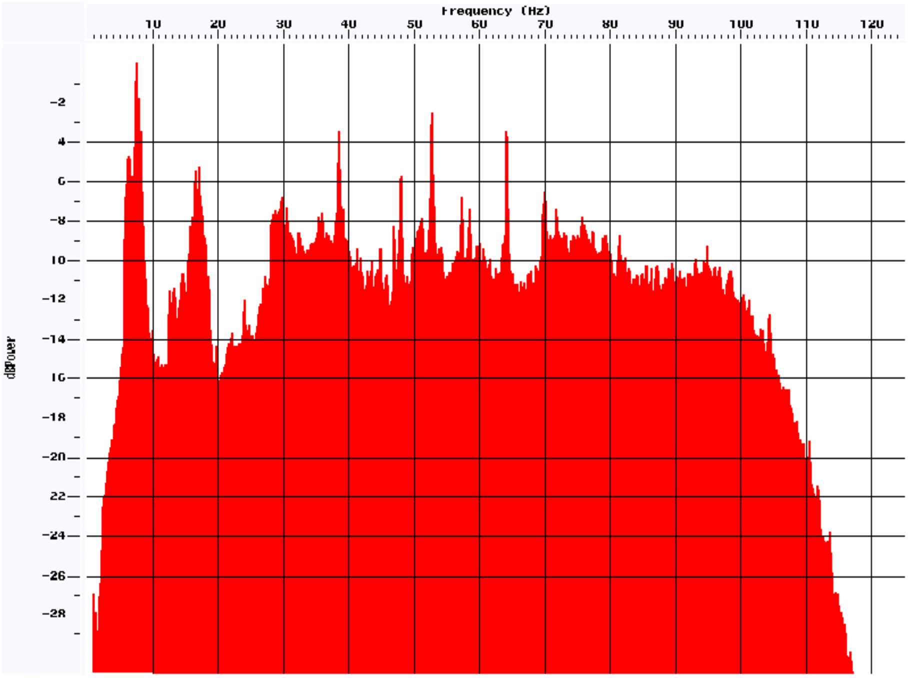

Figure 4.4.2 – Average amplitude spectrum from all traces and time 0.0 to 6.0 s hydrophone gather (Figure 4.4.1). Observe the strong notches around 10 and 20 Hz.

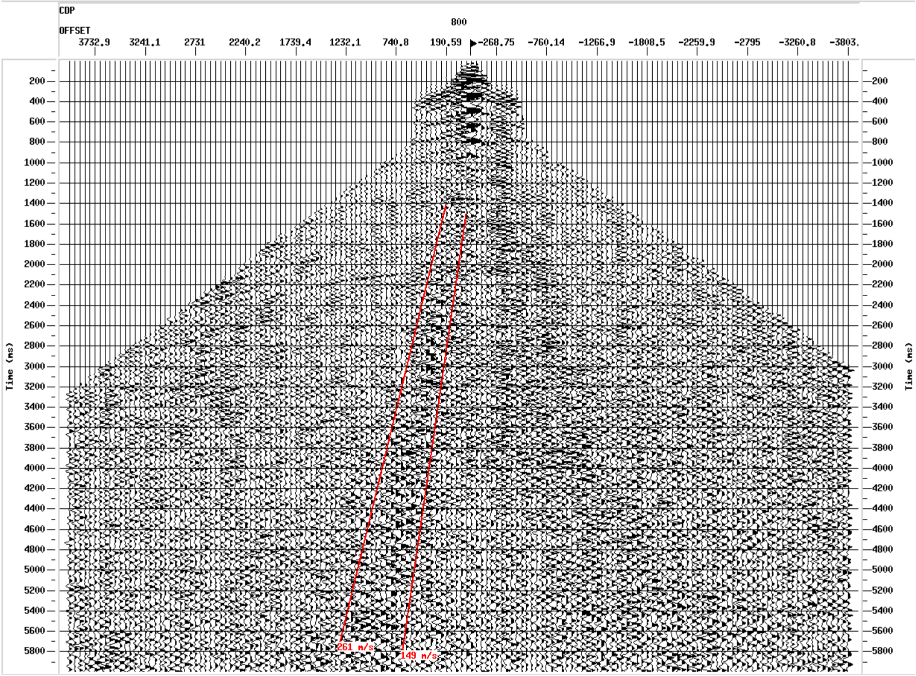

Figure 4.4.3 - Vertical component CDP gather (from a position out of gas chimney). Observe very low frequencies and velocities of Scholte waves.

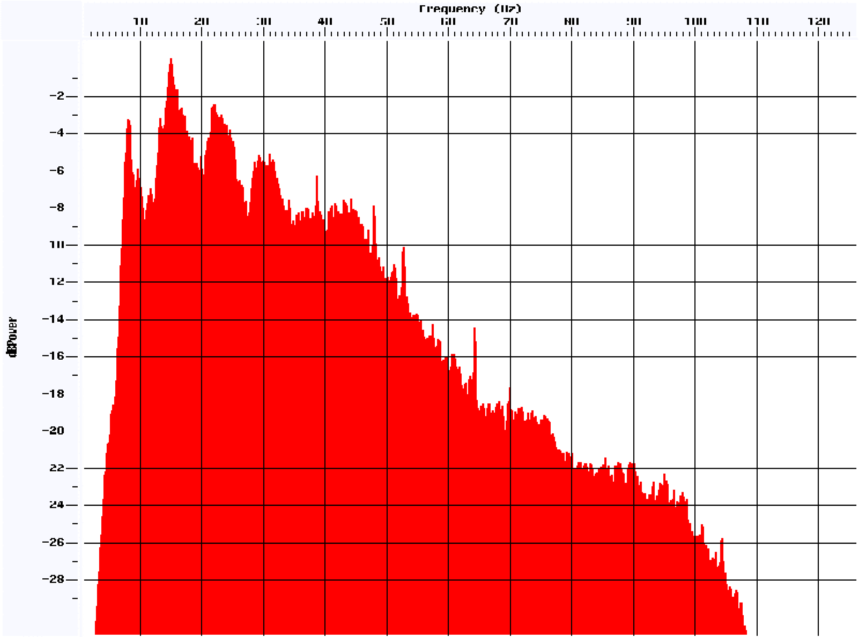

Figure 4.4.4 - Amplitude spectrum from vertical component gather (Figure 4.4.3). Observe strong notches and energy decreases toward higher frequencies.

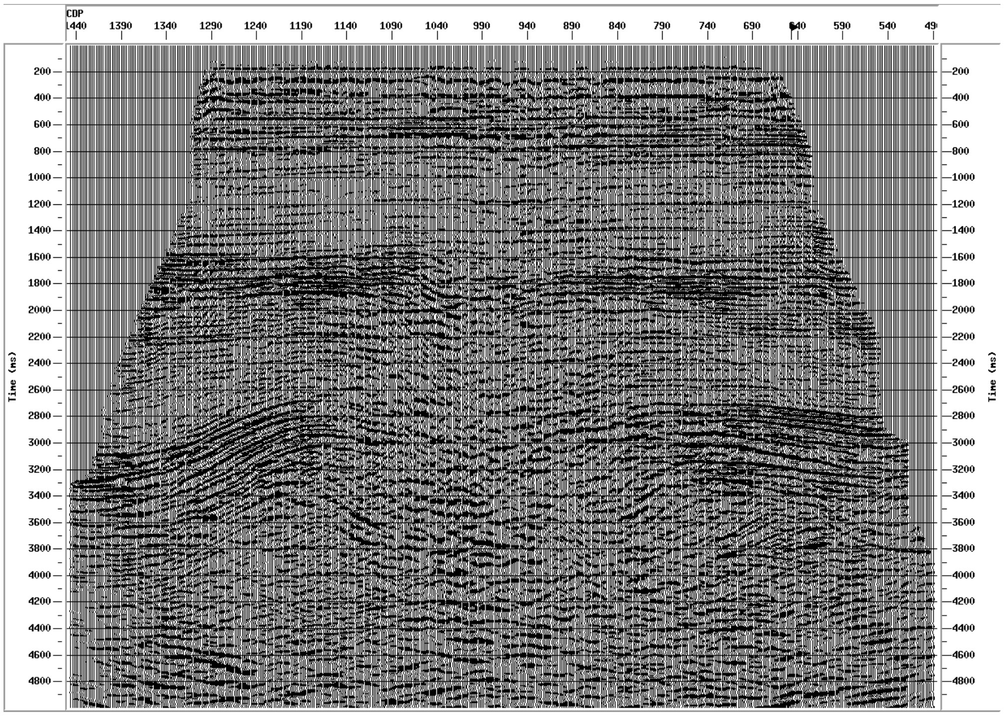

Figure 4.4.5 - Migrated section of hydrophone data. Observe pushdown and reflection-free zone at the centre of the line.

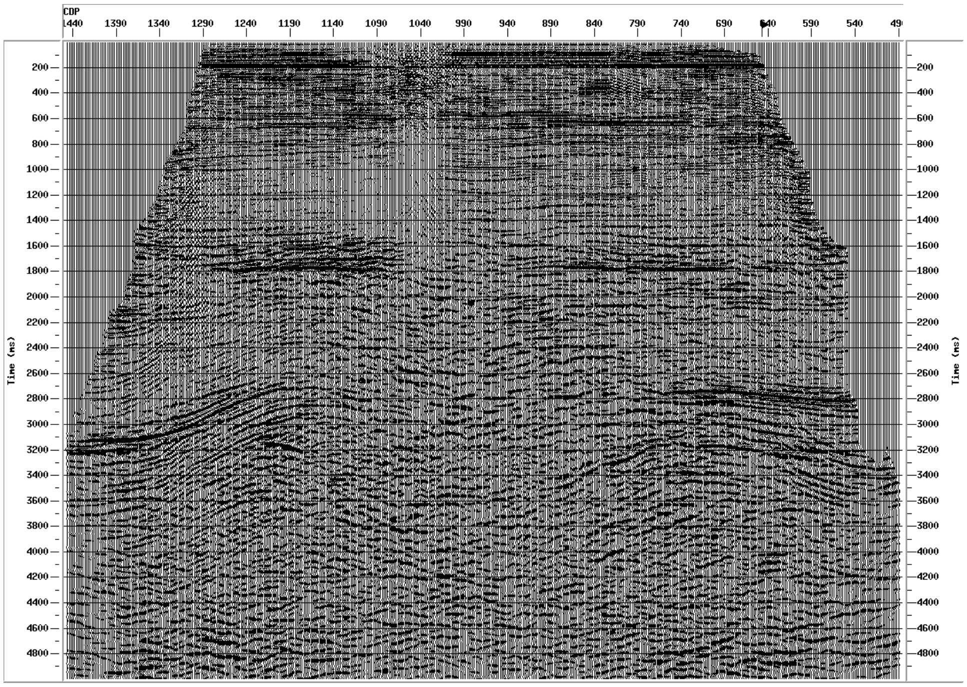

Figure 4.4.6 - Migrated section of vertical component data.

Observations in published data from Valhall (D’Angelo *et al.*, 1997, Leonard and Munns, 1987) permit one to conclude that the strong reflection from CDP 850 to north-east at 2.7 s, and its continuation to south-west after CDP 1150, is related to the top of the chalk (Paleocene Age), relative to both reservoir and pelagic facies. Another important event, between 3.1 s and 3.2 s at north-east of CDP 800, probably represents a Cretaceous unconformity. A pushdown effect is observed in the central part of the section, starting at 1.5s.

The reflection-free zone between CDPs 850 and 1100 below 2.3 s is interpreted as being caused by the strong attenuation and scattering affecting P-wave propagation. This phenomenon is also present in other North Sea oil fields (e.g., Ekofisk). An almost horizontal and highly continuous event at 0.6 s is probably Miocene in age.

IV.4.2 Radial component

The processing sequence used here is based mainly on Harrison’s (1992) work. The first step after resampling and geometry description – which is the same for all components – was to perform a polarity reversal according to the relative position between source and receiver. The polarity for some offset – either positive or negative – has to be changed to account for the opposite polarity found for the shear wave component recorded by the inline and crossline components.

Initially, a CDP processing flow was used to investigate whether PS-S energy (shear-wave energy converted at the sea bottom) is present in the radial channel. Some reflections could be identified around 8.0 s – according to Thomsen *et al.* (1997), PS-S reflections from target should occur around this time – when the lowest velocities present in semblance gathers were picked for stacking, but no continuity was present.

Three different additional sequences were applied in the radial component: P-S common-conversion-point asymptotic binning, converted-wave

DMO, and equivalent offset migration (EOM).

Asymptotic binning estimates an approximation to the common-conversion-point using an asymptotic approximation algorithm (Tessmer and Behle, 1988) based on a single V_P/V_S ratio (section 2.4).

Initially, a constant value of 1.7 for the V_P/V_S ratio was used in the whole section. This was based on Landro *et al.* (1995), who used an average V_P/V_S value of 1.4 for AVO analysis in the sediments from the water bottom to the target. A second processing run was performed with a ratio of 2.5, and much better results were obtained. Strand (1997) relates the use of 2.8 until the top of the reservoir (around 5.5 s in the inline section).

Due to the asymmetrical ray path, ACCP-binning gives a higher fold over a smaller section of the line.

The asymptotic binning method assumes a small (<1.0) offset-to-depth ratio. For this reason, stacked sections processed with 2.5 km offsets (close to the target depth, 2.4 km) and 4.0 km offsets, to verify any possible problem in using the asymptotic approximation, were compared. “Better” results, in terms of reflection continuity, were achieved for 4.0 km offsets, so this value was used during the processing.

An ACCP gather, after asymptotic binning and NMO correction, is presented in Figure 4.4.7. Events between 5.0 and 5.5 s and the one immediately below 5.5 s are interpreted as close to the reservoir. The high amplitude – low frequency reflections between 5.5 and 6.0 s may be due to reverberation from energy trapped inside the chalk layer (channel wave). This hypothesis follows from the high interval velocity observed in this layer, during velocity analysis.

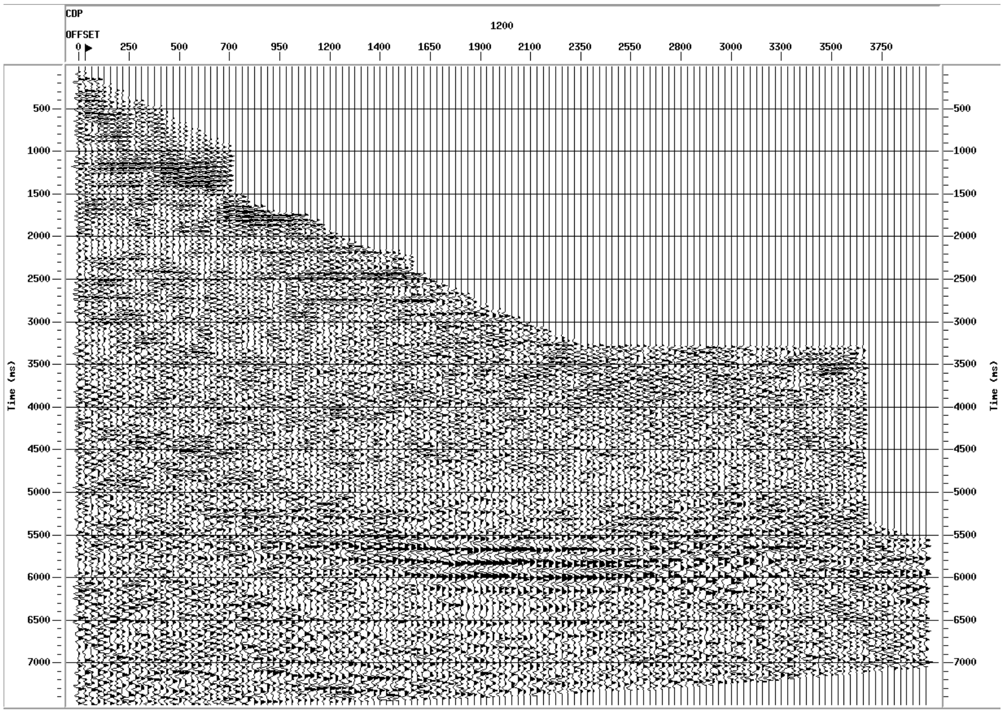

Figure 4.4.7 - NMO-corrected common-conversion-point asymptotic binning (ACCP) gather of radial component data.

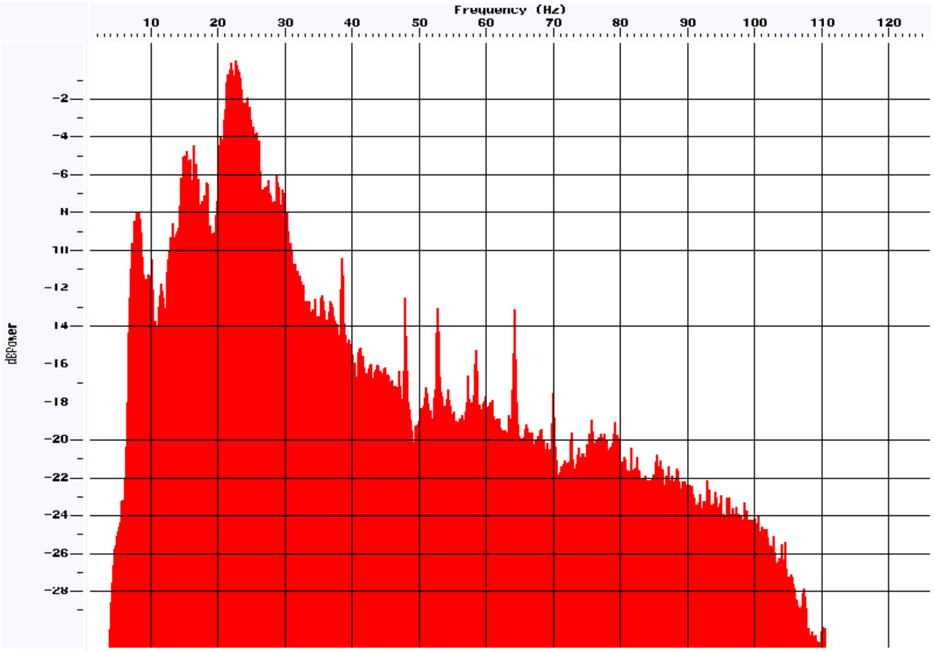

Figure 4.4.8 - Amplitude spectrum of radial component ACCP gather (Figure 4.4.7). Observe the strong notches inside the signal band (5-30 Hz).

Figure 4.4.8 shows the spectrum for this ACCP gather (without NMO correction). Clearly, the notches are present, although not at exactly the same frequencies as in the vertical component. These notches are problematic, as they are very strong over the frequency range where most of the converted-wave energy usually occurs (8-25 Hz).

A pre-stack migration algorithm (Bancroft and Geiger, 1994; Bancroft *et al., 1998*) developed in CREWES and adjusted to converted-wave data by Li and Bancroft (1997a,b) has been used to image these data. This pre-stack migration method creates an intermediate pre-stack data volume, instead of directly obtaining the image section. The intermediate data volume is sorted into common scatter point (CSP) gathers, which provide migration velocity information.

One CSP gather at the same position as that of the ACCP gather in Figure 4.4.7 is presented in Figure 4.4.9. One can see similar events in the two gathers, but the CSP gather seems better.

NMO correction with the migration velocity and conventional CDP stacking applied in CSP gathers complete the entire migration process. For the data presented here, the computer time for this algorithm is close to the time required to image with a converted-wave DMO scheme.

A comparison of the amplitude spectra from the CSP (Figure 4.4.10) and ACCP (Figure 4.4.8) gathers also shows some difference: neglecting the notch effect (which occurs approximately at the same frequencies in both cases), the CSP spectrum is somewhat flatter in the signal bandwidth (8-30 Hz). Two possible explanations are: 1) as the CSP method involves a collecting (stacking) of traces, it can act as a high-frequency filter, consequently increasing the relative energy in the lower frequency spectrum (Prof. Gary Margrave, 1997, personal communication), and/or 2) a Fresnel zone effect (Prof. Larry Lines, 1997, personal communication).

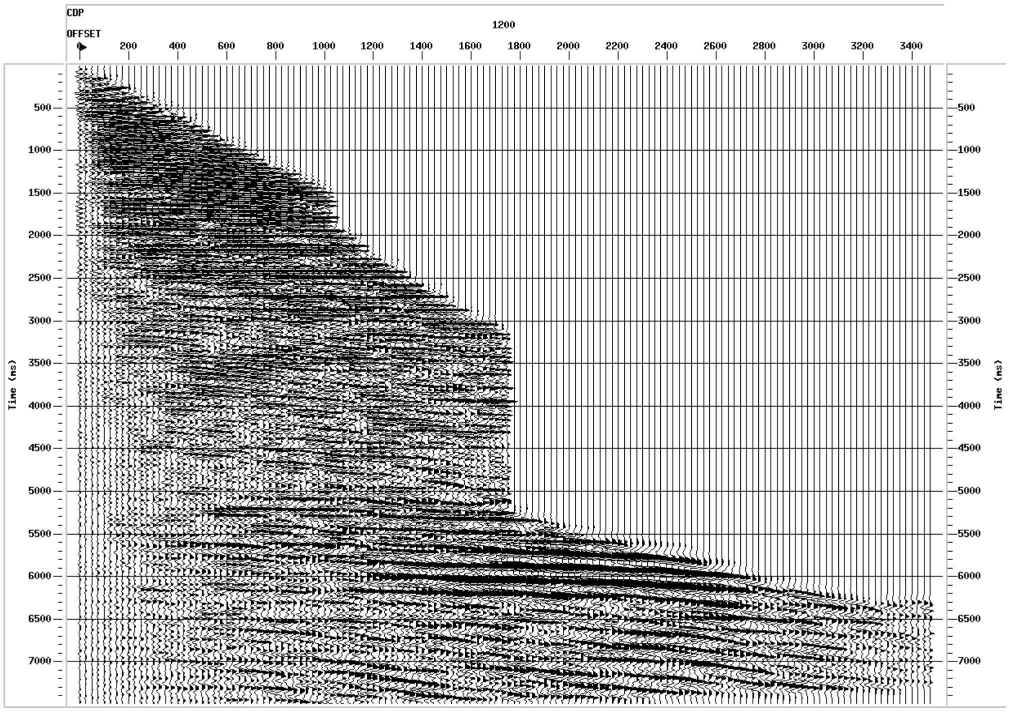

Figure 4.4.9 - NMO-corrected common scatter point (CSP) radial-component gather after equivalent offset migration (EOM). Observe higher energy content than ACCP gather (Figure 4.4.7).

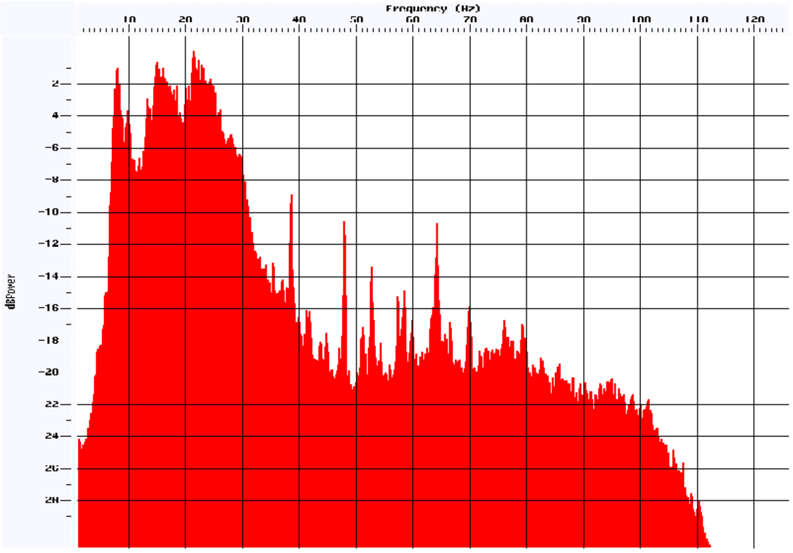

Figure 4.4.10 - Amplitude spectrum of radial-component CSP gather (Figure 4.4.9). Observe the flatten spectrum (neglecting notches) in the signal bandwidth.

In all three sequences (asymptotic binning, converted-wave DMO and

EOM), the velocity interpretation was sometimes difficult. This difficult was due to lateral event discontinuity.

The result of ACCP stacked data is shown on Figure 4.4.11. Due to lower S-wave velocity, the gap and operator length for predictive deconvolution should be changed for the radial and transverse components data. For a V_P/V_S of 2.0, a 50% increase (from P-P data values) in both parameters should be used (Mr. Mark Harrison, *in* Strand, 1997).

A quite continuous reflection, with relatively high frequency, can be followed between 5.0 and 5.5 s in most of the line, and it probably is related to the top of the chalk. Some normal faulting seems to be present (e.g., CDPs 880 and 950). This is consistent with the tectonic evolution of this area (Leonard and Munns, 1987; D'Angelo *et al.*, 1997). The result of a Kirchhoff migration is presented in Figure 4.4.12.

The quality for this line is good, even if its central part has somewhat less continuity than on the structure's flanks. This may be due to the P-wave downgoing path inside the gas rich region and/or some fault-imaging problem.

Figure 4.4.13 shows the result from the sequence converted-wave DMO (no asymptotic binning applied), conventional stack, and Kirchhoff migration in the radial data. A good image is obtained for the target only at some parts of the line.

The final result for the EOM method is shown in Figure 4.4.14. This process gives perhaps a better image than converted-wave DMO for the target. Over the gas chimney, it also works a little better than the asymptotic binning. The EOM method, tested here for the first time on real P-S data, looks very promising in providing an image in an area with significant geophysical problems.

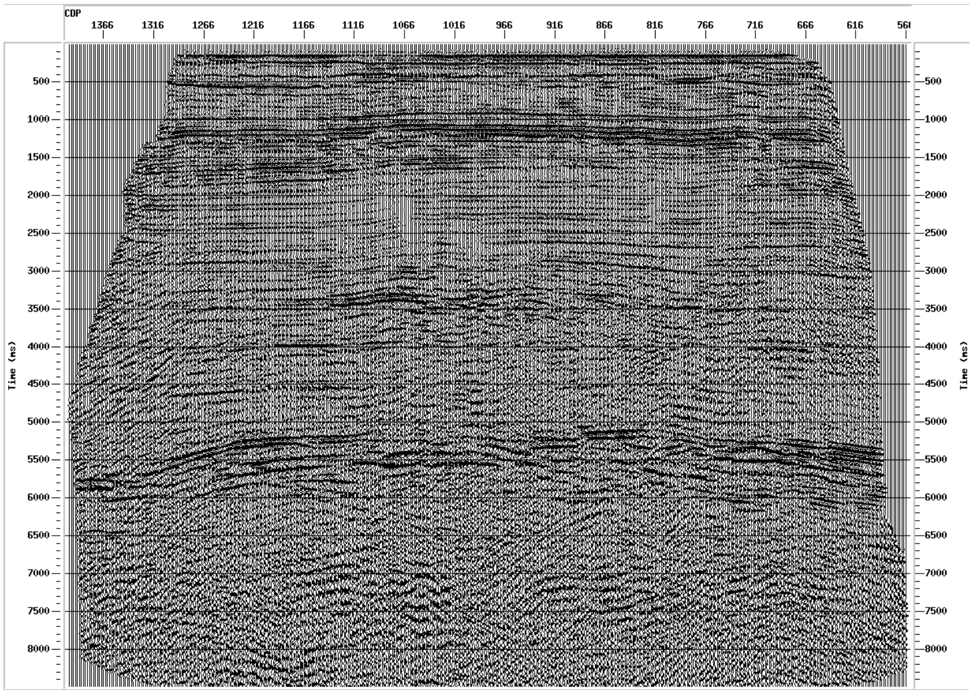

Figure 4.4.11 – Conventional stack using asymptotic binning (with V_P/V_S =2.5) of the radial-component data.

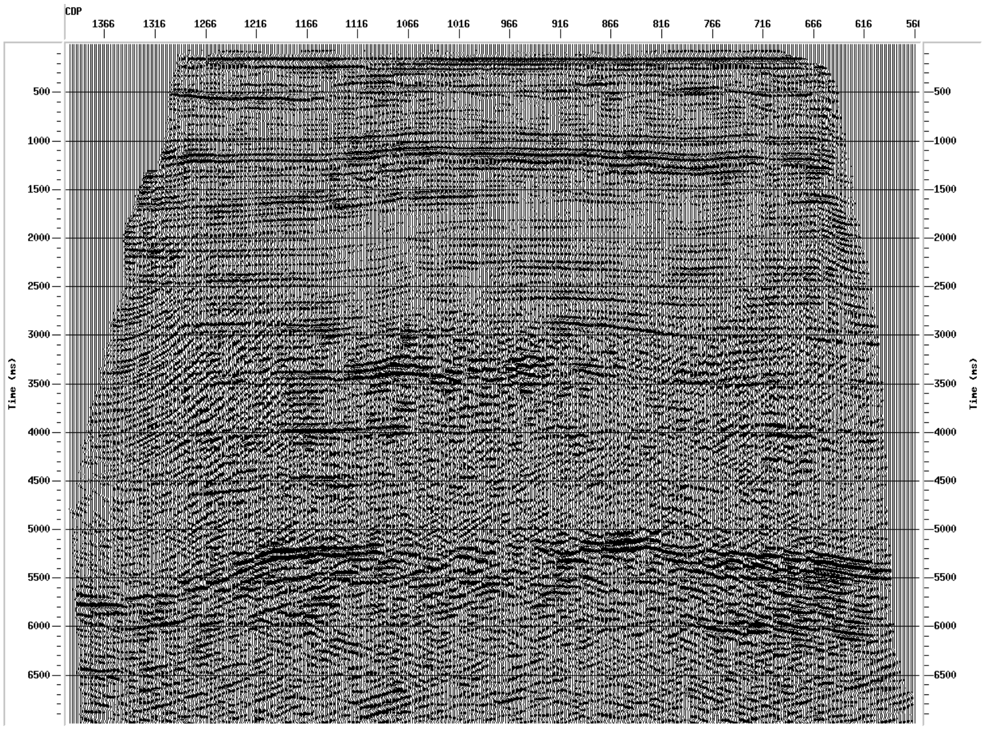

Figure 4.4.12 - Kirchhoff migration on data from Figure 4.4.11.

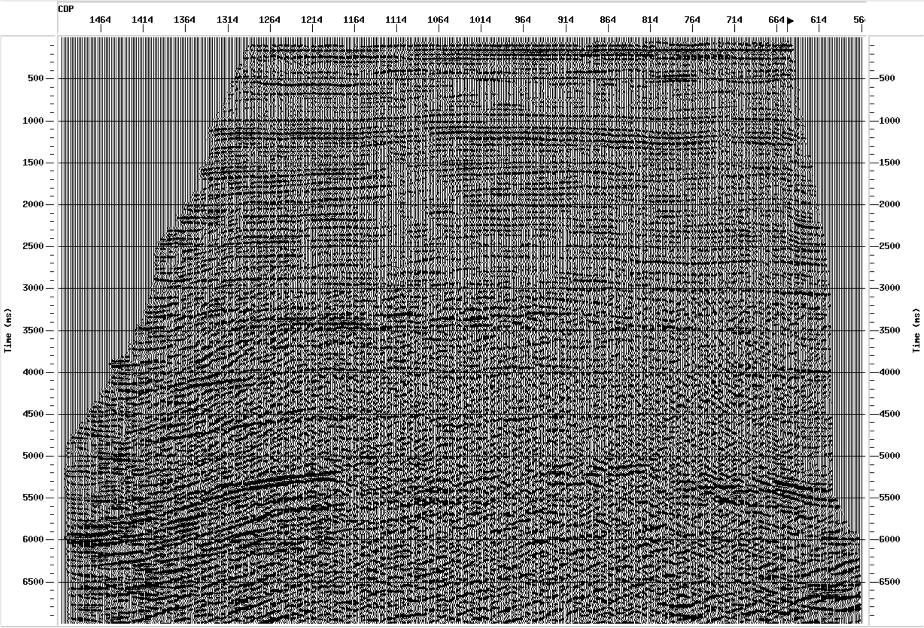

Figure 4.4.13 - Converted-wave DMO, conventional stack, Kirchhoff migration in radial-component data. Compare with Figures 4.4.12 and 4.4.14 (see text for discussion).

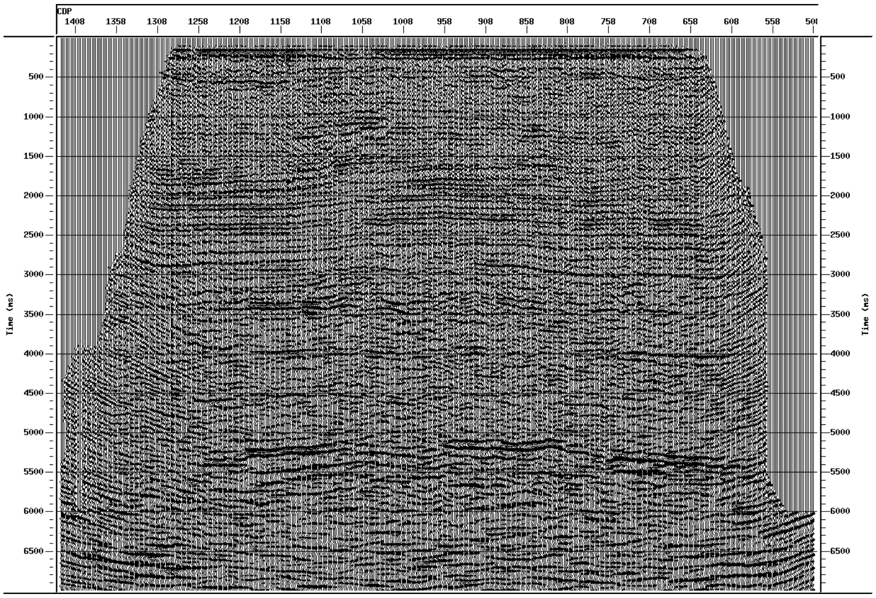

Figure 4.4.14 - Equivalent-offset migration (EOM) and conventional stack in radial-component data. Compare with Figures 4.4.12 and 4.4.13 (see text for discussion).

IV.4.3 Transverse component

The asymptotic binning sequence applied in the radial component was also used in the transverse component. In ACCP gathers not much energy seemed to be present. The stacked section (Figure 4.4.15) shows some coherent events.

Although the transverse component looks similar to the radial, it is much noisier and the reflections are less continuous. This energy can be due to acquisition misalignments, reflections from points out of the sagittal plane and/or anisotropy. Out of the plane energy may not be too severe here, as the line is close to the structure apex (Thomsen *et al.*, 1997; Strand, 1997), S-wave birefringence may have some effect. This may be the case also as there are some fractures in the geological layers. Additional possibilities are geophone coupling and mechanical cross-feed between components.

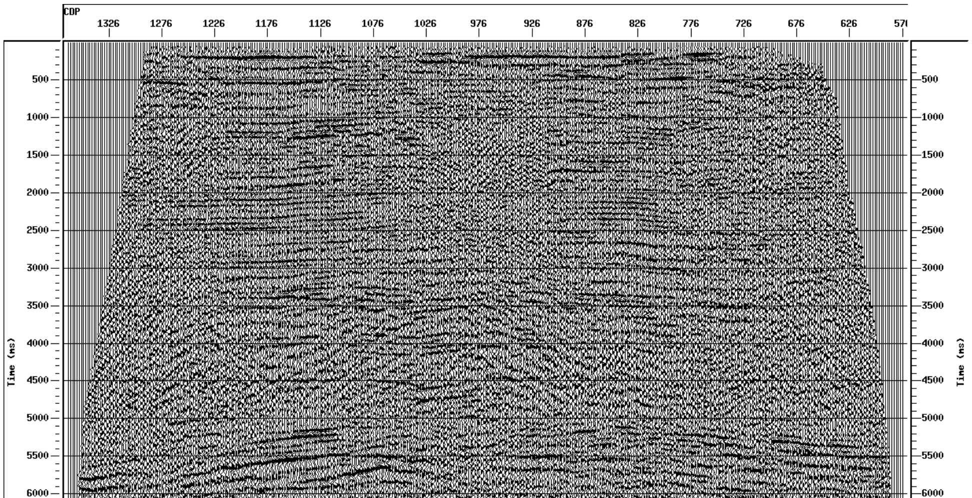

Figure 4.4.15 - Conventional stack (V_P/V_S =2.5) after ACCP (asymptotic binning) in transverse-component data.

IV.4.4 P-S flow in vertical component, P-P flow in radial and transverse components

Tests were performed to investigate both the presence of S-wave energy in the vertical component and P-wave energy in the radial and transverse components. The vertical component processing flow and parameters (velocity, statics, etc.) were applied in radial and transverse components and the asymptotic binning flow (with corresponding velocities and V_P/V_S ratios) in the vertical channel. The resulting stacked sections for vertical (Figure 4.4.16) and radial (Figure 4.4.17) components indicate that there is not very much cross-coupled energy between vertical and horizontal components.

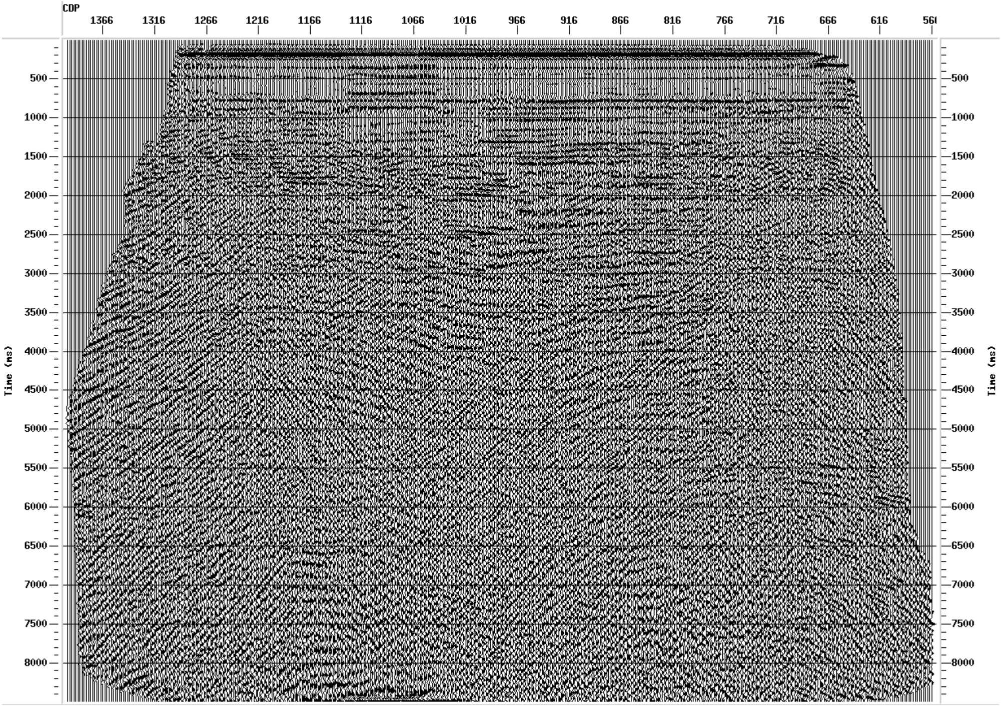

Figure 4.4.16 - P-S flow (ACCP binning and conventional stack) applied in vertical-component data. Events in this section correlates with events in vertical-component data processed with P-P flow (Figure 4.4.6).

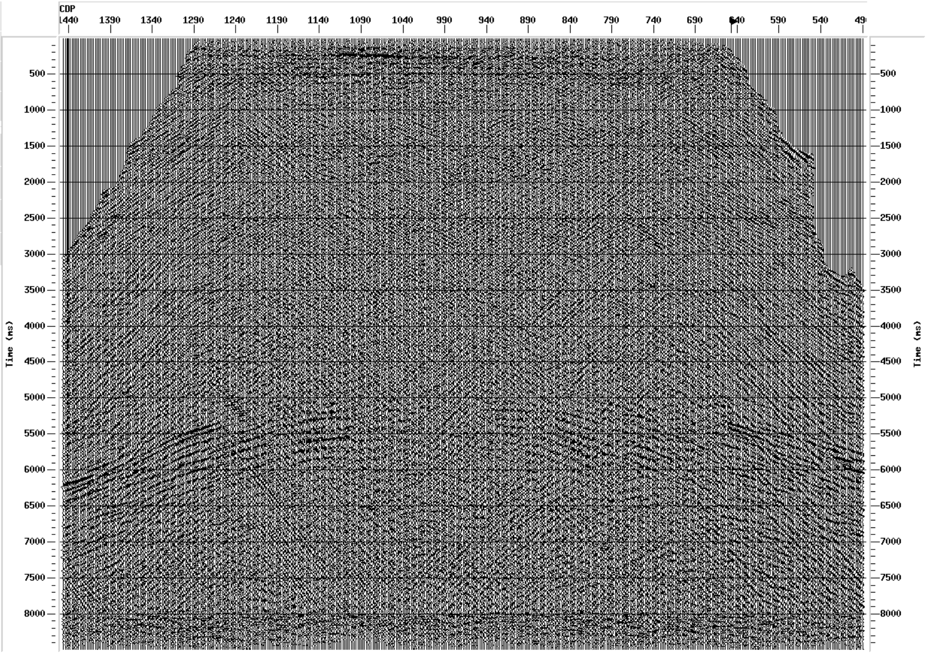

Figure 4.4.17 - P-P flow applied in radial-component data.

IV.5 Discussion

The vertical geophone and the hydrophone components showed a largely reflection-free zone for the target at the middle of the section. These components did not provide interpretable images of the reservoir region.

The radial component gave reasonable P-S images. Four processing flows were applied to the radial component data: conventional CDP processing (for possible PS-S events, i.e., a P- to S- conversion at the sea bottom), asymptotic common-conversion-point binning (ACCP), P-S DMO, and equivalent offset migration (EOM). Convincing evidence of a PS-S event was not found. A comparison among three methods for P-S processing (ACCP binning, converted-wave DMO and EOM) showed that all methods provided some areas of preferred quality. The EOM method shows considerable promise.

Some energy is present in the transverse component, for the same events mapped by the radial component, but with much lower continuity. There are various possible explanations, anisotropy effects being the most likely (SH-SV cross-coupling also being a possibility).

To investigate the presence of P-wave energy in the radial and transverse components, the processing flow for the P-P wave was applied to the radial and transverse data. In addition, the ACCP binning P-S flow was applied to the vertical channel data. The results show that: 1) little P-S energy is present in the vertical component, and 2) only small P-P energy occurs in radial and transverse components.

Strong spectral notches are present in all geophone components and in the hydrophone. These notches, probably related to energy reverberation in the water layer, are especially problematic in the radial component, as they occur at the signal bandwidth of converted (P-S) waves.

Geophone coupling and receiver positioning do not seem to be a problem in this survey.

Chapter V – Processing the Teal South 4C-4D Seismic Survey

V.1 Introduction

The Teal South 4C-4D seismic project is an initiative to investigate the use of multicomponent seismic data in assisting the monitoring of reservoir fluid movements. The Energy Research Clearing House (ERCH) is co-ordinating the project with Texaco – the operators of the Teal South field, on Eugene Island Block 354, in the Gulf of Mexico (Figure 5.1.1). Texaco acquired a first 4C-3D in July 1997, using four ocean bottom cables (OBC). This chapter summarises the acquisition and presents some processing results for the second 4C-3D data set, acquired in April 1999.

Teal South is located 256 km (160 miles) south-west of New Orleans in the Gulf of Mexico; the water depth is approximately constant and around 85 m (280 ft). Oil is produced from unconsolidated Tertiary sands at depth from 1220 to 2440 m (4000 to 8000 ft). Small reservoir volumes and high flow rates result in rapid depletion of the reservoirs. The seafloor is soft (muddy) in the area (Ebrom *et al.*, 1998a; Purnel *et al.*, 1999).

Teal South was selected by ERCH because: 1) it was thought that oil production over a time interval as short as four months could create petrophysical changes in the reservoirs that are strong enough to be detected by surface seismic data; 2) Texaco had already done some time-lapse study in the area, using streamer acquisition, and 3) the relatively small area of the reservoirs limited the size of the 3-D data required.

The field has a shallow reservoir with high production rates and a short projected life. The area is also good as a laboratory for testing new techniques due to its relatively simple geology, and small survey size. The sea floor cables were laid under tension, to ensure regular receiver spacing and horizontal components alignment. For receiver positioning, both acoustic “pingers” attached to the cables and first breaks of the shots were used in the same survey, providing a unique opportunity to compare these two methods (Bole *et al.*, 1999).

For the first OBC 3-D survey, Roche *et al.* (1999) reported that receiver locations were determined precisely by the use of acoustic transponders, but orientation is only approximated. The apparent receiver orientation was obtained using P-wave first arrivals. Some uncertainties observed are attributed by the authors to both computational errors (caused by shallow sediments anisotropy) and physical process (the receiver dual axis gimbals and/or the transducer coupling may have different azimuth sensitivity).

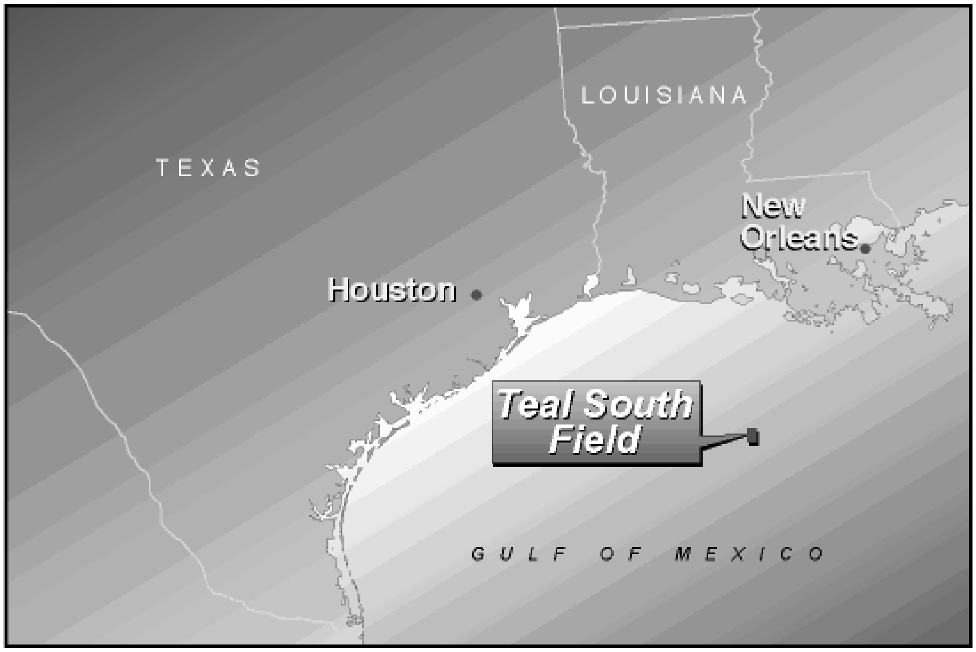

Figure 5.1.1 – Location of the Teal South field in the Gulf of Mexico *(after Ebrom et al., 1998b)*.

In the same data, Purnell *et al.* (1999) used 3-D phase-shift plus interpolation (PSPI) depth migration in pre-stack common-receiver gathers. Before migration, offset-dependent wavefront spreading correction, Q compensation and surface-consistent methods (amplitude compensation, predictive deconvolution, and residual statics) were applied in the data. Comparing the result of this processing with a conventional CDP stack followed by 3-D poststack time migration, they concluded that, for a structural analyses at Teal South, the later sequence produces adequate results.

Ebrom *et al.* (1998a) sampled the Gulf of Mexico sea bottom, as the soft bottom was a concern for using multicomponent OBC seismic in the area. A sample, from the upper 30 cm (1 ft) of sediments below the sea bottom, indicated 95% of fines (clays) and 5% sand and Foraminifera. This confirms that geophone lay on soft sediments – but they concluded good multicomponent data could be acquired in this environment. They also analysed, using direct arrivals, source directivity, finding amplitude changes less than 15% for waves reaching between zero and 50 degrees; they conclude that the source could be considered as omni-directional. The authors also concluded that most energy present in horizontal components is related to conversion at sediments interfaces and not at sea bottom based in modelling using shear velocities from depth migration.

V.2 Seismic data acquisition

Figure 5.2.1 shows a map of shot point and receiver positions. Most information in this section comes from a report by Baker Hughes/Western Geophysical (1999), the acquisition contractor.

Seven cables were used in a fixed configuration. Four cables, each cable with 6 receivers spaced 200 m, were laid along the E-W direction; the distance between cables was 400 m – this is a receiver pattern close to the one used in the first 3-D. Three additional cables (each cable having 4 receivers spaced at 400 m) were laid in a N-S direction, spaced 100 m apart (Figure 5.2.1). The entire cable deployment took five days, in February 1999.

One objective of the second phase of Teal South project was to analyse how different methods of laying the cable on the sea floor might produce different response. For this reason, five cables were buried (trenched) 1 m under the sea floor, one cable laid on sea floor and had the receivers taped to it and another cable was laid on sea floor, and had the receivers taped to the cable and wrapped in sand sacks. A remotely operated vehicle (ROV) was used on cable trenching. The trenched cables are the ones oriented E-W and the westernmost along N-S. The easternmost N-S cable is the one with bags of sand put over the receiver units, and the N-S cable at the middle is the one with the receivers taped to the cable (Figure 5.2.1).

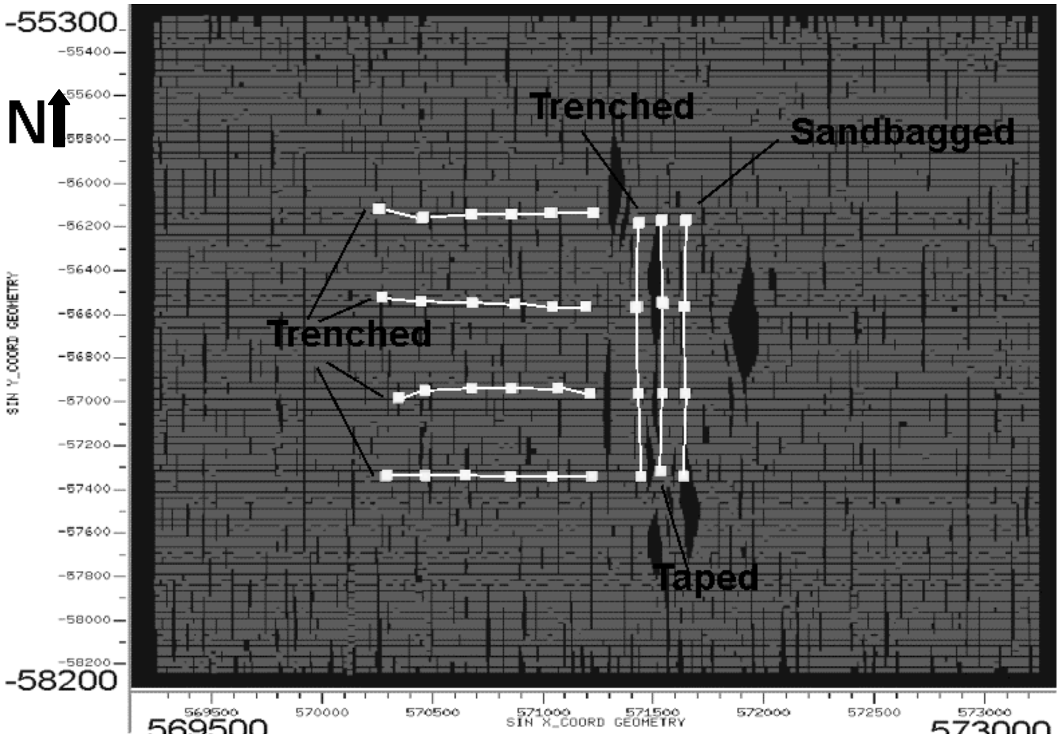

Figure 5.2.1 – Map view of shot point (grey) and receiver (white) position. Observe shot gaps (due to obstacles), four receiver cables along E-W (with six units), and three cables along N-S (four units). E-W cables and westernmost N-S cable were trenched, middle N-S cable was laid on sea-bottom and had receivers taped to the cable and easternmost N-S cable was laid on sea-bottom and had receivers taped and sandbagged. Distances in metres.

Figure 5.2.2 shows a 4-C receiver unit used in the acquisition and the same unit attached (taped) to a cable. Figure 5.2.3 shows how the receivers were sandbagged.

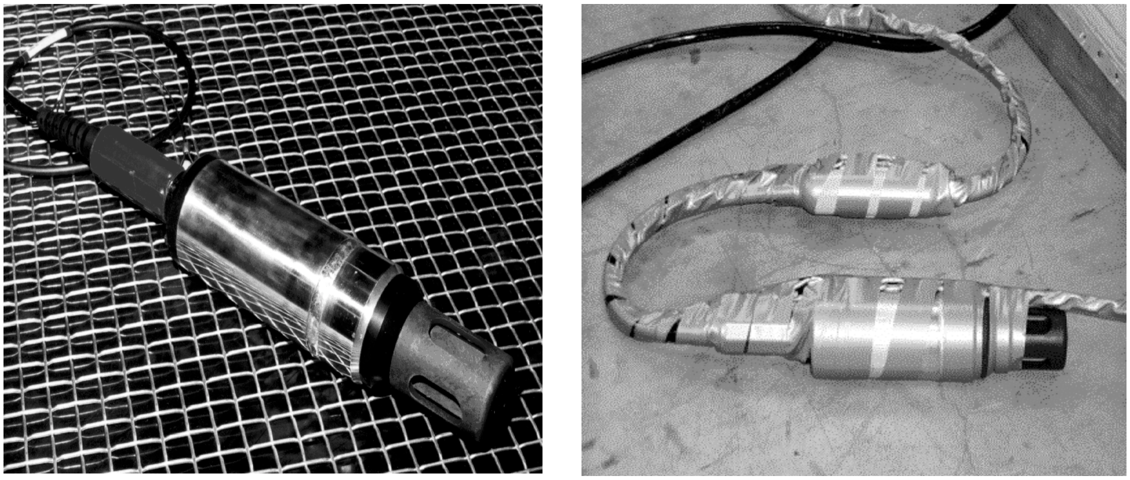

Figure 5.2.2 – 4-C receiver unit used in data acquisition (left) and the same unit attached (taped) to a cable (right) (*after www.erch.com)*.

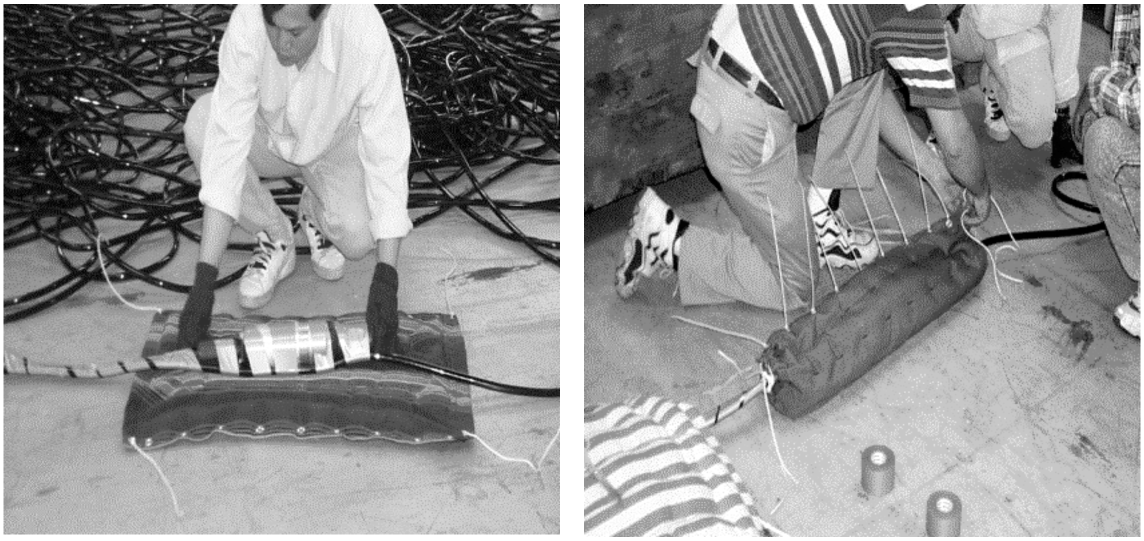

Figure 5.2.3 – 4-C receiver unit of Figure 5.2.2 being sandbagged (*after www.erch.com)*. This method is licensed by Atlantic Richfield Co (Sullivan, 1995).

The shot point grid was 25 x 25 m, over an area of approximately 4 x 3 km^2. In total, there are around 19,200 shots. The data were stored in tapes, located in four different buoys spread in the area. These tapes could record 10 hours of shooting – for this reason, data acquisition started in dawn and stopped at sunset every day. The shooting, in an N-S direction, went from April 12 to 26, using a Western Geophysical boat. Western also supplied navigation (DGPS) and support; I/O supplied the recording instruments, DigiCourse the equipment for receiver location and buoys for cable retrieval and Oceaneering the ROV for cable trenching.

The costs were decreased by the use of cheaper analogue sensors and light cables on the sea floor and placing more expensive recording equipment on the buoys.

Figure 5.2.4 shows one of the recording buoys and the tape being recovered at the end of a working day.

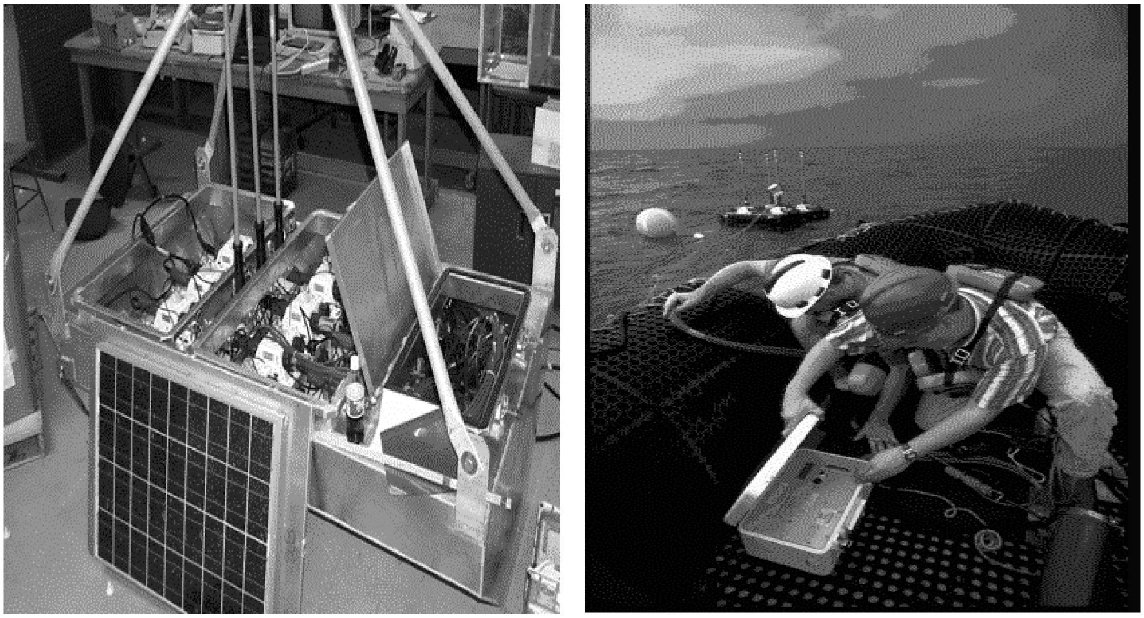

Figure 5.2.4 – Recording buoy (left) and tape with seismic data being recovered (right) (*after www.erch.com)*.

Additional information on the acquisition parameters is presented in Appendix II, based on information from Baker Hughes (1999).

V.3 Pre-processing and quality control

The data were resampled to 4 ms (from the original 2 ms) for all components to save disk space and improve the processing time. The maximum recording was changed to 4.5 s for the vertical and hydrophone components and to 6.0 s for the horizontal (radial and transverse) components. The trace header information was converted from feet to metres.

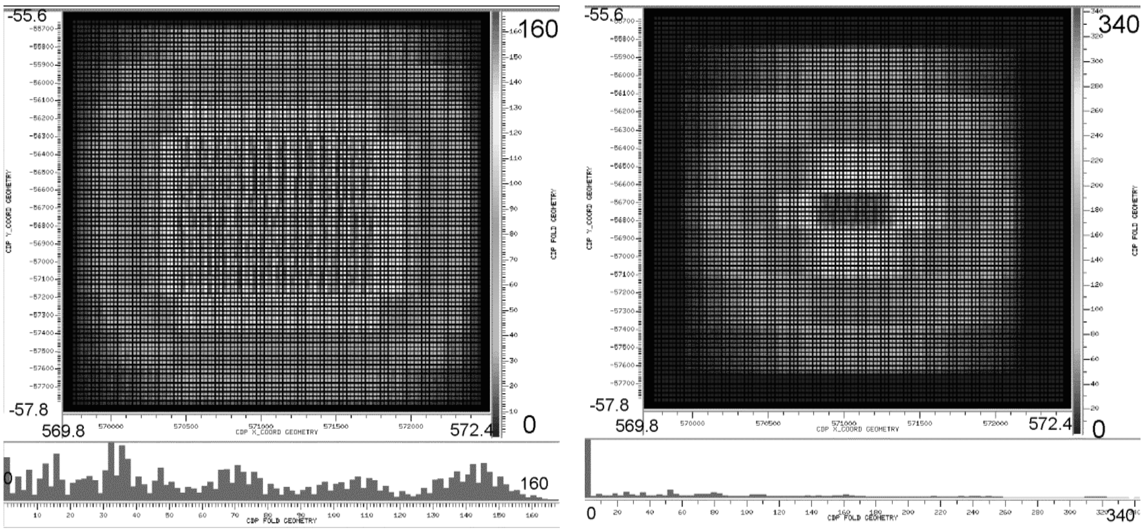

Figure 5.3.1 – Map view of CDP fold for vertical and hydrophone (left) and radial and transverse after ACCP binning using Vp/Vs of 2.0 (right). Note poor coverage distribution and very high number of zero-fold bins (in the histogram) for the horizontal components.

A land configuration was used for the geometry. The CDP fold distribution for all components, when a 25 m bin size is used, is shown in Figure 5.3.1. For the horizontal components, the fold distribution is obtained after asymptotic (ACCP) binning using a V_P/V_S ratio of 2.0. As expected from the high number of shots, a high and homogenous fold is present for vertical and hydrophone. For the horizontal components, the maximum fold valued more than double, but the distribution is more heterogeneous and a smaller area is imaged.

To use the concepts of ‘radial’ and ‘transverse’, the original horizontal components have to be rotated to a new set of orthogonal axis. The radial direction of the new axis is given by the source-receiver azimuth and the transverse by the orthogonal to this direction. Figure 5.3.2 shows an example for a reorientation performed in a source-receiver pair. One can see that the source-receiver energy alignment is very good. This seems to be the case for most offshore surveys with the first arrival propagating in the homogeneous water layers, (Dr. James Gaiser, 1999, personal communication to Prof. Robert Stewart), but this may not be true for land 3-D multicomponent recordings where the first wave must propagate in the "weather" layers (Robert Stewart and Han-Xing Lu, 1999, personal communication). The energy alignment was performed using a time window of approximately 500 ms, centred at the first P-wave break (in general, the direct wave).

Another issue for horizontal component processing is to obtain the correct polarity. For 2-D, the polarity correction is obtained simply by reversing the polarity for symmetric offsets (either positive or negative). For 3-D surveys the polarity reversal may be more difficult to be obtain, and should be performed simultaneously with the reorientation. Figure 5.3.3 shows that ProMAX reorientation also takes care of the necessary polarity correction, by considering the amplitude sign of the signal, and not only its energy or absolute amplitude value.

After rotation to radial and transverse orientations, a time and space variant template muted first break energy. The source depth was "corrected" to the sea bottom using a time shift, so that the sea bottom was the new datum and the water layer was removed from the processing.

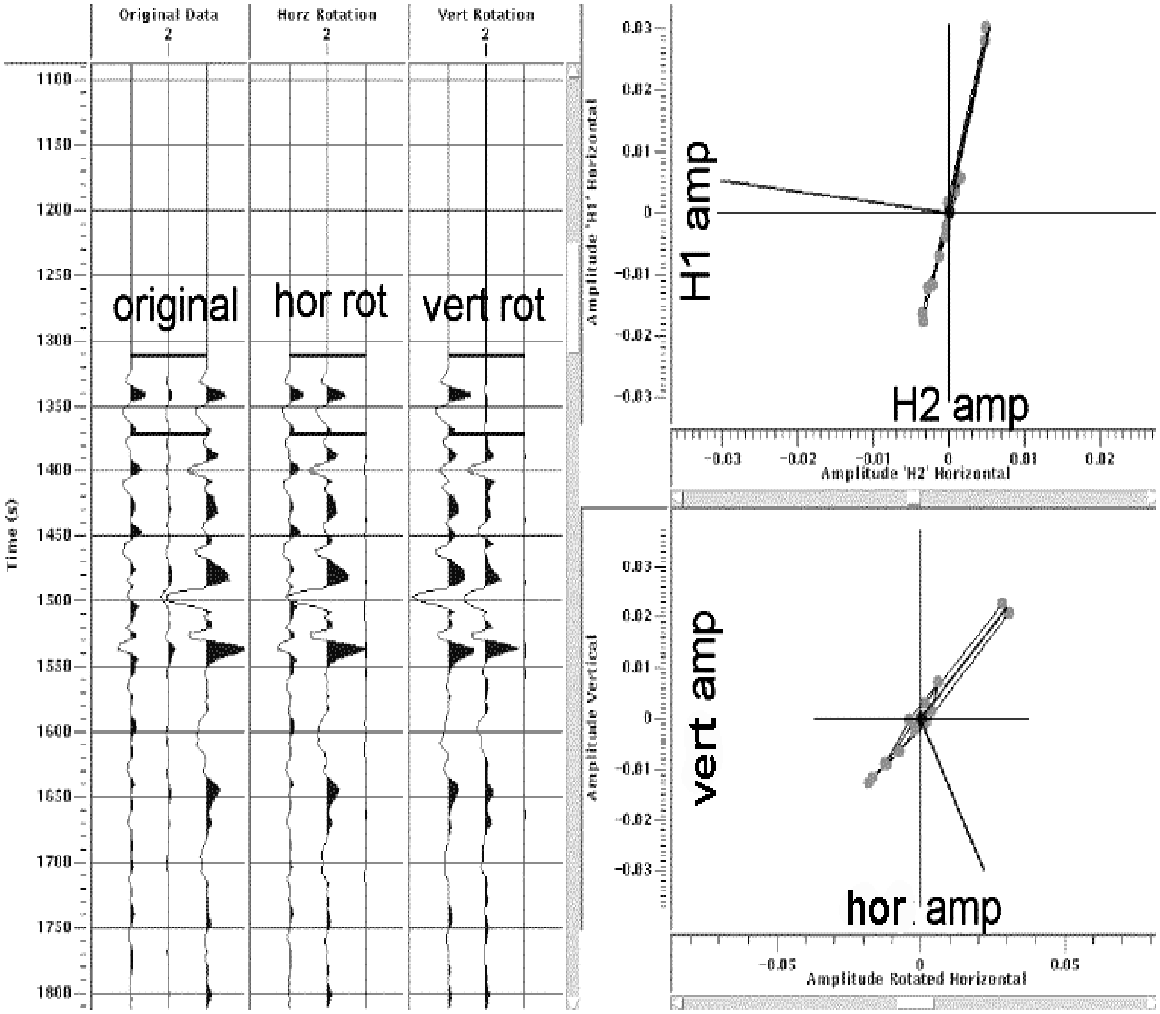

Figure 5.3.2 – Reorientation of horizontal components. On left the input (original) data from a specific source-receiver pair (from left, vertical, radial and transverse components). In the middle, the three components after horizontal rotation: most horizontal energy is aligned in the source-receiver direction (trace 2). At right the traces after vertical rotation (not used in this processing). The thick lines from around 1310 to 1370 ms shows the time window used for the energy alignment. Top right shows the original (acquisition) orientation on thin axis and the energy alignment along the new direction (dots and thick axis). The new radial component is defined by this energy alignment, the new transverse by its orthogonal. Bottom right is as top right, but for a (new) radial and vertical hodogram.

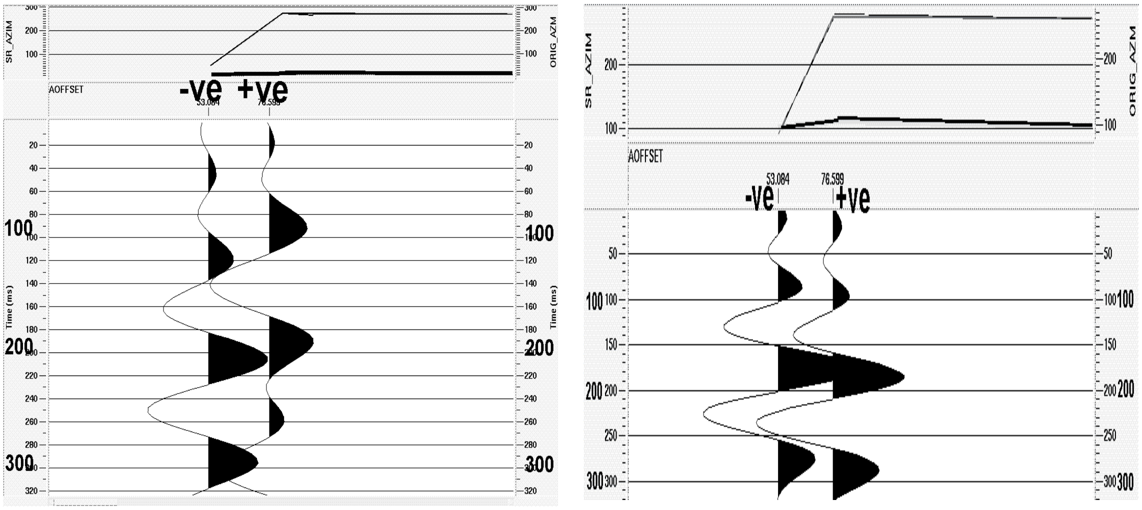

Figure 5.3.3 – Comparison of two radial component traces before (left) and after (right) reorientation. Both traces are related to the same shot point, the left trace for a receiver located west of the shot (negative offset), the trace at right at east of the shot point (positive offset). The thick line at the top shows the original component azimuth (close to 90^0); the thin line the new (source-receiver) azimuth after reorientation. Observe that on the left trace the azimuth is not changed, while for the trace at right an 180^0 phase change occurs. The apparent phase difference is due to different travel time plus different static correction (not applied yet).

A comparison between the average trace energy (amplitude of each sample squared, summed, and the result divided by the number of samples) for all components (after horizontal reorientation is performed), shown in Figure 5.3.4, is a good quality control tool. This process is also good to find which maximum amplitude value should be allowed for each component, so that noise (spike) traces can be zeroed.

Vertical and radial components have the best energy distribution among traces. The hydrophone data may be expected to be somewhat noisy, as there is a strong variation in energy content for adjacent traces. This noise may be due to the inherent higher susceptibility (compared to geophones) of this type of receiver to energy trapped in the water layer as reverberation. One also can see that: 1) the vertical has a lower energy content (mode around 0.001) than all other components, and 2) the horizontal components have much higher maximum values (0.065 for radial and 0.145 for transverse) than vertical (0.026) and hydrophone (0.03).

Higher energy in horizontal components is also generally found on land surveys (e.g., Yao and Roberts, 1993). In marine environments, it may be caused by the sea-bottom acting as a "free surface" for shear-waves (Prof. Jim Brown, 1999, personal communication). However, this is probably not the reason here, as five out of seven cables are buried under one metre of sediment (trenched cables in Figure 5.2.1).

After "top mute" and moving the source datum to sea bottom, noisy traces were muted, using a maximum amplitude value obtained from the average trace energy. Then amplitude recovery was performed, assuming a spherical divergence correction according to a $1/(tV^2)$ equation (Newman, 1973), where t is two-way travel time and V RMS velocity (considered equal to NMO correction velocity). For all components except the vertical, a correction for inelastic effects was also applied, using an attenuation factor (α) of 0.002.

The dominant frequency is another interesting quality control parameter. This is shown in Figure 5.3.5. The hydrophone has the highest dominant frequency (around 40 Hz), but it may be related to more high frequency noise (energy reverberation in the water) than to a high frequency content in the signal amplitude spectrum. The horizontal components have almost the same dominant frequency, which is expected. Also expected (section 2.1) is the lower value for the frequency statistical mode (20 Hz), compared to the hydrophone (40 Hz).

One could expect a higher frequency in the vertical component, but the value is close to the horizontal components. A reason for this (possible) lower frequency content and also for it to be close to the horizontal components is a contamination of shear-wave (converted) energy in the vertical component.

An abrupt variation on dominant frequency occurs in all components (most clearly seen in the hydrophone); no explanation could be found for this behaviour.

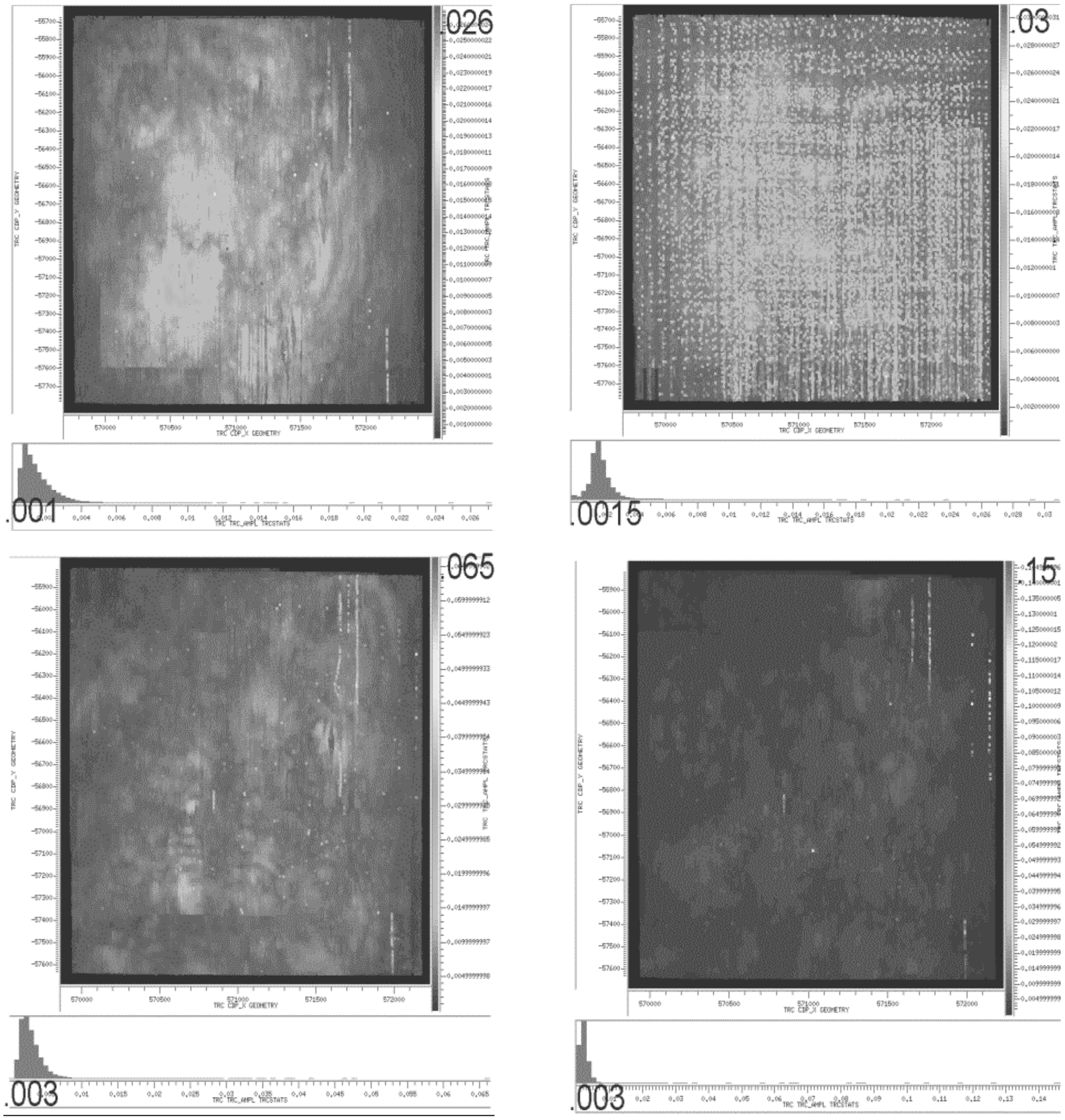

Figure 5.3.4 – Map view of average energy per trace for vertical (top left), hydrophone (top right), radial (bottom left) and transverse (bottom right) components. Observe higher heterogeneity for energy distribution in hydrophone component.

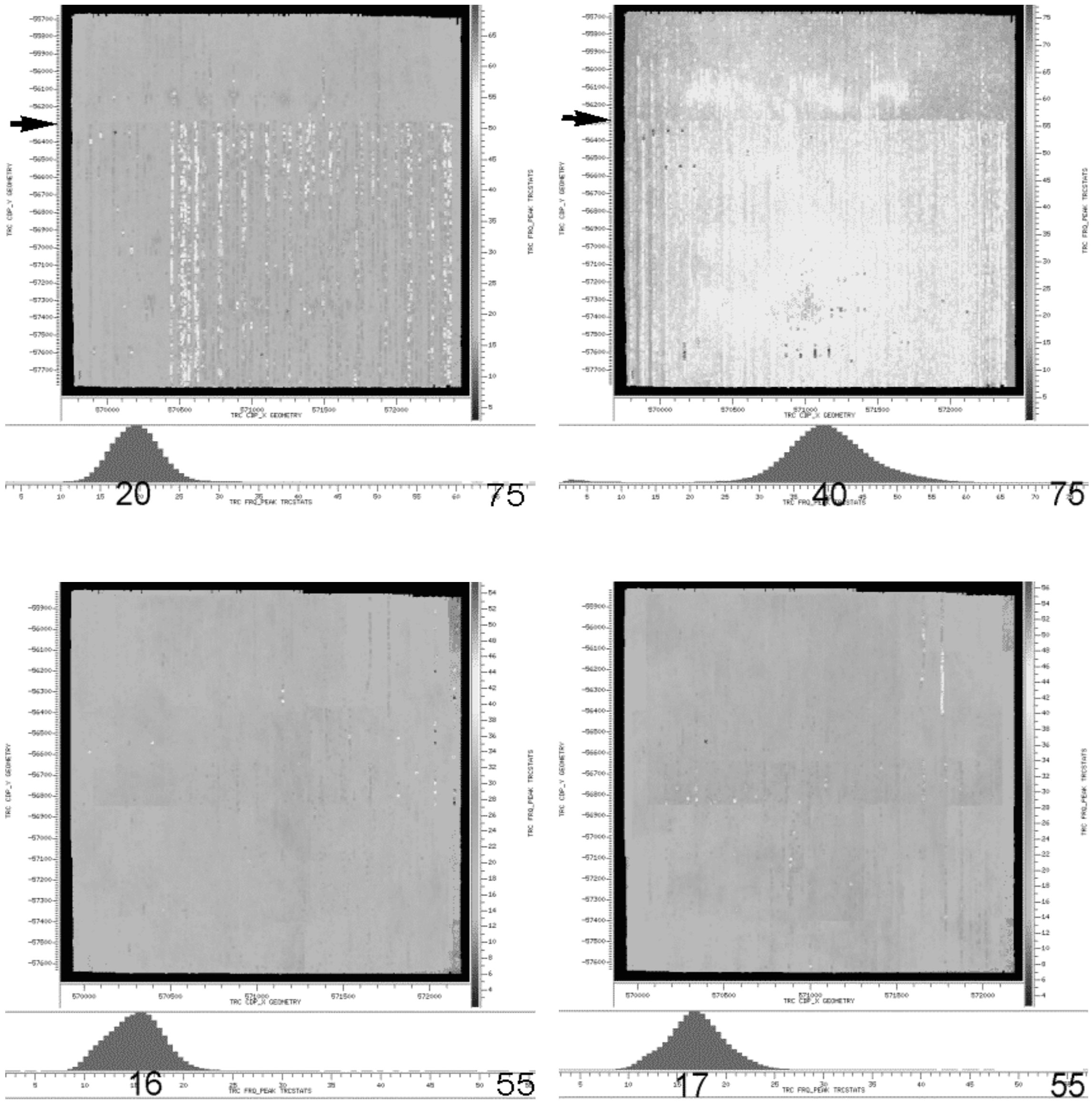

Figure 5.3.5 – Average dominant frequency per trace for vertical (top left), hydrophone (top right), radial (bottom left) and transverse (bottom right). No explanation could be found for the sharp variation in the dominant frequency distribution (most clearly seen in the hydrophone at the arrow location, but present in all components). Relatively low frequency in vertical (20 Hz) may be due to presence of S-wave energy.

V.4 Vertical geophone (P-P reflections) and hydrophone components

A spiking deconvolution with 240 ms operator length (also tested were 80, 160 and 320 ms) and 0.1 % white noise was applied. An example of a CDP gather for both components is presented in Figure 5.4.1. The hydrophone data seems to have better quality, with more continuity in the events and a higher frequency content (although, as previously said, it may be related to energy reverberation). One interesting aspect in the vertical component geophone gather is that some adjacent traces seem very similar to each other. The explanation for this is that these traces are grouped by very close offsets, as can be observed at the top of the picture, where the absolute offset is shown.

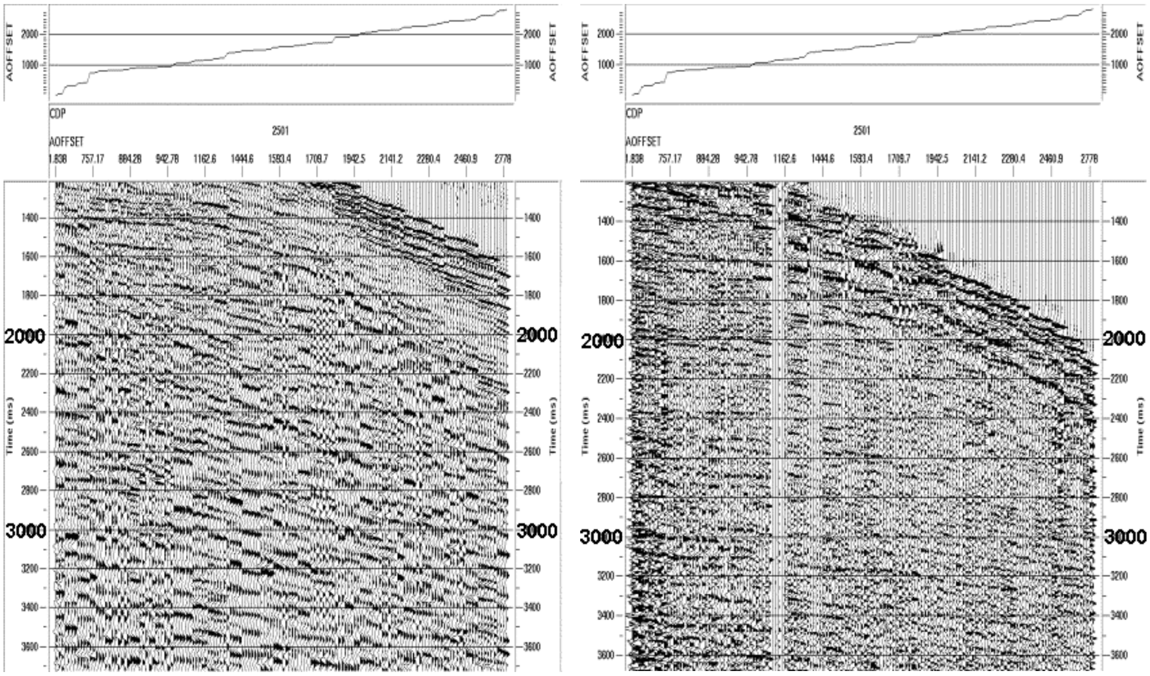

Figure 5.4.1 – Example of CDP gathers for vertical (left) and hydrophone (right) components.

The amplitude spectra for these gathers are shown in Figure 5.4.2. The hydrophone data have strong notches, at frequencies close to the ones expected from the water depth in the area (85 m). The absence of notches in the vertical geophone component could be due to presence of shear-wave energy in this component, which is not refused when a radial data processing flow is applied in vertical component data (section 5.7).

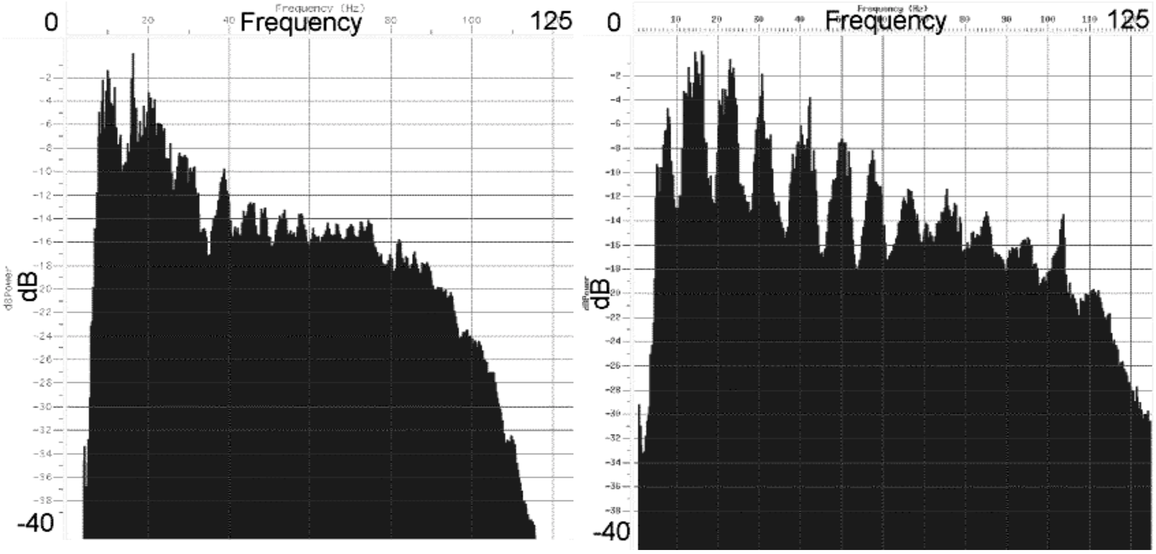

Figure 5.4.2 – Amplitude spectra of CDP gathers (Figure 5.4.1) for vertical geophone (left) and hydrophone (right) components.

The first receiver statics were obtained by hand picking. Picking a continuous event (not necessarily flat) on a common receiver stacked section provided a datum. The picked event was smoothed, so that its ‘regional’ (long wavelength) time variation was preserved and the smoothed event subtracted from the original one. This difference was considered to be caused mainly by receiver statics. This process was iterated four times for the vertical geophone and three times for the hydrophone data.

Source statics were obtained from the vertical geophone component, and considered the same for all other components recording both P-P and P-S reflections. Only residual statics were obtained for shots. The statics were obtained by correlation of the analysed trace (one trace each time) with a ‘pilot’ trace. The pilot trace came from common source stacked data (“shot stack”), with some random noise attenuation process applied. The static value is considered the shift that gives the best correlation between the analysed and the pilot trace, based on a stack power value.

This correlation process was applied three successive times for the source statics. On each successive run, the maximum value allowed for the shift was decreased, from 30 ms on the first run to 15 ms in the last. The results are presented on Figure 5.4.3. The statics are small and are grouped around zero, even for the first run. After three runs, very few shots have statics over +/- 15 ms, and the concentration around zero has a remarkable increase when compared to the first run.

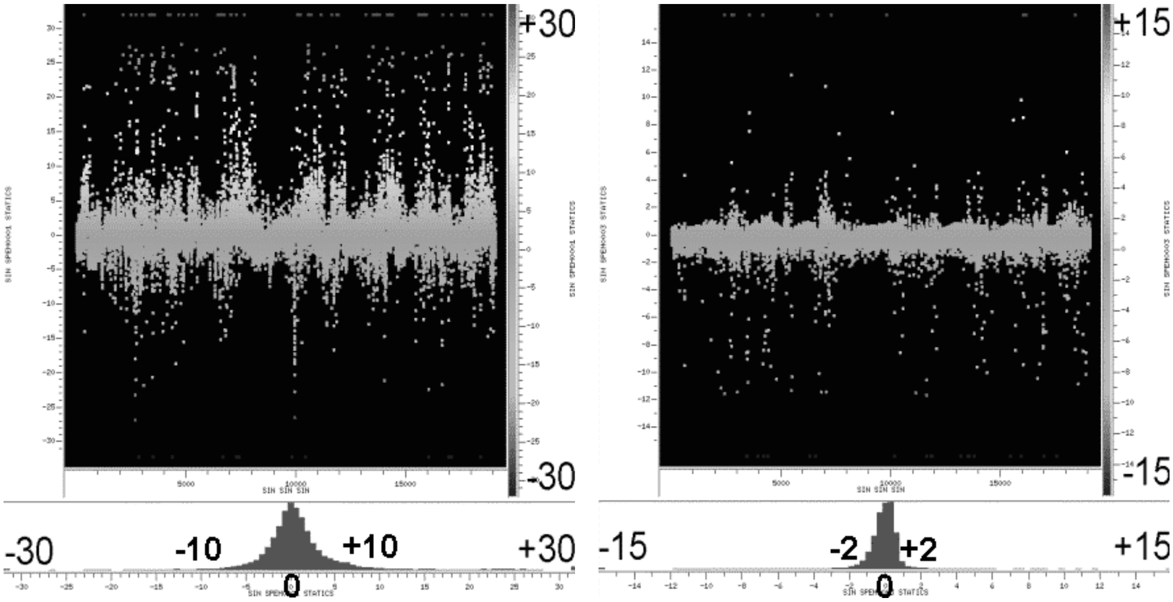

Figure 5.4.3 – Static corrections for the source, obtained in the vertical component and applied to all components. First (left) and third (right) run of residual statics by cross-correlation. No hand statics were applied for the shots.

The same process was used to obtain receiver residual and "trim" statics. Two runs were enough for both vertical and hydrophone. Figure 5.4.4 shows the results of hand and residual statics for the hydrophone.

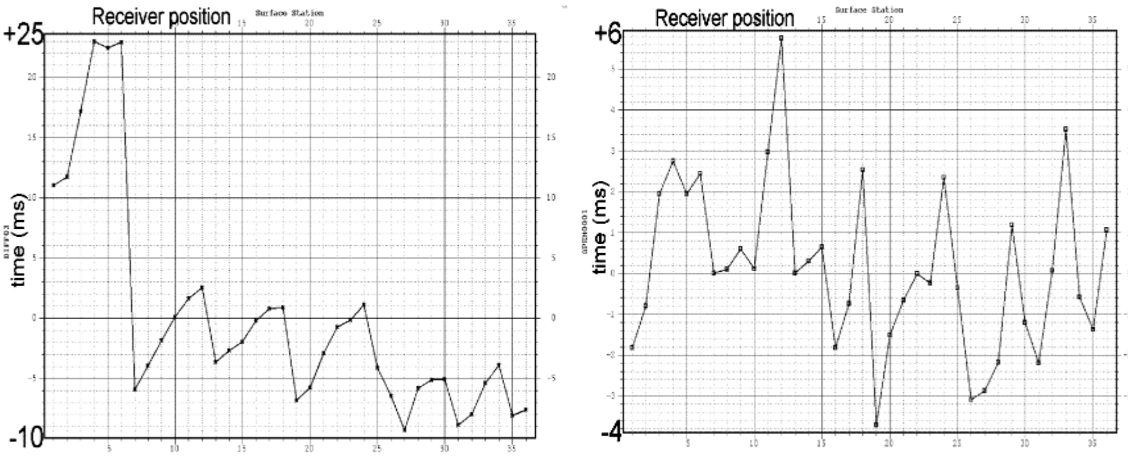

Figure 5.4.4 – Static receiver corrections for hydrophone: hand (left) and residual (right), both after the first iteration.

After statics, a new velocity analysis was performed, and the data sorted by CDP and stacked. Cancellation of the NMO-stretched signal was done using a top mute designed in NMO-corrected CDP gathers, not by a constant (e.g. 30 %) value. As previous reports on this area (Ebrom *et al.*, 1998b) show the presence of dipping events, it was decided to apply dip move out (DMO) to the data. After stack, a finite-difference time migration was applied. The result, with and without DMO, is shown on Figure 5.4.5 (these, and all subsequent sections in this chapter, are in the W-E direction, approximately at the centre of the 3-D survey). As they look quite similar, and no section is better for P-P reflections events at all times, which result is better can be decided only by some interpreter familiar with Teal South area. Regarding velocity analysis, though, Figure 5.4.6 shows very clearly that DMO allows a better velocity picking due to better semblance focusing.

Vertical

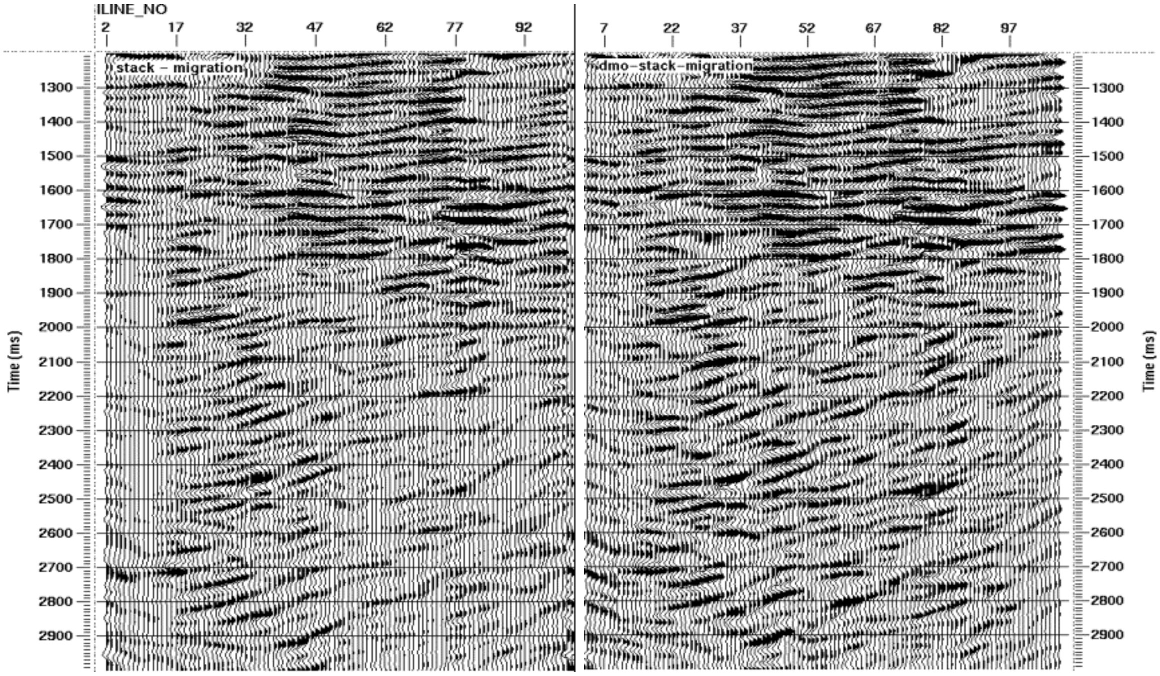

Hydrophone

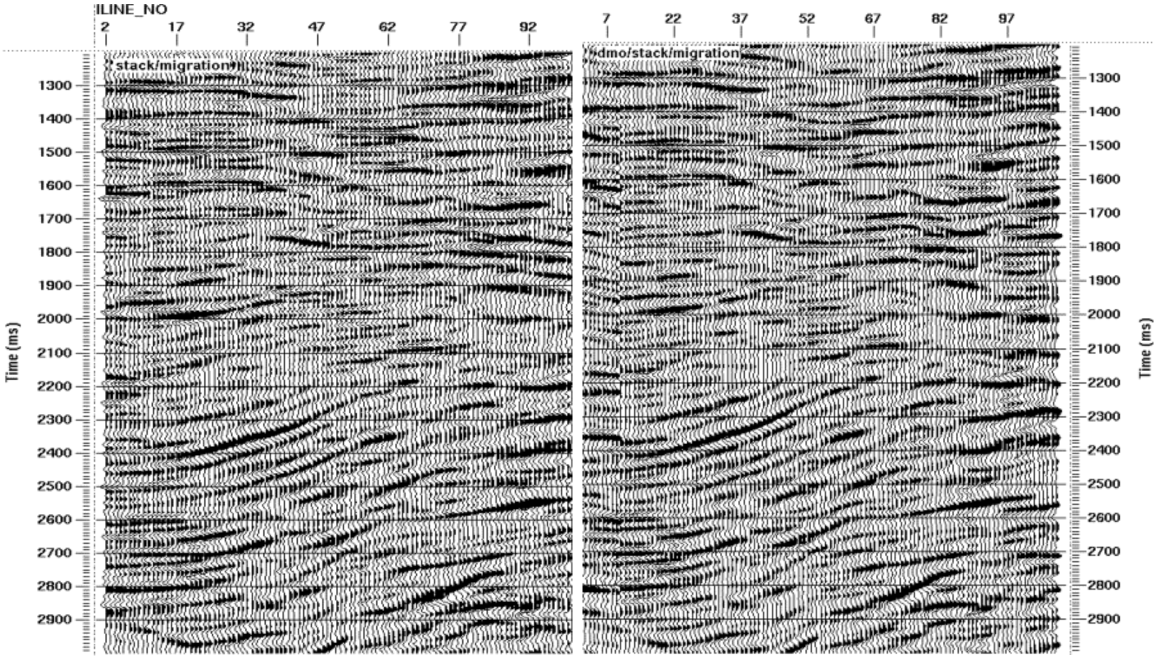

Figure 5.4.5 – Comparison of migrated P-P data without (left) and with (right) DMO for vertical geophone (top) and hydrophone (bottom) components.

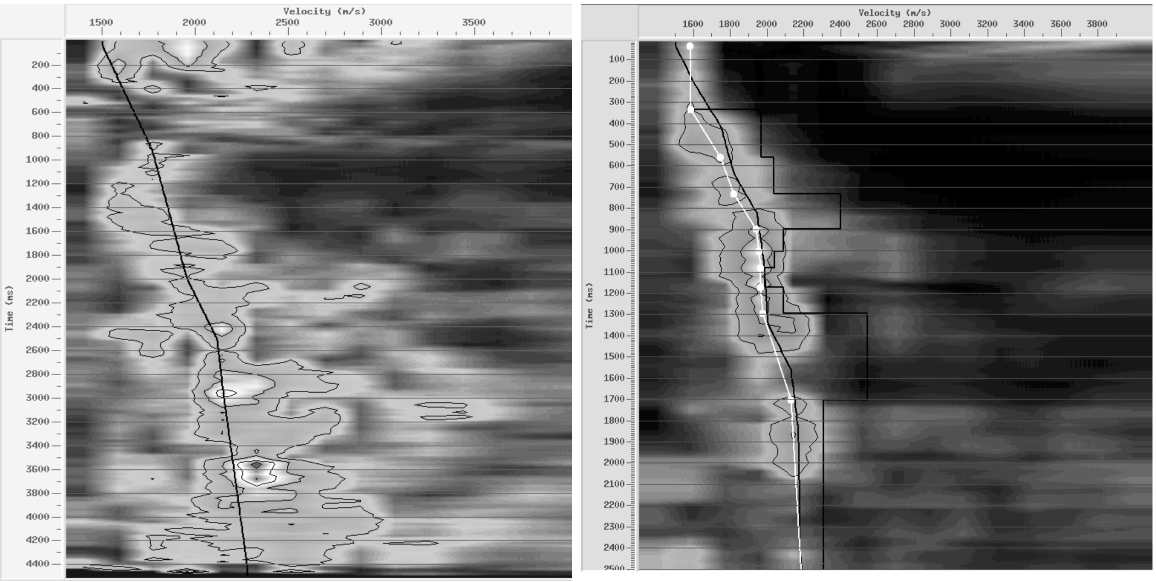

Figure 5.4.6 – Velocity analysis after DMO. Black function show velocity picked on data without DMO, white function velocity picked after DMO.

Figure 5.4.7 shows amplitude spectra of migrated sections (without DMO application) of vertical geophone and hydrophone components.

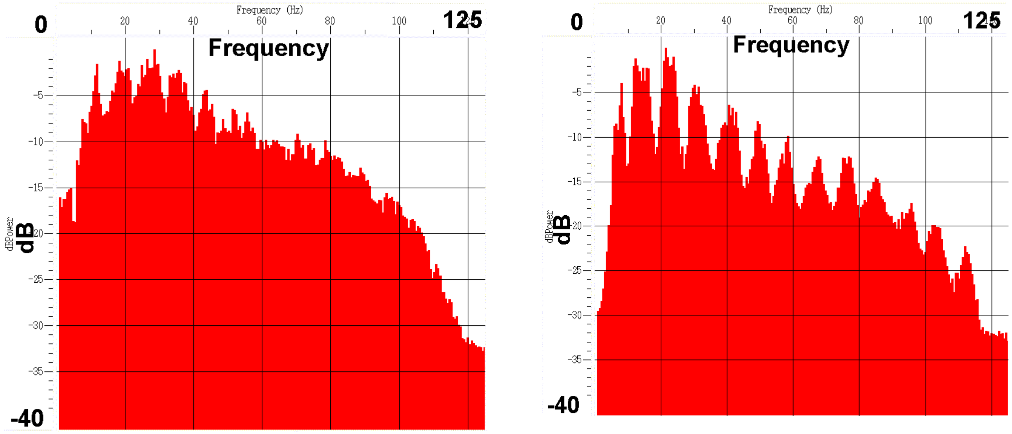

Figure 5.4.7 – Amplitude spectra of stacked and migrated sections (without DMO, Figure 5.4.5) for vertical geophone (left) and hydrophone (right) components.

A 3-D pre-stack time migration algorithm, based on the equivalent offset migration (EOM) concept (Bancroft and Geiger, 1994; Bancroft *et al.*, 1998) and coded into ProMAX by John Bancroft and Xinxiang Li, was applied to the P-P data recorded on the hydrophone and vertical geophone components. The results, presented in Figure 5.4.8, show that EOM method produces a section with lower frequency content and less continuous events. John Bancroft (1999, personal communication) believes this may be caused by a large value on common scatter point (CSP) binning interval. A value of 75 m (compared to 25 m of CDP binning) was used in this processing. The main reason for a bin interval three times bigger than CDP interval is computer time – for each component, to process the whole 3-D took around two weeks in a Sun machine with 1 Gbyte of RAM and 400 MHz processing speed.

A general processing flow for the vertical geophone and hydrophone components is shown in Figure 5.4.9. The final velocity analysis was done on a 250 x 250 m grid.

Vertical

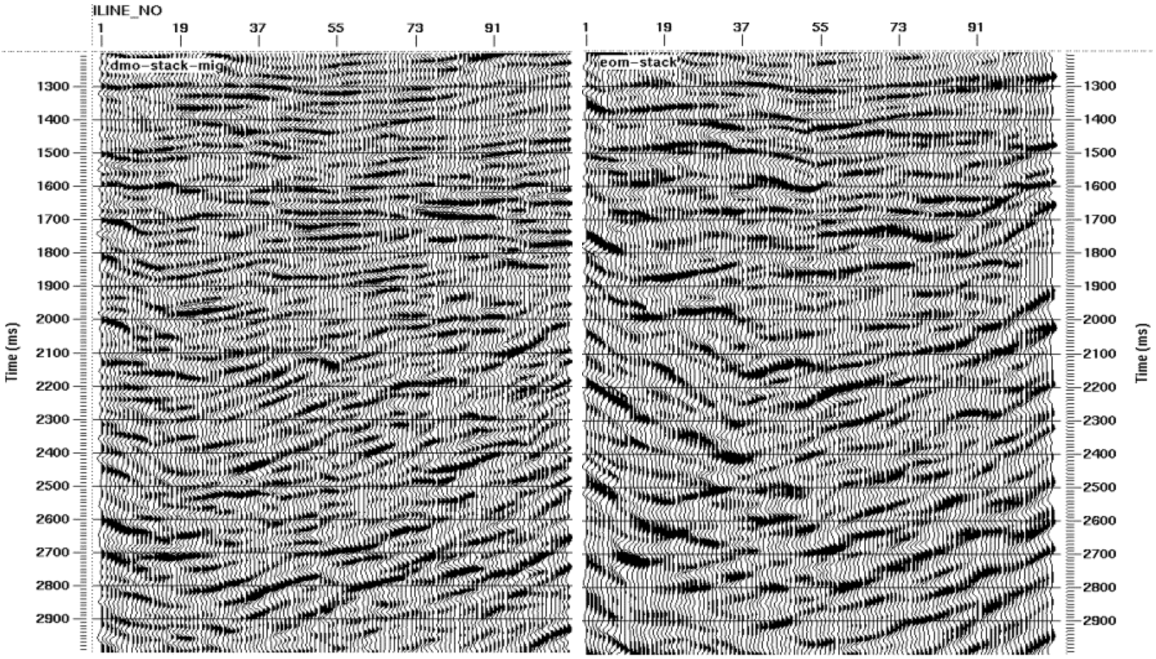

Hydrophone

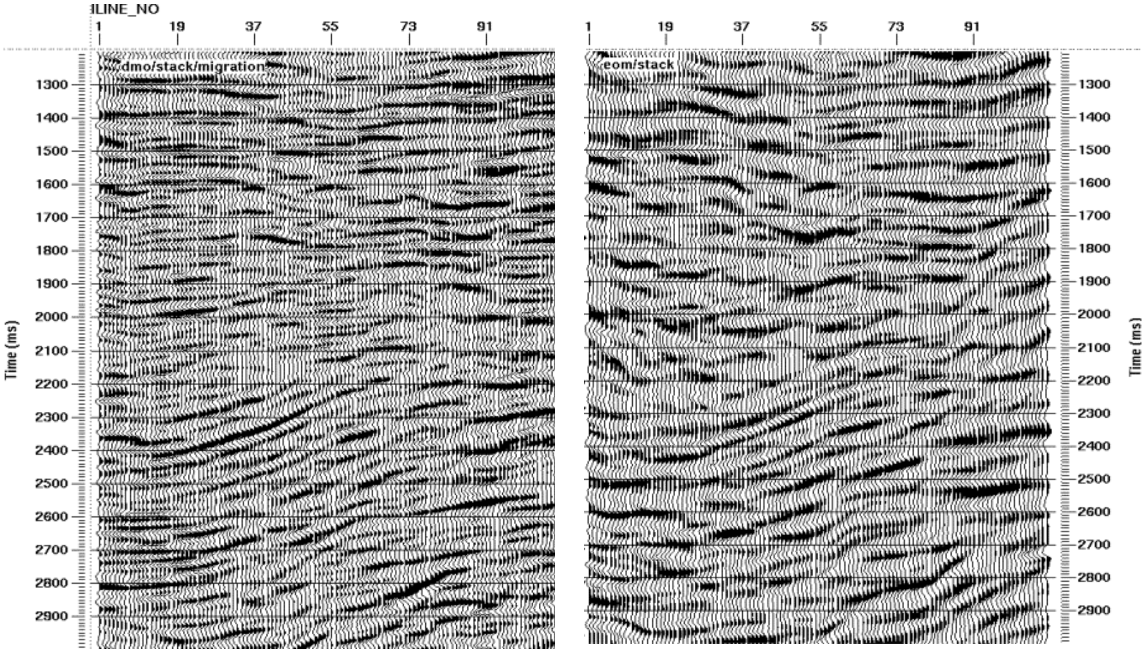

Figure 5.4.8 – Comparison between data after DMO, stack and post-stack finite difference migrated (left) and after EOM and stack (right). Vertical component results are on top and hydrophone at bottom. Observe lower frequency and less event continuity in EOM results.

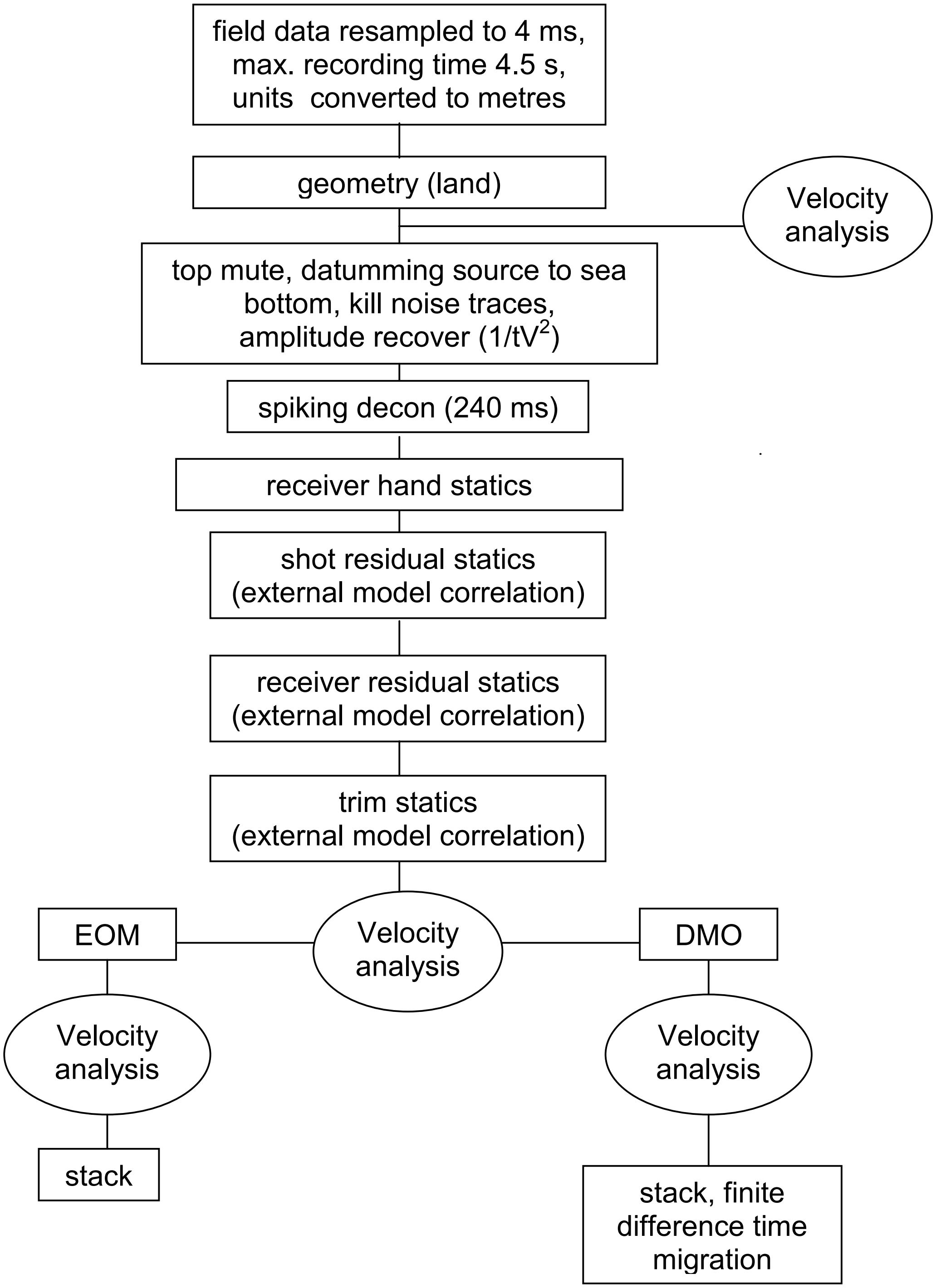

Figure 5.4.9 – Processing flow for vertical and hydrophone component. The shot static was obtained only in the vertical flow. In the hydrophone amplitude recovery, an inelastic correction (α) of 0.002 was also used.

V.5 Radial and transverse (P-SV reflections) geophone components

After reorientation, a processing sequence similar to the one applied to vertical geophone and hydrophone was applied to radial and transverse geophone components. The most significant difference in these data is the nature of the P-P and P-SV reflections process. This difference requires the use of asymptotic common-conversion-point (ACCP) binning, when a point located an infinite depth, for a specific source and receiver location and V_P/V_S ratio, approximates the P- to S- conversion point at each interface (section 2.4).

For both radial and transverse geophone components, the amplitude recovery used a $1/(tV^2)$ (V P-S NMO velocities) equation and inelastic correction (α) of 0.002. No deconvolution was applied to the horizontal components, as some testing on stacked sections suggested best results when no decon was used.

Figure 5.5.1 shows an ACCP gather of the radial component, without receiver statics. The data has a regular quality. As the vertical, some groups of traces look similar due to their close spatial location. Also shown is the amplitude spectrum of this gather. As expected (section 2.1), the frequency content for the P-SV reflections is lower than vertical geophone and hydrophone components recording the P-P reflections (compare with Figure 5.4.2), and a strong drop from –15 to –30 dB occurs from 30 to 40 Hz.

Figure 5.5.2 presents hand (structural) and residual receiver statics for radial geophone component recording of the P-SV reflections. As expected, hand statics are much larger (four to eight times larger) in the radial geophone component recording the P-SV reflections than hydrophone statics (compare with Figure 5.4.4) recording the P-P reflections. The picture also shows that after three consecutive iterations the residual statics becomes very small.

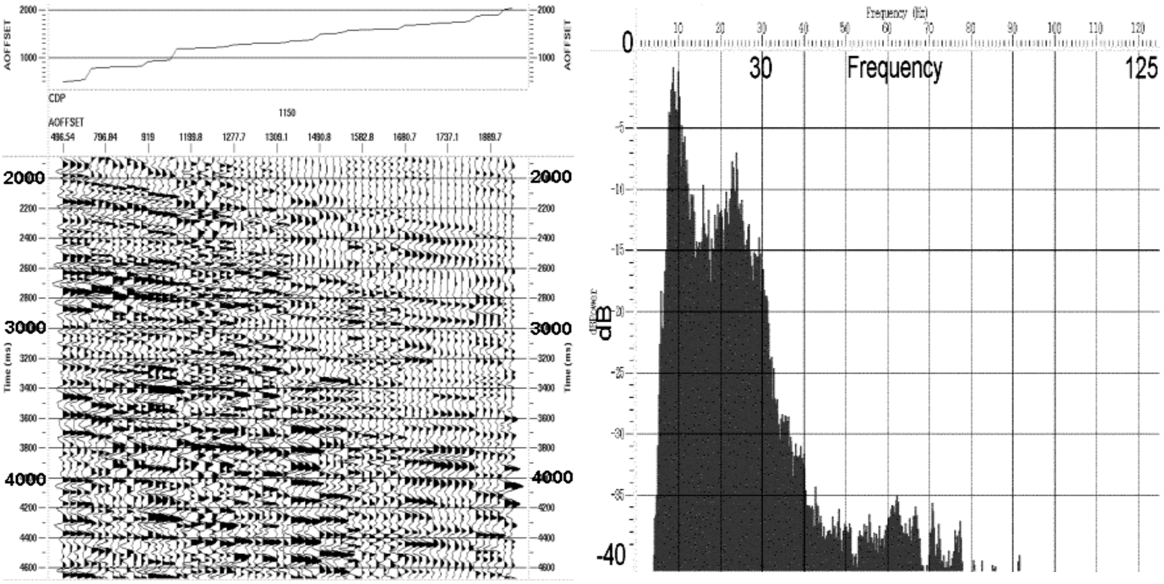

Figure 5.5.1 – Radial component ACCP gather after horizontal reorientation and asymptotic binning (V_P/V_S =2.0) and its amplitude spectrum.

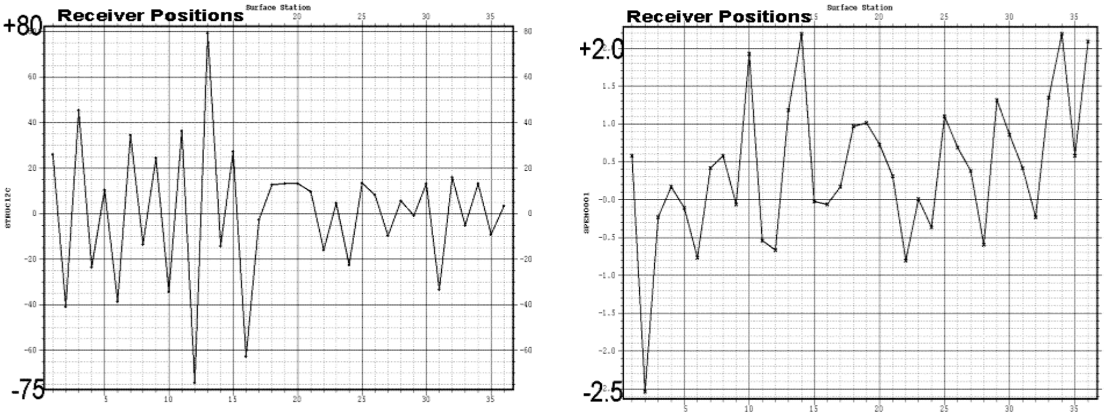

Figure 5.5.2 – Hand (left) and residual (right) radial component receiver statics, both after three runs.

After all statics were obtained, a new velocity analysis was performed and the data stacked. Figure 5.5.3 shows a comparison between radial and transverse geophone components. Clearly, the radial component is of much better quality between that of the P-SV reflections. For this reason, subsequent analyses were performed in the radial geophone data only.

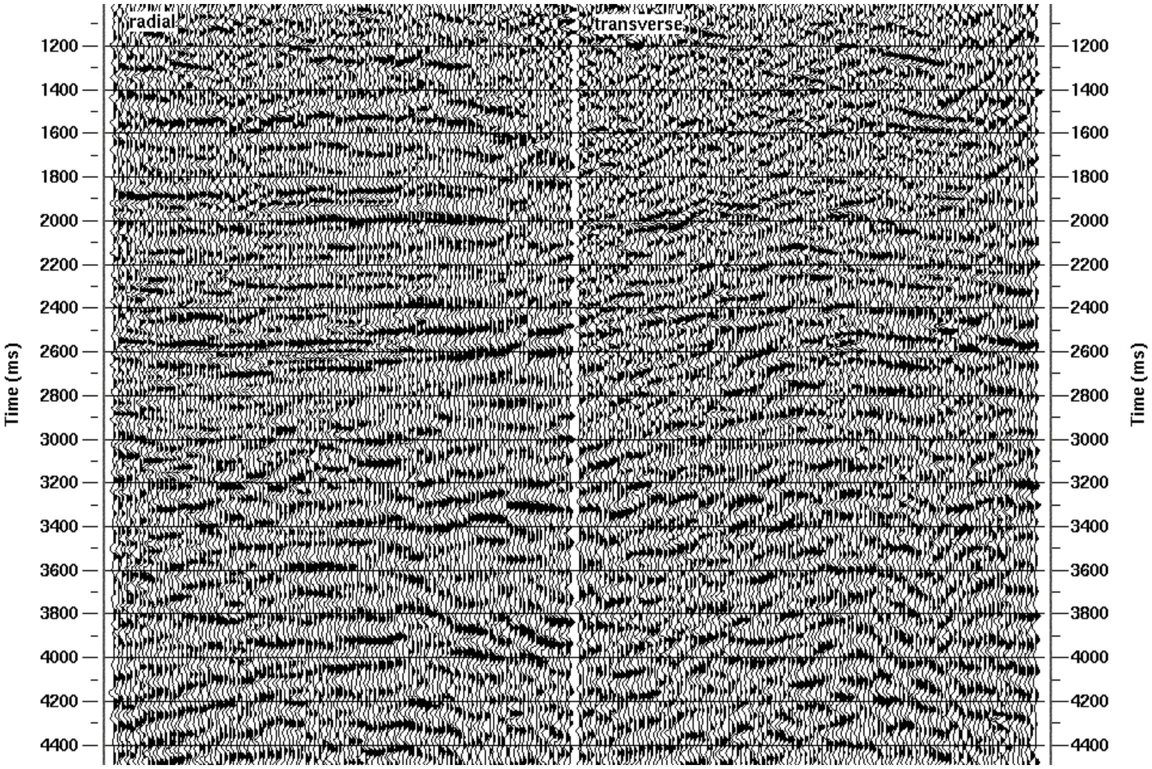

Figure 5.5.3 – Comparison between stacked data after ACCP binning (V_P/V_S = 2.0) from radial (left) and transverse (right) components. The radial component has better quality. Trace interval 25 m.

Converted-wave DMO was applied in both horizontal components. The result for radial is shown in Figure 5.5.4. In general, DMO seems to decrease data quality, generating coherent linear noise (mainly in the shallow part of the section). This may be due to some reasons during the DMO application presented in Harrison (1992), as incorrect phase corrections and/or amplitude weighting, sensitive of the method to velocity errors. For some events, though, it seems to increase continuity – again, the final opinion has to be given by an interpreter of the area.

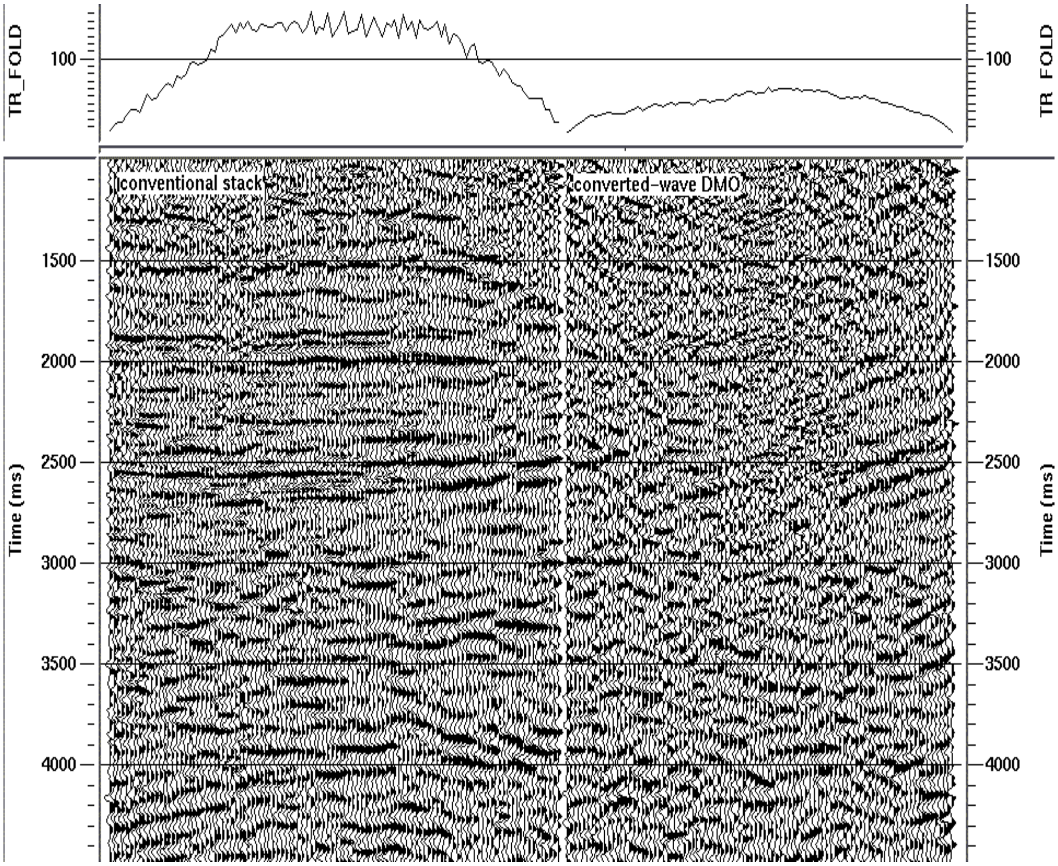

Figure 5.5.4 – Comparison between stacked radial data without (left) and with (right) converted-wave DMO. Bin fold is shown at the top of the sections (folds are different – and more homogeneous in the DMO case – due to DMO binning). Trace interval 25 m.

Another test done in the radial component was the depth-variant stack. This process tries to consider the actual conversion point for different depths. For this, it uses a time and spatial variant V_P/V_S ratio. The results (Figure 5.5.5) show this process did not work well, as the conventional stack presents a more continuous section. The poor result for this method was probably due to incorrect V_P/V_S values used in the calculation of the conversion point.

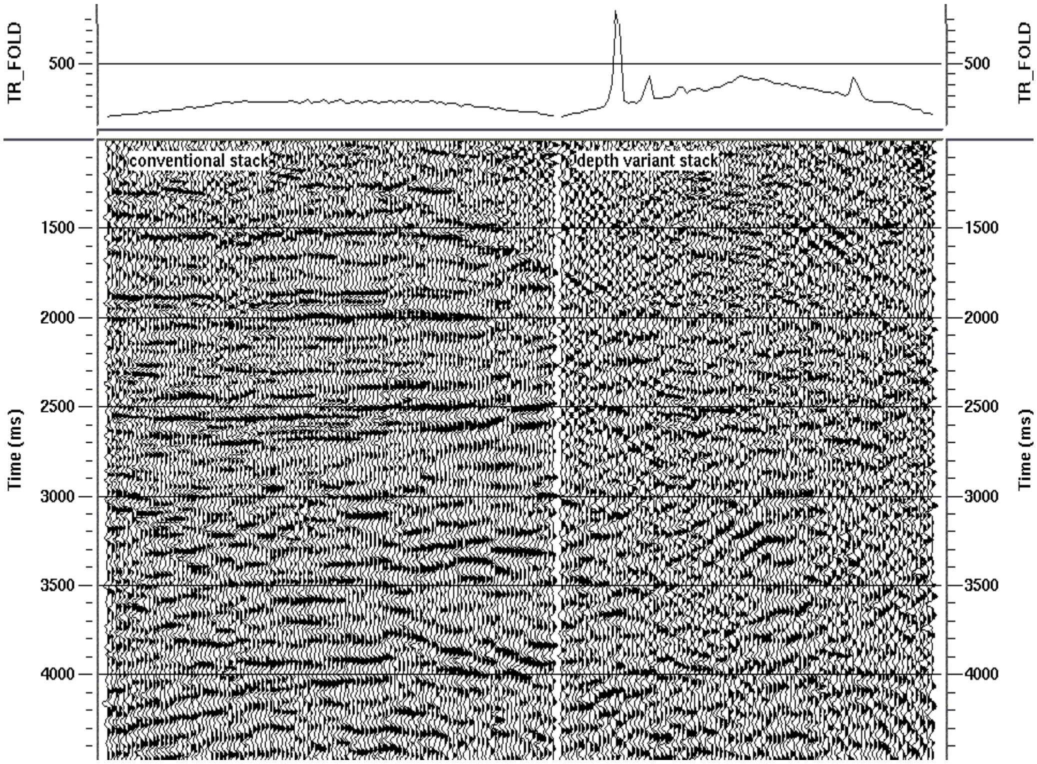

Figure 5.5.5 – Comparison between conventional (left) and depth variant stack (right) for the P-SV data recorded on the radial component. Poor result on depth-variant stack is probably related to use of incorrect V_P/V_S ratios. Bin fold is shown at the top of the sections. Trace interval 25 m.

The use of an effective interval V_P/V_S (equation 2.4.5) value to theoretically account for transversely isotropic media, which affects the location of the P- to S- conversion point in depth as well as laterally, was tested in the radial component. The algorithm used was developed by Dr. Peter Cary based on the theory by Thomsen (1998). Figure 5.5.6 shows the results, which are not good, mainly in the shallow part. As this method is also based on depth-variant conversion point concept (Figure 5.5.5), the conversion points are not precise (as seems to be the case here), the anisotropic correction may be expected to be poor.

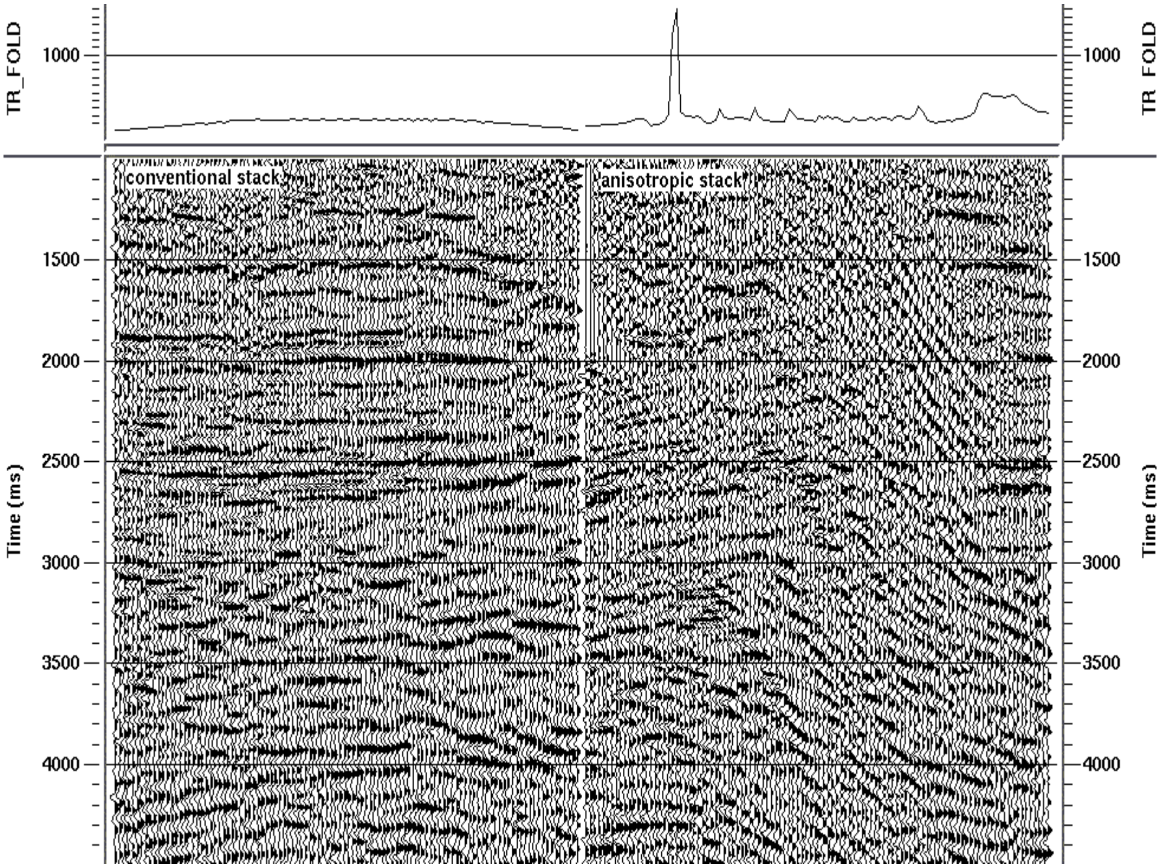

Figure 5.5.6 – Comparison between conventional (left) and anisotropic stack (right) for the P-SV data recorded on the radial component. Bin fold is shown at the top of the sections. Trace interval 25 m.

Also used in the radial component data was the equivalent offset migration (EOM) method. The result (Figure 5.5.7) shows the method did not work very well. The decrease in high frequency content also occurs for this component, as in the hydrophone case for the P-P data (Figure 5.4.7).

Besides the large bin size, a possible additional reason for a poor EOM performance is that the algorithm used here is suitable for data after asymptotic binning, using only an approximation of the conversion point. In other words, it does not estimate the actual conversion point, as in the 2-D algorithm (section 4.4.2).

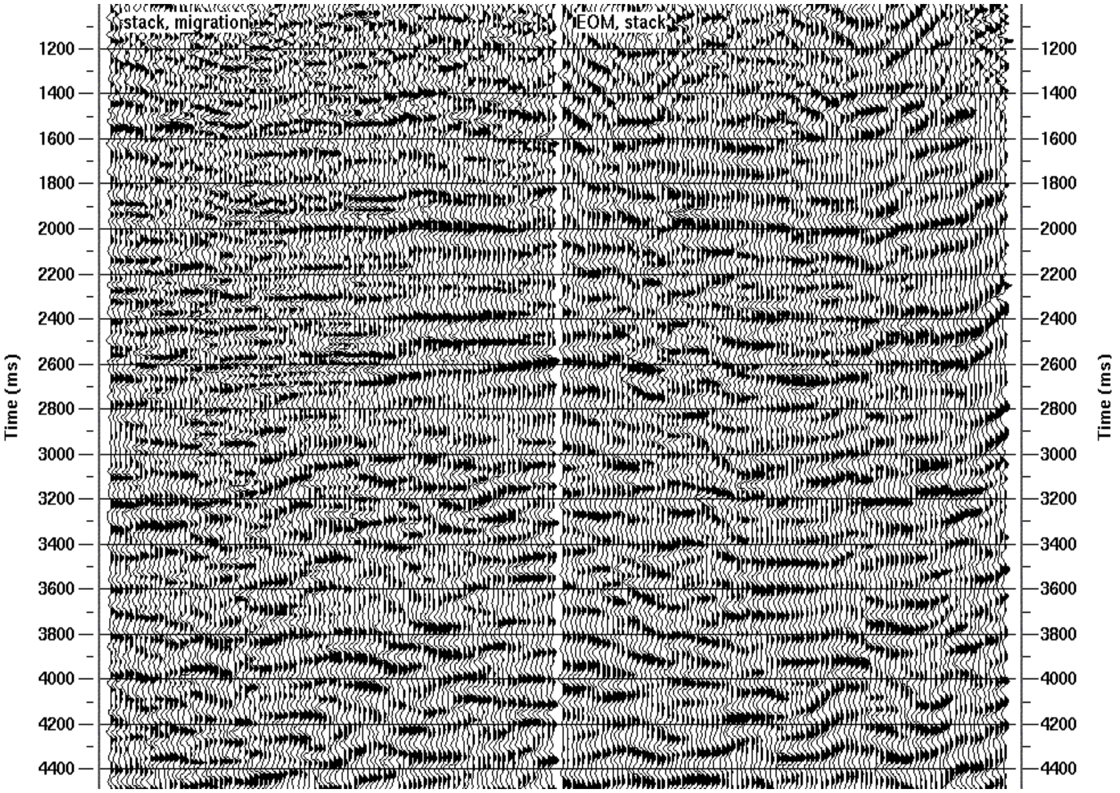

Figure 5.5.7 – Comparison between post-stack finite-difference migration (left) and EOM followed by stack (right). Trace interval 25 m.

Future work for the radial component is related mainly to use of different (higher) V_P/V_S for asymptotic binning; values of 2.5 and (depending on the result of 2.5) 3.0 may be tested.

Figure 5.5.8 shows the processing flow applied in the horizontal components.

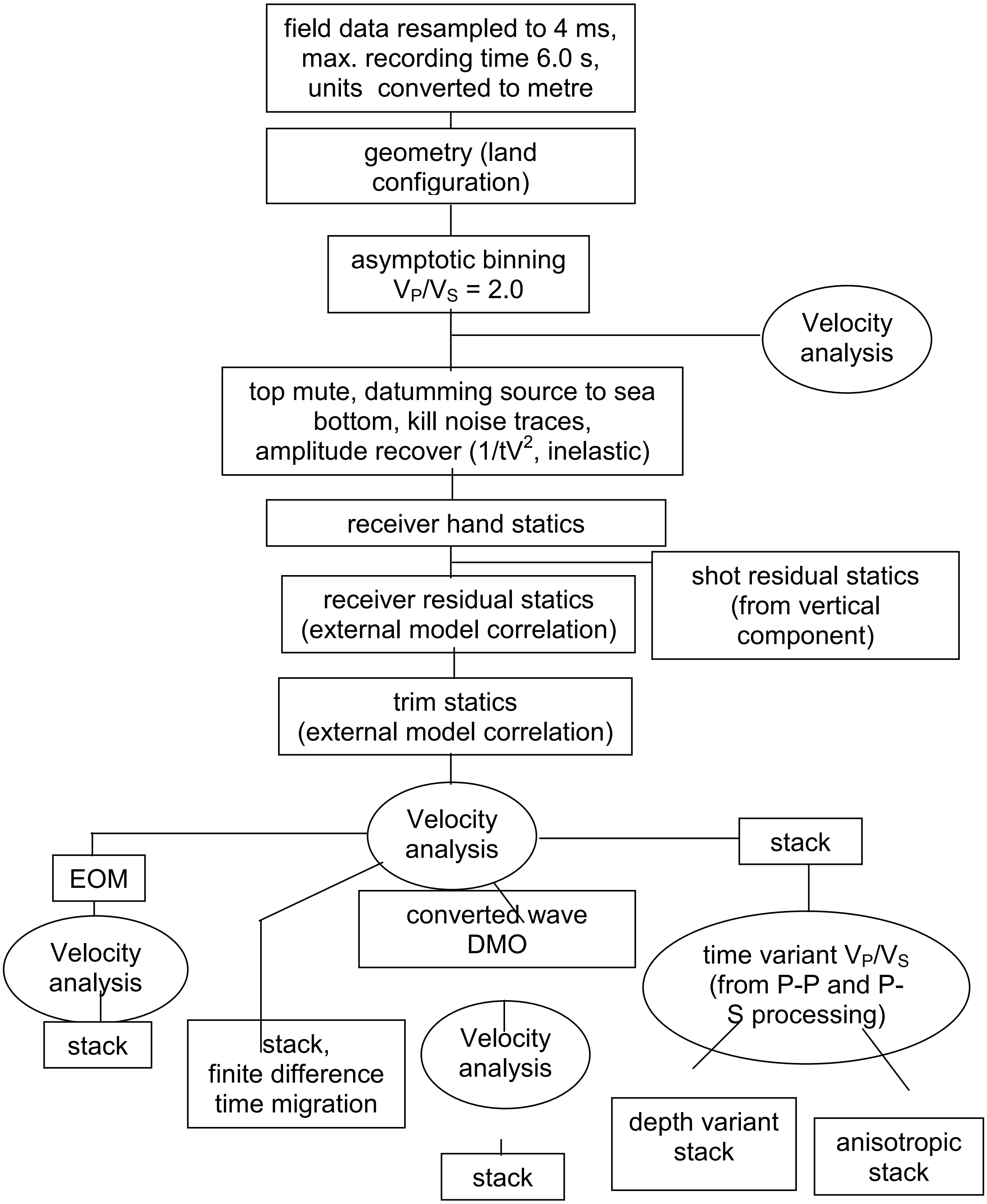

Figure 5.5.8 – Processing flow for radial and transverse components.

V.6 Comparison of cable deployment techniques

As pointed out in the introduction, one purpose of the Teal South project is to evaluate several ocean bottom cable deployment techniques. A comparison of the three methods – trenched cables, taped (cables with sensors "taped" to cable and laid directly on the sea floor) and sandbagged (cables with sensors taped to cables, wrapped with sandbags and laid on the sea floor) – is undertaken. It is assumed that, due to the small distances (around 100 m) between the analysed cables, geological changes could be neglected and a valid comparison mode. The cables to be compared are the ones in the N-S direction, located in easternmost part of the survey (Figure 5.2.1). The same processing parameters (statics, velocities, etc) were used for all cables, and the hydrophone and radial geophone components were used in the analyses of the P-P and P-SV reflections respectively.

Figure 5.6.1 shows a comparison between the trenched cable versus the cable laid on sea bottom with taped receivers. I consider that the trenched cable data has slightly better quality than the taped receivers for both data sets. However, a full interpretation of the geology of the area can provide a final opinion on the interpretation, as the differences may not have a significant effect.

In the trenched / taped and sandbagged receivers comparison (Figure 5.6.2), the differences seem to be even more subtle for the hydrophone data. Nevertheless, it is concluded that, for most reflection events, there is more continuity in the trenched receivers. For the radial component, the sandbagged data seems to be slightly better.

Figure 5.6.3 shows the final comparison, when both cables are laid on the sea bottom and have the receivers taped, but in one cable, sandbags are also put over the receivers. In the hydrophone component (P-P data), the use of sandbags seems to slightly deteriorate data quality. For the radial

Hydrophone

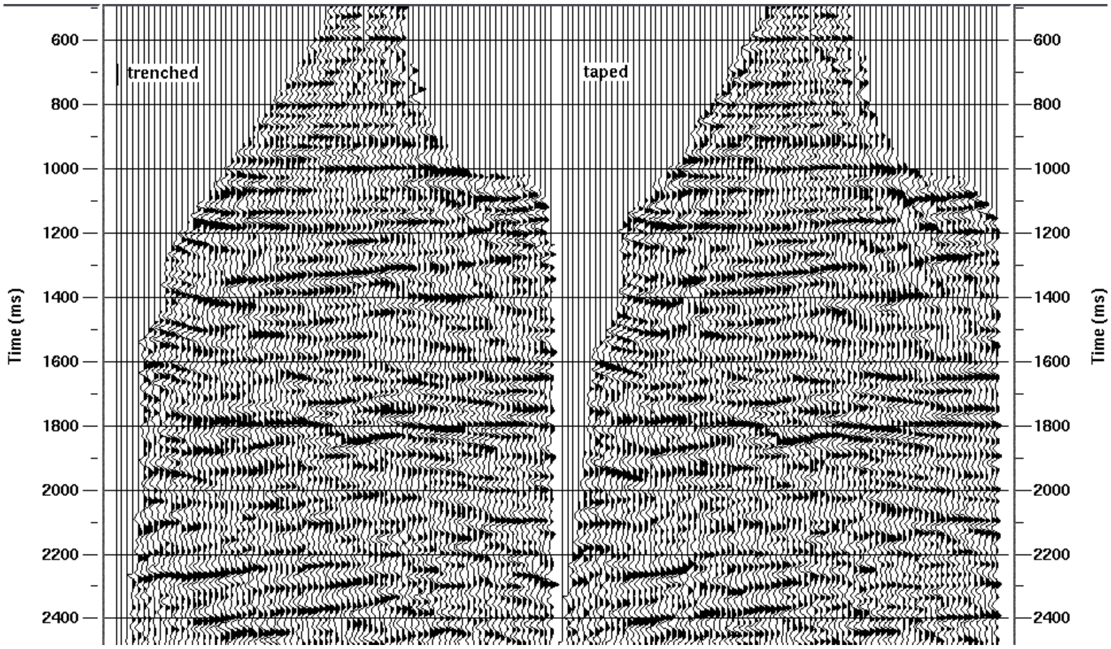

Radial

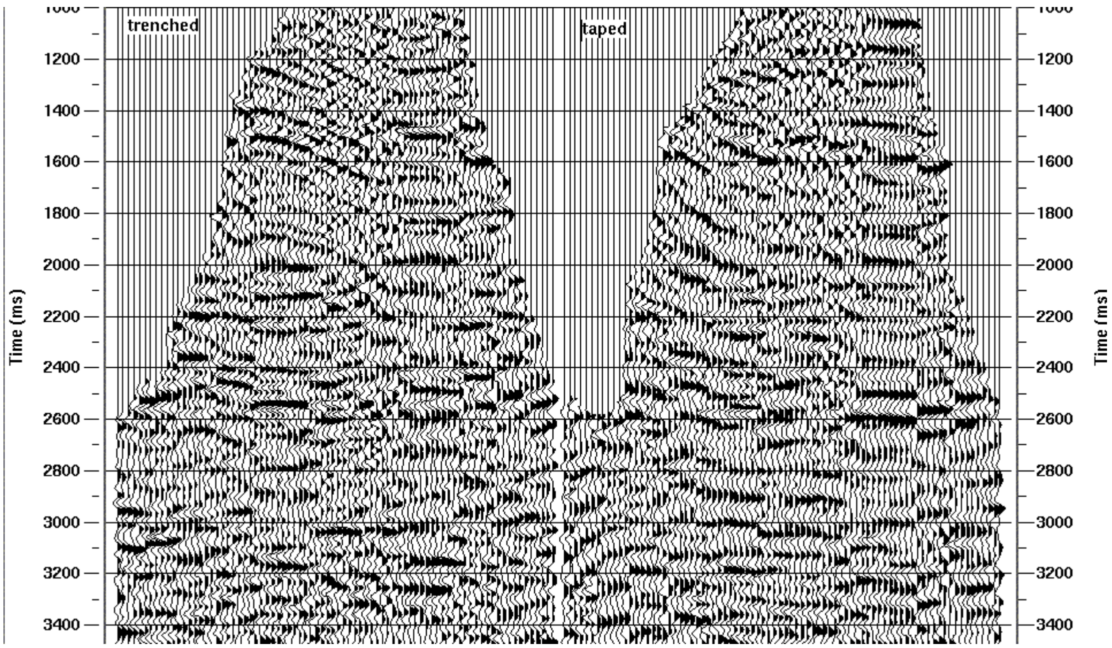

Figure 5.6.1 – Comparison between data collected using cable trenched 1 m below sea bottom (left) and cable with taped receivers (right). Hydrophone recording of the P-P data at top and radial geophone recording of the P-SV data at bottom. Trace distance 25 m.

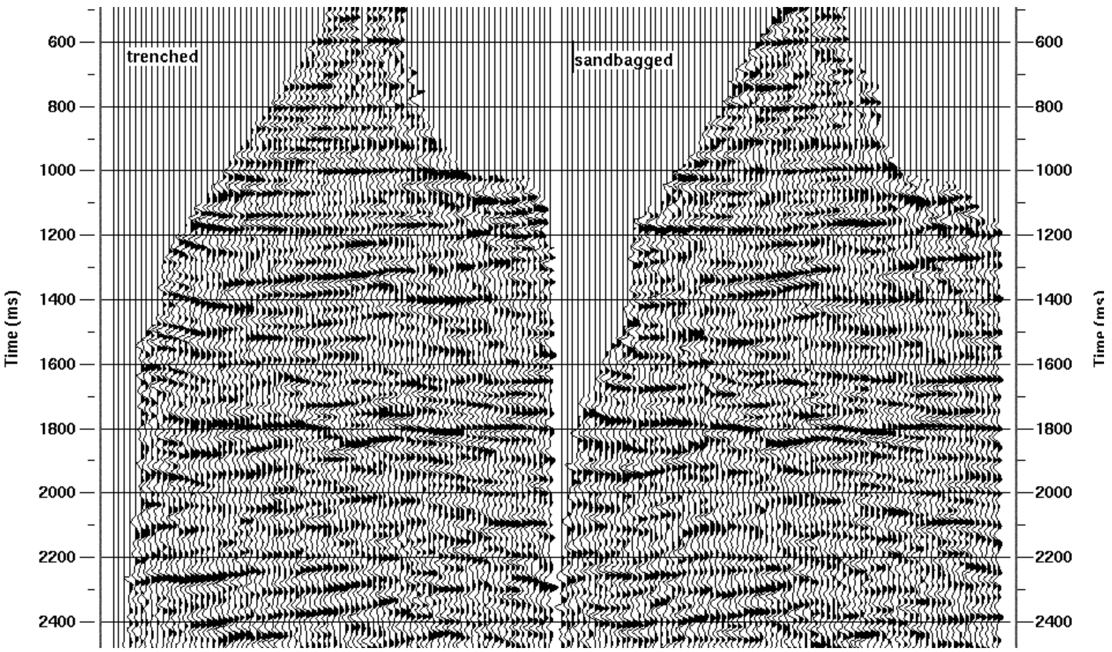

Hydrophone

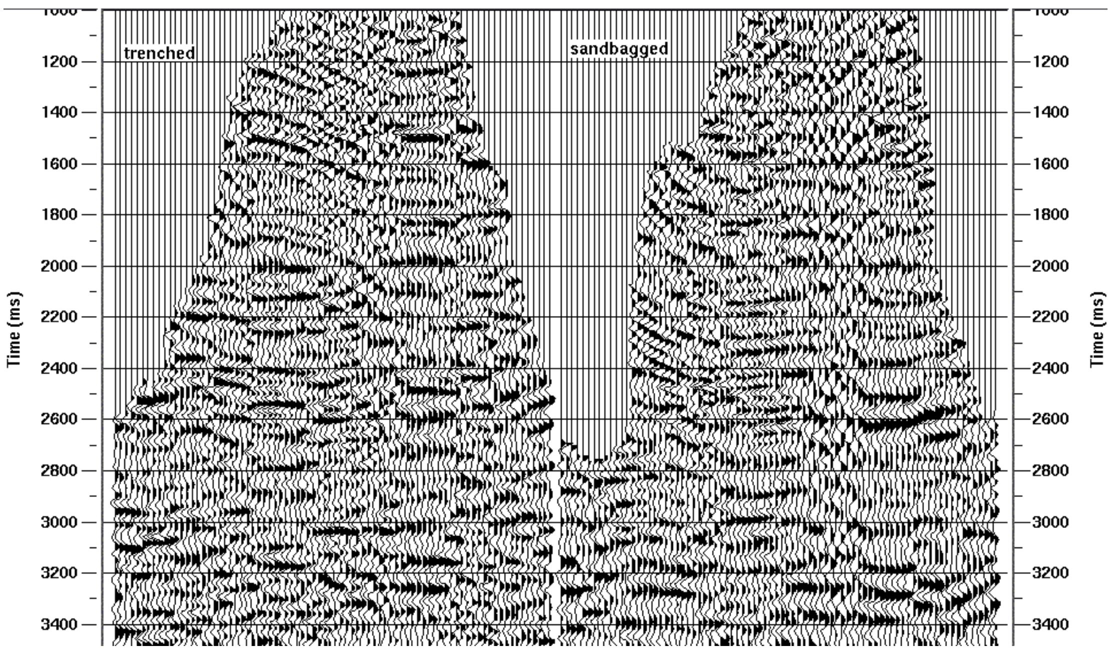

Radial

Figure 5.6.2 – Comparison between data collected from cable trenched (left) and with sensors taped and sandbagged (right). Hydrophone recording of the P-P data at top and radial geophone recording of the P-SV data at bottom. Trace distance 25 m.

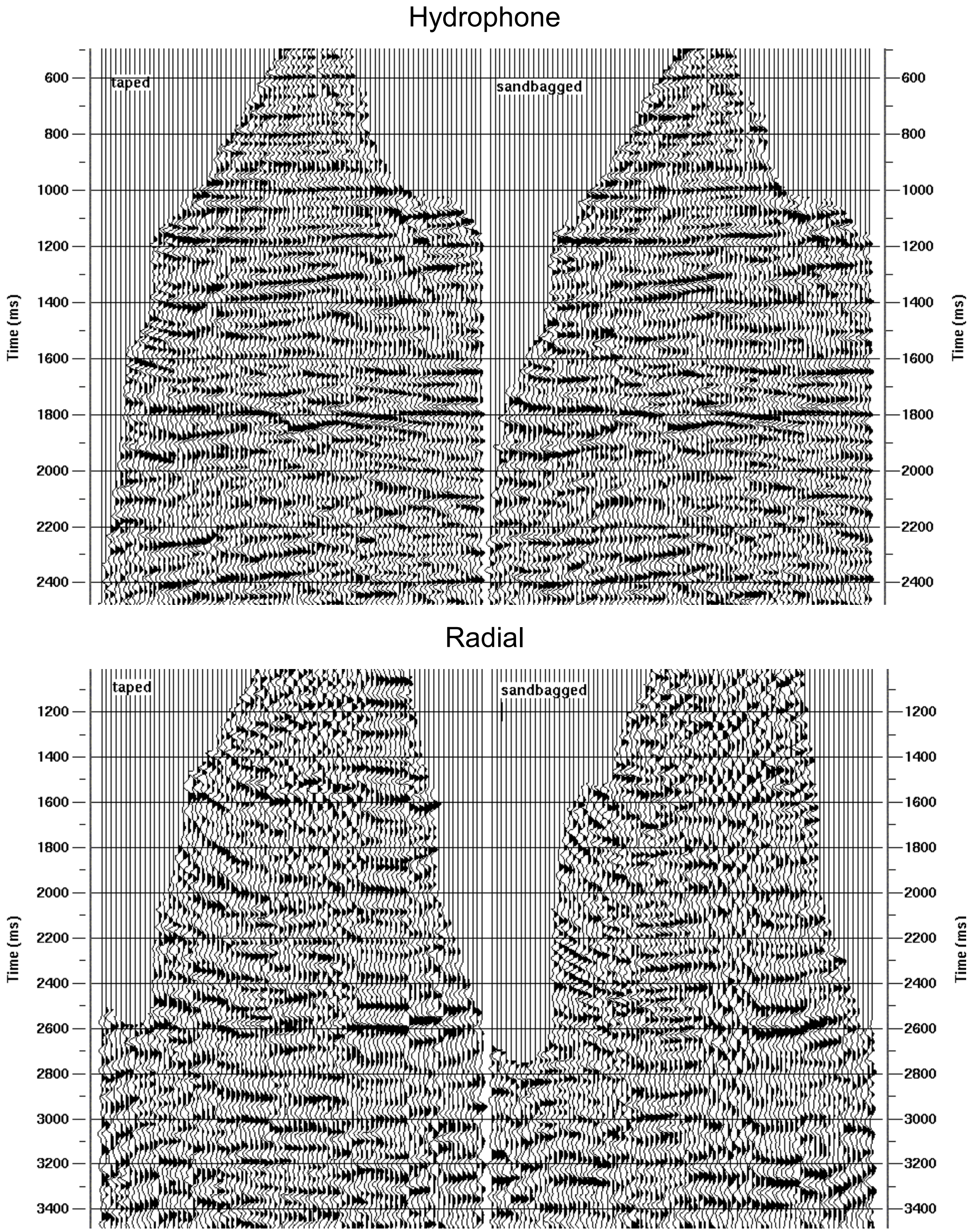

Figure 5.6.3 – Comparison between data collected from cable taped and sandbagged (left) and taped (right). Hydrophone recording of the P-P data at top and radial geophone recording of the P-SV data at bottom. Trace distance 25 m.

geophone component (P-SV data), the only conclusion possible is that there is some difference in data acquired in each system. Which system (if any) gave better results only can be assured by a person with knowledge of Teal South area geology. In my opinion, the taped system gave better results.

Figure 5.6.4 shows amplitude spectrum of the stacked sections presented above. For the hydrophone recording of the P-P data, the sandbagged and trenched spectra look pretty similar. Both seems slightly "better" (i.e. more energy at higher frequencies) than the taped data spectrum. One can conclude the use of bags of sand around both the receivers and the cable section close to the receivers, as described in Sullivan (1995), helps in the recording of higher frequency content data for hydrophone.

For the radial geophone recording of the P-SV data component, though, data from the sandbagged cable seems not as good as data from the other two deployment methods – it shows a decrease of five dB around 20 Hz compared to the trenched and taped data. The trenched seems slightly better than the "taped".

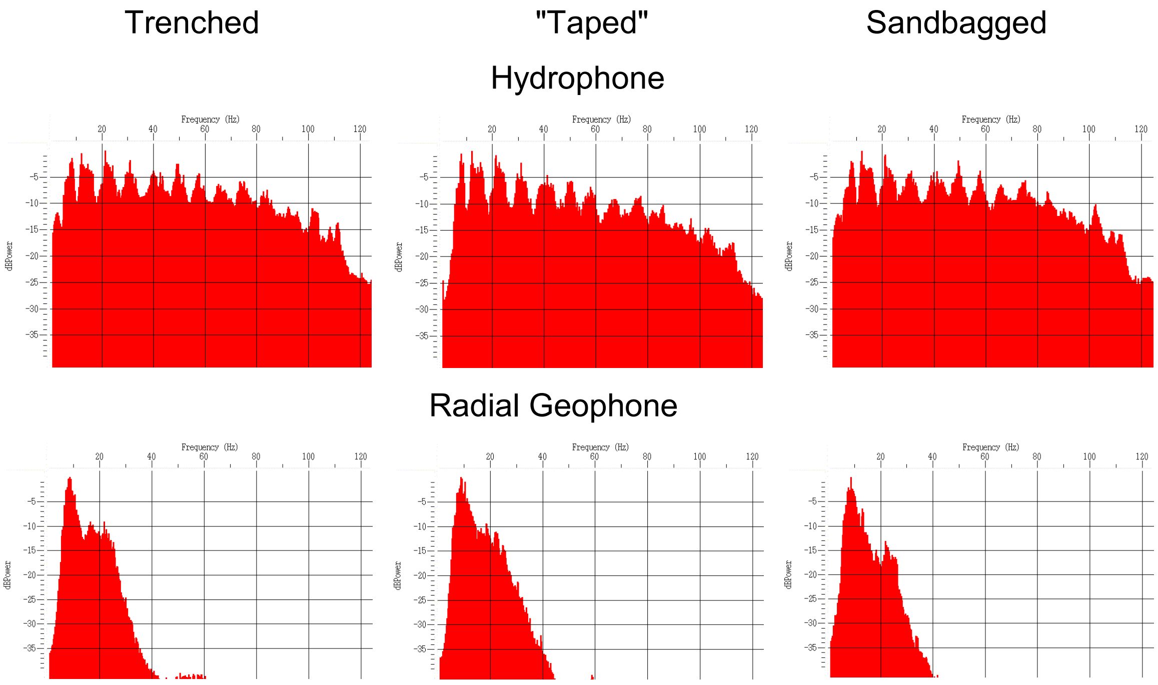

Figure 5.6.4 – Amplitude spectra of stacked section for hydrophone recording of the P-P data (top) and radial geophone recording of the P-SV data (bottom) components data.

V.7 - P-S energy in vertical geophone component, P-P in radial geophone

To consider the possibilities of P-wave energy in the radial component, the vertical component processing flow – shown in Figure 5.4.8 – and its parameters (including statics and velocities functions) were applied in the radial component data after reorientation. From the result, presented in Figure 5.7.1, it can be seen that almost no coherent events are obtained. This suggests that little P-P energy is present in the radial component, probably because the compressional energy is arriving at sea bottom with emergence angle close to zero.

In a similar way, the presence of shear wave energy in the vertical component geophone was observed by applying the radial component flow (shown in Figure 5.5.8) to the vertical component geophone data. One can see (Figure 5.7.2) that many events are present, showing that the vertical geophone data may be highly contaminated with converted-wave (P-S) energy. Indication of this leakage have already been presented in this chapter – namely, the lower frequency content and the absence of receiver ghost in the vertical geophone component in comparison to the hydrophone.

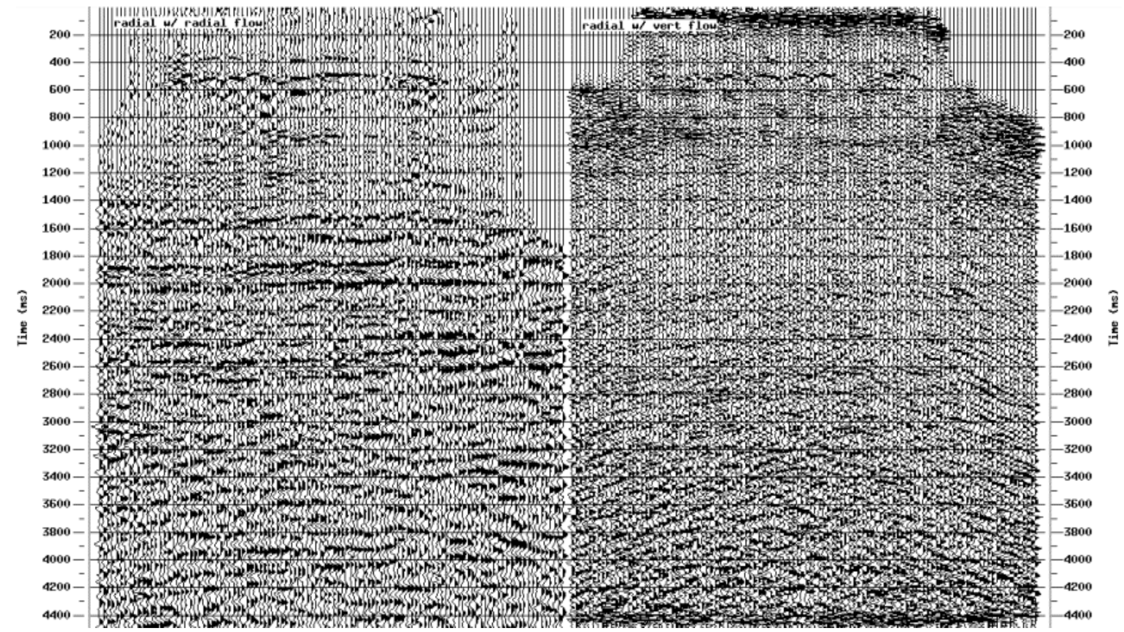
P-S flow

P-P flow

Figure 5.7.1 – Comparison between radial component data processed with 'conventional' flow (shown in Figure 5.5.8), at left, and the same data processed with P-wave parameters, at right. Trace interval 25 m.

The presence of shear-wave energy in the vertical component is not predicted from theory. It was shown in chapter III that, as a general rule in marine sediments, most up-going seismic energy (either P- or S-) is transmitted through the interfaces as the same mode of the incident wave. Even when this is not the case, one could expect that, if P-S energy is present in the vertical geophone component, P-P energy also should occur in the horizontal components, as both modes would approach the sea-bottom far from the vertical direction and/or all the geophones could be tilted.

However, this is not seen here and in some examples presented in the literature (e.g. Yuan e*t al.* 1998; Li and Yuan, 1999). Ebrom *et al.* (1998a), analysing the first 3-D in Teal South (Phase I), also found converted-wave energy in the vertical component, but no compressional energy in the radial component.

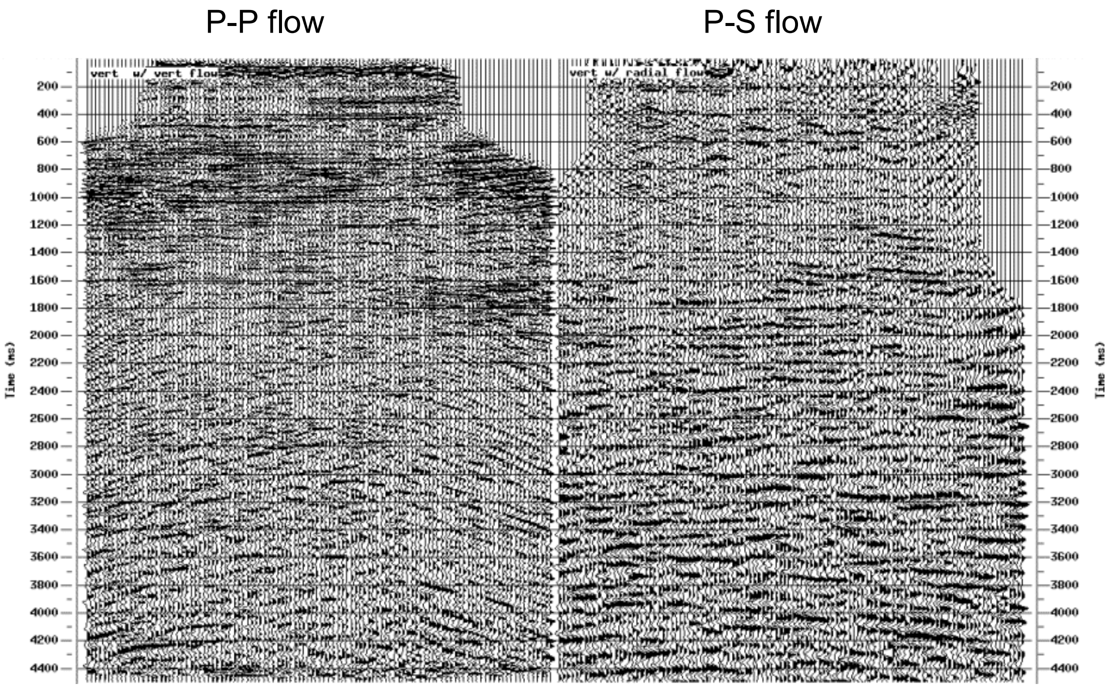

Figure 5.7.2 – Comparison between vertical geophone data processed with ‘conventional’ flow (shown in Figure 5.4.8), at left, and the same data processed with radial component flow (shown in Figure 5.5.8), at right. The presence of S-wave energy in the vertical component is clear. Trace interval 25 m.

Yuan e*t al.* (1998) report the presence of much stronger water layer reverberation in the hydrophone than in the vertical geophone component in OBC data from North Sea (water depth around 90 m). They relate this to the strong impedance contrast of the sea bottom, in a way that source and receiver ghost cancel some multiples in the vertical geophone, but not in the hydrophone (see Figure 5.7.3). They also found strong evidence of converted-wave data in the vertical component (and no P-wave energy in the radial, as in Teal South), but do not connect this to the relative absence of receiver ghost in the vertical geophone component. A high impedance contrast at the sea floor, associated with a very low (around 2.0) V_P/V_S ratio in the shallow sediments, indeed can cause a much higher amplitude response in the geophone than in the hydrophone, as explained by Brown and Yan (1999).

Still, two issues remains: 1) Yuan e*t al.* (1998) show V_P/V_S ratio over 3.5 in the shallow data (less than 500 ms), and, more important, 2) almost all papers, as published on receiver ghost attenuation using hydrophone and vertical component geophone, do mention the same intensity of receiver ghost effect in both sensors. If not, the dual-sensor technique (Barr and Sanders, 1989) would not be feasible. One probably cannot consider different system responses as the reason for this discrepancy.

Theoretically, it could be considered that Scholte (interface) waves might cause these different responses in vertical geophone and hydrophones (which may not record them) components, due to their elliptical displacement. However, Scholte waves are, in general, of low amplitude. Also, as these waves are strongly attenuated during stacking (due to their very low velocities), it is unlikely that continuous events seen in Figure 5.7.2 can be related to interface waves.

Dr. Peter Cary (1999, personal communication) also found, analysing Mahogany (Gulf of Mexico) OBC data, the presence of a receiver ghost effect in the amplitude spectrum in the hydrophone but not in the vertical geophone component. He considered this is caused by interference of another multiple (e.g., water bottom multiple) with the receiver ghost – this interference would attenuate the ghost in the vertical component, but not in the hydrophone (Figure 5.7.3). He thinks the relatively high ocean bottom reflectivity (around 0.4) is responsible for this attenuation. Brown and Yan (1999) consider the same idea, on theoretical and numerical modelling bases (Figure 5.7.3).

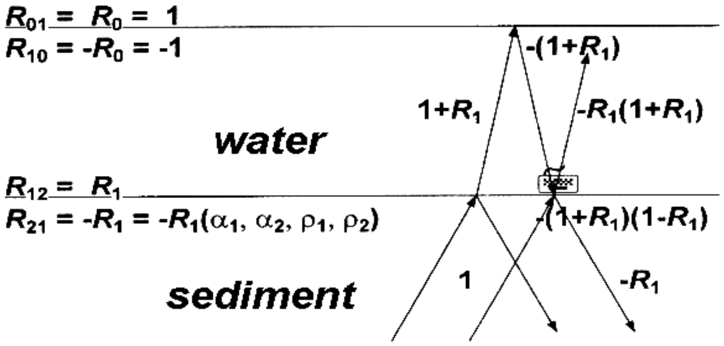

	primary	1st multiple	2nd multiple
W phone	$1+R_1$	$-(1+R_1)(1+R_1)$	$R_1(1+R_1)^2$
Z phone	$1+R_1$	$(1-R_1)(1+R_1)$	$-R_1(1-R_1^2)$
ratio $\frac{W}{Z}$	1	$-\frac{1+R_1}{1-R_1}$	$-\frac{1+R_1}{1-R_1}$

Figure 5.7.3 – Effect of receiver-ghost (receiver-side multiple) in hydrophone (W phone) and vertical geophone (Z phone) components for up-going P-P energy close to vertical. For high (≥ 0.35) R_1 (sea-bottom reflection coefficient), receiver ghost is more attenuated in the vertical geophone (Z) than in the hydrophone (W) component (*modified from Brown and Yan, 1999)*.

Li and Yuan (1999), analysing 4-C data from the North Sea, consider this phenomenon being caused by a coupling problem, in a way that some horizontal movement also causes motion in the vertical component of the sensor. The authors propose that a mechanical fault in the design of the cable system – especially for gimballed geophones – is responsible for this problem. However, they do not present any proof or reason on how and why this hypothesis should be valid. Based on the work of Samson *et al.* (1995), the authors also state that it is difficult to obtain a good coupling for horizontal components in gimballed geophones.

One can reasonably disagree with this, as several examples are presented in the literature of good quality OBC data acquired with a gimballed system.

Dr. Eivind Berg also relates (Robert Stewart, 1999, personal communication), based on confidential tests in Norway, that it appears to be the cable system, and not gimballed sensors, that causes cross-coupling.

At this point, it seems that the most reasonable conclusion one may have is that there is some acquisition issues yet to be completely understood and solved in the OBC technique.

The separation of these energy modes in the appropriate components is considered as future work. It has to be pointed, however, that if most spurious energy present in a component is not due to up going wavefield far from vertical, most theoretical algorithms for energy separation probably will not work. This is clearly the case for energy leakage caused by some acquisition problem.

V.8 – Azimuthal anisotropy (VTI) checked by azimuth stack

A simple approach was used to search for the presence of anisotropy (other than non-transverse isotropy) in the Teal South area (for both P-P and P-S waves): stack hydrophone and radial geophone component grouped by opposite range of azimuths.

The basic assumption is that if there is no anisotropy, or if there is only transverse isotropy with vertical axis asymmetry (VTI), data stacked from the opposite range of azimuth should be similar. One can consider that VTI anisotropy is expected in this area, as in most marine geological basins, due to the possible existence of a thick (several hundreds metres) package of shales.

This hypothesis assumes no major geological changes will occur among different CDPs (or ACCPs, for the P-S case) bins collected in each data set.

The azimuth ranges were formed every 45^0 (0^0 to 45^0, 45^0 to 90^0, and so on). Then opposite ranges (e.g., 0^0 to 45^0 and 180^0 to 225^0) were stacked and compared. The results are shown in Figure 5.8.1. The azimuth ranges selected 9for comparisons are 0^0 to 45^0 *vs* 180^0 to 225^0 and 90^0 to 135^0 *vs* 270^0 to 315^0.

There are some differences for symmetric azimuth ranges in both components. Although a detailed comparison is prejudiced by low signal-to-noise ratio, especially in the radial component, one may have a preliminary conclusion that some anisotropy is present. If one is interested in obtaining quantitative values of the amount of anisotropy present, additional analyses are necessary.

An additional complication for P-S analysis would be to separate the effects of individual anisotropy present in the downgoing P-wave from the upcoming S-wave.

Hydrophone (P-P)

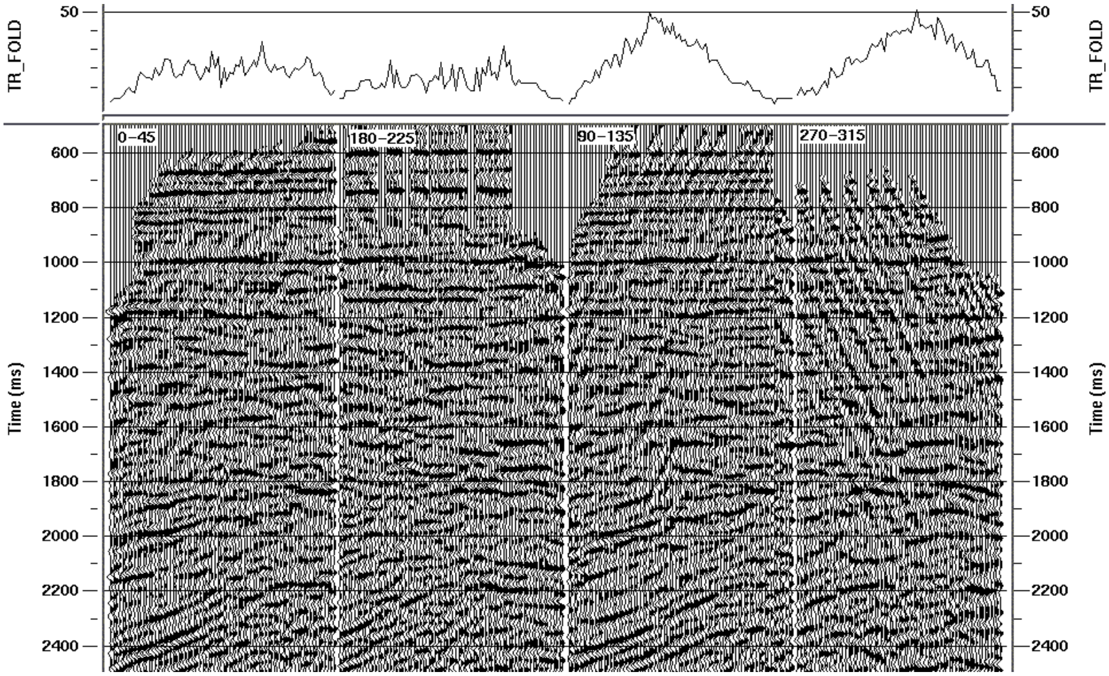

Radial Geophone (P-SV)

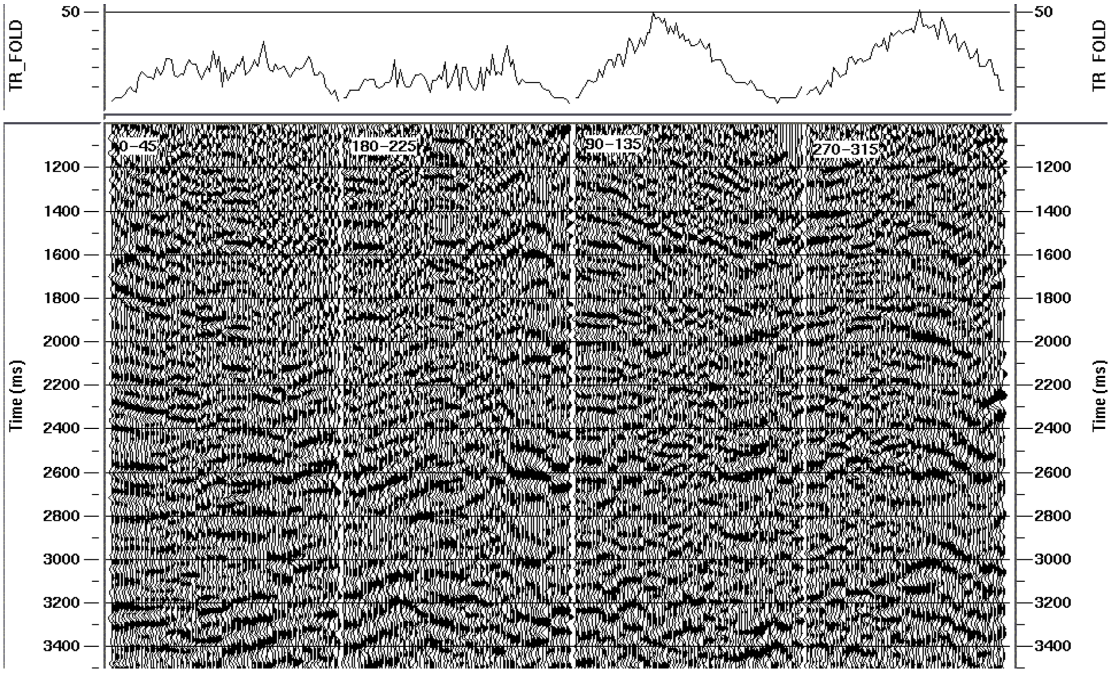

Figure 5.8.1 – Azimuth stack for P-P (hydrophone, at top) and P-SV (radial geophone, at bottom) data. Compare 0^0-45^0 to 180^0-225^0 and 90^0-135^0 to 270^0-315^0. Bin fold shown at top of the picture. Trace distance 25 m.

V.9 – Acquisition footprints

To consider the existence of possible acquisition footprints – caused by source and/or receiver distribution and survey orientation – time slices were analysed in hydrophone and radial geophone components to consider the P-P and P-SV data.

This check was performed after some questions and suggestions by Prof. Don Lawton, who was concerned about this issue during survey design for the Teal South Phase III (Don Lawton, 1999, personal communication).

Figure 5.9.1 presents a time-slice, at 1.0 s for hydrophone and 1.5 s for radial components. The north-south source vessel orientation (Figure 5.2.1) can be clearly seen in the data, mainly in the P-SV data recorded on the radial geophone component. The reason for the shot point orientation footprint to be stronger in the radial component may be related to less data present at this time in this component due to deeper top mute than the hydrophone.

Deeper time-slices, shown in Figures 5.9.2 (2.0 s for hydro, 3.0 for radial) and 5.9.3 (hydro at 3.0 s and radial at 4.5 s), also indicate the presence of source position footprint.

P-P (hydrophone) at 1.0 s

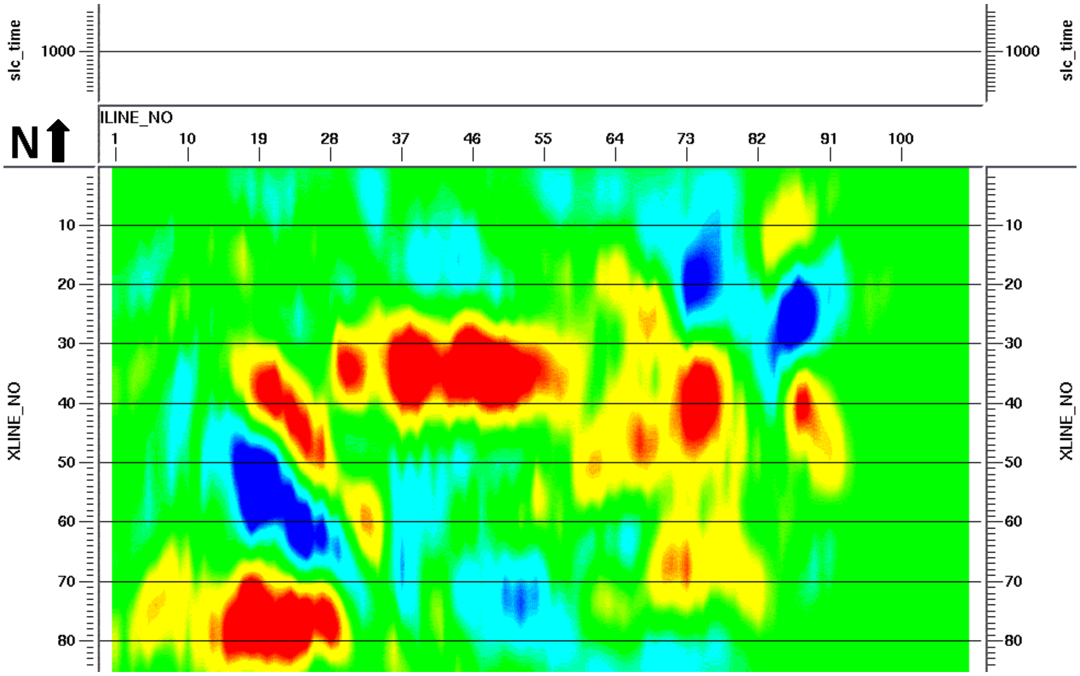

P-SV (radial geophone) at 1.5 s

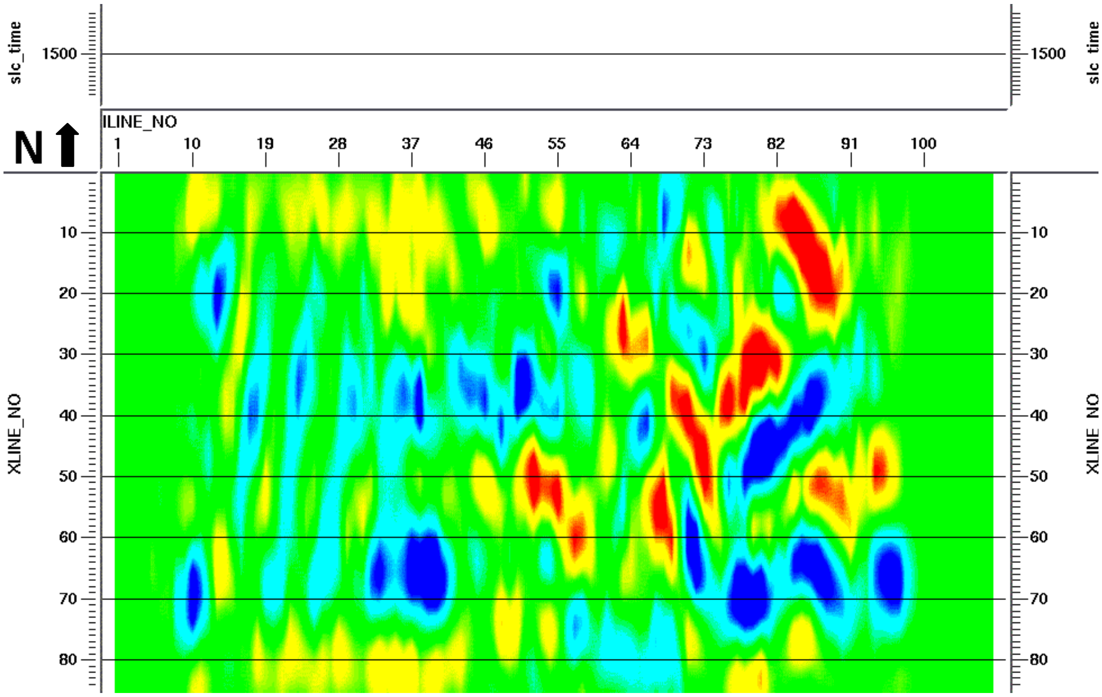

Figure 5.9.1 – Time-slices for P-P (hydrophone) at 1.0 s (top) and P-SV (radial geophone) at 1.5 s (bottom). Effect of shot point direction (along N-S) is clear in the data, especially in the P-SV data.

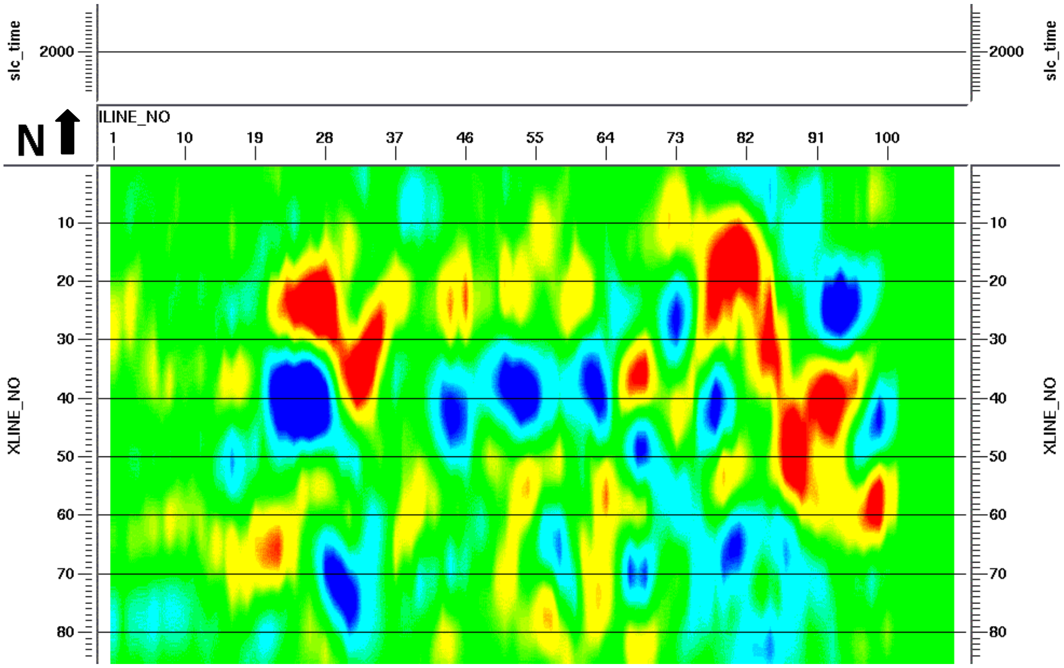
P-P (hydrophone) at 2.0 s

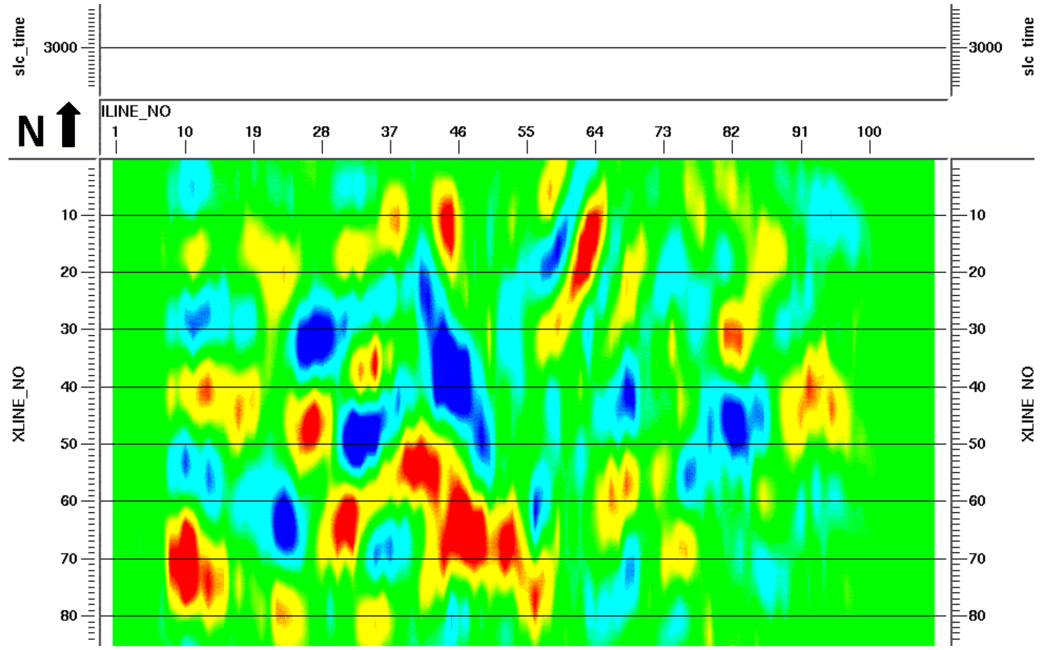
P-SV (radial geophone) at 3.0 s

Figure 5.9.2 – Time-slices for P-P (hydrophone) at 2.0 s (top) and P-SV (radial geophone) at 3.0 s (bottom). The shot point footprint (N-S direction) can be seen in both data sets.

P-P (hydrophone) at 3.0 s

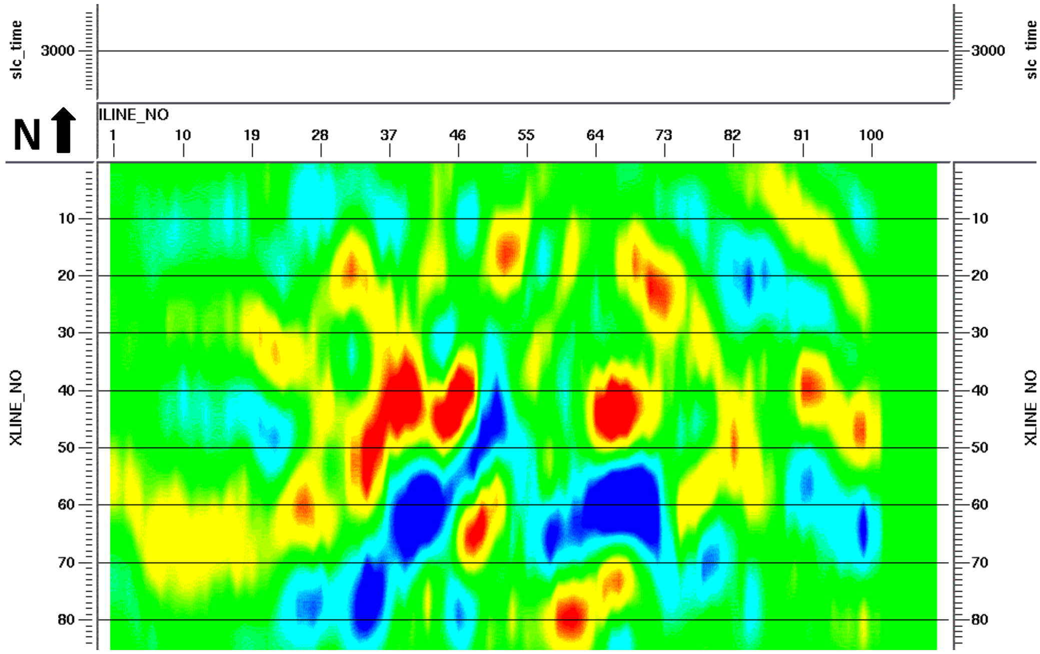

P-SV (radial geophone) at 4.5 s

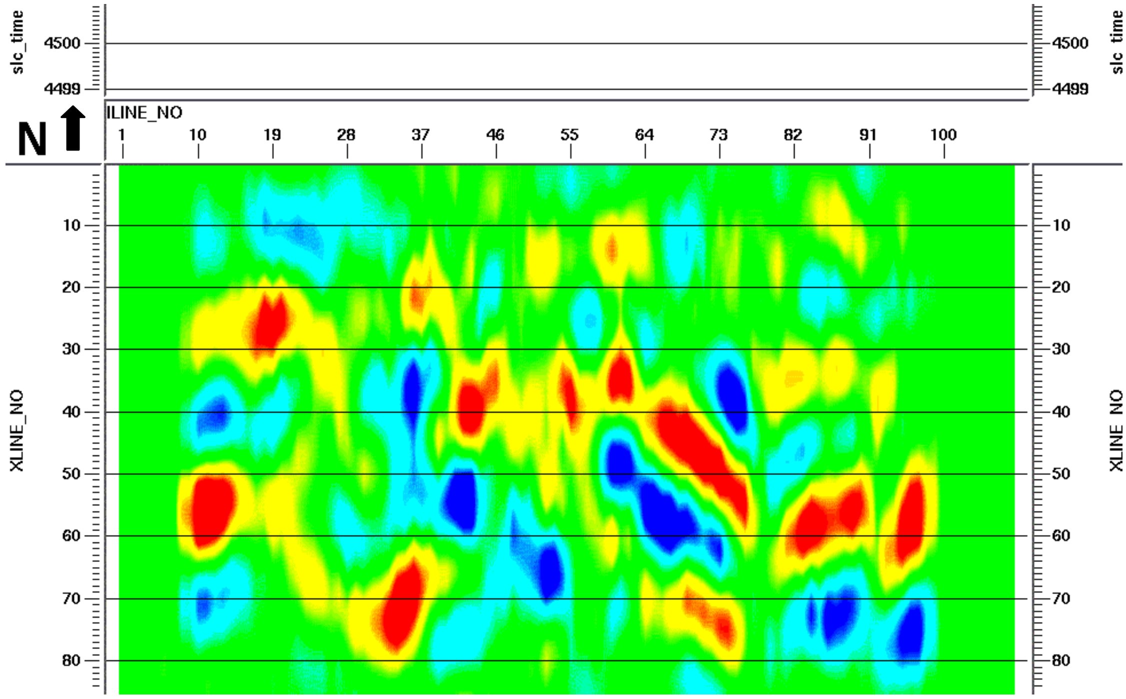

Figure 5.9.3 – Time-slices for P-P (hydrophone) at 3.0 s (top) and P-SV (radial geophone) at 4.5 s (bottom). The shot point footprint (N-S direction) can be seen in both data sets.

V.10 - Discussion

Repeated 4C-3D seismic surveys have been acquired over the Teal South field, Gulf of Mexico. This chapter presented preliminary processing of the second 4C-3D data set, acquired in the spring of 1999.

Good separation between radial and transverse geophone component was achieved during polarity reorientation in the pre-processing phase. Polarity correction for horizontal geophone components was performed with polarity reorientation.

The horizontal geophone components recording the P-SV data have higher amplitudes than vertical geophone and hydrophone recordings of the P-P data.

Source and receiver statics could be satisfactorily solved for P-P reflections recorded on hydrophone, vertical geophones, and for P-SV reflections recorded with the radial geophone component.

"Conventional" and CREWES specific process flows were applied to the data. The best quality was present on the P-P hydrophone, followed by the P-P vertical geophone and then the P-SV recorded on the radial geophone.

The equivalent offset migration (EOM) method, a pre-stack migration algorithm developed in CREWES, gave results with lower frequency than conventional stack-migration sequence for all components.

In the P-SV data recorded on the radial geophone component, converted-wave DMO did not present good results. Depth variant and anisotropic (VTI) stacks did not work well in the P-SV (radial geophone component), probably due to the use of incorrect depth-variant V_P/V_S ratios.

From the three methods used on cable deployment (trenched, sandbagged, lain), these preliminary results suggest that no option is significantly better than the others. In seismic sections analyses, trenched give slightly better results for the hydrophone and sandbagged for the radial. Regarding frequency content, taped is not as good as the other two for the hydrophone (although differences are not very significant); for the radial component, trenched seems slightly better than the other two methods, and sandbagged data shows energy decrease in signal band.

No compressional wave energy was found in the radial geophone component, but the vertical geophone component is contaminated with converted-wave energy. This cross-coupling energy may be related to acquisition problems. If this is the case, algorithms for energy separation probably will not work.

Anisotropy may be indicated, by obtaining different stacking results for opposite range of azimuth angles, on both P-P and P-S data.

Some acquisition footprint, caused by shooting line direction, is present in the data.

The use of different V_P/V_S ratios for asymptotic binning processing of the radial component is recommended as future work priority.

Chapter VI – Vertical Cable: Survey Design and Preliminary Processing

VI.1 Introduction

In conventional marine seismic acquisition, a ship tows both the source (a set of air guns) and the receivers (pressure sensitive hydrophones, placed in a cable called a streamer). For most 3-D surveys, two or more streamers are towed at the same time. In a typical configuration, each streamer has a length of 3,500 to 6,000 m and the minimum cable separation is 50 m.

Due to water currents, these cables may have a ‘feathering’, or lateral movement, that can reach 45°, and even more. In areas with hydrocarbon production facilities, platforms and buoys become obstacles for the passing of the vessel towing these cables, making necessary the use of some alternative approach.

Among the techniques generally used to overcome this problem (e.g., undershooting and ocean bottom cables), the vertical-cable concept has been attempted. Using vertical-cables, very good results have been achieved in the Gulf of Mexico, mainly for sub-salt imaging (Krail 1994b; 1997), and the North Sea (Ebrom *et al*., 1998a; Nolte *et al*., 1999).

The concept is similar to the 3-D VSP, but instead of using a well or wells, a set of cables in the vertical position is used. Each cable has hydrophones at different depths to record the wavefield generated by a shooting vessel. The cables are kept in the vertical position by the use of buoys at their top and anchors at their bottom.

The quality of seismic images often improves when high data redundancy is available: stacking usually gives a higher signal-to-noise ratio and further enhancement follows from the use of different offsets and azimuths. The number of times a point (or a bin) is imaged for different source and receiver positions is called the coverage, fold, or multiplicity. Adequate fold is required to achieve a good image, so pre-survey planning must be accomplished, based on geological and petrophysical information, to define the acquisition parameters.

The results of coverage, offset, and azimuth distribution for some acquisition geometries, receiver configurations and water depths for a marine extensional basin geological model using vertical cables are presented and discussed in this chapter. The reflection points were obtained using 3-D ray tracing. General equations for fold values were obtained from the results of these analyses.

Initial processing, using data generated from 3-D ray tracing over a geological model (obtained from real 3-D seismic data interpretation), was also performed, using the equivalent offset migration (EOM) concept.

VI.2 Vertical cable technique: overview and examples

The vertical-cable genesis lies in the marine walkway VSP, with an obvious difference – and advantage – of not needing a drilled well. It is also based on US Navy antisubmarine warfare technology (Krail, (1994b; George, 1996). Texaco Inc., which some years ago allowed its use by Petroleum Geo-Services (PGS), patented this method (Petzet, 1995; George, 1996).

The basic idea of this technique is to use the receivers (piezoelectric sensor or hydrophones) in a vertical configuration, instead of horizontal, which is the usual case in marine seismic acquisition. Figure 6.2.1, extracted from Krail (1997), compares acquisition schemes for conventional (streamer) and vertical cable methods.

One can see that, as for OBC, real 3-D acquisition geometry is recorded in the vertical cable, compared to 3-D images obtained by several 2-D parallel lines in the streamer approach.

In land, the use of 3-C receivers is an additional benefit, but the discussion in this chapter will be restricted to hydrophones-only data.

Instead of being placed in a cable (streamer) filled with a special low-density oil, the vertical cable hydrophones are attached to the outside of a high-strength stress member. To reduce water current drag, a fairing is attached to the cable (Krail, 1993).

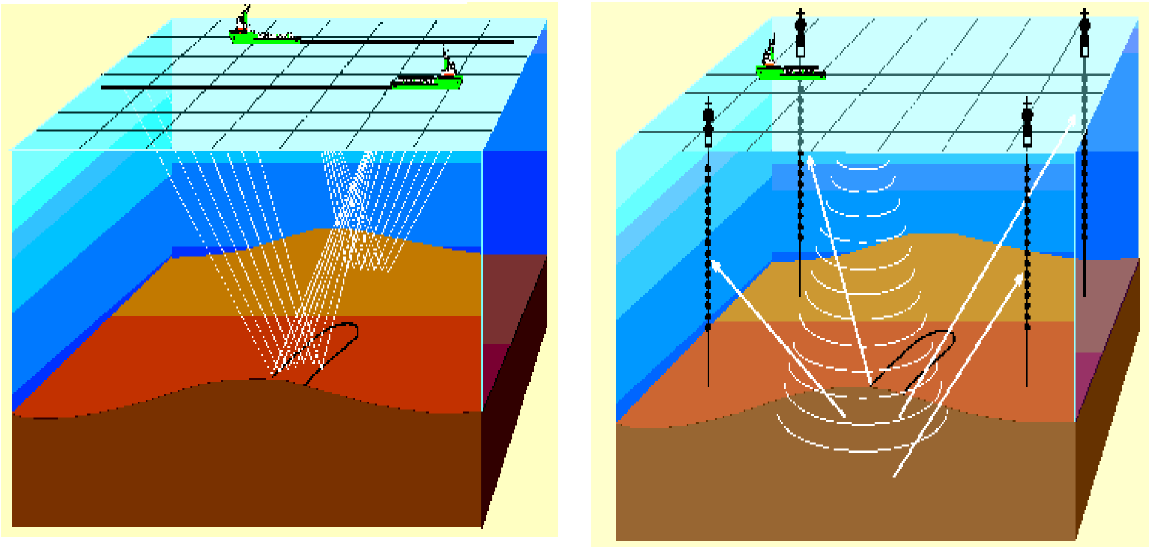

Figure 6.2.1 – Acquisition schemes for streamer (left) and vertical cable (right) *(after Krail, 1997).*

Keeping the electrical and mechanical integrity of the cables and hydrophones under high hydrostatic pressure is a significant issue (Krail, 1994b). A cable is kept in the vertical position using buoys at its top end and anchor at its bottom end. A vertical cable scheme, extracted from Krail (1994a), is shown in Figure 6.2.2.

In general, 3-D pre-stack depth migration in the receiver domain is applied to the data. Using the reciprocity assumption, the relatively sparsely located hydrophones are considered as sources and the relatively closely spaced shot points are considered as receivers (Figure 6.2.3). In this way, good subsurface sampling is obtained and aliasing is less of a problem.

According to Leach (1997), the downgoing wavefield (water-surface receiver ghost) can be – after proper processing – stacked to the up-going (primary) energy to increase signal-to-noise ratio.

Guimarães *et al.* (1998) show the direct (up-going) energy gives a denser sampling close to the cable. On the other hand, the ghost energy, although sparser, illuminates regions farther away from the cables (Figure 6.2.3).

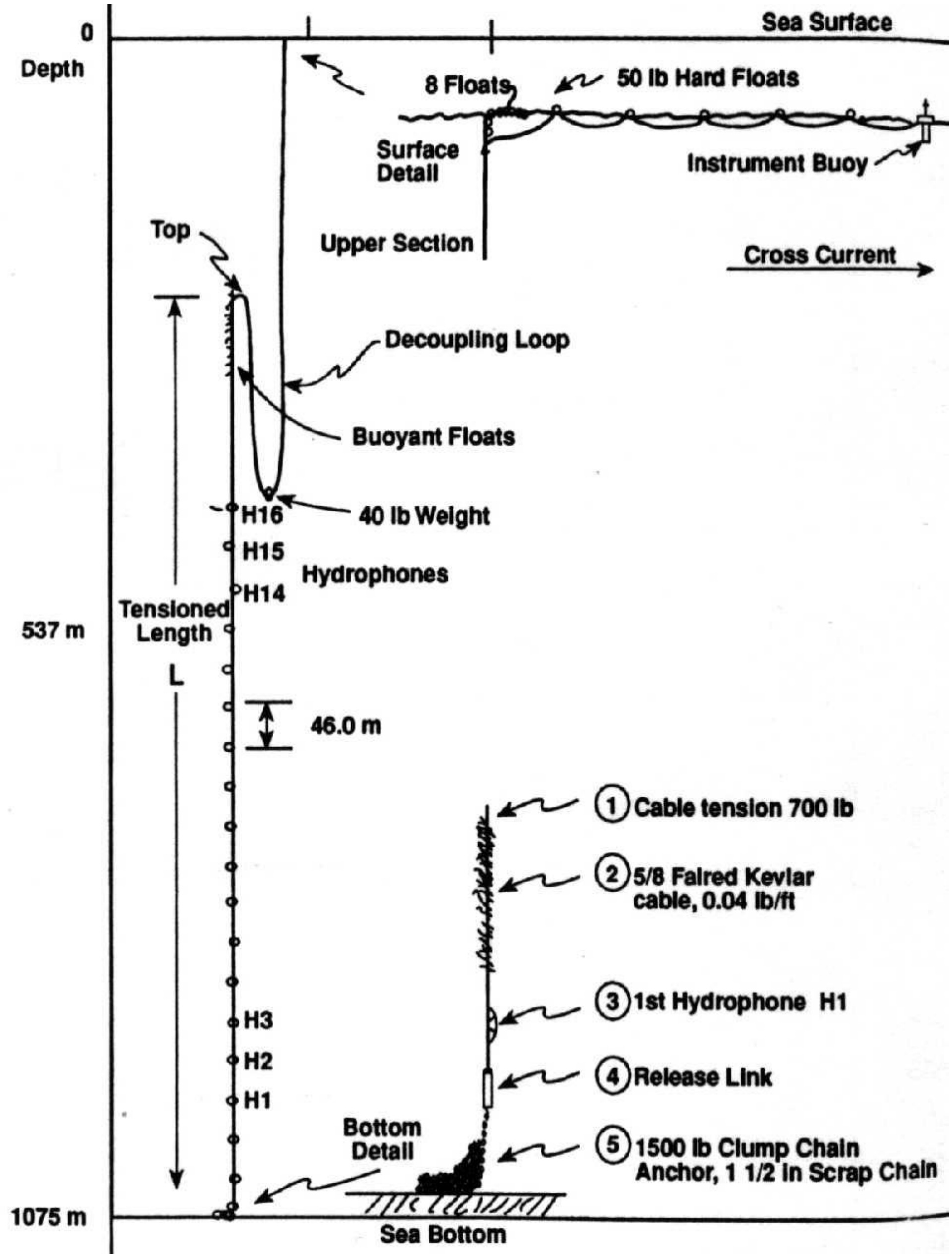

Figure 6.2.2 – Scheme of a vertical-cable *(after Krail, 1994a).*

The first vertical-cable acquisition reported in the literature was done in the Gulf of Mexico, in 1987, using three cables, for a common geological problem in that area: imaging of sand reservoirs against flanks of a salt dome (Krail, 1994b).

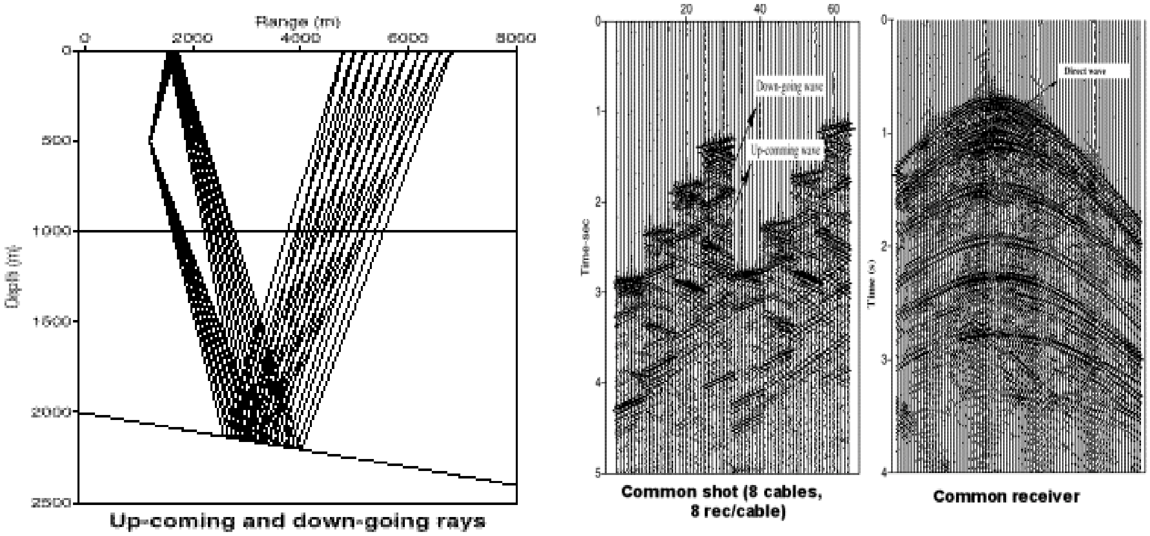

Figure 6.2.3 – On left, indication of up- and down-going rays' illumination. On right, example of shot (left) and receiver (right) gathers of physical modelling data. Both pictures after Guimarães *et al.* (1998).

In 1992, and again in the Gulf, the method was used to image below the salt. In that survey, presented by Krail (1994b), six cables were used at water depths greater than 1,000 m. The data, acquired in an 11 x 8 km^2 area, were processed using 3-D pre-stack depth migration. A comparison between these data and conventional (streamer) 3-D data showed clearer images for sub-salt reflections from the vertical-cable. However, this comparison may not be quite fair, as a poststack migration was used in the conventional data processing. Nevertheless, the results are shown in Figure 6.2.4. The acquisition cost was considered as a half of a conventional 3-D seismic, as the time to collect the data was drastically reduced. This happens because: 1) it is much easier for the source vessel to manoeuvre through obstacles without towing a streamer, and 2) no infill lines (to obtain the desired fold) are necessary (Krail, 1994b). No comments, though, are made about the time spent to deploy and remove the cables.

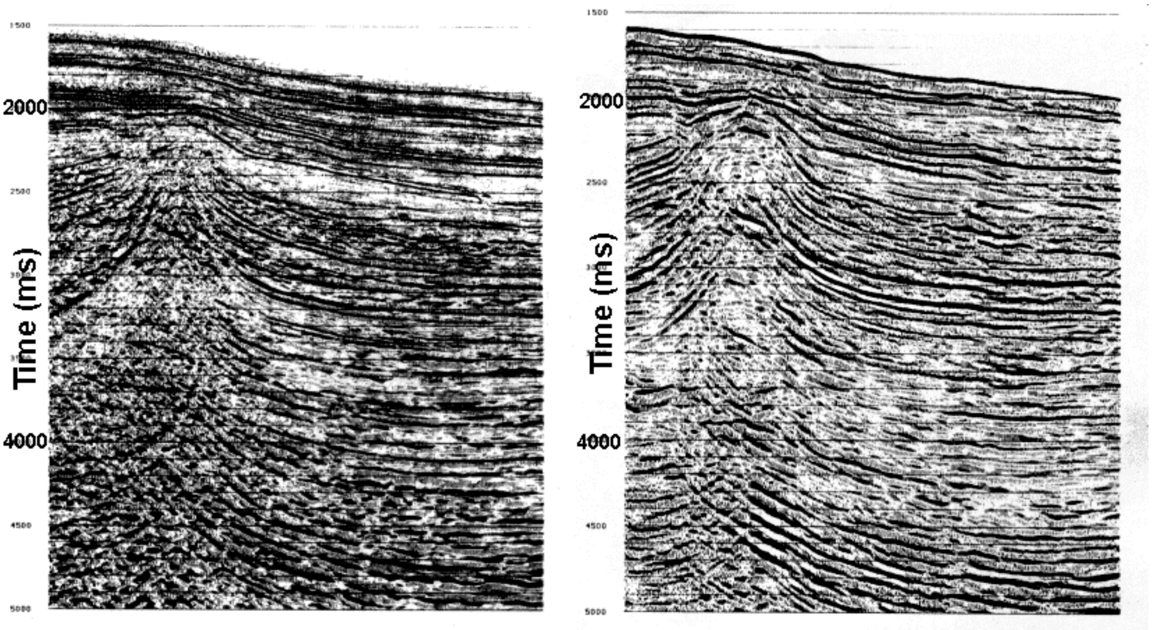

Figure 6.2.4 – Comparison between data from Gulf of Mexico, acquired with streamer and processed with 3-D post-stack migration (left), and data acquired with vertical cable and processed using 3-D pre-stack depth migration (right) *(after Krail, 1994b).*

Anderson *et al.* (1997) present an equal comparison between streamer and vertical cable (as both data had pre-stack depth migration applied) in the Gulf of Mexico. In that survey, 12 cables (16 hydrophones, spaced 45 m, per cable) on a 1.6 x 1.8 km^2 spacing grid, were used to cover 99 different cable positions in a total area of 14 x 16 km^2. The shot point and shooting line interval were 50 m and 40 m, respectively. The streamer data was acquired with a 2-boat operation, both vessels proceeding along the inline direction with a 6-km distance between them. The authors consider the results for both methods (Figure 6.2.5) are similar, even for complicated small-scale structures.

Another survey is reported from 1989, at water depth of 600 m, offshore Louisiana. A total of 180 shooting lines with a 9-km length, and both shot point and line spacing of 50 m, were acquired. A 12-channel cable was used. The recorded data was transmitted to the shooting boat through digital telemetry. Individual channels monitoring performed real-time quality control. The tilt from the vertical direction was less than five degrees (Krail, 1991, 1993).

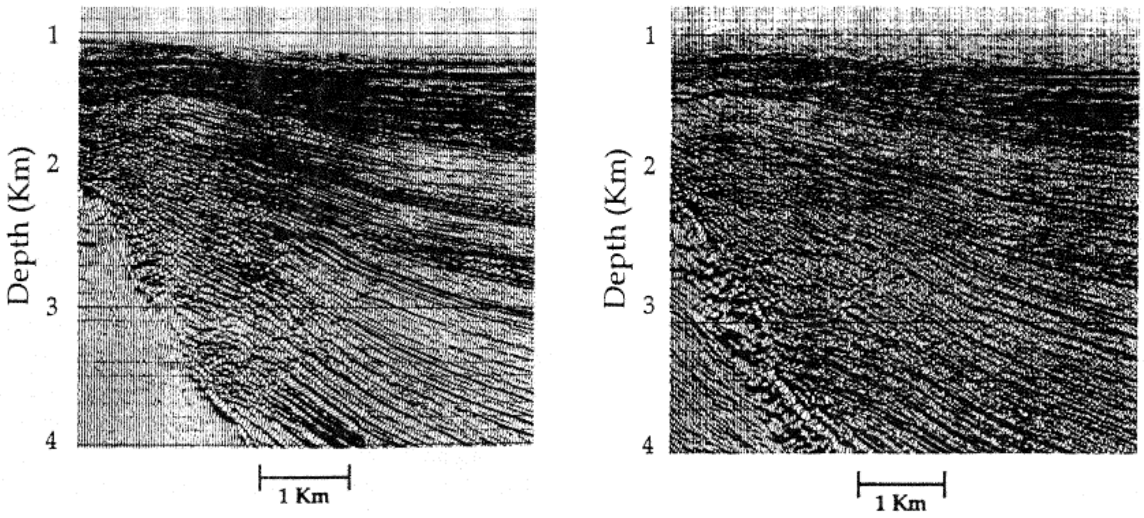

Figure 6.2.5 – Comparison between streamer (left) and vertical cable (right) sections, showing a salt diapir. Both data processed with 3-D pre-stack depth migration *(after Anderson et al., 1997).* The authors conclude the results are similar.

One use of vertical cable outside of the Gulf of Mexico is given by Leach (1997). This case is from Strathspey Field, North Sea (water depth approximately 145 m, or 440 feet). Twelve cables were deployed on a 3 x 4 km^2 grid, each cable holding 16 hydrophones spaced at eight metres. Six swaths were planned, covering 8 x 6.4 km^2 in the subsurface. Storms during the acquisition moved cables and buoys as much as 200 m away from their initial sites. The whole processing cost was around US$ 700,000, compared to an estimation of US$ 8 to 10 million for a conventional (streamer) data set with the same number of traces (60 million). This was the second attempt in the world for a large-scale vertical-cable survey. According to Leach (1997), if four more cables were available, four swaths could be used instead of six, significantly reducing cost.

Krail (1997) reports another survey in Gulf of Mexico deep water, which may be the same reported in Krail (1994b), as the area (80 km^2), water depth (1,200-1,500 m) and number of cables (six) are the same. The distance between cables was 1.6 km, and each cable had 16 hydrophones. Using a shot point interval of 25 m and 400 shot points per line, 40 lines with 40 m spacing were acquired. A receiver domain pre-stack migration was applied – so, 16 pre-stack migrations were done for each cable.

As for the winter of 1997/1998, the recording was done using tape drives inside the buoys. For every shot, a selected trace is sent to the shooting vessel through radio, for quality control purposes (Petzet, 1995; George, 1996).

Guimarães *et al.* (1998) present the results of a physical modelling (1:30,000 geometrical scale factor) data acquired using the vertical-cable technique in a model similar to the Salt Canopy 3-D SEG/EAGE numerical salt model, reported by Sekharan *et al.* (1997). Their main purpose was to verify both the merits and problems of this technique. The scaled acquisition geometry is 1,650-m cable distance, eight cables, eight hydrophones per cable and 100 m hydrophone distance. A brick-type-shooting pattern of 25 x 25 m was obtained after eight swaths were combined. They obtained good results using up-going (direct) and down-going (reflected at water surface) data together.

Moldoveanu *et al.* (1997) presented a comparison, on two small 3-D surveys in the Gulf of Mexico (55 to 60 m water depth), between streamer and vertical hydrophone array with radio telemetry system. The processing flows were the same, except for downgoing attenuation through wavefield separation for the vertical data. The results show stronger water-layer reverberation attenuation, better signal-to-noise ratio, and improved resolution in the vertical hydrophone array than the streamer section.

A major deep-water oil discovery is reported to occur using vertical-cables in an area 150-km Southeast of New Orleans, at 1,000 m water depth (Petzet, 1995; George, 1996). Conventional seismic data showed prospective zones, but apparently they were not large enough. However, with vertical-cable additional objectives were seen. A wildcat well (5,400 m deep) produced oil from a layer 870 m below a tabular salt formation.

In comparison to conventional acquisition, the vertical-cable advantages reported by Krail (1991, 1993, 1994b, 1997), Anderson *et al.* (1997), Leach (1997), and Sekharan *et al.* (1997) are:

- less background noise;
- the acquisition is less susceptible to weather conditions, which is important in places like North Sea, off West Africa and the storm zone of Southeast Asia;
- up- and down-going waves (and correspondent images) may be separated;
- a less rigid and easier-to-reconfigure geometry is possible, which is especially useful when 3-D pre-stack migration is used;
- as several azimuths are sampled, true 3-D imaging is possible (conventional 3-D marine data is obtained through the shooting of several closely spaced 2-D lines);
- no common mid-point assumption is used (this is a major concern in Gulf of Mexico sub-salt imaging), as the data are 3-D pre-stack migrated;
- on small 3-Ds, costs are considerably reduced, as smaller boats can pull the source, eliminating the large distances required for turning a vessel pulling long streamers;
- the coverage is better as the boats can get closer to any obstruction;
- 3-D pre-stack depth migration (done in receiver domain) is much cheaper than on streamer data; and
- for complex geologic structures, a more uniform distribution of reflection points from an interface can be obtained.

A higher resolution, when compared to streamer data, is claimed for this technique (Petzet, 1995; George, 1996; Leach, 1997), but the reason presented for this (less noise at higher frequencies) may not occur in some environments.

A potential advantage over OBC, not mentioned in the literature, is the possibility of acquisition in areas where the sea bottom has oil and/or gas production pipelines over it. They may make the use of ocean bottom cables difficult, or even impossible. A hard sea-bottom, like basalt or reefs (including cold-water carbonates, which may occur in deep to ultra deep water) may also prohibit the use of bottom cables.

Another potential advantage is for 4-D seismic, as a closer to constant receiver positioning and response can be obtained on time-lapse surveys, without the coupling variation concern that may be present for ocean bottom receivers.

As for the beginning of the year 2000, one additional advantage of vertical cables over ocean bottom cables is their ability to work in deep (400 m) to ultra-deep (2,000 m, and beyond) water.

Acquisition costs have a wide variation, according to geographical area, time of the year, water depth and survey size. In 1998, an 80 km^2 3-D deep-water survey offshore Brazil would be 2.5 times the cost of a conventional (streamer) 3-D (Bill Pramik, 1998, personal communication).

VI.3 Survey design: geological model and ray tracing

A straightforward 2.5-D geological model was created using the numerical modelling program GX 3D-VSP^{TM}, from GX Technology. No multiple reflections and down-going reflected energy from the sea surface was considered for the ray tracing. The source was placed at sea level (zero depth).

The model intends to represent an area of passive continental margin. It consists of four layers, including a target (Figure 6.3.1). The shallowest layer is the sea or a weathering (50 m thick) layer. Depths of 50, 500, and 1,000 m were used for the sea-bottom. Below the water (or weathering), there are two layers of Tertiary age, representing sand and shales deposited in a shallow to deep-water environment. They are separated by an unconformity. The target, inside the lower Tertiary layer, has top and bottom slightly curved (thickness varying from zero to 10 m over a 1,000 m horizontal distance, Figure 6.3.2). It petrophysically represents an unconsolidated sandstone turbidite. Only the reflection points from the top of target interface were used for analyses.

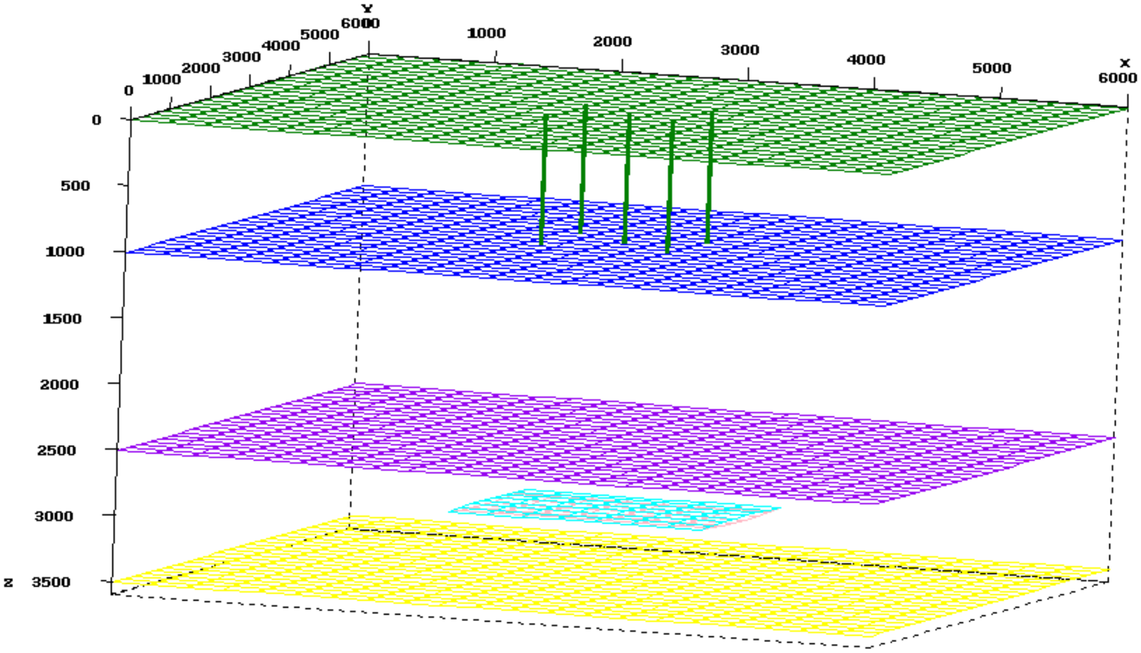

Figure 6.3.1 – 3-D view of the geological model (1,000 m water depth). Target is the fourth interface from top, around 3,000 m. Five cables are also shown. Distances in metres.

In some models, a 6% dip along X direction was applied to all layers (Figure 6.3.2b).

The total area of the model is 6 x 6 km^2, and the target is 2 x 2 km^2. All layers below the water are perfectly elastic. All layers but water, weathering and target have a constant linear increase of velocity with depth. Density values were obtained using Gardner's relationship (except for water, for which a value of 1.05 was used) and shear wave velocities using Poisson's' ratio. Table 6.3.1 presents elastic parameters and thickness for each layer.

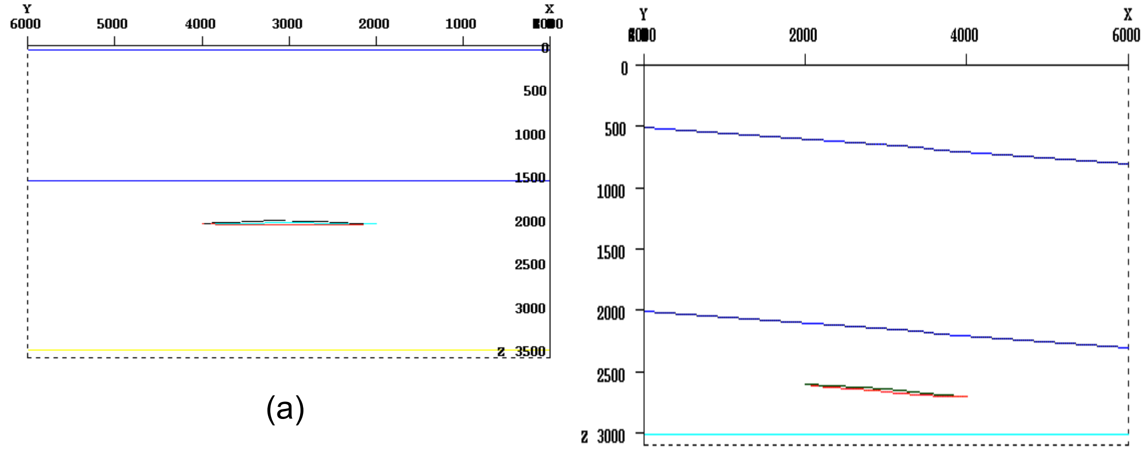

(a)

(b)

Figure 6.3.2 – (a) vertical section along Y-axis showing slight curvature of target (around 3,000 m) for the 50 m water depth model; (b) vertical section along X-axis showing interfaces (including target) dipping around 6% for the 500 m water depth model. Maximum target thickness 20 m. (distances in metres, not to scale).

Layer	$V_P = V_O + aZ$ (m/s)	Poisson Ratio	Thickness (m)
Water/ Weathering	Vp=1500, a=0/ Vp=1500,a=0	0.5/ 0.43	50,500,1000/ 50
Tertiary I	Vo=1600, a=0.5	0.4	1000,1500
Tertiary II	Vo=2350, a=0.4	0.36	1000
Target	Vp=2100, a=0	0.39	0-20 (curved)

Table 6.3.1- Velocity parameters, Poisson's ratio and thickness values for layers in the numerical geological model.

Two shot point configurations were used: 1) 100 m shot point distance (along X axis) and 200 m shooting line spacing (along Y axis, Figure 6.3.3); and 2) 50 m for shot point distance and 100 m shooting line spacing. The later, although more realistic, was in general avoided due to the much longer computer time. As these parameters are underestimated for marine acquisition, one can consider that in real acquisitions, values much greater than the ones obtained here will be obtained for coverage. Both shooting configurations cover 4 x 4 km^2, so there is a 1 km aperture to all sides of the target (Figure 6.3.3).

One cable at the centre of the model (3.0 km X and Y coordinates) was used for most rays tracing. Some examples with two, four, and eight cables were also tested. Figures 6.3.1 and 6.3.3 show the position for a single and four "central" cables. In general, 16 hydrophones per cable were used, as this is close to the number of receivers currently placed in a cable for most vertical-cable surveys.

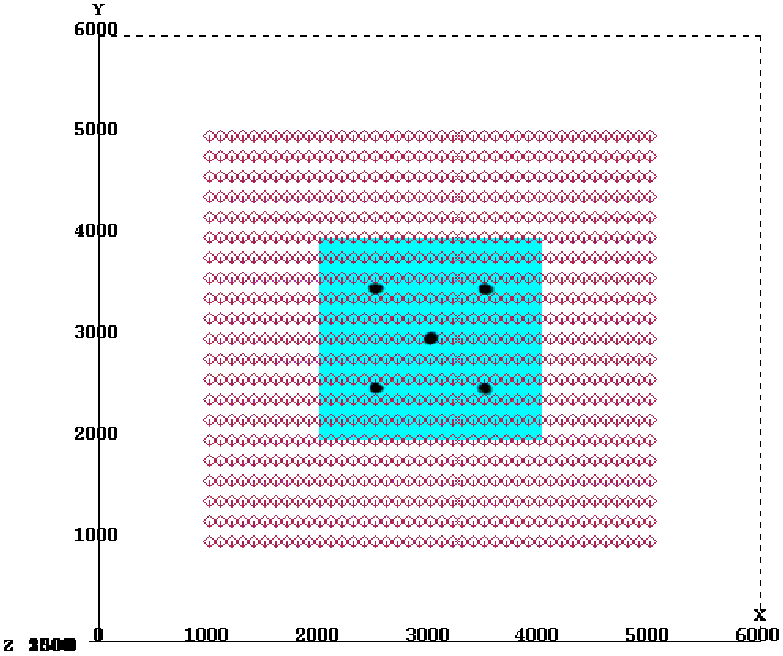

Figure 6.3.3 – Top (map) view of model limits (0 to 6,000), shot point grid (diamonds, from 1,000 to 5,000) and target (grey square, 2,000 to 4,000). Five cables are also shown, indicated by black dots. Distances in metres.

The computer CPU time for the ray tracing varied from 4 to 50 hours, depending on numbers of receivers, cables and shot points, in a Sun Ultra 1/140 MHz workstation.

Pereyra (1988, 1992) presents the ray tracing method used in 3D-VSP^{TM}. It consists of a global (bending) two-point ray tracing technique, which works in complex media. A simple shooting algorithm provides starting rays for the two-point module, which then uses receiver continuation to generate coherent ray families. This quickens the ray tracing process. The representation of many geological unconformities (e.g., normal and reverse faults, pinchouts, and salt domes) is possible with this method.

Figure 6.3.4 shows an example of rays being traced from a single shot and captured in several receivers along a vertical cable.

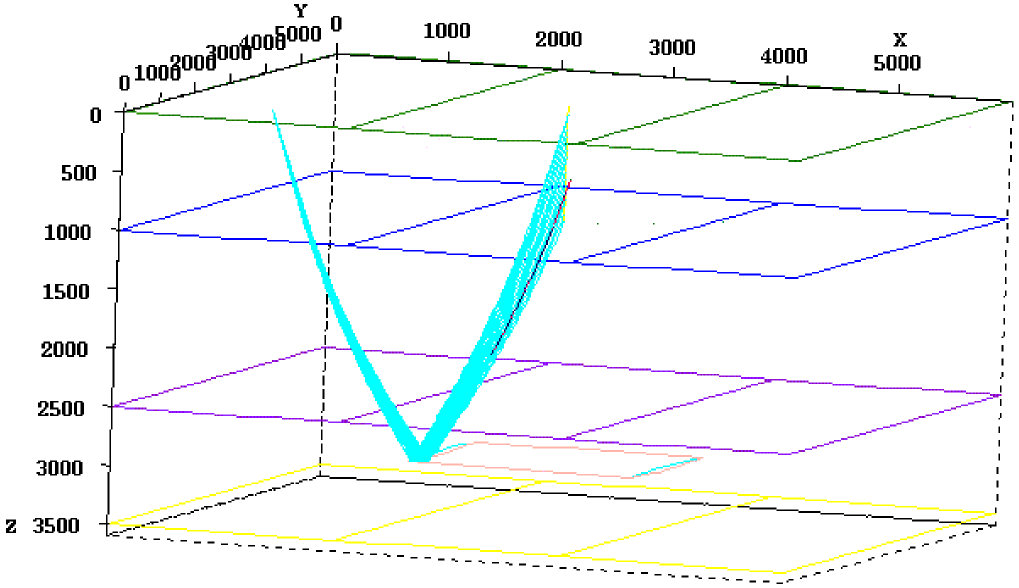

Figure 6.3.4 – Example of source-receivers ray paths. Source at sea-level and receivers along cable at the centre of the model.

The most important ray tracing parameters (GX, 1994, 1997) used in GX 3D-VSP^{TM} were:

- *propagation mode*: P-wave only or P-S conversion at target; in marine cases, for P- to S- conversion, the energy was converted back to P- at the sea bottom, so a PP-SP mode was used (Figure 6.3.5);

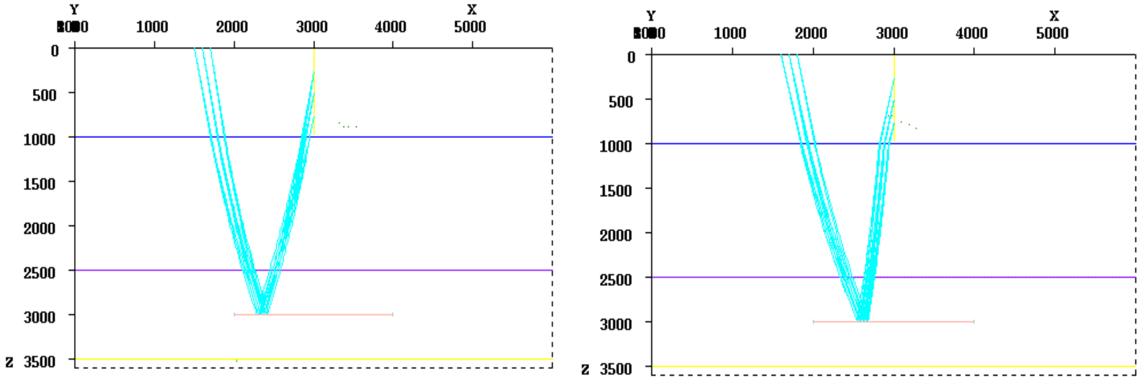

Figure 6.3.5 – Vertical profiles (along X direction) showing source-receiver rays for three shots in the P-P (left) and PP-SP (right) modes. Observe PP-SP images points close to the cable.

- *ray shooting mode*: 2-point continuation. Once a shot-to-receiver path has been found, the other receiver reflections are obtained using receiver continuation; this fastens the ray tracing; and
- *search control*: a value of two was used for primary, inline, and crossline parameters; these parameters – which vary from 1 to 100 – specify the searching density used during ray tracing. The *primary* field controls how dense the search is on the horizon during the first and final passes of ray tracing. It should increase according to the model complexity (GX, 1997). *Inline* (along the longest axis of receiver pattern) and *crossline* (perpendicular to inline) control how searching is performed in the receiver array. The bigger they are, the more precise (and slower) the ray tracing procedure is. Ms. Susan Collins, a technical support geophysicist from GX, recommended the value of two for the geological model used in this study.

The coverage, offset, and azimuth distributions were calculated using a simple Matlab function, presented in Appendix III. Matlab plot function *pcolor* was used to plot fold, azimuth, and offset of the surveys in each specific acquisition geometry.

VI.4 Target imaging: results and comments

Figure 6.3.3 shows a map for the shot-point configuration, used when the shooting line direction is along the X-axis. Most models used this pattern. In all figures, the maximum fold achieved for one case was used as a normalisation value for all other cases, to permit a comparison between different acquisition geometries. A bin size of 100 x 100 m was used in all analyses.

Figure 6.4.1 shows the fold results for the geological model of Figure 6.3.1 when the water depth is 500 m and a single cable at the model centre (3.0 km for X and Y coordinates) is used. Two different situations are analysed: 16 hydrophones (from 30 to 480 m at 30 m interval) and 32 hydrophones (15 to 480 m at 15 m interval), both with a 100 x 200 m shot point (SP) grid (100 m in X direction).

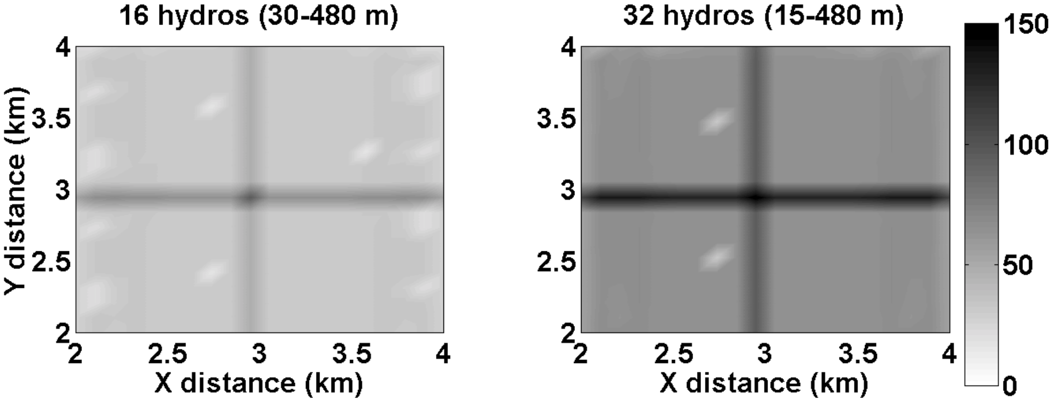

Figure 6.4.1 – Fold for one cable at centre and 500 m water depth: 16 hydrophones spaced 30 m (left) and 32 hydrophones spaced 15 m (right). Shot point grid 100 X 200 m. Observe coverage more than doubles when twice receivers are used.

One can see the fold has a homogeneous and smooth distribution over the target, except close to the cable position (centre of the model). The average value for fold (around 30) can be considered only modest for a marine 3-D. Using twice number of receivers, the average fold more than duplicates (from around 30 to around 80), showing how important the use of shorter hydrophone distance may be.

Another effective way to increase the coverage is halving shot point and shooting line intervals (Figure 6.4.2). Increasing the number of shot by four, the average fold roughly increases by the same amount (from 30 to around 140). Besides a more homogeneous fold distribution, the use of more shot points has two other advantages over the use of more receivers: 1) currently it is unlikely that more than 20 receivers/cable are available to be used, which limits the minimum receiver distance; and, 2) the closest shot point grid used here (50 x 100 m) is still wide compared to conventional shooting values.

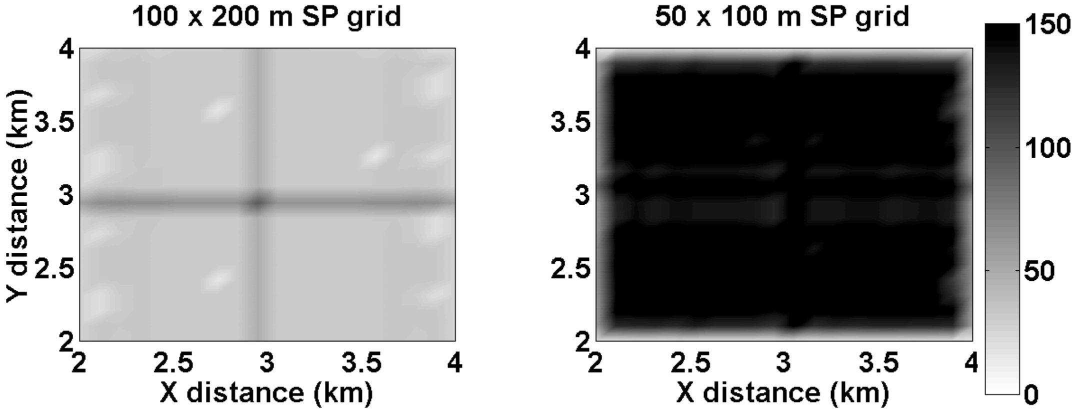

Figure 6.4.2 – Fold for one cable (with 16 hydrophones spaced 30 m) at centre and 500m water depth; shot point grid of 100 x 200 m (left) and 50 x 100 m (right). Smaller shooting grid gives higher and more homogenous coverage.

The fold for converted wave – P- to S- at target and S- to P- at water bottom – is presented in Figure 6.4.3. It can be seen that a high (around 100) and homogenous fold is obtained, but for a smaller area than the P-P image. This result is expected, as most conversion points are located closer to receiver than to source (see Figure 6.3.5). Some ways to overcome this problem may include: 1) the use of longer offsets, but how large this offset increase has to be was not checked here, 2) use of more cables (analysed later in this section), and/or 3) consider downgoing energy reflected from sea surface. The first option, although more expensive, may be necessary due to the difficulties in ghost identification of PP-SP mode in real data.

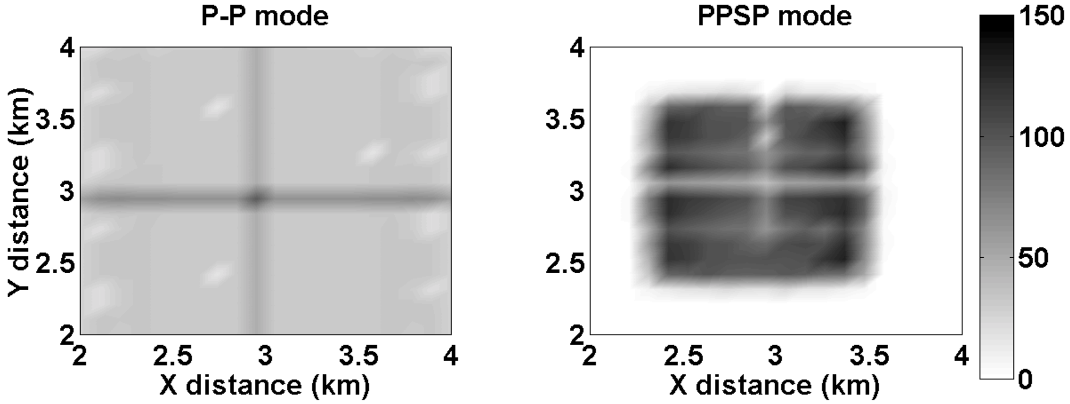

Figure 6.4.3 – Fold for one cable at centre, 500 m water depth, 16 hydrophones spaced 30 m, SP grid 100 X 200 m. At left, P-P mode, at right PP-SP mode. Converted wave gives higher and more homogeneous coverage, but over a smaller area than P-P.

As the target top is slightly curved (10 m depth difference on 1,000 m distance along Y direction, Figure 6.3.2a), when two cables are used in orthogonal alignments, some differences will occur. When two cables (1 km apart) are on the X-axis (coordinates (2.5,3.0) and (3.5,3.0)) of the model, a fair fold (around 80) is obtained for most of the target (left in Figure 6.4.4). However, if the two cables are used along the Y-axis (coordinates (3.0,2.5) and (3.0,3.5)), the average fold has a significant decrease (less than 50, right in Figure 6.4.4).

The conclusion is that when curved interfaces are present, the cables should be aligned in the longitudinal axis of the structure rather than in the transverse.

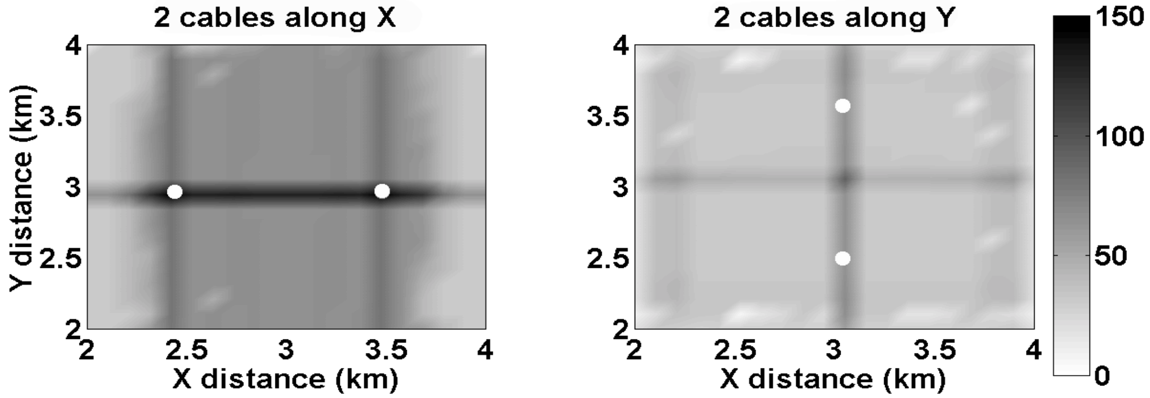

Figure 6.4.4 – Fold for 500 m water depth, 16 hydrophones (spaced 30 m) per cable and 100 x 200 m shot point grid. On the left, two cables parallel to X-axis (constant Y), on the right two cables along Y-axis (constant X). Cable position indicated by white dots. Different results due to slight curvature of top target (Figure 6.3.2a).

The results for four cables are presented in Figure 6.4.5. A realistic number of receivers per cable (16) and a larger than realistic shot point – due to computer time – grid (100 x 200 m) were used. A centred and equally-spaced 4-cables ("central") geometry – cables coordinates (2.5,2.5), (2.5,3.5), (3.5,2.5) and (3.5,3.5) – shows a high (over 120) and relatively homogenous fold over most of the target (left in Figure 6.4.5). The fold decreases on both directions from the centre, this being more rapidly at corners.

When the same number of cables is used in a "corner" configuration – cables positioned on target corner limits, coordinates (2,2), (2,4), (4,2), and (4,4) – the fold both decreases and looses homogeneity in the distribution (middle in Figure 6.4.5).

An additional four-cable geometry was also tested: to place the cables in the middle of target sides (coordinates (3,0), (4,3), (3,4), and (0,3)). Higher fold is obtained than using "corner" configuration (right in Figure 6.4.5), but the fold distribution is much more heterogeneous than in the "central" design.

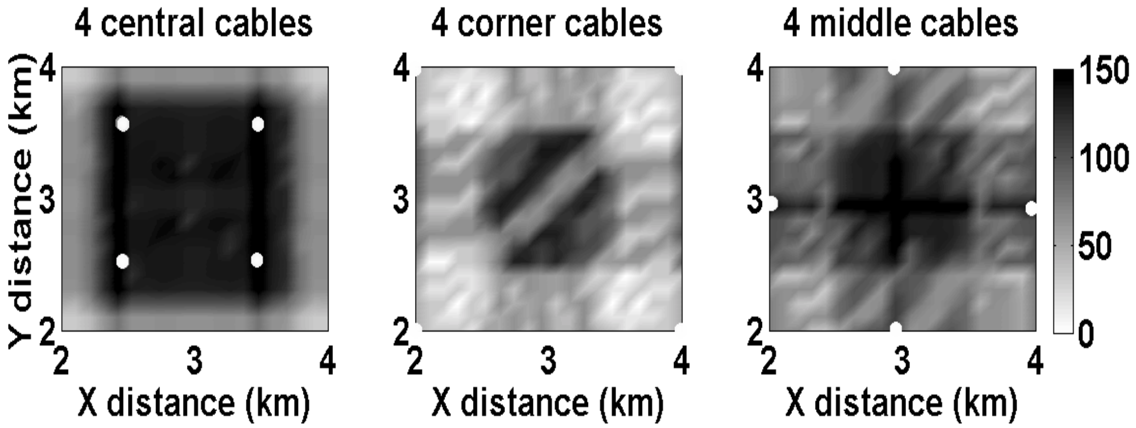

Figure 6.4.5 – Fold for 500 m water depth, 16 hydrophones per cable, 100 x 200 m shot point grid and 4 cables. From left to right: "central", "corner" and "middle" configurations. Cable positions showed by white dots. Higher and more homogeneous distribution is obtained using "central" design.

Therefore, deploying the cables in a "central" configuration is better than a "corner" or "middle" one. It if probably because more shot points contribute for imaging the target for central cables, as in this design the shooting aperture is larger.

For a dipping layer (profile shown in Figure 6.3.2b), besides the expected loss of coverage along the dipping direction, the best shooting direction is also a concern. Figure 6.4.6 shows the results for two orthogonal shooting directions: parallel to dip (left), with 100 x 200 shot point grid, and strike (right), using a 200 x 100 m shooting grid. A slightly more homogeneous and higher fold is obtained for shooting along dip direction. One has to remember that the analysed interface has not only the dip, but also some curvature, which causes some scattering in the reflected energy.

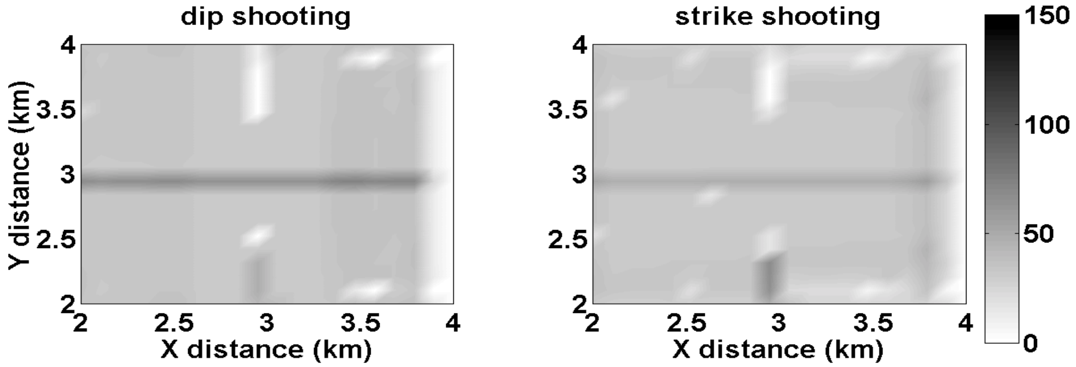

Figure 6.4.6 – Fold for dipping layers (6% dip to the right, see Figure 6.3.2b), water depth 500m, 1 cable at centre, 16 hydrophones spaced 30 m. Shooting along dip (left) and strike (right) directions. Dip direction shooting slightly more homogeneous.

Shooting in the dip or strike direction is not an easy decision to make. A dominant dip direction may not be present, or fault planes may be oriented on opposite direction to main dip. Strike acquisition favours AVO analysis, as correction for dip variations at incidence angles would not be necessary. It is also better for velocity analysis. Dip acquisition has the advantage of giving a better sampling in the direction where it is most important to have it. As a general conclusion in the literature (e.g., Larner and Ng, 1984), neither direction is best for all purposes.

Extending the idea of the previous test, one may ask what happens when the shooting direction is neither along strike or dip. A diagonal shooting grid, with shooting lines parallel to a target diagonal top view, was used for one analysis. The result, shown in Figure 6.4.7, indicates that a strong acquisition footprint will occur for this configuration, so it should be avoided whenever possible.

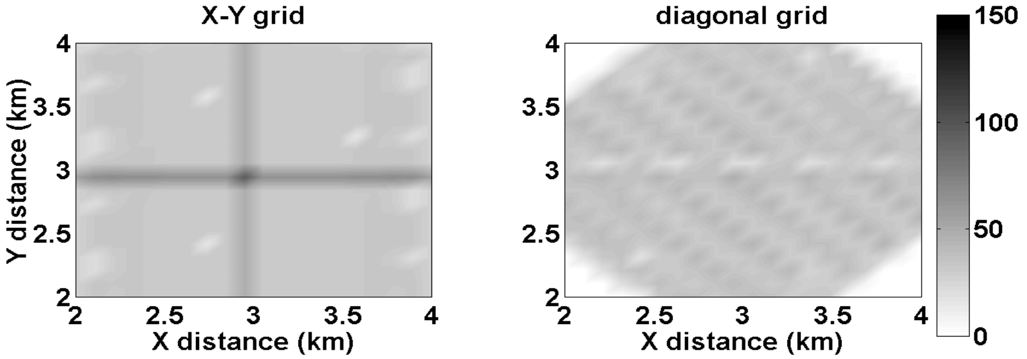

Figure 6.4.7 – Comparison between shot point grid along X-Y direction (left) and grid 45^0 to X- and Y-axis (right). 500 m water depth, one cable, 16 hydrophones 30 m apart, shot point distance 100 m, shooting line distance 200 m. Observe significant footprint for diagonal grid shooting direction.

The behaviour for deeper water (1,000 m) is now considered. Figure 6.4.8 presents results when one cable is used. For 16 hydrophones 60 m apart (from 60 to 960 m depth), only reasonable fold is not obtained (coverage is under 50) over most of the target. The target top curvature causes less coverage to be present towards the centre, along a constant X. Using twice receivers (30 m apart, from 30 to 960 m) increases the fold values roughly by two times, keeping the same imaging distribution.

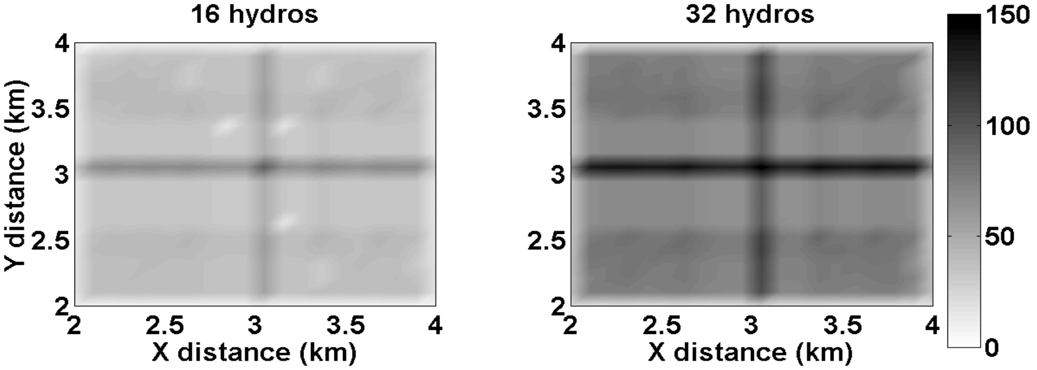

Figure 6.4.8 – Comparison between 16 hydrophones spaced 60 m (left) and 32 receivers spaced 30 m (right) for a single cable at 1,000 m water depth. Shot point grid 100 x 200 m. As for water depth of 500 m, the coverage merely doubles.

If a limited number of receivers per cable are available, one may ask which is the best option: use of a regular receiver distribution, or concentration of most hydrophones in the shallow or deep section of the cable? The first choice (regular receiver distribution) has already been presented (left in Figure 6.4.8). The second (shallower) and third (deeper) cases are shown in Figure 6.4.9.

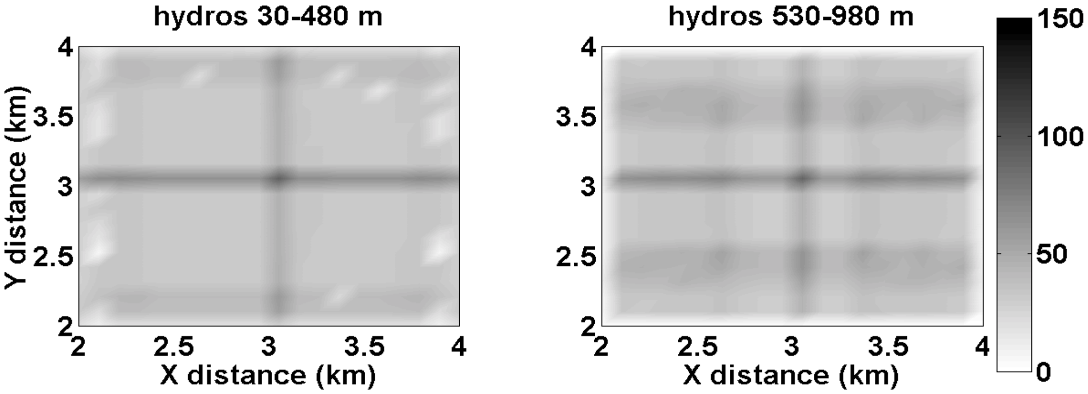

Figure 6.4.9 – Comparison between “shallow” (left) and “deep” (right) receiver array. Water depth 1,000 m, one cable, 16 sensors spaced 30 m, shot point grid 100 x 200 m. See text for discussion.

When the receivers are placed in the shallow part of the cable (30 to 480 m at 30 m apart), a slightly better fold distribution is obtained than if a regular spacing is used along the whole cable (compare with Figure 6.4.8). However, a small decrease in fold values also occurs over some areas.

If the receivers are used in the deeper part (530 to 960 m, 30 m apart), the fold values increase (compared to distribution along the whole cable and distribution in the shallow part). The coverage homogeneity, though, becomes poorer compared to the shallow array (it is similar to a whole-cable distribution). On the other hand, placing the receivers in the deeper environment has the advantage of reducing noise (Bill Pramik, 1999, personal communication).

These results may have an impact with real data when using vertical cable (or 3D-VSP) is acquired, as one may have to decide which will be the most important aspect of the data acquisition: signal-to-noise ratio, fold values, or fold distribution.

As for 500 m water depth, more homogeneous and higher coverage are obtained using a smaller grid size for the shot point geometry (Figure 6.4.10) than increasing the numbers of receivers (Figure 6.4.8). This issue may be even more important for deeper waters, where it can be more difficult to handle a large number of hydrophones in the cable.

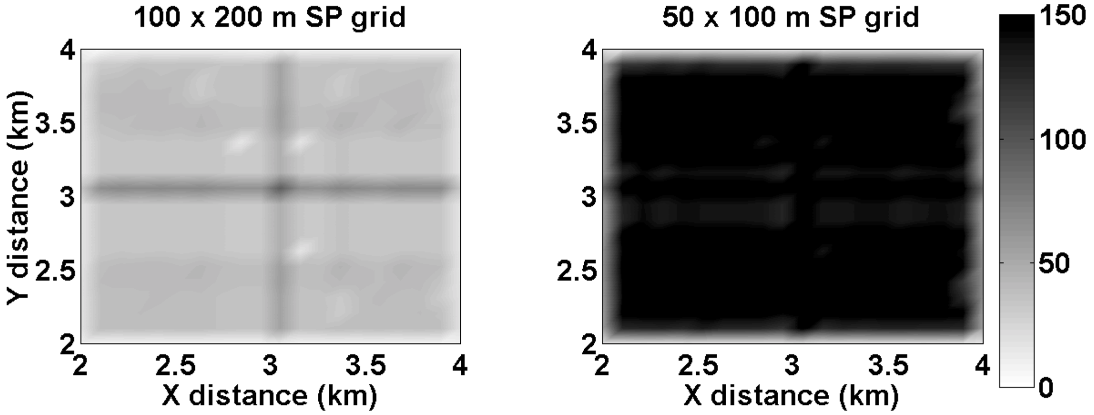

Figure 6.4.10 – Comparison between 100 x 200 m (left) and 50 x 100 m (right) shot point grids. Water depth 1,000 m, one cable, 16 hydrophones spaced 60 m. Much higher and better distributed coverage occurs for a smaller shot point grid.

When four cables are used with the “central” configuration explained before, the result is very good, regarding both fold values and distribution, except for the target corners (Figure 6.4.11). A comparison between 500 m and 1,000 m water depths (Figure 6.4.5) shows that deeper water is favourable for the vertical cable when more than one cable is used in an optimised configuration, as the subsurface sampling obtained is superior.

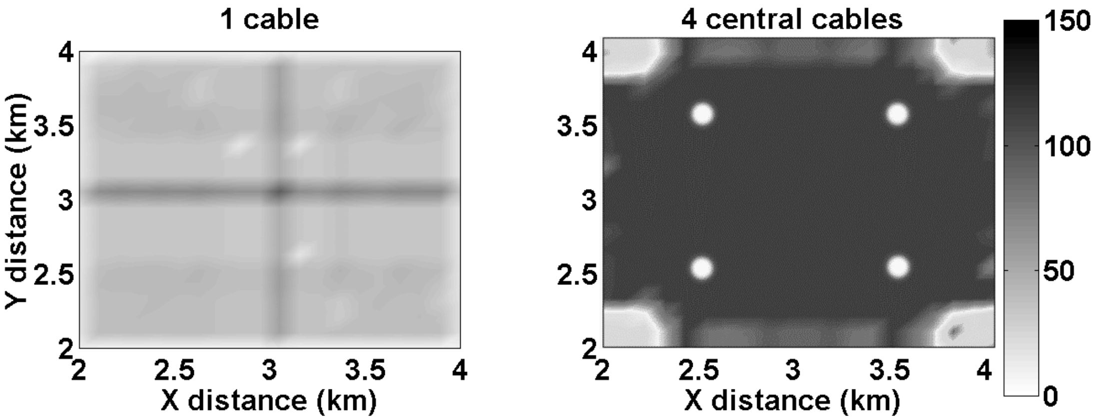

Figure 6.4.11 – Comparison between one single cable (left) and four cables in a "central" configuration (right). Water depth 1,000 m, 16 receivers spaced 60 m, shot point grid 100 x 200 m. The use of four cables presents more improvement here than for the 500 m water depth case (see Figure 6.4.5).

If the target were located 500 m (around 15%) shallower than in previous examples, slightly higher fold values would occur (Figure 6.4.12, compared with Figure 6.4.8), but no significant difference can be observed. The same is true for a target 500 m deeper (Figure 6.4.12, right) than in the examples presented. Therefore, the results obtained here can be extrapolated, to some extent, for target depth variations up to 15 %.

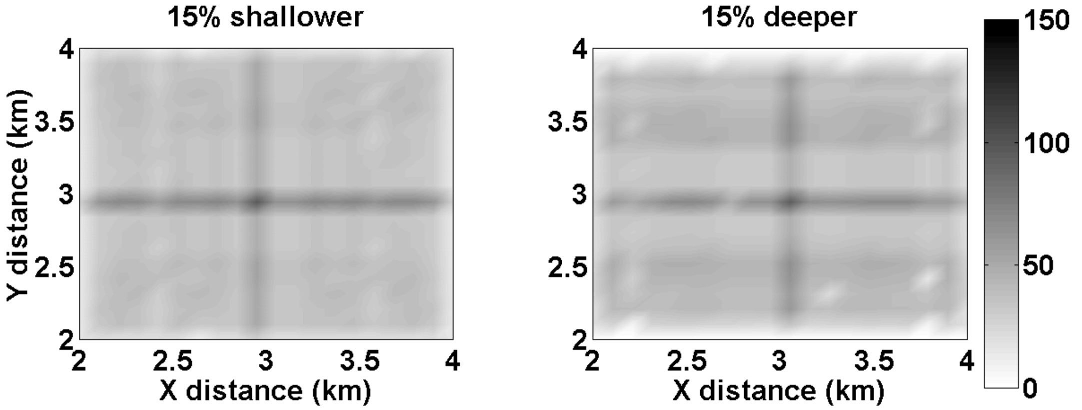

Figure 6.4.12 – Comparison for target shallower (left) and deeper (right) than previous examples. Water depth 1,000 m, one cable, 16 hydrophones 60 m apart, shot point grid 100 x 200 m.

The effect of dipping layers for deeper water was also verified. The result, presented in Figure 6.4.13, shows that, as in the 500 m water depth case, a relatively high dip (for the geological basin model analysed in this work) does not alter significantly the coverage for vertical cable acquisition.

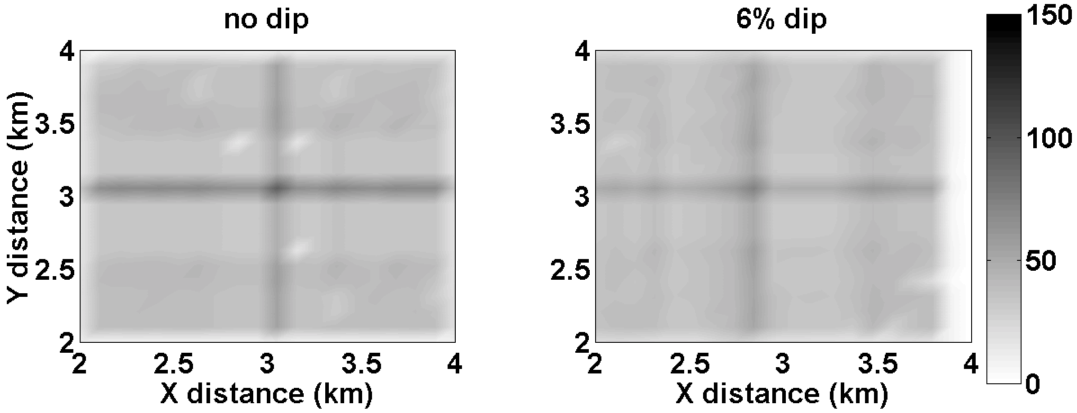

Figure 6.4.13 – Comparison between coverage for no dipping (left) and dipping layer for 1,000 m water depth. One cable, 16 hydrophones spaced 60 m, shot point grid 100 x 200 m. Fold variation in the presence of dip can be considered as minimum.

Converted wave imaging – P- to S- reflection at subsurface interfaces and converted back to a P-wave at the sea bottom – results in a high and well distributed fold, but restricted around the central area (Figure 6.4.14). The response here is close to that one from 500 m water depth model (Figure 6.4.3).

Two ways to improve the sampling were tested: use of more cables and larger shooting aperture. From the results, presented in Figure 6.4.14, one can conclude that the use of more cables gives a higher and more homogeneous fold. However, this option is probably much more expensive, in general, than the use of larger source-receiver offsets.

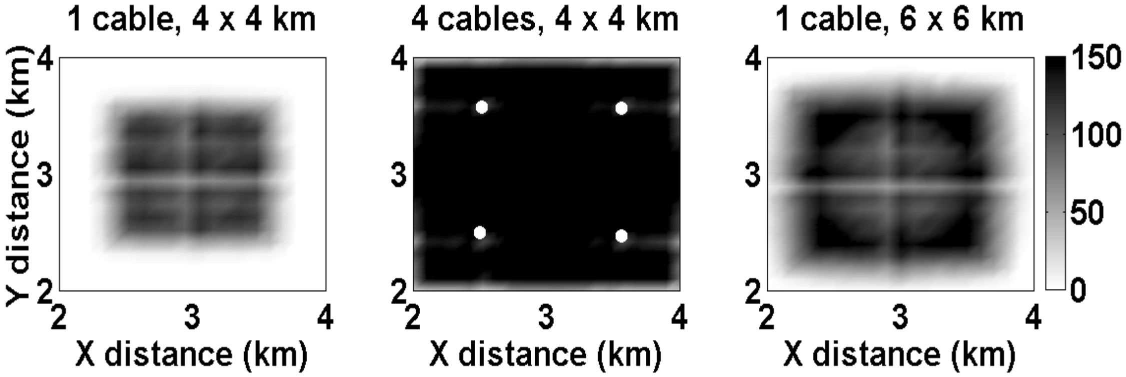

Figure 6.4.14 – Comparison for PP-SP mode among the use of one (left) and four (middle) cables in a 4 x 4 km^2 shooting aperture and one cable in a 6 x 6 km^2 shooting aperture. 1,000 m water depth, 16 receivers per cable 60 m apart, shot point grid 100 x 200 m. Although the use of four cables gives better results, to increase shooting aperture is probably much cheaper.

The fold analysis for shallow water (50 m), comparing with 500 m (Figure 6.4.1) and 1,000 m (Figure 6.4.8), shows that, *when only one cable is used* (left in Figure 6.4.15), the thickness of the water layer is not very important in terms of the target fold. This means the vertical cable technique can also be applied to shallow water, at least in a continental margin passive basin.

However, when more cables are used (Figure 6.4.15, middle), the benefits on fold values and distribution are much smaller than for deeper water (compare with Figures 6.4.5 and 6.4.11). PP-SP mode has the same behaviour of deeper water.

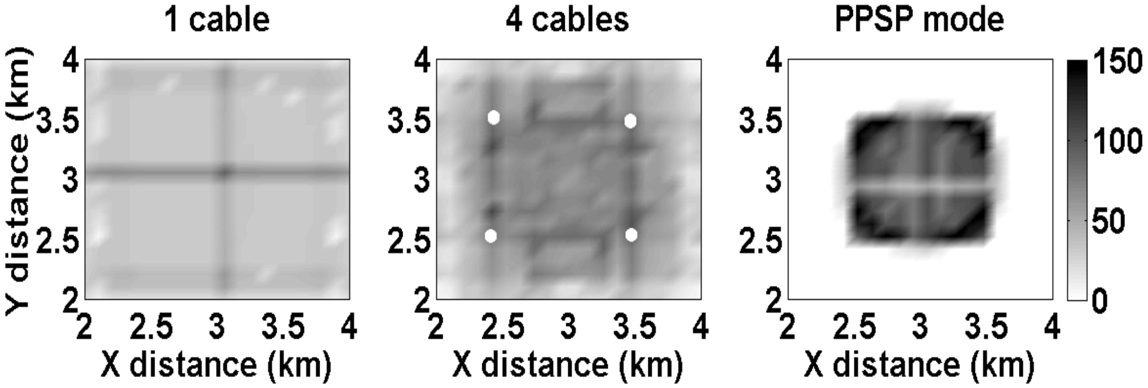

Figure 6.4.15 – Coverage for shallow (50 m) water depth: one cable (left), four central cables (middle) and PP-SP mode (right). All uses 16 hydros/cable and 100 x 200 m shot point grid. See text for discussion.

The final exercise regarding fold was for the land environment. The results show a very homogeneous and reasonable (around 30) fold for a single cable (Figure 6.4.16, left). When more cables (middle in Figure 6.4.16) are used, the coverage increases – although, as for shallow water, the improvements are not as good as for deep-water environments. PP-SP mode experiment (Figure 6.4.16, right) also presents the problem of smaller coverage area.

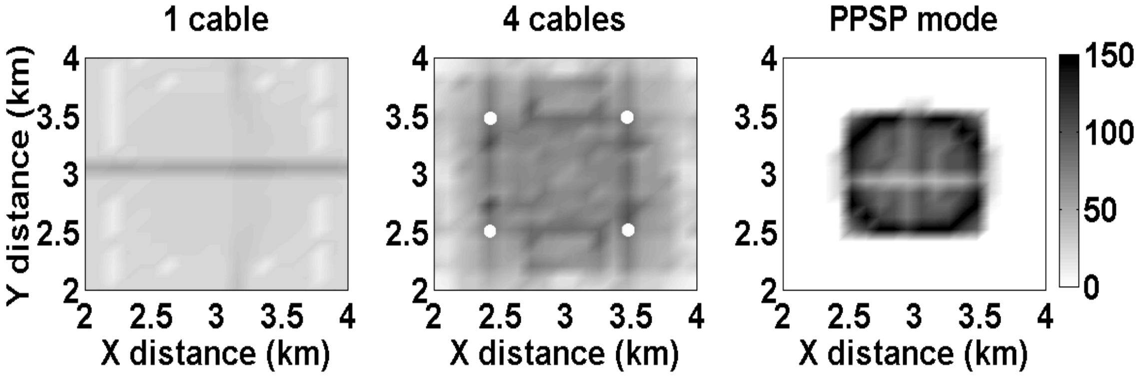

Figure 6.4.16 - Coverage for land (weathering layer 50 m thick): one cable (left), four central cables (middle) and PP-SP mode (right). All uses 16 hydros/cable and 100 x 200 m SP grid.

Analyses of offset and azimuth behaviour, for 500 m water depth, were also done. Offset ranges were defined according to maximum offset: near offset means offset from zero to one-third of the maximum offset, middle from one- to two-thirds and far from two-thirds to maximum offset. Azimuths were grouped in 60^0 interval and the opposite groups added for display.

When a single cable is used, the results are straightforward, as no complex geological structure is present: the offset distribution is close to concentric circles for different ranges (left column in Figure 6.4.17). The same conclusion is true for azimuths: the ranges which contribute to subsurface

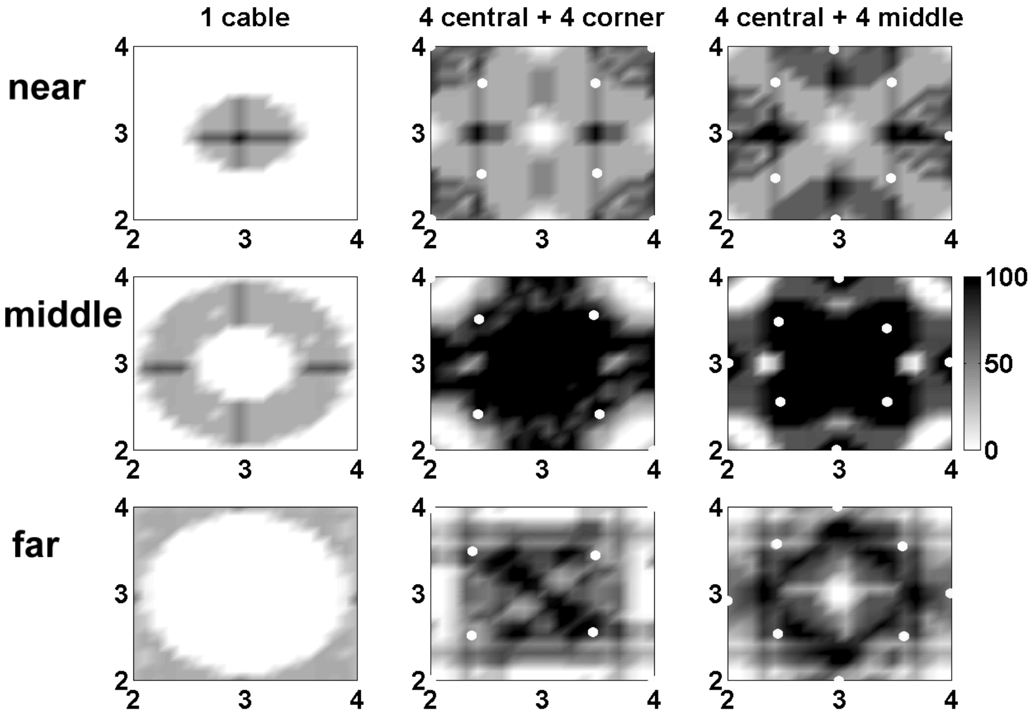

Figure 6.4.17 – Offset distribution: near (upper row), middle (central row) and far (lower row) for one cable (left column), four “central” plus four “corner” cables (middle column) and four “central” plus four “middle” cables (right column). Water depth 500 m, 16 hydrophones per cable, shooting grid 100 x 200 m. Cable position shown by white dots (except for left column, which has one cable at model centre).

sampling are the ranges obtained as if azimuth measures were done for the cable at the centre of a hypothetical circle (left column in Figure 6.4.18).

One can then conclude that a poor offset and azimuth sampling will occur if few cables are used, or if they are very far apart.

When more cables are available, the results for offset and azimuth are determined by just summing the values from each individual cable. The results can have a complex shape, as can be seen in Figures 6.4.17 and 6.4.18 (middle and right columns in both figures) for two different eight-cable configurations.

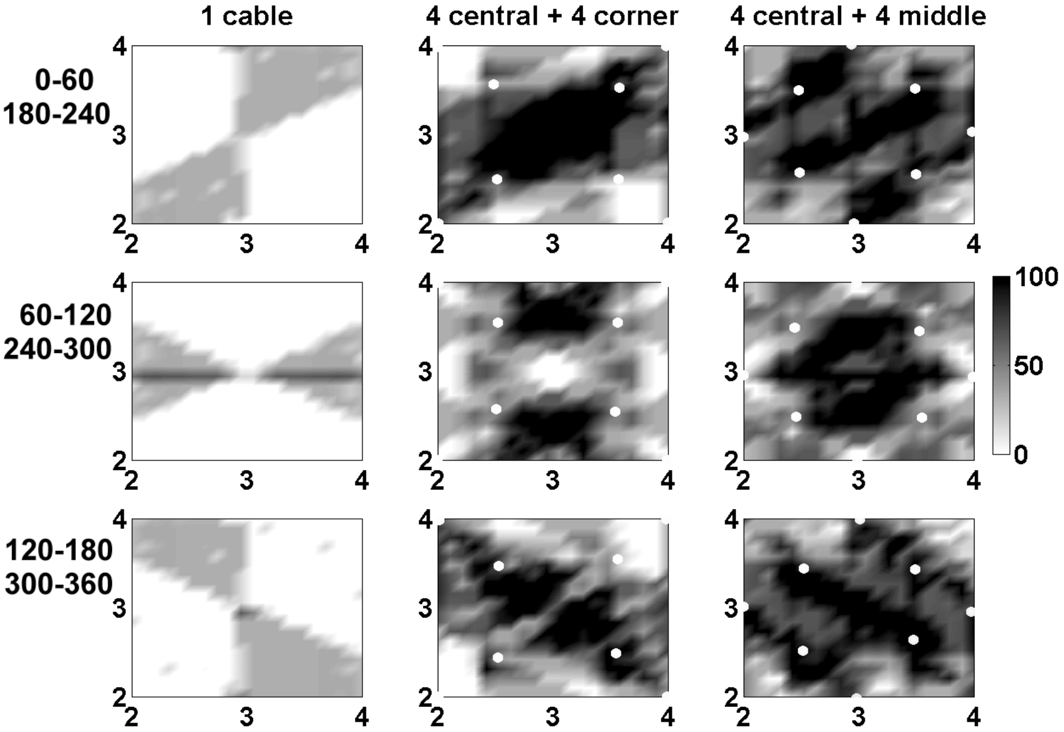

Figure 6.4.18 – Azimuth distribution: 0^0 to 60^0 plus 180^0 to 240^0 (upper row), 60^0 to 120^0 plus 240^0 to 300^0 (central row) and 120^0 to 180^0 plus 300^0 to 360^0 (lower row) for one cable (left column), four “central” plus four “corner” cables (middle column) and four “central” plus four “middle” cables (right column). Water depth 500 m, 16 hydrophones per cable, shooting grid 100 x 200 m. Cable position shown by white dots (except for left column, which has one cable at model centre).

Regarding offset sampling in the specific examples shown here, it is difficult to say if the use of eight cables distributed in a “central” and “corner”

(Figure 6.4.17, middle column) configuration is more desirable than the “central” and “middle” (Figure 6.4.17, right column). Although they are not similar, both have a highly heterogeneous behaviour. One may think the coverage distribution is slightly less heterogeneous in the “central” plus “corner” case.

The azimuth distribution when several cables are used (middle and right columns in Figure 6.4.18) has, also, strong variation. The “central” plus “middle” configuration seems to be slightly better, though.

The main conclusion is offset and azimuth distribution may have a very complex distribution, when several cables are used.

VI.5 Empirical expressions for coverage

From the results of the survey design analyses using numerical modelling data presented in the previous section, some expressions for the coverage were obtained. These equations may be used with some confidence in an area which has a geology similar to the model described here – offshore extensional sedimentary basins. Besides, it is assumed that they may give preliminary indication in survey design for most geological environments.

The expressions were obtained by polynomial fitting (least squares), in *Matlab*, over average data from selected representative bins in several model surveys analysed in the previous section. The model parameters – which are considered to define the ranges under which each equation will be valid – used to obtain this expression are:

- water depth ranging from 50 to 1,000 m;
- slight dips (6%); it included shooting along dip and inline directions;
- up to 15% difference (shallower and deeper) in target depth;
- onshore survey (weathering zone 50 m thick);
- shot point grid 100 x 200 m and bin size 100 x 100 m.

The first expression approximates the relation between coverage with *number of cables* and *hydrophones per cable*.

$$F \approx H + 20 * C, \tag{5.5.1}$$

where F is fold, H is number of hydrophones per cable and C is number of cables.

This expression may be valid only when C is much smaller than H.

The second expression relates fold with the *number of hydrophones per cable*. The model parameters are the same as above, except for the number of cables (set constant to one) and the number of hydrophones per cable.

$$F \approx 2.25 * H \tag{5.5.2}$$

The third expression correlates fold to *shot point and shooting line distance (or shot-point grid)*. It was obtained for a single cable and 16 receivers per cable.

$$F \approx 40 * (100/\Delta x) * (100/\Delta y), \tag{5.5.3}$$

Δx and Δy shot point distance along X and Y axis, respectively.

The next expression is for *water depth*, using a single cable, 16 hydrophones per cable, and a 100 x 200 shot point grid.

$$F \approx 32 + 0.01 * z^2, \tag{5.5.4}$$

z water depth in metres.

One can see water depth is not very important in terms of bin coverage, when a single cable is used. There was not data enough to obtain an expression for more than one cable.

For different receiver depths, an expression could not be obtained, but we found that allocating the receivers deeper could increase the fold up to 30%. Nevertheless, one has also to pay attention for the fold distribution.

VI.6 3-D vertical cable processing using EOM

VI.6.1 Introduction

Equivalent offset migration (EOM) is a Kirchhoff pre-stack migration method developed in CREWES (Bancroft and Geiger, 1994; Bancroft *et al.*, 1998), which uses the concept of common scatter points (CSP).

Bancroft and Xu (1998) have extended the use of 3-D EOM for vertical receiver array processing. The authors processed a 3D-VSP in the Blackfoot area (southern Alberta).

Since then, EOM has been used for vertical receiver arrays in numerical modelling data of increasing complexity (*e.g.* constant velocity, layered and linear increasing velocity media) and size. Bancroft *et al.* (1999), analysing illumination and resolution of scatter points, concluded that to illuminate a structure surface, the vertical cables would require a separation that is less than the depth of interest.

In this section, the use of EOM to process a large volume of 3-D data is presented.

The data was generated using 3-D ray tracing over a geological model obtained from seismic interpretation performed in 3-D seismic data acquired over a Brazilian offshore giant oil field. Velocity variations in three directions were obtained by using the 3-D processing velocities.

It is shown that EOM is capable of handling a very large amount of data, giving a good seismic response in a reasonable amount of computer time. However, the results also show that strong noise - not attenuated by stacking - may be created in the process. This noise is probably associated with uncorrected amplitude effects during Kirchhoff summing.

VI.6.2 Geological model and ray tracing

The geological model used in this section (Figure 6.6.2.1) is based on the 3-D seismic interpretation of a giant deep-water oil field, offshore Brazil. The oil field is located in a continental passive margin basin, developed in the late Mesozoic during the separation of nowadays South America and Africa continents.

Sediment lithologies are mainly of sands and shales deposited in a shallow to deep-water environment, with some associated limestone. The reservoir is a deep water unconsolidated sandstone turbidite.

The model was composed of five layers. They are, from top to bottom, water, Upper Miocene, Lower Miocene, Oligocene, and Cretaceous (Figure 6.6.2.1, Table 6.6.2.1). Four interfaces were considered for seismic data generation: sea bottom, Lower/Upper Miocene boundary, Miocene/Oligocene boundary, and a reservoir target inside the Oligocene layer (Figure 6.6.2.1).

	V_P (m/s)			Density (g/cm^3)		
Layer	Minimum	Mean	Maximum	Minimum	Mean	Maximum
Water	1500	1500	1500	1.05	1.05	1.05
Upper Miocene	1920	1980	2075	2.05	2.08	2.09
Lower Miocene	2420	2550	2775	2.17	2.20	2.25
Oligocene	2855	3055	3500	2.27	2.30	2.38
Cretaceous	3045	3330	3755	2.30	2.35	2.43

Table 6.6.2.1 - P-wave velocities and densities of model layers: minimum, maximum, and average.

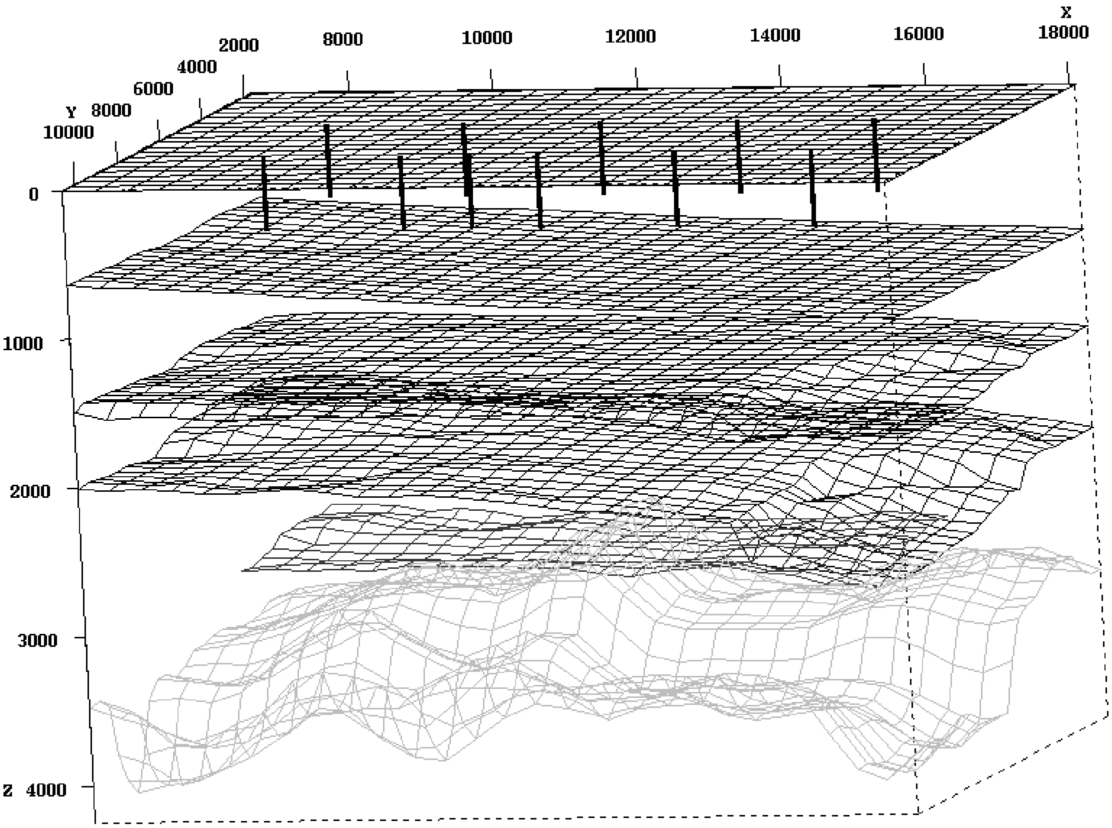

Figure 6.6.2.1 – 3-D view of the geologic model. From top to bottom the interfaces are sea level (model top, at depth zero), sea bottom, Upper/Lower Miocene boundary, Miocene/Oligocene boundary, reservoir (smallest area extent horizon), and Cretaceous (model bottom). Note that the Cretaceous, gently dipping to east (increasing X), is the most structured interface. Cretaceous interface was not considered in seismic data generation. Most vertical cables are also shown. Distance in metres.

Maximum model depth is 4 km. All interfaces but target have area extension of 11.5 km (E-W direction) by 9 km (N-S direction). Target dimensions are approximately 8.5 (E-W) x 4.2 (N-S) km^2 (Figure 6.6.2.2).

Velocity variations in all directions across the model were obtained through conversion of seismic processing velocities to interval velocities using Dix's equation. For each (X,Y) position, the velocity was constant inside each layer. The processing velocity grid was resampled from 500 x 500 m to 1000 x 1000 m, to simplify (and increase the speed of) the ray tracing.

Quality factors (*Q*) varying from 30 (for shallow sediments) to 80 (deepest layer), common in these lithologies, were used in the model. Density values were obtained using Gardner's relationship (except for water, where a constant value of 1.05 was applied). High Poisson's ratios – 0.4 for the sediment below the water, and 0.3 for the deepest layer – were used to obtain shear wave velocities due to the poor consolidation of the sediments.

Ten cables, laid in a grid approximately 2 x 3 km^2, were initially used. The shot point grid had to be relatively large – 100 x 100 m – due to the long ray tracing time. The maximum source-receiver offset was between 6,000 and 8,000 m. Each cable had 16 hydrophones, with a 30 m depth interval, from 30 to 480 m. Figure 6.6.6.2 shows a map view of the model, indicating shot point grid used for two specific cables.

For the ray tracing, the numerical modelling program GX 3D-VSP^{TM}, presented in section 6.3, was used. The algorithm is really 3-D, so reflections out of the source-receiver vertical plane (sagittal plane) are also considered. No multiple reflections or down-going reflected energy from the sea surface were considered for the ray tracing. Only the P-P wave field was recorded. The others ray tracing parameters (*ray shooting mode* and *search control*) have the same values of the previous section.

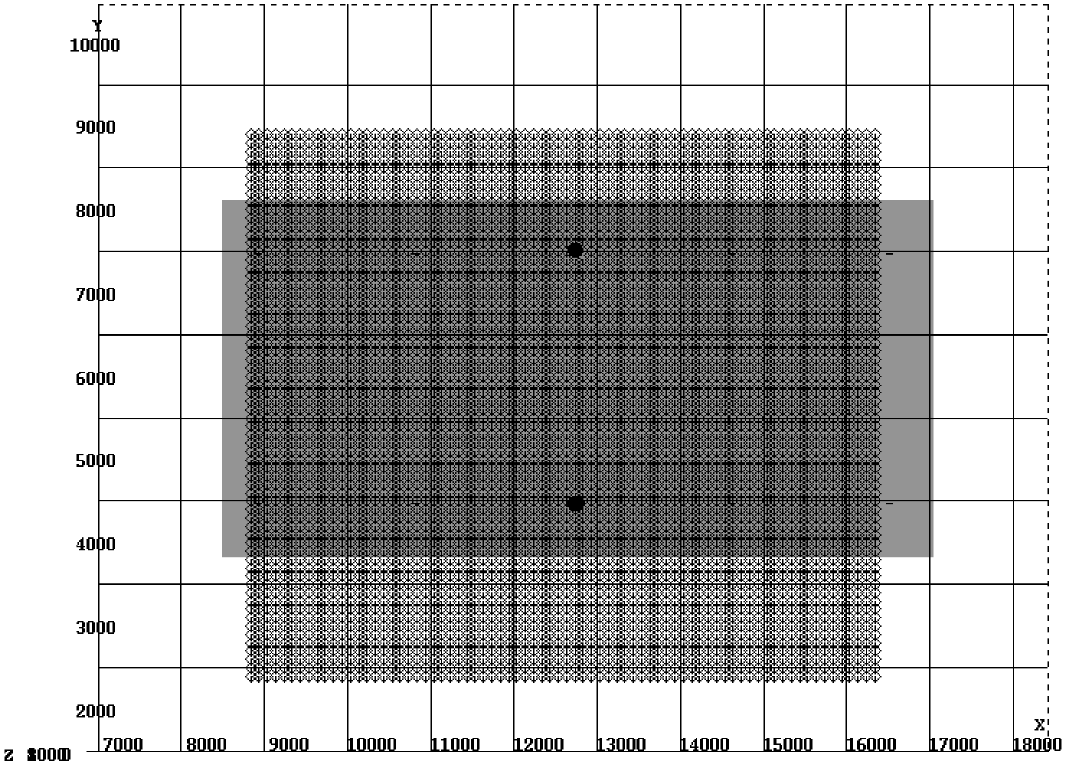

Figure 6.6.2.2 – Map view of the shot point grid (the rectangle from approximately 9000 to 16500 along X and 3000 to 9500 along Y) and reservoir (the rectangle from approximately 8500 to 17000 along X and 4300 to 8500 along Y). This shot point grid was used for the two cables indicated by black circles. Distances in metres.

Ray tracing amplitudes were obtained by Zoeppritz equations, as presented by Young and Braile (1976). The reflection coefficients were convolved with a 30 Hz zero-phase Ricker wavelet.

Using a Sun Ultra 10/400 MHz workstation, the CPU computer time for the ray tracing varied from seven to ten days for each cable. The whole data set had around 50,000 shot points and 800,000 traces.

Figure 6.6.2.3 shows some rays propagating in the model and Figure 6.6.2.4 shows some examples of shot gathers from the numerical modelled seismic data.

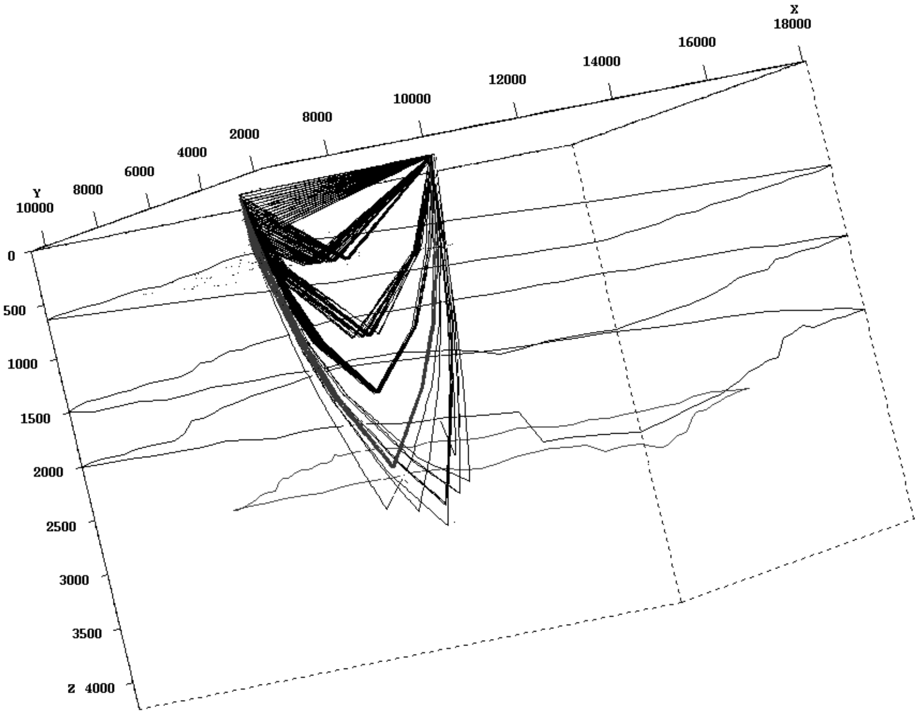

Figure 6.6.2.3 – Rays propagating through the model for one shot point and 16 receivers placed in a cable. The direct wave is also shown.

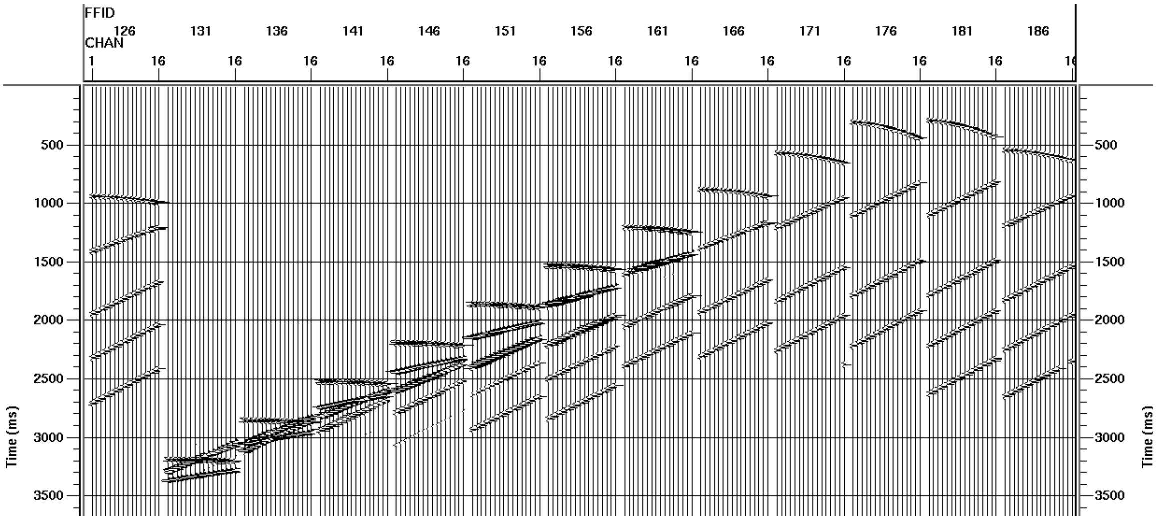

Figure 6.6.2.4 – Numerical model shot gathers. The events (top to bottom) are direct waves and reflections from sea bottom, Upper/Lower Miocene boundary, and Miocene/Oligocene boundary and target reservoir. Reflections from the target reservoir are not captured in all shot gathers.

VI.6.3 Data processing: results and comments

The Seismic Unix (SU) suite of algorithms was used in all stages of the data processing, except for velocity analysis and some displays (done using ProMAX), and the EOM, coded in C and Fortran by John Bancroft and Yong Xu.

A preliminary velocity function, obtained from averaging the model interval velocity values (Table 6.6.2.1), was used to obtain initial values for the pre-stack migration. After the migration, velocity analysis was done by semblance using ProMAX. The velocity functions from the second analysis were used for stacking, to give the final processing result. Stacking velocities are 2-D velocities, extracted from the velocity cube along the desired seismic line direction.

Necessary static corrections due to receiver depth (Bancroft and Xu, 1998) are easier to perform on marine than land data, as the velocity can be obtained with accuracy and considered as constant. The practical problem of determining exact receiver depth and position determination remains, though this is not the case for numerical model data.

Although SU is a 2-D package, EOM runs in a 3-D mode. This means that to obtain the final amplitude of a single sample *all* available data is used. Output from EOM can be a single 2-D line, in any desired direction, or a group of several parallel 2-D lines, with any distance desired between them.

The most important parameters to be defined by the user are the bin spacing in common scatter point (CSP) gathers and the number of bins in each gather (Bancroft and Xu, 1998). Bin spacing usually equals half the shot point distance. The number of bins per gather determines the maximum aperture, so that the larger the number, the more precise the method becomes, although at the expense of more computer time. A value equal to the maximum depth of interest is often a good guess.

Figure 6.6.3.1 shows some CSP gathers after EOM. We can see reflections with close to hyperbolic behaviour and, around them, some diffuse energy. After NMO correction and stacking, most of this diffuse energy – but not all – will vanish. The presence of this energy in CSP gathers may be due to 1) poor velocity analysis, and/or 2) bad processing parameter choice, and/or 3) indicates that the method needs some additional refinements.

The EOM algorithm used here was designed to verify the kinematics. Improved amplitude scaling of the CSP gathers and tapering of the NMO correction may help to reduce the noise (John Bancroft, 1999, personal communication).

One can see that in the CSPs (Figure 6.6.3.1) the direct wave has almost completely vanished. This is probably caused by the very poor energy alignment in this event, as the velocity used is for two-way travel times.

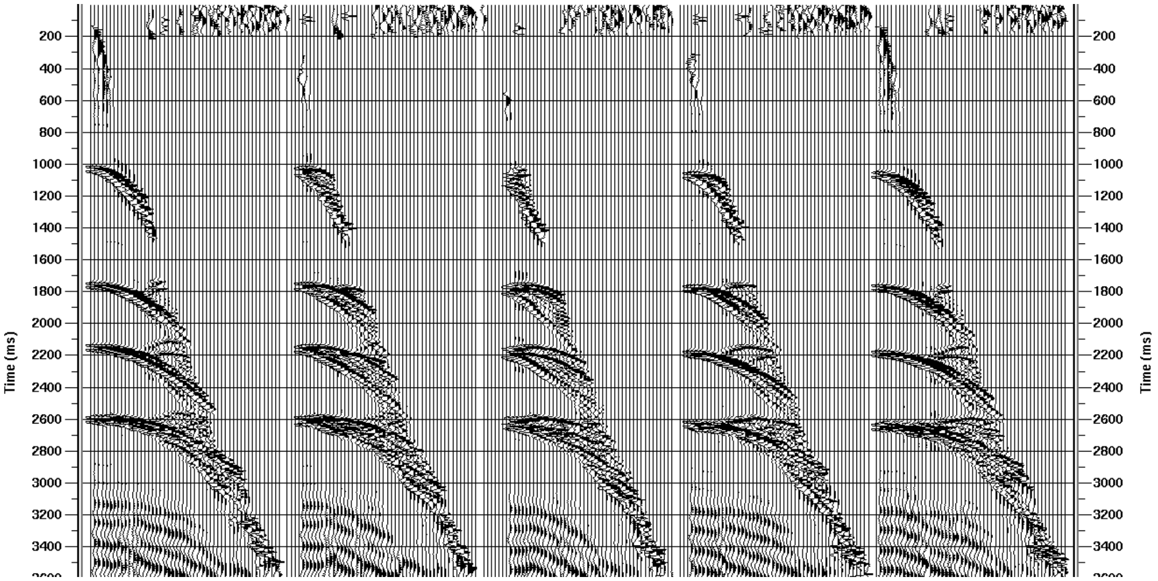

Figure 6.6.3.1 – Common scatter point (CSP) gathers after EOM, without NMO correction. Events from top to bottom are reflections from sea bottom, Upper/Lower Miocene boundary, Miocene/Oligocene boundary and reservoir target. After NMO correction and stack, most (but not all) diffuse energy around hyperbolic reflections will vanish. Observe direct wave has vanished. Noise above 200 ms and below 3400 ms is due to display gain.

The remaining diffuse energy, not attenuated during NMO and stack, appears in the final stacked section as strong amplitude noise, as shown in

Figure 6.6.3.2.

A poor image in the deepest event (reservoir target) in Figure 6.6.3.2 may be caused by poor stacking velocities and/or the amplitude-scaling problem mentioned above.

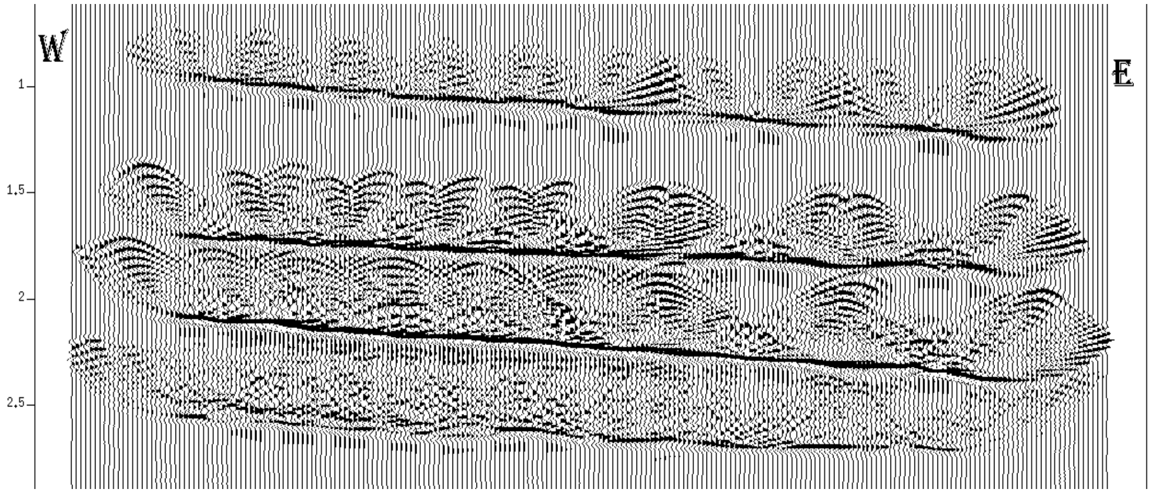

Figure 6.6.3.2 – Stacked section after EOM. Noise is caused by diffuse energy generated during EOM that was not attenuated with NMO correction and stack.

Figure 6.6.3.3 presents a general flow for vertical cable processing using EOM.

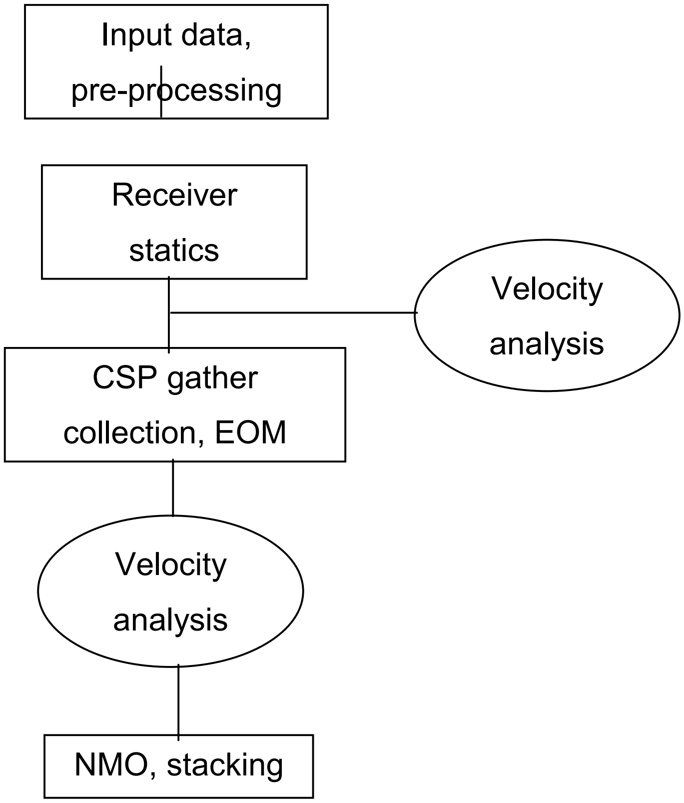

Figure 6.6.3.3 – Vertical cable processing flow using EOM. The receiver statics correction step may be difficult and time consuming for real data.

VI.7 Discussion

This chapter discussed the design of seismic surveys, using vertical cables, which can best image the target geology in the most economic way. Thus, one is interested in questions of source and receiver distribution and the resultant target coverage.

Analysis of coverage (fold) for regular grids of cells (bins) in vertical-cable acquisition was done for a straightforward, 2.5-D synthetic case. The model describes a passive continental margin environment in a Mesozoic basin. Acquisition geometries with different numbers of vertical cables, hydrophones per cable, numbers of shot points, and water depths were analysed. Three-dimensional ray tracing was used to obtain the reflection point from a target layer.

It has been shown that survey design is a crucial and critical aspect in vertical cable seismic acquisition.

Using a single cable, good fold and lateral coverage can be obtained with a reasonable number of receivers per cable and modest shot point spacing. In addition, in a single-cable configuration, the fold behaviour is independent of the water depth. However, poor offset and azimuth distributions per bin occur.

When several cables are used, offset and azimuth distribution can be significantly improved by optimised cable positioning. Different water depths give distinct imaging when several cables are used in an optimised configuration.

If converted waves (PP-SP mode) are to be acquired, high fold is obtained close to cable position, but larger source-receiver offsets and/or more cables are necessary for a given target area. Use of down going energy, although theoretically possible, may be too complicated in real data.

When moderate dips (up to 6%) are present, the imaging is not strongly affected. A better shooting direction (dip or strike) is not clearly defined, even in the presence of dips – however, shooting should be aligned to either layers dip or strike. For several cables and curved interfaces, cable alignment should be done along structure longitudinal axis.

Concentrating receivers in cable’s deeper section may give higher fold than either regular receiver distribution along the whole cable or placing them in the shallow part of the cable. Another advantage is the lower ambient noise. However, the fold distribution is not as good.

It was found that the conclusions obtained in this work could be extrapolated for target depth variations of 15 %.

Suggestions for future work regarding 3-D vertical cable survey design are comparison with streamer and OBC acquisition and take into account downgoing energy (especially for converted wave analysis).

An option that may be interesting, although not analysed in this thesis, is the use of a hexagonal pattern for sources and receivers. For a function which has wavenumber spectrum limited by a circle, a hexagonal pattern can be done using fewer samples than a rectangular one (Petersen and Middleton, 1962). For example, Bardan (1996) reports a reduction of 13.4% in the source sampling. Mersereau (1979) claims that more efficient signal processing operators can be designed for hexagonal grids. Even if it may be interesting from the theoretical point of view, the use of hexagonal patterns is not used in marine seismic acquisition – the only exception to my knowledge the work by Bardan (1996).

General expressions relating coverage with seismic acquisition parameters and water depth were empirically derived using coverage results on a target, obtained from ray tracing. It is believed that these expressions may work as a preliminary indication for vertical cable survey design.

Preliminary processing was applied, using EOM, in data generated by numerical modelling (3-D ray tracing) over a geological model obtained from seismic interpretation performed in seismic data acquired over a Brazilian offshore oil field. The processing results show EOM is capable of handling a large data set (800,000 traces), but some noise, probably associated with miscorrected amplitude effects during Kirchhoff summations, remains to be attenuated.

Chapter VII – Conclusions

An overview of the ocean bottom and vertical cable techniques has been presented.

Elastic parameters for shallow marine sediments were obtained from literature information and geotechnical data from offshore Brazil. A second-order equation for V_S as a function of depth in marine sediments was derived empirically from zero to 140 m below the sea floor. This equation is similar to that of Hamilton (1976,1979), but improves the very shallow velocity prediction.

Analyses of transmission and reflection coefficients for compressional- and shear-wave energy mode conversion were performed for the sea bottom and a subsurface reflector (a typical hydrocarbon reservoir top of Tertiary age). I find that most S-wave reflection data recorded on the ocean floor by OBC surveys is expected to be up-coming S energy converted from a P wave at an interface at depth and not from downgoing P-to-S conversion at the ocean floor reflected back from depth as an S wave. It was also concluded that, using elastic assumptions, mode conversion (P- to S- and S- to P-) of the up-going energy is negligible in the shallow (above 160 m) sediments, and not very strong on the sea-floor.

A real data example is presented on using converted-waves, recorded by an OBC, to solve an imaging problem in a giant offshore oil field in the North Sea. Conventional P-P data fails to produce interpretable seismic data due to the presence of gas in the sediments lying over the reservoir (a Cretaceous chalk). Continuous reflections were obtained for the reservoir using the radial component data under a variety of P-S processing assumptions.

Also presented was the processing of a 4C-3D OBC data set, from the Gulf of Mexico. Good separation between the radial and transverse components was achieved during reorientation. Source and receiver statics could be satisfactorily solved, inclusive of the radial component. Conventional and CREWES specific flows were applied to the data. The best data quality appears to be present on the hydrophone (giving a P-P section), followed by data from the vertical component (P-P section) and then the radial channel (P-S sections).

Among the three methods used for cable deployment (trenched, sandbagged, and lain on the seafloor), no option was found to be significantly better. In analysis of the seismic sections, the trenched results give slightly better results for the hydrophone and sandbagged receivers for the radial component. Regarding frequency content, the taped installation is not as good as the other two for the hydrophone (although differences are not very significant); for the radial component, the trenched receivers may provide slightly better records than the other two methods. The sandbagged data shows energy decrease in the signal band.

Depth variant and anisotropic (VTI) stacks did not work well in the radial component, probably due to a poor estimation of V_P/V_S values.

Little compressional wave energy was found in the radial component records, but the vertical component is contaminated with converted-wave energy. This is perhaps related to the receiver response. An acquisition footprint, caused by shooting line direction, is present in the data.

The last chapter discussed the design of seismic surveys acquired with receivers in vertical arrays. Using a single vertical cable, good fold and lateral coverage can be obtained. However, poor offset and azimuth distribution per bin occurs. When more cables are used, offset and azimuth distribution can be improved.

Concentrating receivers in cable deeper section may give higher fold than either regular receiver distribution along the whole cable or placing them in the shallow part of the cable. Another advantage is the lower ambient noise. However, the fold distribution is not as good. It was found that the conclusions obtained in this work could be extrapolated for target depth variations of 15 %.

General expressions relating coverage with seismic acquisition parameters and water depth were empirically derived. These expressions may work as a preliminary indication for vertical cable survey design acquisition parameters.

Preliminary processing results show that the EOM imaging method is capable of handling a large vertical-cable data set, but some noise, probably associated with miscorrected amplitude effects during Kirchhoff summations, remains to be attenuated.

References

Amundsen, L., Arntsen, B., Kristensend, A., Rogno, H. and Sollid, A, 1999, Multicomponent seabed seismic data: a tool for improved imaging and lithology fluid prediction: *Offshore Technology Conference 1999*, paper OTC 10939.

Anderson, J., Sukup, D., Boyd, S., Noponen, I., Cai W. and Delome, H., 1997, 3D vertical cable processing to obtain a prestack depth migrated image: *59th EAGE Conference and Technical Exhibition*, paper A054.

Anno, P.D., 1986, Two critical aspects of shear-wave analysis: statics solution and reflection correlations: *Shear-wave Exploration*, ed. S.H. Danbom and S.N. Domenico, Geophysical Development Series volume 1, SEG.

Arntsen, B., Sollid, A. and Hilde, E., 1999, Imaging trough gas-filled sediments using marine shear-wave data: *Geophysics*, **64**(3): 668-677.

Ayres A. and Theilen F., 1999, Relationship between P- and S-wave velocities and geological properties of near-surface sediments of the continental slope of the Barents Sea: *Geophysical Prospecting*, **47**:431-441.

Baker Hughes/Western Geophysical, 1999, Energy Research Clearing House, Teal South Phase II 4D/4C, Eugene Island Block 354, Gulf of Mexico, South Louisiana, USA, Spring 1999, Job Number 060-99-001, Final Report.

Baldwin, K.C., de Alba, P.A. and Jones, A.N., 1991, Relationship between acoustic and mechanical properties of two marine clays: *Shear Waves in Marine Sediments*, eds. J.M. Hovem *et al.*, pages 95-102. Kluwer Academic Publishers.

Bale, R., Farmer, P., Hansen, J.O., Nichols D. and Palacharla, G., 1998, Prestack Depth Migration of Converted Wave in Anisotropic Media: *68th Annual Meeting SEG Expanded Abstracts*, paper SP 2.2., pages 1108-1111.

Bancroft, J.C. and Geiger, H.D., 1994, Common reflection point gathers [for pre-stack migration]: *64th Annual Meeting SEG Expanded Abstracts*, pages 672-675.

Bancroft, J. C., Geiger, H. D., and Margrave, G. F., 1998, The equivalent offset method of prestack time migration: *Geophysics*, **63**(6): 2042-2053.

Bancroft, J.C. and Xu, Y., 1998, Equivalent offset migration for vertical receiver arrays: *CREWES Project Research Report*, volume 10, chapter 11.

Bancroft, J.C., Xu, Y. and Rodriguez-Suarez, C., 1999, Resolution of seismic data acquired with vertical receiver arrays: *CREWES Project Research Report*, volume 11, chapter 18.

Bardan, V., 1996, a hexagonal sampling grid for 3D recording and processing of 3D seismic data: *58th EAGE Conference Extended Abstracts*, paper P061.

Barr, F.J. and Sanders, J.I., 1989, Attenuation of water-column reverberations using pressure and velocity detectors in a water-bottom cable: *59th Annual Meeting SEG Expanded Abstracts*, paper SA 2.6, page 653.

Barr, F.J., Paffenholtz, J. and Rabson, W., 1996, The dual-sensor ocean bottom cable method – attributes, North Sea tests and recent advances: *58th EAGE Conference Extended Abstracts*, paper B018.

Beasley, C.J., Chambers, R., Workman, R., Craft, K. and Meister, L., 1999, Repeatability of 3-D ocean bottom cable seismic surveys: *Sixth International Congress of the Brazilian Geophysical Society*, paper SBGf405.

Berg, E., Svenning, B. and Martin, J., 1994a, SUMIC – a new strategic tool for exploration and reservoir mapping: *56th EAGE Conference Expanded Abstracts*, paper G055.

Berg, E., Svenning, B. and Martin, J., 1994b, SUMIC: multicomponent sea-bottom seismic surveying in the North Sea – data interpretation and applications: *64th Annual Meeting SEG Expanded Abstracts*, paper IM 1.6, p. 477-480.

Berg, E.W., Amundsen, L., Morten, A. and Mjelde, R., 1996, Fluid imaging using densely spaced OBS-data from the Voring basin: *58th Mtg. EAEG, Extended Abstracts*, Session B027.

Berteussen, K., Fromyr, E., Rokkan, A, Langhammer, J. and Strand, C., 1997, Acquisition of multi-component data by 'Dragged array': *59th Mtg. EAEG Extended Abstracts*, paper B021.

Biot, M.A., 1956a, Theory of propagation of elastic waves in fluid-saturated porous solid, I: Low-frequency range: *Journal of Acoustic Society of America* **28**:168-178.

Biot, M.A., 1956b, Theory of propagation of elastic waves in fluid-saturated porous solid, II: High-frequency range: *Journal of Acoustic Society of America* **28**:179-191.

Bole, J., Zinn, N. and Stupel, M., 1999, Seismic detector positioning in a 4D/4C OBC survey using both acoustic and first breaks: *First Break*, **16**(9): 305-309.

Breeding, S.K., Dunn, D.A. and Orsi, T.H., 1991, Shear wave velocities of glacio-marine sediments: Barrents Sea*: Shear Waves in Marine Sediments*, eds. J.M.

Hovem *et al.*, pages 149-156. Kluwer Academic Publishers.

Briggs, K.B., 1991, Comparison of measured compressional and shear wave velocity values with predictions from Biot theory: *Shear Waves in Marine Sediments*, pages 121-130. Kluwer Academic Publishers.

Brink, M., Granger, P.Y., Manin, M. and Spitz, S., 1996, Seismic methodologies for a 3 components sea floor geophone experiment on a potential flat spot in the Voring Basin: *58th EAGE Conference Extended Abstracts*, paper B020.

Brown, R.J. and Yan, Y., 1999, Suppression of water-column multiples in multicomponent seafloor data: Preliminary results and proposal: *CREWES Research Report*, volume 11, chapter 25.

Bryan G.M. and Stoll R.D., 1988, The dynamic shear modulus of marine sediments: *J. Acoustical Society America*, **83**: 2159-2164.

Brzostowski, M., Zhu, X., Altan, S., Thomsen, L., Barkved, O. and Rosland, B., 1999, 3-D Converted-Wave Processing Over the Valhall Field: *69th Annual Meeting SEG Expanded Abstracts*, paper SAVO/MC 1.3.

Caldwell, J., 1999, Marine multicomponent seismic-acquisition technologies: *Offshore Technology Conference 1999*, paper OTC 10981.

Caldwell, J., Christie, P., Engelmark, F., McHugo, S., Ozdemir, H., Kristiansen, P. and MacLeod, M., 1999, Shear Waves Shine Brightly: *Oilfield Review,* **11**(1): 2-15.

Castagna, J.P., Batzle, M.L. and Eastwood, R.L., 1985, Relationships between compressional-wave and shear-wave velocities in clastic silicate rocks:

Geophysics, **50** (4): 571-581.

Danbom, S.H. and Domenico, S.N., 1986, *Shear-wave Exploration*, Geophysical Development Series volume 1, SEG.

D'Angelo, R.M., Brandal, M.K. and Rorvik, K.O., 1997, Porosity Detection and Mapping in a Basinal Carbonate Setting, Offshore Norway, *in Carbonate Seismology*, ed. by Ibrahim Palaz and Kurt J. Marfurt, Geophysical developments series, no. 6, SEG, pages 321-336.

Dohr, G.P., 1985, *Seismic Shear Waves*, Editor. Part A: Theory, Part B: Applications: Handbook of Geophysical Exploration, Volumes 15A,15B. Geophysical Press.

Duennebier, F.K. and Sutton, G.H., 1995, Fidelity of ocean bottom seismic observations: *Marine Geophysical Researches*, **17**:535-555.

Durham, L.S., 1999, 4-C, 4-D Seismic the next waves: *AAPG Explorer,* April, pages 12-15.

Eaton, D. W. S., Slotboom, R. T., Stewart, R. R. and Lawton, D. C., 1990, Depth-variant converted-wave stacking: *60th Annual International Meeting, SEG*, Expanded Abstracts, pages 1107-1110.

Ebrom, D., Nolte, B., Purnell, G., Sukup, D. and Krail, P., 1998a, Analysis of multicomponent seismic data from offshore Gulf of Mexico: *68th Annual Meeting SEG Expanded Abstracts*, pages 162-165.

Ebrom, D., Krail, P., Ridyard, D. and Scott, L., 1998b, 4-C/4-D at Teal South: *The Leading Edge*, **17**(10): 1450-1453.

Entralgo, R.D. and Wadsworth, J.F., 1999, Teal South 4D-4C Acquisition Phase II (A Time Lapse Laboratory Field Study): *Sixth International Congress of the Brazilian Geophysical Society*, paper SBGf178.

ERCH, 1999, Energy Research Clearing House. http//www.erch.org.

Esteves, M.G.P., 1996, *Movimentos de massa: um estudo de integracao de dados geologicos, geofisicos, geotecnicos e oceanograficos*: M.Sc. Thesis, Universidade Federal Fluminense, Brazil *(in portuguese)*.

Farmer, C.L. and Barkved, O.I., 1997, Influence of syn-depositional faulting on thickness variations in chalk reservoirs – Valhall and Hod Fields: *Petroleum Geology of Northwest Europe: Proceedings of the 5th Conference*. Geological Society of London.

Fromm, G., Krey, Th. and Wiest, B., 1985, Static and dynamic corrections: *in* Dohr, G. *(ed.) Seismic Shear Waves*, Handbook of Geophysical Exploration, **15a**: 191-225.

Gaiser, J.E., 1998, Compensating OBC data for variations in geophone coupling: *68th Annual Meeting SEG Expanded Abstracts*, paper SP 12.6, pages 1429-1432.

Gaiser, J.E. and Jackson, A.R., 1998, 3-D PS-wave midpoint transformation in variable media: *68th Annual Meeting SEG Expanded Abstracts*, paper SP 12.3, pages 1417-1420.

Gaiser, J.E., 1999a, Enhanced PS-wave images and attributes using prestack azimuth processing: *69th Annual Meeting SEG Expanded Abstracts*, paper

SAVO/MC 1.4.

_______, 1999b, Coupling Analysis of Teal South Phase II Data: *ERCH 4C-4D Forum*, October, Houston.

Geis, W.T., Stewart, R.R., Jones, M.J. and Katopodis, P.E., 1990, Processing, correlating, and interpreting converted shear-waves from borehole data in southern Alberta: *Geophysics*, **55**:660-669.

George, D., 1996, From targeting submarines to acquiring accurate 3D seismic: Vertical-cable seismic launched by PGS-Texaco alliance: *Offshore*, March, p.30-31.

Granholm, P.-G., Larsen, D.O., Torudbakken, B. and Willersrud, K., 1996, Data-focused exploration in a frontier area, including ocean bottom seismic – a case study from the Nyk high in the Voring Basin, Norway: *58th EAGE Conference Extended Abstracts*, paper P162.

Guimarães, M.G., Sekharan, K.K., Sukup, D. and Krail, P., 1998, 3-D Pre-stack depth migration of vertical cable data over SEG/EAGE physical model: *68th Annual Meeting SEG Expanded Abstracts*, paper SP 4.6, pages 1182-1185.

Gulati, J.S. and Stewart, R.R., 1997, Analysis of mode conversions over high-velocity layers: *CREWES Research Report*, volume 9, chapter 25.

GX Technology, 1994. 3D-VSP^{TM} User Guide: Release 2.0 Edition, November 1994.

GX Technology, 1997. A guide to 3D-VSP^{TM} Seismic Simulation: Release 4.2, March 1997.

Hamilton, E. L., 1976, Shear-wave velocity versus depth in marine sediments: a review: *Geophysics*, **41**: 985-996.

_____ 1979, V_P/V_S and Poisson's ratio in marine sediments and rocks: *Journal of the Acoustical Society of America*, **66**(4): 1093-1101.

Harrison, M.P., 1992, *Processing of P-SV Surface-Seismic Data: Anisotropy Analysis, Dip Moveout, and Migration*: Ph.D. thesis, The University of Calgary, Department of Geology and Geophysics. 229 pages.

Hovem, J.M., Richardson, M.D. and Stoll, R.D., 1991, *Shear Waves in Marine Sediments*. Proceedings of the Conference on Shear Waves in Marine Sediments, La Spezia, Italy, October 15-19, 1990. Kluwer Academic Publishers, 593 pages.

Hughes, S., Barton, P., Harrison, D. and Johnson, M., 1995, Exploration in the Faeroe-Shetland Basin using densely spaced arrays of ocean bottom seismometers: *EAGE 57TH Conference and Technical Exhibition*, paper C002.

Iverson, W.I., Fahmy, B.A. and Smithson, S.B., 1989, V_PV_S from mode-converted P-SV reflections: *Geophysics*, **54**(7): 843-852.

Japsen, P., 1998, Regional velocity-depth anomalies, North Sea chalk: a record of overpressure and Neogene uplift and erosion: *AAPG Bulletin*, **82**(11):2031-2074.

Jin, S., 1999, Characterizing reservoir by using jointly P- and S-wave AVO analyses: 69th *Annual Meeting SEG Expanded Abstracts*, paper SAVO/MC 1.1.

Johnson, S.H. and McAlister, R.E., 1981, Bottom seismometer observation of airgun signals at Lopez Island: *Marine Geophysical Research,* **5**:87-102.

Kolbjornsen, K., Larsen, L.O., Kristiansen, P. and Berteussen, K.A., 1991, Monitoring of an underground flow by sea bottom seismic instruments – A case study: *53rd Mtg. EAEG* Abstracts 202-203, paper B051.

Kommedal, J.H., Barkved, O.I. and Thomsen, L.A., 1997, Acquisition of 4 Component OBS Data – a case study from the Valhall field*: 59th Mtg. EAEG, Extended Abstracts,* session: B047*.*

Krail, P.M., 1991, Case history vertical-cable 3D acquisition: *53rd EAEG Meeting*, paper B052, page 206.

_____, 1993, Sub-salt acquisition with a marine vertical-cable: *63rd SEG Meeting*, paper WS2.5, page 1376.

_____, 1994a, Measurements of cable shape in a cross current: *Geophysics*, **59**(7): 1156-1159.

_____, 1994b, Vertical-cable as a subsalt imaging tool: *The Leading Edge*, **13**(8): 885-887.

_____, 1997, Vertical-cable marine seismic acquisition: *Offshore Technology Conference*, paper OTC 8315, pages 347-355.

Krebes, E., 1989, *Seismic Theory and Methods*: GOPH 645 Course notes, Fall 1996, University of Calgary, Geology & Geophysics Department.

Kristiansen, P., 1998, Application of marine 4C data to the solution of reservoir characterization problems. 68th *Annual Meeting SEG Expanded Abstracts*, paper RC 1.8, pages 908-909.

Kubena, M.E. and Post, M.L., 1992, *Factual data report on soil investigation, offshore Brazil*: PETROBRAS / Fugro-McClelland Engineers B.V. Reports N-2850-701, 702, 703, 801, and 802. PETROBRAS Internal Reports.

Landro, M., Buland, A. and D'Angelo, R., 1995, Target-oriented AVO inversion of data from Valhall and Hod fields: *The Leading Edge*, **14**(8): 855-861.

Landro, M., 1999, Virgil Kauffman Gold Medal Award for Eivind W. Berg: *The Leading Edge*, **18**(10): 1195-1196.

de Lange, G., 1991, Experience with the seismic cone penetrometer in offshore site investigations: *Shear Waves in Marine Sediments*, eds. J.M. Hovem *et al.*, pages 275-282. Kluwer Academic Publishers.

Larner, K. and Ng, P., 1984. 3-D Marine seismic survey direction: strike or dip?: *54th Annual Meeting SEG Expanded Abstracts*, paper MAR1.5.

Lavoie, D. and Anderson, A., 1991, Laboratory measurements of acoustic properties of periplatform carbonate sediments: *Shear Waves in Marine Sediments,* eds. J.M. Hovem *et al.*, pages 111-120, Kluwer Academic Publishers.

Lawton, D.C., 1993, Optimum bin size for converted wave 3-D asymptotic mapping: *CREWES Research Report*, volume 5, chapter 28.

Lawton, D.C. and Hoffe, B.H., 1999, Some issues for 3C-3D OBC seismic data: *CREWES Research Report*, volume 11, chapter 19.

Leach, P., 1997, Strathspey vertical-cable seismic survey: a North-Sea first: *Offshore Europe Conference (SPE International)*, Aberdeen, Scotland, 9-12 September 1997, SPE 38508.

Leonard, R.C. and Munns, J.W., 1987, *Valhall*, *in* Geology of the Norwegian Oil and Gas Fields, ed. by A.M. Spencer *et al*., Graham & Trotman, pages 153-163.

Lewis, B.T.R. and Tuthill, J.D., 1981, Instrumental waveform distortion on ocean bottom seismometers: *Marine Geophysical Research,* **5**:79-86.

Li, X. and Bancroft, J.B., 1997a, Converted wave migration and common conversion point binning by equivalent offset: *67th Annual SEG Meeting*, Expanded Abstracts, pages 1587-1590.

Li, X. and Bancroft, J.C., 1997b, A new algorithm for converted wave pre-stack migration: *CREWES Research Report*, volume 9, chapter 26.

Li, X.-G., Keys, R.G., Mack, H. and Xu, S., 1999, Converted-wave processing of 4C OBC data: *Offshore Technology Conference 1999*, paper OTC 10982.

Li, X.-Y., MacBeth, C., Hitchen, K., Hanssen, P., 1998, Using converted shear-waves for imaging beneath basalt in deep water plays: *68th Annual Meeting SEG Expanded Abstracts*, paper SP 10.6, pages 1369-1372.

Li, X.-Y. and Yuan, F., 1999, Geophone orientation and coupling in three-component sea-floor data: a case study: *Geophysical Prospecting*, **47**(6):995-1014.

Loncarevic, B.D., 1983, *Ocean Bottom Seismometry in* CRC Handbook of Geophysical Exploration at Sea, R.A. Geyer and J.R. Moore ed., CRC Press, Inc.

Longshaw, S.K., Sunderland, J. and Horn, I., 1998, Mode Conversion and Multiples: *68th Annual Meeting SEG Expanded Abstracts*, paper SP 9.6, pages 1340-1342.

Macelwane, J.B. and Sohon, F.W., 1936, *Introduction to Theoretical Seismology, Part I: Geodynamics*. John Wiley & Sons, 366 pages.

MacLeod, M.K., Hanson, R.A., Hadley, M.J., Reynolds, K.J., Lumley, D., McHugo, S. and Probert, A., 1999, The Alba Field OBC Seismic Survey: *Sixth International Congress of the Brazilian Geophysical Society*, paper SBGf423.

Margrave, G.F., Lawton, D.C. and Stewart, R.R., 1998, Interpreting channel sands with 3C-3D seismic data: *The Leading Edge,* **17**(4): 509-513.

Maxwell, P.W., 1999, A new seismic sensor – at last!: *The Leading Edge*, **18**(10): 1182-1183.

McBarnet, A. (ed.), 1997a, Western and Geco-Prakla vie for 4C glory: *First Break*, **15**(9): 285.

McBarnet, A. (ed.), 1997b, 4C – new dimension in marine seismic: *First Break*, **15**(9): 292-293.

McBarnet, A. (ed.), 1997c, Companies gear up to meet ocean bottom survey technology challenge: *First Break*, **15**(10): 334-336.

Mersereau, R.M., 1979, The processing of hexagonally sampled two-dimensional signals: *Proceedings of the IEEE*, **67**(6): 930.

Mjaaland, S., Sparkman, G. and Thomsen L., 1999, Subject: Benchmarking Vector Fidelity of Seismic Acquisition Systems: *www.erch.com*.

Mjelde, R., Sellevoll, M.A. and Berg, E.W., 1991, Shear-waves from 3-C ocean bottom seismographs indicative of anisotropy in the lower crust: *53rd EAEG Meeting,* Expanded Abstracts, paper D034, pages 382-383.

Mjelde, R., Berg, E.W., Strom, A., Riise, O., Shimamura, H., Shiobara, H., Kodaira, S. and Kanazawa, T., 1995, Three-component ocean bottom seismograph used in prospecting in the Voring Basin, N. Norway: *65th Annual International Meeting, SEG*, paper PP2.12, pages 537-540.

Moldoveanu, N., Combee, L., Van Baaren, P., Addessi, D. and Stubbington, L., 1996, Repeatability of the seismic experiments for 4D seismic in transition zone surveys: *66th Annual International Meeting, SEG*, paper ACQ 1.2, pages 5-8.

Moldoveanu, N., Henman, R., Vlasin, J. and Spradley, M., 1997, Bottom referenced vertical hydrophone arrays-towed streamers – a comparison study: *EAGE 59th Conference and Technical Exhibition*, paper B019.

Munns, J.W. and Mullen, D., 1987, Fault Detection using Borehole Seismic Surveys: *Atlas of Seismic Stratigraphy*, AAPG Studies in Geology # 27, volume 1, pages 117-118.

Muskhelishvili, N.I., 1963, *Some Basic Problems of the Mathematical Theory of Elasticity: Fundamental Equations, Plane Theory of Elasticity, Torsion, and Bending*. Translated from the Russian by J.R.M. Radok. P. Noordhoff (Groningen, Netherlands). 718 pages.

Nazir, A and Alcock, T., 1992, *Valhall field – the first ten years*: *in* North Sea oil and gas reservoirs-3, Aasen, J.0. (ed.), Kluwer Academic Publishers.

Newman, P., 1973, Divergence effects in a layered earth: *Geophysics*, **38**: 481-488.

Nolte, B., Sukup, D. and Bishop, K., 1999, Anisotropic Prestack Depth Migration of Converted-Wave Data from the Gulf of Mexico: *69th Annual Meeting SEG Expanded Abstracts*, paper SAVO/MC 1.2.

Nur, A., 1993, *Rock Physics Short Course at Campinas State University (UNICAMP)*, São Paulo, Brazil, November.

O'Brien, M.J. and Etgen, J.T., 1998, Wavefield imaging of complex structure with sparse, point-receiver data: *68th Annual Meeting SEG Expanded Abstracts*, paper SP10.5, pages 1365-1368.

Orren, R., 1999, Choosing the right site for ocean bottom seismic surveys: *First Break*, **17**(9): 299.

Pereyra, V., 1988, Two-point ray tracing in complex 3-D media: *58th SEG Meeting*, paper SI 5.6, pages 1056-1060.

_____, 1992, Two-point ray tracing in general 3D media: *Geophysical Prospecting*, **40**:267-287.

Petersen, D.P. and Middleton, D., 1962, Sampling and reconstruction of wave-number limited functions in n-dimensional Euclidean spaces: *Information and Control*, **5**: 279.

Petzet, G.A. , 1995, Texaco partnership to offer marine 3D seismic method: *Oil and Gas Journal*, December 11, p.26-27.

PGS, 1996, *Multicomponent Seabed Seismic Survey ("Dragged Array"), Valhall Oilfield*. Internal Report.

Purnell, G.W., Nolte, B.J., Krail, P.M. and Ebrom, D.A., 1999, Analysis of 4-C data for AVO effects at Teal South, Eugene Island 354: *Offshore Technology Conference 1999*, paper OTC 10984.

Richardson M.D., Muzi E., Miaschi B. and Turgutcan F., 1991, Shear wave velocity gradients in near-surface marine sediment: *Shear Waves in Marine Sediments* (eds J.M. Hovem *et al.*), pages 295-304. Kluwer Academic Press.

Richart , F.E., Hall Jr., J.R. and Woods, R.D., 1970, *Vibrations of Soils and Foundations*. Prentice-Hall, 414 pages.

Richart, F.E., 1975, Some effects of dynamic soil properties on soil-structure interaction: *Journal of the Geotechnical Engineering Division*, American Society of Civil Engineers, **101**(GT12): 1197-1240.

Robertson, P.K., Campanella, R.G., Gillespie, D. and Rice, A., 1986, Seismic CPT to measure in-situ shear wave velocity: *Journal of Geotechnical Engineering*, **112**(8): 791-803.

Roche, S., Maxwell, P. and Fisseler, G., 1999, Teal South 4C/3D survey: a model for 4C/4D seismic data acquisition: *Offshore Technology Conference 1999*, paper OTC 10983.

Roed, K., Dietrichson, E., Ireson, D. and Howe, D., 1996, The design, manufacture and deployment of buried sea-bed detectors in deep water for 4-D seismic monitoring. A case history: *66th Annual Meeting SEG Expanded Abstracts*, paper PP4.4, pages 1076-1078.

Samson, C., Barton, P.J. and Karwatowski, J., 1995, Imaging beneath an opaque basalt layer using densely sample wide-angle OBS data: *Geophysical Prospecting*, **43**:509-527.

Sanders, J.I. and Starr, J.G., 1999, The ocean bottom cable: a modern marine multicomponent system: *Offshore Technology Conference 1999*, paper OTC 10986.

Sekharan, K.K., Guimarães, M.A.G., Jackson, R.A, Ebrom, D.A, Krail, P. and Sukup, D., 1997, 3D marine data acquisition and processing over ACTI/EAGE physical model using vertical hydrophone cables: *Offshore Technology Conference*, paper OTC 8350, pages 575-578.

Sheriff, R.E. and Geldart, L.P., 1995, *Exploration Seismology*, Second Edition, Cambridge University Press, 592 pages.

Sonneland, L., Roed, K. and Navrestad, T., 1995a, Sub-sea seismic: acquisition and data analysis procedures: *Offshore Technology Conference 1995*, paper OTC 7658.

Sonneland, L., Rod, K., Hutton, G. and Tjostheim, B., 1995b, The impact of sub-sea seismic: *57th EAEG Conference and Technical Exhibition Expanded Abstracts*, paper E039.

Stewart, R.R., 1997, *3-C Seismic Exploration Course Notes* - GOPH 699.01, Fall 1997, The University of Calgary, Department of Geology and Geophysics.

Strand, C., 1997, *Processing of a 4-Component Ocean Bottom Seismic Dataset from the Valhall Field*: M.Sc. Thesis, Department of Geophysics, University of Oslo.

Sullivan, L.B., 1995, Marine Geophones: Improvement of Seafloor Coupling and Suppression of Flow-Induced Noise: *Offshore Technology Conference 1995*, paper OTC 7656.

Sutton, G.H., Duennebier, F.K. and Iwatake, B., 1981a, Coupling of ocean bottom seismometers to soft bottoms: *Marine Geophysical Research,* **5**:35-52.

Sutton, G.H., Lewis, B.T.R., Ewing, J., Duennebier, F.K., Iwatake, B. and Tuthill, J.D., 1981b, An overview and general results of the Lopez Island OBS experiment: *Marine Geophysical Research,* **5**:3-34.

Tatham, R.H. and Stoffa, P.L., 1976, V_P/V_S – A potential hydrocarbon indicator: *Geophysics*, **41**:837-849.

Tatham, R.H. and McCormack, M.D., 1991, *Multicomponent Seismology in Petroleum Exploration*: Investigation in Geophysics Series Volume 6, SEG. 248 pages.

Tessmer, G. and Behle, A., 1988, Common Reflection Point Data-Stacking Technique for Converted Waves: *Geophysical Prospecting*, **36**:671-688.

Theilen, F.R. and Pecher, A., 1991, Assessment of shear strength of the sea bottom from shear wave velocity measurements on box cores and in-situ: *Shear Waves in Marine Sediments*, eds. J.M. Hovem *et al.*, pages 67-74. Kluwer Academic Publishers.

Thomsen, L., 1986, Weak elastic anisotropy: *Geophysics*, **51**:1954-1966.

Thomsen, L., Barkved, O.I., Haggard, W., Kommedal, J. and Rosland, B.O., 1997, Converted wave imaging of Valhall reservoir: *59th EAGE Conference Extended Abstracts*, paper B048.

Thomsen, L., 1998, Converted-Wave Reflection Seismology over Anisotropic, Inhomogeneous Media: *68th Annual Meeting SEG Expanded Abstracts*, paper SS 3.4, pages 2048-2051.

Thomsen, L., Barkved, O.I. and Rosland, B.O., 1999, The 3D/4C OBS survey at Valhall: *Offshore Technology Conference 1999*, paper OTC 10937.

Tree, E., 1999, Vector Infidelity in Ocean Bottom Recording: *ERCH 4C-4D Forum*, October, Houston.

Wiest, B. and Edelmann, H.A.K., 1984, Static corrections for shear wave sections: *Geophysical Prospecting*, **32**: 1091-1102.

Yao, Z.S. and Roberts, R., 1993, Observations of BABEL P- and S-wave polarizations: *Proceedings of the 9th Workshop Meeting of the Commission on Controlled Source Seismology*, Moscow 27-30 September.

Young, G.B. and Braile, L.W., 1976, A computer program for the application of Zoeppritz's amplitude equations and Knott's energy equations: *Bulletin of Seismological Society of America*, pages 1881-1885.

Yuan, J., Yang, X., Ziolkowski, A. and Strijbos, F., 1998, Processing 4-C sea-floor seismic data: a case example from the North Sea: *68th Annual Meeting SEG*

Expanded Abstracts, paper MC1.1, pages 714-717.

Zachariadis, R.G., Thomason, H.B. and Teague, H.E., 1983, Ocean Bottom Seismometers in Seismic Exploration Surveys: Planning and Operations: *53rd Annual Meeting SEG Expanded Abstracts*, paper S15.6, p.468-470.

Zachariadis, R.G. and Bowden, E.A., 1986, Ocean bottom cable: a fixed multichannel sea floor reflection system: *56th Annual Meeting SEG Expanded Abstracts*, paper S4.4.

Zelikovitz, S.J. and Prothero, W.A., 1981, The vertical response of an ocean bottom seismometer: analysis of the Lopez Island vertical transient tests: *Marine Geophysical Research,* **5**:53-78.

Zhang, Q., San, Z., Brown, R.J. and Stewart, R.R., 1994, VSP interpretation from Joffre, Alberta: *CREWES Project Research Report*, volume 6, chapter 33.

Appendix I – Acquisition parameters for the Valhall seismic survey (after PGS, 1996)

Source

- Type: Bolt Longlife airguns
- Volume: 3180 cu. in.
- Pressure: 2000 or 2500 psi
- Configuration: 8 guns/subarray, 2 subarrays
- Depth: 6 m
- 25 m shot point interval
- Length: 16.65 m
- Peak/bubble ratio: 14.1
- Gun synchronisation: +- 1ms

Ocean bottom equipment

- Type: Chesapeake 24 bit modules
- Length: 175 m
- Skin material: steel armour
- Groups per cable: 8
- Group interval: 25 m
- Active group length: single station
- Input impedance: 6.05 Mohm
- Hydrophone: Basys BM-4, sensitivity –196 dB re 1V/μPa, capacitance 2.7nF
- Geophone: SM-4 10 Hz, sensitivity 28.8 V/m/s, coil resistance 375 Ohm

Recording

- Instrument: IBM Sentry
- Low cut filter: 4.5 Hz, 18 dB/oct

- High cut filter: 200 Hz, > 200 dB/oct

Navigation

- Company: Fugro, Geoteam
- Primary: DGPS Starfix
- Secondary: DGPS Seastar
- GPS receivers: Trimble 4000 DS
- Navigation software: PCSeis
- Tailbuoy gun array: Geotrack

Appendix II – Acquisition parameters for Teal South seismic survey (after Baker Hughes, 1999).

Source: 2 sub arrays of 750 in^3 each, 3,000 +/- 100 psi, depth 3.0 +/- 0.5 m, acoustic output 39.0 bar-m peak-to-peak (3-128 Hz).

Receivers: 4-C receivers in 7 ocean-bottom cables.

Recording: 24 bits remote recording boxes, 2 ms sampling interval, record length 6 seconds, low-cut filter out (3 Hz 12dB/octave), high cut 200 Hz.

Navigation: DGPS; source tracking by GPS antenna on each gun string, receiver location to be compute using first break.

Appendix III - Matlab function used to obtain bin fold, azimuth and offset distribution

```
function[fold,maxoffset,nearoffset,middleoffset,faroffset,azi060,azi60120,azi1201
80,azi180240,azi240300,azi300360]=bin11(xref,yref,xsou,ysou,xrec,yrec,binx,bin
y,maxnbinsx,maxnbinsy,azi)
%
%[fold,maxoffset,nearoffset,middleoffset,faroffset,azi060,azi60120,azi120180,azi
%180240,azi240300,azi300360]=bin11...
%       (xref,yref,xsou,ysou,xrec,yrec,binx,biny,maxnbinsx,maxnbinsy,azi);
%
% obtains fold, offsets (near, middle and far) and azimuths (6 sectors) for each
%bin in a 3D seismic survey
%
%input: xref,yref,xsou,ysou,xrec,yrec: x,y coordinates of reflection point,
%       source and receiver
%      binx, biny: bin dimensions in x and y
%      maxnbinsx,maxnbinsy: maximum number of bins in x and y
%      azi: source-receiver azimuth
%
% Carlos Rodriguez, oct/98 (based on nov/97 bin.m)
%

% sizing variables

x1=maxnbinsx;
y1=maxnbinsy;
  fold(x1,y1) = 0;
  nearoffset(x1,y1) = 0;
  middleoffset(x1,y1) = 0;
```

```
  faroffset(x1,y1) = 0  ;
  azi060(x1,y1) = 0;
  azi60120(x1,y1) = 0;
  azi120180(x1,y1) = 0;
  azi180240(x1,y1) = 0;
  azi240300(x1,y1) = 0;
  azi300360(x1,y1) = 0;

%%%%%%%%%%%%%%%%%%%%%%%%%%%%%%%%%%%%%%%%%%%

% the first loop obtains offset and corrects for negative azimuths

n1=1;
while(n1<=length(xref))
 deltax = xsou(n1) - xrec(n1) ;
 deltay = ysou(n1) - yrec(n1) ;
 offset(n1)= sqrt(deltax*deltax + deltay*deltay);

% this loop is for data (e.g.,GX) where positive (0=Y+ axis,90=X+ axis) and
% negative azimuths are present; it also checks for azimuth=0
 if azi(n1)<=0
  azi(n1) = azi(n1) + 360 ;
 end

 n1=n1+1;
end

maxoffset=max(offset)
n2=1;
```

```
% the second loop obtains fold,near,middle and far offsets
% and azimuth distribution for all bins

while(n2<=length(xref))
 nbinx = ceil((xref(n2)-2000)/binx);    % 2000 used as origin for model1
 nbiny = ceil((yref(n2)-2000)/biny);    % (target min x and y)

  if nbinx<=0           % check if x or y reflection point is below min x or y
   nbinx=1;             % or over max x or y (this may be necessary due to
  elseif nbinx>maxnbinsx % internal Matlab approximations)
   nbinx=maxnbinsx;
  elseif nbiny<=0
   nbiny=1;
  elseif nbiny>maxnbinsy
   nbiny=maxnbinsy;
  end

 fold(nbinx,nbiny) = fold(nbinx,nbiny) + 1;

 if (offset(n2)<(maxoffset/3))
  nearoffset(nbinx,nbiny) = nearoffset(nbinx,nbiny) + 1;
 elseif (offset(n2)>(maxoffset*0.6667))
  faroffset(nbinx,nbiny) = faroffset(nbinx,nbiny) + 1;
 else
  middleoffset(nbinx,nbiny) = middleoffset(nbinx,nbiny) + 1;
 end

 if (azi(n2)<60)
  azi060(nbinx,nbiny) = azi060(nbinx,nbiny) + 1;
 elseif (60<=azi(n2)&azi(n2)<120)
```

```
  azi60120(nbinx,nbiny) = azi60120(nbinx,nbiny) + 1;
 elseif (120<=azi(n2)&azi(n2)<180)
  azi120180(nbinx,nbiny) = azi120180(nbinx,nbiny) + 1;
 elseif (180<=azi(n2)&azi(n2)<240)
  azi180240(nbinx,nbiny) = azi180240(nbinx,nbiny) + 1;
 elseif (240<=azi(n2)&azi(n2)<300)
  azi240300(nbinx,nbiny) = azi240300(nbinx,nbiny) + 1;
 else
  azi300360(nbinx,nbiny) = azi300360(nbinx,nbiny) + 1;
 end
n2=n2+1;

end
```